SISSA
Scuola
Internazionale
Superiore di
Studi Avanzati

Physics Area - PhD course in
Astrophysics and Cosmology

Gravitational waves throughout galaxy evolution: stellar BH mergers and heavy SMBH seeds.

Candidate:
Lumen Boco

Advisors:
Andrea Lapi
Carlo Baccigalupi

Academic Year 2020 - 2021

Declaration of Authorship

I, Lumen Boco, declare that this thesis titled, "Gravitational waves throughout galaxy evolution: stellar BH mergers and heavy SMBH seeds." and the work presented in it are my own. I confirm that:

- This work was done wholly or mainly while in candidature for a research degree at this University.
- Where any part of this thesis has previously been submitted for a degree or any other qualification at this University or any other institution, this has been clearly stated.
- Where I have consulted the published work of others, this is always clearly attributed.
- Where I have quoted from the work of others, the source is always given. With the exception of such quotations, this thesis is entirely my own work.
- I have acknowledged all main sources of help.
- Where the thesis is based on work done by myself jointly with others, I have made clear exactly what was done by others and what I have contributed myself.

Signed:

Date:

"*The effort to understand the universe is one of the very few things that lifts human life a little above the level of farce, and gives it some of the grace of tragedy.*"

Steven Weinberg

SCUOLA INTERNAZIONALE SUPERIORE DI STUDI AVANZATI

Abstract

SISSA
Physics area

Doctor of Philosophy

Gravitational waves throughout galaxy evolution: stellar BH mergers and heavy SMBH seeds.

by Lumen Boco

The main goal of my thesis is to carefully characterize different astrophysical processes leading to gravitational wave (GW) emission, strongly relying on theoretical and observational astrophysical basis. From an observational point of view, current interferometers (Advanced Laser Interferometer Gravitational wave Observatory/Virgo (AdvLIGO/Virgo)) and future detectors (Einstein Telescope (ET), Cosmic Explorer (CE), Deci-hertz Interferometer Gravitational wave Observatory (DECIGO), Laser Interferometer Space Antenna (LISA)) will greatly enlarge the number of detected GW events. However, in order to extract meaningful information about various astrophysical phenomena and improve our knowledge on cosmology and fundamental physics from this large sample of observational data, a correct modelization of the impact of different astrophysical processes on GWs rates is necessary.

The marking feature of all the work is an accurate and deep study of the galactic environment, making use of classic theoretical arguments and recent observational results in the galaxy formation and evolution field. Galactic properties, such as star formation rate, gas and stellar density, metallicity, can have a profound impact on stellar and compact object evolution and on the ensuing GW emissions. In particular, throughout the thesis I focused on the study of 2 different channels of GW production: merging of isolated double compact object binaries of stellar origin (neutron stars and stellar black holes) and dynamical merging of stellar and, eventually, primordial black holes in the central regions of early-type galaxy progenitors.

In the context of double compact object merging binaries, given the relevance of gas-phase metallicity for all the stellar and binary evolution processes, the main effort of my work is in the characterization of a metallicity dependent cosmic star formation rate density. I compute this term in various ways, highlighting the impact of different galactic prescriptions, such

as galaxy statistics and metallicity scaling relations. In particular I focus on the gas-phase metallicity, showing that the two main empirical scaling relations present in literature, the Mass Metallicity Relation and the Fundamental Metallicity Relation, hold substantially different results at high redshift ($z > 2$), with the Fundamental Metallicity Relation featuring relatively high metallicitites $Z \sim 0.4 - 0.5\, Z_{\odot}$ and the Mass Metallicity Relation predicting a significant metallicity drop $Z < 0.1\, Z_{\odot}$. I discuss the reasons and possible biases originating this discrepancy, arguing in favor of the Fundamental Metallicity Relation or of a slowly declining Mass Metallicity Relation. I also present a chemical evolution model to deal with metallicity from a theoretical point of view and I find a pleasant agreement between the model and the Fundamental Metallicity Relation. Finally, I show the impact of these different astrophysical prescriptions on the merging rates and on the properties of compact objects binaries, such as their chirp mass or time delay distribution. I complete the work forecasting the ensuing GW detection rates with present and future detectors, as well as the expected lensed event rates and the stochastic GW background.

As for the dynamical merging channel, recent observations of the extremely star-forming and gas-dense environments in the central regions of early-type galaxy progenitors at $z \gtrsim 1$, inspired the idea for the proposal of a new mechanism for the growth of supermassive black hole seeds. This envisages the migration and merging of compact objects via gaseous dynamical friction toward the galactic center where a central black hole accumulates mass thanks to these continuous merging events. I show that, under reasonable assumptions, the process can build up central BH masses of order $10^4 - 10^5\, M_{\odot}$ within some 10^7 yr, so effectively providing heavy seeds before standard (Eddington-like) disk accretion takes over to become the dominant process for further BH growth. Remarkably, such a mechanism may provide an explanation, alternative or complementary to other processes, for the buildup of billion solar masses black holes in quasar hosts at $z \gtrsim 7$, when the age of the Universe $\lesssim 0.8$ Gyr constitutes a demanding constraint. This process naturally present a possibility to be tested via detections of the gravitational waves produced by mergers between the migrating compact objects and the growing central black hole. I also make predictions for the produced stochastic GW background which extends over a wide range of frequencies $10^{-6} \lesssim f\,[\mathrm{Hz}] \lesssim 10$, very different from the typical range originated by mergers of isolated binaries. I show that both the single events and the background could be revealed by future ground- and space-based interferometers as ET, DECIGO and LISA.

This Ph.D. thesis is based on the following publications and submitted papers:

1. Merging Rates of Compact Binaries in Galaxies: Perspectives for Gravitational Wave Detections, by **Boco, L.**; Lapi, A.; Goswami, S.; Perrotta, F.; Baccigalupi, C.; Danese, L.; *The Astrophysical Journal, Volume 881*(2), Page 157, August 2019.

2. Growth of Supermassive Black Hole Seeds in ETG Star-forming Progenitors: Multiple Merging of Stellar Compact Remnants via Gaseous Dynamical Friction and Gravitational-wave Emission, by **Boco, L.**; Lapi, A.; Danese, L.; *The Astrophysical Journal, Volume 891*(1), Page 94, March 2020.

3. Evolution of Galaxy Star Formation and Metallicity: Impact on Double Compact Object Mergers, by **Boco, L.**; Lapi, A.; Chruslinska, M.; Donevski, D.; Sicilia, A.; Danese, L.; *The Astrophysical Journal, Volume 907*(2), Page 110, February 2021.

4. Growth of Massive Black Hole Seeds by Migration of Stellar and Primordial Black Holes: Gravitational Waves and Stochastic Background, by **Boco, L.**; Lapi, A.; Sicilia, A.; Capurri, G.; Baccigalupi, C.; Danese, L.; *Journal of Cosmology and Astroparticle Physics, Volume 2021*(10), Page 035, October 2021.

5. New Analytic Solutions for Galaxy Evolution. II. Wind Recycling, Galactic Fountains, and Late-type Galaxies, by Lapi, A.; Pantoni, L.; **Boco, L.**; Danese, L.; *The Astrophysical Journal, Volume 897*(1), Page 81, July 2020.

6. Exploring galaxies-gravitational waves cross-correlations as an astrophysical probe, by Scelfo, G.; **Boco, L.**; Lapi, A.; Viel, M.; *Journal of Cosmology and Astroparticle Physics, Volume 2020*(10), Page 045, October 2020.

7. Einstein, Planck and Vera Rubin: relevant encounters between the Cosmological and the Quantum Worlds, by Salucci, P.; Esposito, G.; Lambiase, G.; Battista, E.; Benetti, M.; Bini, D.; **Boco, L.**; Sharma, G.; Bozza, V.; Buoninfante, L.; Capolupo, A.; Capozziello, S.; Covone, G.; D'Agostino, R.; De Laurentis, M.; De Martino, I.; De Somma, G.; Di Grezia, E.; Di Paolo, C.; Fatibene, L.; Gammaldi, V.; Geralico, A.; Ingoglia, L.; Lapi, A.; Luciano, G.G.; Mastrototaro, L.; Naddeo, A.; Pantoni, L.; Petruzziello, L.; Piedipalumbo, E.; Pietroni, S.; Quaranta, A.;

Rota, P.; Sarracino, G.; Sorge, F.; Stabile, A.; Stornaiolo, C.; Tedesco, A.; Valdarnini, R.; Viaggiu, S.; Yunge, A. A. V. *Frontiers in Physics, Volume 8*, Page 579, February 2021.

8. Intensity and anisotropies of the stochastic Gravitational Wave background from merging compact binaries in galaxies, by Capurri, G.; Lapi, A.; Baccigalupi, C.; **Boco, L.**; Scelfo, G.; Ronconi, T.; *Journal of Cosmology and Astroparticle Physics*, accepted.

9. The effects of the initial mass function on Galactic chemical enrichment, by Goswami, S.; Slemer, A.; Marigo, P.; Bressan, A.; Silva, L.; Spera, M.; **Boco, L.** ; Grisoni, V.; Pantoni, L.; Lapi, A.; *Astronomy & Astrophysics, Volume 650*(10), Page A203, June 2021.

10. Gravitational waves × HI intensity mapping: cosmological and astrophysical applications, by Scelfo, G.; Spinelli, M.; Raccanelli, A.; **Boco, L.**; Lapi, A.; Viel, M.; *Journal of Cosmology and Astroparticle Physics*, submitted.

11. The evolution of compact massive quiescent and star-forming galaxies derived from the R_e-R_h and $M_\star$-M_h relations, by Zanisi, L.; Shankar, F.; Fu, H.; Rodriguez-Puebla, A.; Avila-Reese, V.; Faisst, A.; Daddi, E.; **Boco, L.**; Lapi, A.; Giavalisco, M.; Saracco, P.; Buitrago, F. Huertas-Company, M.; Puglisi, A.; Dekel, A.; *Monthly Notices of the Royal Astronomical Society, Volume 505*(3), Page 4555, August 2021.

12. The Overall Black Hole Mass Function. I. Stellar Black Holes and Light Seed Distribution, by Sicilia, A.; Lapi, A.; **Boco, L.**; Spera, M.; Di Carlo, U. N.; Mapelli, M.; Shankar, F.; Alexander, D. M.; Bressan, A.; Danese, L.; *The Astrophysical Journal*, submitted.

13. The impact of the FMR and starburst galaxies on the (low-metallicity) cosmic star formation history, by Chruslinska, M.; Nelemans, G.; **Boco, L.**; Lapi, A.; *Monthly Notices of the Royal Astronomical Society*, accepted.

Acknowledgements

Prima di tutto voglio ringraziare il mio supervisor Andrea Lapi, non solo per avermi aiutato a "scovare" questo progetto e a superare le mie indecisioni, ma per avermi poi guidato attraverso esso con pazienza, ascoltando e discutendo ogni mia idea, dalle migliori alle più assurde. Ascolto e fiducia: questi gli elementi che non mi sono mai mancati durante il percorso. Ringrazio anche Luigi Danese, la cui brillantezza è sempre stata per me fonte di ispirazione.

Un grazie di cuore va ad Anna, la cui costante presenza, nonostante i molti spostamenti e cambiamenti, mi ha fatto vivere ogni posto come se fosse casa. Grazie per aver riempito la mia vita con mille idee e progetti. E, fra una partita al Signore degli Anelli e l'altra, non ti ho mai ringraziata abbastanza per aver trasformato le mie passioni in nostre passioni.

Grazie ai miei genitori e alla mia famiglia per avermi insegnato che l'unica cosa non effimera al mondo è la fame di conoscenza, la quale è come una roccia solida, impossibile da scalfire anche nei momenti difficili. Grazie anche per il sostegno continuo e incondizionato. Nonostante la lontananza so che ci siete e che mi siete vicini.

Un grazie a Trento e alle persone conosciute lì, le esperienze fatte saranno un bagaglio che mi accompagnerà per tutta la vita. Allo stesso modo ci tengo a ringraziare tutti gli amici di Trieste: nonostante la città non piacesse a nessuno, abbiamo creato un gruppo speciale, forte e pieno di vita, vivendo questo periodo insieme con massima felicità e spensieratezza. In particolare devo ringraziare Gigi: avere un possesso palla dell 80% a FIFA è stato uno fra i più grandi boost alla mia autostima. Dall'altra parte, le legnate che prendo a Gwent compensano. Senza contare tutti i discorsi di fisica e astrofisica, fonti di ispirazione per molte idee. Peccato per il mancato paper in collaborazione, lo faremo all'IMGU!

Contents

List of Figures

List of Tables

List of Abbreviations

ΛCDM	**L**ambda **C**old **D**ark **M**atter
AdvLIGO	**Adv**anced **L**aser **I**nterferometer **G**ravitational waves **O**bservatory
AGN	**A**ctive **G**alactic **N**uclei
ALMA	**A**tacama **L**arge **M**illimeter/submillimeter **A**rray
ALPINE	**A**LMA **L**arge **P**rogram to **IN**vestigate C^+ at **E**arly Times
BAO	**B**aryonic **A**coustic **O**scillations
BBN	**B**ig **B**ang **N**ucleosynthesis
BH	**B**lack **H**ole
CDM	**C**old **D**ark **M**atter
CE	**C**osmic **E**xplorer
CMB	**C**osmic **M**icrowave **B**ackground
CO	**C**ompact **O**bject
COSMOS	**COSM**ic Ev**O**lution **S**urvey
DCO	**D**ouble **C**ompact **O**bject
DECIGO	**D**eci-hertz **I**nterferometer **G**ravitational wave **O**bservatory
DE	**D**ark **E**nergy
DF	**D**ynamical **F**riction
DLA	**D**amped **L**yman-**A**lpha
DM	**D**ark **M**atter
ECDFS	**E**xtended **C**handra **D**eep **F**ield-South **S**urvey
EM	**E**lectro**M**agnetic
EOS	**E**quation **O**f **S**tate
ET	**E**instein **T**elescope
FIR	**F**ar **I**nfra**R**ed
FLRW	**F**riedmann **L**emaître **R**obertson **W**alker
FMR	**F**undamental **M**etallicity **R**elation
GHMF	**G**alactic **H**alo **M**ass **F**unction
GOODS	**G**reat **O**bservatories **O**rigins **D**eep **S**urvey
GSMF	**G**alaxy **S**tellar **M**ass **F**unction
GR	**G**eneral **R**elativity
GW	**G**ravitational **W**ave
HDM	**H**ot **D**ark **M**atter
HUDF	**H**ubble **U**ltra **D**eep **F**ield
IGM	**I**nter**G**alactic **M**edium

IMF	**I**nitial **M**ass **F**unction
IR	**I**nfra**R**ed
ISCO	**I**nnermost **S**table **C**ircular **O**rbit
ISM	**I**nter**S**tellar **M**edium
KAGRA	**KA**mioka **GRA**vitational wave detector
LF	**L**uminosity **F**unction
LIGO	**L**aser **I**nterferometer **G**ravitational waves **O**bservatory
LISA	**L**aser **I**nterferometer **S**pace **A**ntenna
LSS	**L**arge **S**cale **S**tructure
MOSDEF	**MOS**FIRE **D**eep **E**volution **F**ield
MS	**M**ain **S**equence
MSG	**M**ain **S**equence **G**alaxy
MZR	**M**ass Metallicity(**Z**) **R**elation
NFW	**N**avarro **F**renk **W**hite
NIR	**N**ear **I**nfra**R**ed
NS	**N**eutron **S**tar
pBH	**p**rimordial **B**lack **H**ole
SBG	**S**tar**B**urst **G**alaxy
SCUBA	**S**ubmillimetre **C**ommon-**U**ser **B**olometer **A**rray
SED	**S**pectral **E**nergy **D**istribution
SFG	**S**tar **F**orming **G**alaxy
SFH	**S**tar **F**ormation **H**istory
SFR	**S**tar **F**ormation **R**ate
sSFR	**s**pecific **S**tar **F**ormation **R**ate
SFRF	**S**tar **F**ormation **R**ate **F**unction
SGWB	**S**tochastic **G**ravitational **W**ave **B**ackground
SHOES	**S**upernova **H0** for the **E**quation of **S**tate
SIS	**S**ingular **I**sothermal **S**phere
SMBH	**S**uper**M**assive **B**lack **H**ole
SMG	**S**ub**M**illimeter **G**alaxy
S/N	**S**ignal to **N**oise ratio
SN	**S**uper**N**ova
UV	**U**ltra**V**iolet
VLA	**V**ery **L**arge **A**rray
WDM	**W**arm **D**ark **M**atter
ZAMS	**Z**ero-**A**ge-**M**ain-**S**equence

Physical Constants

Speed of Light	$c = 2.99792458 \times 10^{10}\,\mathrm{cm\,s^{-1}}$
Constant of gravitation	$G = 6.67 \times 10^{-8}\,\mathrm{g^{-1}\,cm^3\,s^{-2}}$
Parsec	$\mathrm{pc} = 3.09 \times 10^{18}\,\mathrm{cm}$
Year	$\mathrm{yr} = 3.16 \times 10^{7}\,\mathrm{s}$
Solar mass	$\mathrm{M}_\odot = 1.99 \times 10^{33}\,\mathrm{g}$
Solar luminosity	$L_\odot = 3.90 \times 10^{33}\,\mathrm{erg\,s^{-1}}$
Proton mass	$m_p = 1.66 \times 10^{-24}\,\mathrm{g}$
Boltzmann constant	$k_B = 1.38 \times 10^{-16}\,\mathrm{erg\,K^{-1}}$
Reduced Hubble constant	$h = 0.67$
Hubble constant	$H_0 = 100\,h\,\mathrm{km\,s^{-1}\,Mpc^{-1}}$
Critical density	$\rho_c = 2.8 \times 10^{11}\,h^2\,\mathrm{M_\odot\,Mpc^{-3}}$
Total matter density parameter	$\Omega_M = 0.32$
Baryon density parameter	$\Omega_b = 0.05$
Lambda density parameter	$\Omega_\Lambda = 0.68$
Solar metallicity	$Z_\odot = 0.0153$
Solar oxygen abundance	$12 + \log(O_\odot/H_\odot) = 8.76$

Chapter 1

From cosmology to galaxy evolution

The observation of the sky has accompanied the history of human kind since ancient times. Observation of stars, planets and celestial objects and the study of their positions and motions provided an enormous source for myths and spiritual beliefs, but they also laid the foundations for the biggest scientific and philosophical revolutions in human history. Even the sun itself, with its periodic motion, has always regulated the habits of each living organism on the Earth and it made possible to define the concept of time, which is strictly related to any scientific thought. In the modern ages sky observations led to the scientific revolution between the XVII and the XVIII century with the progressive breakthrough of the heliocentric system, whose scientific and philosophical implications have profoundly marked the human history up to our days. The detailed observations and study of the motion of celestial bodies built the bases for the the theory of gravity itself, which was the first great unification of forces and phenomena made by human kind, one of the key aspects of modern science.

However it was only on 1920 that cosmology in its modern fashion began to be talked about. Before that date we were completely blind on the real size of the Universe, with many scientists believing that all the observable objects in the sky were contained in the Milky Way. In 1920, Edwin Hubble, at Mount Wilson observatory, was able to identify a Cepheid variable star inside the "Andromeda nebula" and to determine its distance from the Earth, arriving to the conclusion that "Andromeda nebula", as well as many other spiral nebulae, were entirely other galaxies. The existence of many distant galaxies completely changed our way to look at the Universe and, combining the recent theory of General Relativity with images of galactic spectra, cosmological studies begun. Cosmology and galaxies observations are two scientific fields born together and have remained tightly coupled. On the one hand observations of galaxies at large scales have been and are still expected to be one of the most promising probes for cosmology, on the other

hand any galaxy formation and evolution theory must lay on a cosmological framework.

In the next Section I deal with the description of the structure and evolution of the Universe (Section 1.1). I then move to the evolution of scalar perturbations leading to the formation of dark matter halos (Section 1.2) and galaxies (Section 1.3). Throughout the Chapter I rely on the following classic textbooks on cosmology and galaxy evolution: Weinberg 1972, 2008; Ryden 2003; Mo et al. 2010; Cimatti et al. 2020. I warn the reader that this Chapter is introductory and meant to present the main cosmological results and some elements of galaxy formation and evolution that will be extensively used throughout the thesis. The reader only interested in new research aspects can directly proceed to Chapter 2.

1.1 Universe background

In this Section I aim at describing the background structure of the Universe at large scales exploiting the cosmological principle (Section 1.1.1), to understand its dynamical evolution (Section 1.1.2) and to build a predictive cosmological model based on the main observational results (Section 1.1.3).

1.1.1 Geometry

In order to understand the geometry of the Universe, I make use of the cosmological principle, which enforces a set of symmetries that can be used to uniquely derive the spacetime metric, without even selecting a theory of gravity. However, throughout the thesis, I will use General Relativity (GR) as the standard framework. Since GR is a metric theory, its connections are completely specified by the metric; therefore the determination of the latter is enough to account also for the dynamics of spacetime, allowing me not to independently construct a connection field.

Cosmological principle

The cosmological principle states that the Universe is spatially homogeneous and isotropic on large scales or, equivalently, it is isotropic around any point. This means that it is symmetric under the 3 spatial translations and the 3 spatial rotations. For many years the cosmological principle was just an assumption inspired by the Copernican principle stating that humans are not privileged observers of the Universe. However, years later, it received a progressive support by observations from Cosmic Microwave Background

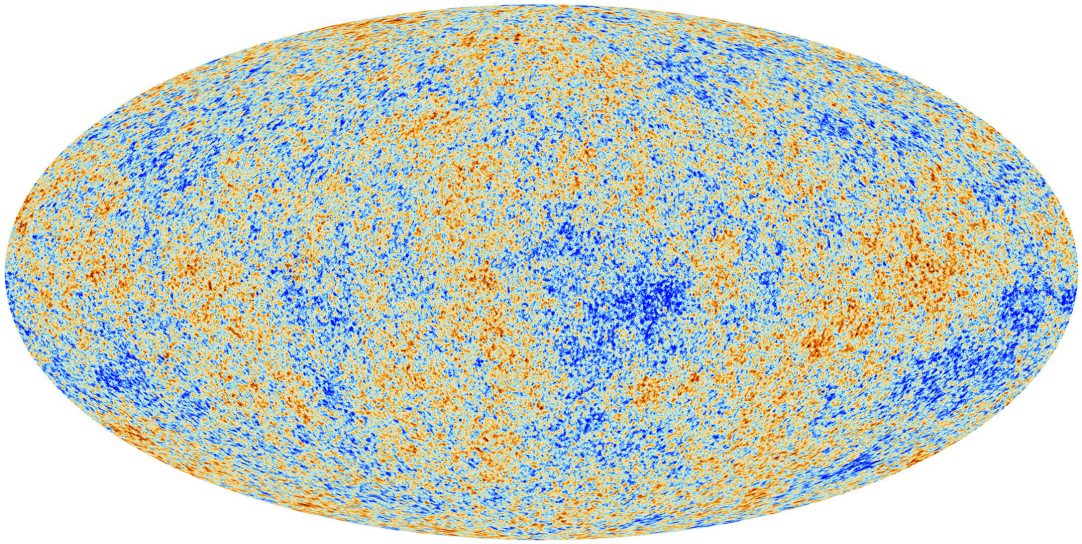

FIGURE 1.1: Map of the Cosmic Microwave Background radiation from Planck. Credits: https://www.esa.int/ESA_Multimedia/Images/2013/03/Planck_CMB.

(CMB) to Large Scale Structure (LSS). In particular, CMB detection gave us the picture of a highly isotropic Universe even at recombination epoch on scales much larger than the horizon at that time, with fluctuations in photon temperature of the order of $\delta T/T \sim 10^{-5}$ (see Figure 1.1). In addition, maps of the galaxies distribution at the present time are approximately homogeneous and isotropic on scales $\gtrsim 100$ Mpc, confirming the validity if the cosmological principle even at present epoch (see Figure 1.2).

FLRW

Starting from the cosmological principle, I reconstruct the space-time metric, known as Friedmann-Lemaître-Robertson-Walker (FLRW) metric. The geometrical implication of the cosmological principle is that space has 6 killing vectors, corresponding to the 3 spatial translations and rotations, which is the maximum number of killing vectors allowed for a 3 dimensional space, i.e. space is said to be maximally symmetric.

A property of a maximally symmetric space is that its metric is uniquely specified by the curvature and by the sign of its eigenvalues. In other words any metric with the same curvature and the same number of eigenvalues with same sign can be mapped to another metric with the same characteristics. Therefore, using only the curvature as a free parameter, I can choose

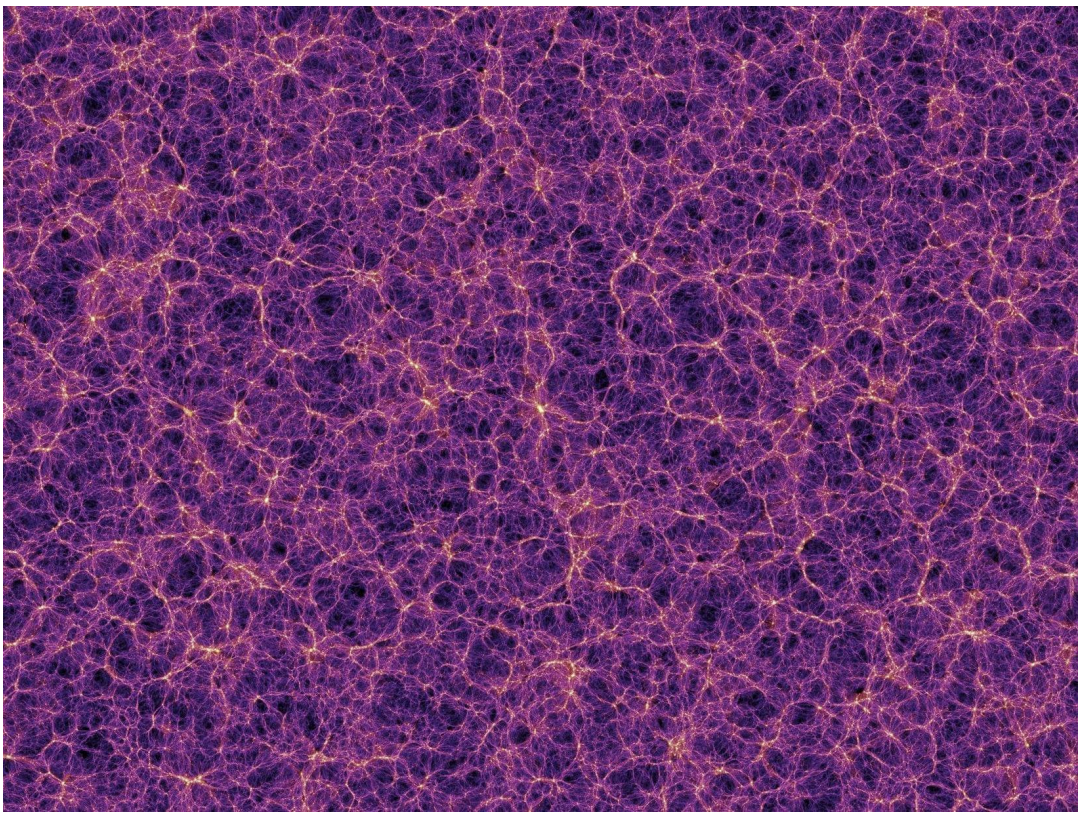

FIGURE 1.2: Map of the Large Scale Structure. Credits: Springel et al. 2006.

a convenient coordinate system to study the spatial metric. One of the simplest choices is to write down the general metric of a sphere or a pseudosphere embedded in an higher dimensional Euclidean space. After the definition of $a \equiv 1/K$ and $k \equiv K/|K|$, where K is the Gauss curvature, I can write down the line element for space as:

$$\mathrm{d}s^2 = a^2 \left(\mathrm{d}\vec{x}^2 + k \frac{(\vec{x}\,\mathrm{d}\vec{x})^2}{1 - k\,x^2} \right) \tag{1.1}$$

The overall space-time is not maximally symmetric, but it contains a 3 dimensional maximally symmetric subspace. This means that it is possible to choose a universal time t such that the subspaces at constant t are maximally symmetric. The line element can be written as:

$$\mathrm{d}s^2 = -\mathrm{d}t^2 + a(t)^2\, h_{ij}(x)\, \mathrm{d}x^i\, \mathrm{d}x^j \tag{1.2}$$

where $a(t)$ is a function of the t coordinate alone and h_{ij} is the metric of

the maximally symmetric subspace[1]. A detailed proof of this can be found in Weinberg 1972, but, intuitively, it is clear that a dependence of a on the spatial point x would break homogeneity and a dependence of the element g_{00} on x makes the definition of the proper time, and so also the function $a(t)$, spatial dependent, breaking again homogeneity. The parameter $a(t)$ is called the scale factor since it sets the scale of the spatial geometry and, in the case of positive curvature, it can be really regarded as the radius of the Universe.

Finally, I can rewrite the spatial part of the metric in spherical coordinates, getting the FLRW metric:

$$\mathrm{d}s^2 = -\mathrm{d}t^2 + a(t)^2 \left(\frac{\mathrm{d}r^2}{1 - k\, r^2} + r^2\, \mathrm{d}\Omega^2 \right) \tag{1.3}$$

The only free parameter is the spatial curvature, which is related both to k, taking the value of -1, 0 or $+1$ for a negatively curved, flat or positively curved Universe, and to $a(t)$. Being $a(t)$ a function of time, the Universe is not static a priori and its dynamical evolution is related to the temporal evolution of the parameter $a(t)$ whose dynamics is determined using Einstein field equations (see Section 1.1.2).

Redshift, cosmological distances and horizons

In a non static Universe with FLRW metric the proper distance to an object, say a galaxy, is function of time. Assuming to be at the origin of the coordinate system, to compute the proper distance to an object at (r, θ, ϕ) at fixed time t_{obs} one should integrate over the radial geodesic of the FLRW metric defined by $\mathrm{d}s = a(t)\, \mathrm{d}r / \sqrt{1 - k\, r^2}$, obtaining:

$$d_p(t_{\mathrm{obs}}) = a(t_{\mathrm{obs}}) \int_0^r \frac{\mathrm{d}r'}{\sqrt{1 - k\, r'^2}} = a(t_{\mathrm{obs}})\, S_k^{-1}(r) \tag{1.4}$$

with

$$S_k(r) \equiv \begin{cases} \sin r & k = +1 \\ r & k = 0 \\ \sinh r & k = -1 \end{cases} \tag{1.5}$$

[1] Notice that it is always possible to rescale the variable t such that the g_{00} element of the metric is -1. Thus the metric shown in equation (1.2) is fully general for a 4 dimensional space with a 3 dimensional maximally symmetric subspace.

Proper distance can also be conveniently rewritten as:

$$d_p(t_{\rm obs}) = a(t_{\rm obs}) \int_{t_{\rm e}}^{t_{\rm obs}} \frac{{\rm d}t'}{a(t')} \tag{1.6}$$

where $t_{\rm e}$ is the emission time of a photon emitted at the position r of the considered object.

Since it is related to the scale factor, the proper distance between two free falling observers at rest, evolves with time as:

$$\dot{d}_p = d_p\, \dot{a}/a \tag{1.7}$$

where $\dot{a}$ is the time derivative of the scale factor. Therefore it is customary to define the comoving distance as $d_c \equiv d_p/a$, such that it remains constant between two free falling observers. A temporal change of the radial coordinate r is instead due to peculiar motions of astronomical objects and the time derivative dr/dt is usually called peculiar velocity.

Unfortunately the proper and comoving distances are not measurable quantities and, since cosmological results are heavily based on observations, it is important to have ways to measure distances basing on observable properties.

In order to introduce operative definitions of distances, let me first define redshift, a key quantity in cosmology, being tightly connected with observations, representing the frequency shift of light traveling through spacetime. For a radial inward light ray:

$${\rm d}t = -a(t)\, \frac{{\rm d}r}{\sqrt{(1 - k\, r^2)}} \tag{1.8}$$

Therefore, if a light ray left the source at (t_1, r_1), it reaches an observer at the origin at time t_0 defined by:

$$\int_{t_1}^{t_0} \frac{{\rm d}t}{a(t)} = \int_0^{r_1} \frac{{\rm d}r}{\sqrt{(1 - k\, r^2)}} \tag{1.9}$$

If the source is comoving with the observer, the right hand side is constant and, differentiating the equation above, it gives:

$$\frac{\delta t_1}{\delta t_0} = \frac{a(t_1)}{a(t_0)} \rightarrow \frac{\nu_1}{\nu_0} = \frac{a(t_0)}{a(t_1)} \equiv 1 + z \tag{1.10}$$

where δt_1 is the time interval between the emission of two light signals by the source and δt_0 is the time interval between the arrival of the two light signals

at the origin. In the second passage I have used the definition of frequency $\nu = 1/\delta t$ and in the last equivalence I set $a(t_0) = 1$ and defined $1+z \equiv 1/a(t)$. The quantity z is called redshift; if $z < 0$ it is called blueshift (I will use the word redshift to generically mean z).

Once redshift has been defined, I turn to the definitions of measurable distances: the luminosity and the angular diameter distances and to their relation with the comoving distance. Let me start with the luminosity distance: if the intrinsic luminosity L of an object is known a priori and its flux f is measured, the luminosity distance can be defined via the inverse square law:

$$f = \frac{L}{4\pi\, d_L^2} \rightarrow d_L = \sqrt{\frac{L}{4\pi\, f}} \tag{1.11}$$

To find the relation between luminosity and comoving distance let me consider a FLRW Universe. Photons emitted by a source at comoving distance r, reaching an observer at the origin at $t = t_0$ will be spread over a sphere of proper radius $d_p(t_0) = S_k(r)^{-1}$, whose area is $4\pi\, S_k(r)^{-2}$. The intrinsic luminosity of a source will be affected by redshift in a twofold way: on the one hand the photon energy is reduced by a factor $1+z$ due to the frequency shift, on the other hand the arrival time separation δt_0 is larger with respect to the emission time separation δt_e by the same factor $1+z$. Therefore the intrinsic luminosity must be divided by $(1+z)^2$, obtaining an inverse square law of the form:

$$f = \frac{L}{4\pi\, S_k(r)^{-2}\,(1+z)^2} \tag{1.12}$$

The ensuing luminosity distance is $d_L = S_k^{-1}(r)\,(1+z) = d_c\,(1+z)$. Luminosity distance is easy to measure via equation (1.11) once the intrinsic luminosity of an object is known and, knowing the redshift, it can be promptly related to the proper and comoving distance.

Similar arguments holds for the angular diameter distance which instead can be measured once the intrinsic length l of an object in the sky is known as:

$$d_A = \sqrt{\frac{l}{\delta\theta}} \tag{1.13}$$

with $\delta\theta$ being the observation angle. It can be shown that $d_A = S_k(r)^{-1}/(1+z) = d_c/(1+z) = d_L/(1+z)^2$.

I conclude the Section defining some other useful quantities: the cosmological comoving volume and the particle horizon. The infinitesimal cosmological comoving volume is defined as:

$$\mathrm{d}V_c \equiv d_c^2 \, \mathrm{d}d_c \, \mathrm{d}\Omega \tag{1.14}$$

The particle horizon is instead defined as the maximum distance light can travel from the beginning of the Universe to the observation time t_{obs}:

$$r_{\mathrm{PH}}(t_{\mathrm{obs}}) = a(t_{\mathrm{obs}}) \int_0^{t_{\mathrm{obs}}} \frac{\mathrm{d}t'}{a(t')} \tag{1.15}$$

1.1.2 Dynamics

In Section 1.1.1 I focused on the structural and geometrical properties of the Universe. I want now to study its dynamics in order to understand its past and, possibly, predict its future history. I start illustrating Hubble observations and the discovery of the expansion of the Universe and then I derive the Friedmann equations for the evolution of the scale factor.

The Hubble law

In equation (1.10) I have introduced the concept of redshift or blueshift and the fact that such a shift in light frequency is dependent on the scale factor ratio between the time of emission and observation of light. An operative way to measure redshift of distant objects, such as galaxies, is to measure their spectral absorption lines and compare their wavelengths with the ones measured on Earth experiments. By 1925 Vesto Slipher had measured the redshift of some tens of galaxies finding that the vast majority of them was redshifted ($z > 0$). In 1929, Hubble extended the galaxy sample confirming Slipher's result and was able to measure the distance r from some of the galaxies in its sample. He found a linear relationship between redshift and distance known as the Hubble law:

$$z \simeq \frac{H_0}{c} r \rightarrow v_H \simeq H_0 \, r \tag{1.16}$$

where $H_0 \simeq 500\,\mathrm{km\,s^{-1}\,Mpc^{-1}}$, as measured by Hubble, is called the Hubble constant. In the second equality I have enforced the interpretation of cosmological redshift as a Doppler shift defining a radial recessional velocity $v_H \equiv c\,z$. However this interpretation could be misleading and it is valid only at $z \ll 1$ since cosmological redshift does not depend on the rate of change of the scale factor when light is emitted, but on the overall change of

the scale factor during the light travel. The Hubble law, showing that furthermost galaxies are receding from us faster than nearby ones, imply that the Universe is undergoing an isotropic expansion around any point in space, confirming the validity of the cosmological principle. The recessional motion of galaxies at a rate proportional to their distance from each other is usually referred to as the Hubble flow.

With better observations, the determination of the Hubble constant has been significantly lowered and progressively improved, narrowing its error to $\sim$ 1%. Still, a satisfactory value for H_0 has not been agreed, with a $\sim 4\sigma$ tension between low and high redshift probes. From low redshift measurements, mainly based on distance ladder calibration of supernova luminosities by the Supernova $H0$ for the Equation of State (SHOES) collaboration, the Hubble constant attains values $H_0 \simeq 74.0 \pm 1.4\,\mathrm{km\,s^{-1}\,Mpc^{-1}}$, while from high redshift measurements, mainly based on temperature anisotropies of the cosmic microwave background (CMB) by the Planck collaboration, it is obtained $H_0 \simeq 67.4 \pm 0.5\,\mathrm{km\,s^{-1}\,Mpc^{-1}}$. This discrepancy appears also exploiting other low and high redshift probes such as strong lensing, supporting the SHOES result, and baryonic acoustic oscillations (BAO) data, supporting the Planck result.

The Hubble law is simply another way of expressing equation (1.7) at $z \simeq 0$, where the Hubble constant is defined as: $H_0 \equiv \dot{a}(t_0)/a(t_0)$. Since equation (1.7) is generally valid at any redshift, it is useful to define the Hubble parameter $H(z) \equiv \dot{a}/a$ as a function of redshift. The Hubble parameter is widely used in cosmology and it is customary to express the distances, volume and horizon defined in Section 1.1.1 in terms of it:

$$d_p(z) = \frac{1}{1+z_{\mathrm{obs}}} \int_{z_{\mathrm{obs}}}^{z} \frac{\mathrm{d}z'}{H(z')} \tag{1.17}$$

$$d_c(z) = \int_{z_{\mathrm{obs}}}^{z} \frac{\mathrm{d}z'}{H(z')} \tag{1.18}$$

$$\mathrm{d}V_c = \frac{1}{H(z)} \left(\int_0^z \frac{\mathrm{d}z'}{H(z')} \right) \mathrm{d}z\, d\Omega \tag{1.19}$$

$$r_{\mathrm{PH}} = \frac{1}{1+z_{\mathrm{obs}}} \int_{z_{\mathrm{obs}}}^{\infty} \frac{\mathrm{d}z'}{H(z')} \tag{1.20}$$

Another useful and widely used horizon definition involving the Hubble parameter is the Hubble horizon, which better catch the maximum scale of interactions at a given cosmic time. Hubble horizon is defined as:

$$\mathrm{r_H(z_{obs})} = \frac{1}{\mathrm{H(z_{obs})}} \tag{1.21}$$

Friedmann equations

As shown in Section 1.1.1, once specified the sign of the curvature, the FLRW metric is dependent only on the scale factor $a(t)$. Studying the dynamical evolution of this factor is the key to understand the past history and the future of the cosmos. This can be done by plugging the FLRW metric into the Einstein field equations. Since the derivation of FLRW metric comes from the cosmological principle, I implement the assumption of large scale homogeneity and isotropy also in the energy-momentum tensor, which takes the form:

$$T_{\mu\nu} = (\rho + p)\, u_\mu\, u_\nu + p\, g_{\mu\nu} \tag{1.22}$$

where ρ is the total density and p the total pressure of the matter and radiation fields and $u^\mu \equiv dx^\mu/d\tau$. The Einstein field equations reduce to 2 independent differential equations called Friedmann equations:

$$\left(\frac{\dot{a}}{a}\right)^2 + \frac{k}{a^2} = \frac{8\pi G}{3}\,\rho \tag{1.23}$$

$$\frac{\ddot{a}}{a} = -\frac{4\pi G}{3}\,(\rho + 3\,p) \tag{1.24}$$

The combination of these two equations give the energy conservation equation:

$$\dot{\rho} + 3\frac{\dot{a}}{a}\,(\rho + p) = 0 \tag{1.25}$$

In order to solve the system on the 3 unknown $a(t)$, $\rho(t)$ and $p(t)$, it is usually chosen an equation of state (EOS) of the form $p = w\,\rho$, where w can be different for different components of the Universe. Friedmann equations imply that, once an EOS has been selected for each field in the Universe, the time evolution of the scale factor is strictly connected to the density of matter and radiation fields.

As for the EOS, non relativistic cold particles, such as baryons and dark matter (see Section 1.1.3), are, to a good approximation, considered pressureless ($w \simeq 0$), while for relativistic particles, like photons, it can be shown that $w \simeq 1/3$ is a good approximation. Vacuum energy also deserves a mention: since for vacuum $T_{\mu\nu} \propto g_{\mu\nu}$ it can be shown that energy and pressure are related by $p = -\rho$, meaning $w = -1$.

The density evolution as a function of the scale factor can be found solving equation (1.25), obtaining $\rho \propto a^{-3(1+w)}$. Therefore for non relativistic cold matter $\rho \propto a^{-3}$, for relativistic hot radiation $\rho \propto a^{-4}$ and for vacuum energy $\rho \propto$ constant, exactly equal to the behaviour of a cosmological constant.

Using this result on the first Friedmann equation (1.23) gives the time evolution of the scale factor: $a(t) \propto (t/t_0)^{2/(3+3w)}$, valid for $w \neq -1$. At early times, when the density is dominated by radiation $a(t) = (t/t_0)^{1/2}$, at intermediate times, when cold matter is the dominant component $a(t) = (t/t_0)^{2/3}$. Finally, at late times, when the energy budget is dominated by the vacuum energy or cosmological constant the solution of equation (1.23) reads: $a(t) = e^{H_0 (t-t_0)}$, implying an accelerated expansion of the Universe.

The fact that the scale factor was increasing at early times, lead to the idea of the Big Bang: a singularity point when the scale factor reaches the value $a = 0$, thought as the beginning of the Universe. Still, at large enough density and small scales GR breaks down, failing in the description of the very early stages of the universe $t \lesssim 10^{-43}$ s. Models of modified gravity, such as inflation or bouncing models, are usually invoked in order to avoid the initial singularity, but still a full theory of quantum gravity is needed in order to describe the physics at sub-planckian scales.

1.1.3 Building the ΛCDM

In Section 1.1.2 I have shown that the evolution of the Universe is tightly related to its components and their densities. In this Section I discuss the main cosmological probes used to investigate what is the Universe made of. Then I proceed to do a cosmic inventory, listing the matter and radiation fields present in the Universe and the latest constraints on their energy density. A useful definition is the density parameter for a given element X, i.e. the ratio between its energy density and the critical density of the Universe at a given redshift: $\Omega_X(z) \equiv \rho_X(z)/\rho_c(z)$ where the critical density is $\rho_c(z) \equiv 3H(z)^2/8\pi G$. When the parameter Ω_X is evaluated at the present day ($z = 0$) it is usually indicated as $\Omega_{X,0}$. Notice that the first Friedmann equation (equation (1.23)) can be rewritten as: $H(z) = H_0 \sqrt{\sum_X \Omega_{X,0} (1+z)^{3(1+w_X)}}$ with w_X being the equation of state of the element X.

Main cosmological probes

Thanks to the many different cosmological probes and to the huge amount of information they bring about the state of the Universe, we are used to say that we live in the era of precision cosmology. In this Section I briefly mention just the most important observables which have helped in the construction of the current cosmological model: ΛCDM.

Cosmological probes widely adopted in the near Universe are:

- Type Ia supernovae (SNe): they are extremely bright explosions originated by white dwarfs accreting mass from a stellar companion. Their

absolute luminosity L is related to the shape of the light curve. For this reason they have been extensively used as standard candles to measure luminosity distances and, consequently, determining cosmological parameters. Thought being very bright and easy to detect, their luminosity is not know a priori and must be calibrated using other types of closer standard candles such as chepeid variable stars.

- Galaxy clustering: it is often used to measure Baryonic Acoustic Oscillations, whose scale is fixed by early Universe physics. Therefore, measuring the 2 point correlation function between galaxies is a way to obtain angular distances. Moreover matter power spectrum, traced by the distribution of galaxies, and in particular the scale at which it peaks, provides useful constraint for the total matter energy density parameter.

- Weak lensing of galaxies: measuring the distortion of distant galaxies images due to weak gravitational lensing from intervening structures in the photons path is a good probe of the matter distribution at intermediate redshifts ($z \sim 1$), which in turn, can be converted in an estimation of cosmological parameters

- CMB lensing: it is the study of the distortion of CMB photons due to the Large Scale Structure between $z = 0$ and $z \sim 1100$. As for the case of galaxies weak lensing it can be a good probe for cosmological parameters

- Strong lensing: it could be used for cosmological parameters estimation since geometrical properties and time delays of lensed multiple images are dependent on cosmology and on the theory of gravity itself. However, errors in the time delay measurements are huge and, in order to be a probe as good as the aforementioned, thousand strong lensing events would be needed.

Early Universe probes are instead:

- Big Bang Nucleosynthesis (BBN): it is the process of formation of light nuclei such as deuterium, helium and lithium in the first $\sim$ 15 minutes of the Universe life, when temperature dropped below $\sim 10^9$ K. Abundances predicted by BBN theory are dependent on the baryon energy density parameter $\Omega_{b,0}$. Measurements of pristine light elements abundances in primordial gas clouds, through Lyman alpha forest observations, or in stars, once enrichment due to stellar evolution has been subtracted, place stringent constraint on this parameter.

- Cosmic Microwave Background: it is the radiation emitted at $z = z_{\rm rec} \simeq 1100$, when temperature drops below ~ 3000 K and electrons and protons can recombine to form hydrogen and helium atoms. At that time photons decouple from baryons and free stream toward us. The strong isotropy of CMB photons temperature, of the order of $\delta T/T \sim 10^{-5}$, is a solid proof of the cosmological principle and of the Big Bang theory in general (see Figure 1.1). However the power spectrum of temperature anisotropies provides precious information on cosmological parameters. Such a power spectrum is shown in Figure 1.3. It appears flat on large scales $\delta\theta \gtrsim 1^\circ$, bigger than the horizon scale at recombination, meaning that primordial perturbations have almost equal power at all scales. At smaller scales, instead, the power spectrum start oscillating due to the gravitational contraction of the baryon photon fluid in dark matter potential wells and to the subsequent rarefaction due to photon pressure. The heights and positions of CMB peaks are related to cosmological parameters. In particular the first peak position tells the apparent size of the horizon at recombination and so it places constraints on the curvature of the Universe. The second peak, instead, corresponds to fluctuations which had time to complete an entire oscillation and are at maximum rarefaction. Its height with respect to the first peak, and in general the height of even peaks (rarefactions) with respect to odd peaks (contractions), is a measure of the baryon energy density. The third peak is instead related to the total matter density. The next peaks at smaller scales are damped due to photon pressure which tries to smooth out perturbations. The damping is stronger especially for perturbations entering in the horizon during radiation domination, i.e. on smaller scales. Therefore the amplitudes of these peaks bring information on the matter radiation equality epoch and, consequently, on the energy density of matter with respect to radiation.

- CMB B-modes: I also mention B-modes of CMB photons polarization as a possible future proxy for primordial tensor modes. Detection of these tensor modes could bring a lot of information about mechanisms in act in the very early Universe such as inflation.

Radiation

Though the number density of photons is vastly larger than the number density of baryons, with a ratio of the order of $\sim 10^9$, their temperature at present is so low that the photons energy density is negligible $\Omega_{r,0} \sim 5 \times 10^{-5}$. Still,

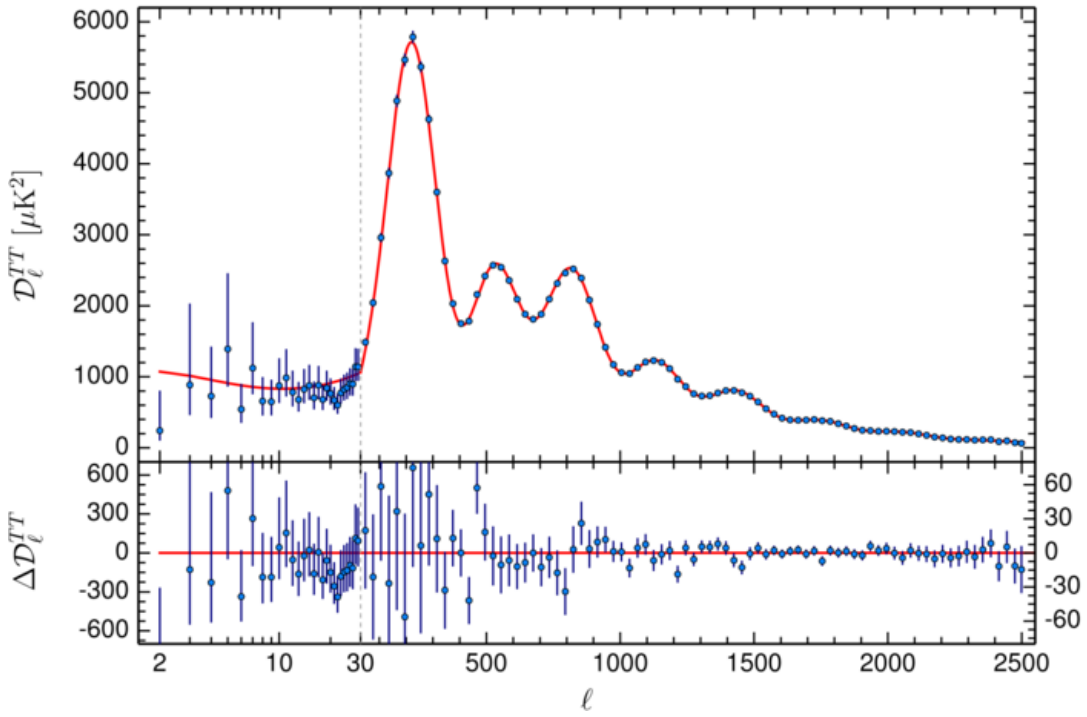

FIGURE 1.3: Power spectrum of CMB temperature anisotropies from Planck. Credits: https://www.cosmos.esa.int/web/planck/picture-gallery.

when the Universe was younger and hotter, radiation dominated the energy budget up to the equivalence redshift $z_{\rm eq} \simeq 3400$ when cold matter start dominating. Other contributions to radiation energy comes from gravitational waves produced by various possible mechanism in the early and late Universe, but their contribution is subdominant even with respect to light. I will discuss more about GW energy density coming from astrophysical processes in Sections 2.6 and 3.6.

Baryonic matter

With the term baryonic matter it is meant the totality of non relativistic particles included in the standard model of particle physics, i.e. the totality of baryons, but also mesons, leptons and gauge bosons except the photon and the graviton. Baryonic matter can be found in stars, but also in compact objects such as brown and white dwarfs and neutron stars (NSs), in planets and in the form of gas in the interstellar and intergalactic medium (ISM and IGM). Measuring the amount of stellar luminosity in a given cosmological volume and assuming a mass to light ratio it is possible to roughly compute an energy density for stars, getting $\Omega_{\star,0} \sim 0.0027$ (Fukugita & Peebles 2004). ISM and IGM can be detected via luminous emission in different bands, depending on temperature, density and composition of the gas, and give a significant contribution to the total baryonic mass density. Stringent constraints on the overall baryonic energy density come from predictions of Big Bang Nucleosynthesis and measurements of the amount of deuterium and other light elements in clouds of primordial gas. Other strong constraints come from the analysis of the spectrum of CMB temperature anisotropies. The resulting baryon energy density at present is $\Omega_{b,0} \sim 0.05$ (see Tumlinson et al. 2017 for a review of the abundances of different baryonic components).

Dark matter

Dark matter (DM) is a peculiar kind of matter which interacts only gravitationally, not emitting or absorbing electromagnetic radiation. First evidences of a missing unseen mass were found in 1933 by Zwicky who was studying the dispersion velocity of galaxies in the Coma cluster. Visible stars and galaxies in the clusters were not enough to provide a deep potential well to keep the system bounded. He concluded that the cluster should contain a huge amount of "dunkle Materie" (dark matter, Zwicky 1933). It was only in the 1970s-1980s that dark matter was invoked to explain galaxies rotation curves (Rubin et al. 1980), especially the flat outer part traced by neutral hydrogen. Other evidences in the late Universe of dark matter existence are

strong lensing observations with the most striking example being the Bullet cluster.

However the most important indications for dark matter existence and constraints on its abundance come from early Universe with CMB observations. First of all the level of anisotropies of the photon-baryon fluid at recombination is of the order of $\sim 10^{-5}$, which is too low, at least 2 order of magnitude, to lead to the overdensities we observe in the late Universe; another source of anisotropies and gravity is required to form the observed structures. Moreover, from the CMB anisotropy peaks it is possible to separately recover the energy density of baryons and of the total non relativistic matter, as explained above. The latest constraint on the dark matter energy density at present day is $\Omega_{\mathrm{DM},0} \simeq 0.265$, with the total matter density (DM+baryons) being $\Omega_{\mathrm{M},0} \simeq 0.315$.

Since dark matter particles have never been detected, we still do not know what dark matter is made of. Still, some observationally based considerations are in order. The first one is that there are different kind of particles or objects not emitting light or emitting an undetectable amount of it. Even standard model particles (baryons) could be dark matter if they are in collapsed objects such as black holes (BHs). Thought CMB and BBN constraints, being able to fix the abundance of baryonic matter at early times, have ruled out this hypothesis, there is still the possibility that some black holes formed in the primordial Universe, right after inflation (primordial black holes), could constitute a part of dark matter. However, the idea that they could account for all the necessary DM energy density is now ruled out combining various observations, mainly microlensing results and CMB constraints (see Sasaki et al. 2018; Carr et al. 2017, 2020). Therefore the mostly accepted hypothesis is that dark matter should be some exotic kind of particle not included in the standard model, which is able to interact only gravitationally.

The DM particles mass is strictly related to their temperature, allowing us to divide DM models in 3 different categories: hot dark matter (HDM) with mass $m \lesssim 0.2\,\mathrm{eV}$, cold dark matter (CDM) with mass $m \gtrsim 1\,\mathrm{GeV}$ and warm dark matter (WDM) with mass $m \sim 1\,\mathrm{KeV}$. Since temperature is a proxy of typical velocities of DM particles, it is possible to place constraints on the correct model requiring the DM thermal velocity being smaller or equal than the typical velocities needed to form gravitationally bound structures of a certain scale. HDM models, in general, tend to form only large scale bound structures and so they are ruled out. The most accepted paradigm for dark matter is CDM, where structures are formed even at small scales. However, also CDM has its own issues: indeed CDM-only numerical simulations predict that dark matter should cluster hierarchically, producing a

large amount of small substructures, called satellites, and a smaller number of large main structures. While the number of large structures is typically in agreement with observations, the quantity of substructures predicted by simulations is order of magnitudes larger than what is detect. This is usually called the missing satellites problem (Kauffmann et al. 1993; Klypin et al. 1999). For example, for the Milky Way, semi-analytical models and numerical simulations predict $\gtrsim$ 100 dwarf satellite galaxies, while only $\sim$ 10 are observed. Missing satellites problem is a theoretical challenge which any new dark matter model should face.

Dark energy

Dark energy (DE) is an unknown form of energy which leads the Universe to an accelerated expansion phase at present day. In order to have accelerated expansion an equation of state with $w < -1/3$ is required (see equation (1.24)). As for the case of dark matter, even evidences for dark energy are plenty and deriving from various probes at different scales and cosmic times. Historically, the first evidence comes from stellar archaeological observations. If the contribution of dark energy to the total energy density of the Universe is not taken into account, the age of the Universe can be estimated as: $t_0 = 2/3\, H_0 \simeq 9.2 \pm 1$ Gyr. However some of the oldest globular clusters ages are constrained to be $\sim 12 - 13$ Gyr (see Jimenez et al. 1996; Carretta et al. 2000; Hansen et al. 2002) and most of globular clusters show a stellar population with age $\gtrsim 11$ Gyr, larger than the estimated age of the Universe. The inclusion of dark energy into the game enlarges the cosmic age estimation circumventing the problem. But the first clear evidence for the accelerated cosmic expansion and the first measurement of dark energy density came in 1998 from Riess and Perlmutter (Riess et al. 1998; Perlmutter et al. 1999), respectively in the High-z Supernova Search Team and in the Supernova Cosmology Project. They used type Ia supernovae as standard candles to measure the luminosity distance as a function of redshift. They were able to fit a value for the local deceleration parameter $q_0 \equiv -\ddot{a}(t_0)/H_0 \simeq -0.55$ consistent with a dark energy equation of state $w_{\rm DE} \simeq -1$ and an energy density $\Omega_{\rm DE,0} \simeq 0.7$. Other constraints on dark energy can be inferred by CMB angular power spectrum. The position of the first peak is a probe of the curvature of the Universe which is found to be almost flat $k \simeq 0$, so that the first Friedmann equation evaluated at t_0 reduces to $\Omega_{\rm M,0} + \Omega_{\rm DE,0} \simeq 1$. As explained above, from smaller scales acoustic peaks it is possible to derive $\Omega_{\rm M,0} \simeq 0.315$, so obtaining $\Omega_{DE,0} \simeq 0.685$. The latest determination of the DE equation of state is $w_{\rm DE} \simeq -1.03 \pm 0.03$.

Different theoretical models have been proposed to explain dark energy and the accelerated expansion. The most accepted one is the cosmological constant Λ, which enters in the GR lagrangian as $\mathcal{L} = R - 2\Lambda$ and in the Friedmann equations acts as a term with constant $\rho_\Lambda = \Lambda/8\pi G$, exactly as a vacuum energy. However, the cosmological constant interpretation has its own drawbacks such as the famous fine tuning and coincidence problems. These issues can be mitigated in other models of dark energy such as quintessence models (Caldwell et al. 1998) at the price of adding a scalar field, the quintessence, with a dynamically changing equation of state. Under suitable conditions it can be demonstrated that such a scalar field mimics the behaviour of the cosmological constant in the present day Universe. Up to now the most accepted model remains the cosmological constant that, in combination with the cold dark matter paradigm, gives the name to the entire cosmological model: ΛCDM.

1.2 Evolution of perturbations and DM halos

In Section 1.1 I have dealt with the background structure and dynamics of the Universe, also mentioning the behaviour of density perturbations in the baryon-photon fluid before recombination, at $z \geq 1100$. In this Section, instead, I focus on the evolution of non relativistic matter perturbations, which lead to structure formation. This treatment well represents CDM perturbations before decoupling, when baryons are still relativistic, and the whole matter content of the Universe after decoupling, when baryons become non relativistic. Still, baryonic physics, being governed also by electromagnetic interactions, can be complicated, so here I neglect the role of such interactions and I consider all the non relativistic matter to behave as dark matter, an approximation which is not too crude given that dark matter makes $\sim 85\%$ of the total non relativistic matter. In Section 1.2.1 I focus on the evolution of a matter overdensity in the linear and non linear regime and I define the concept of virialized dark matter halo, in Section 1.2.2 I derive the DM halo mass function and in Section 1.2.3 I study the structure and evolution of DM halos.

1.2.1 Evolution of the density contrast

In order to study non relativistic perturbations evolution, it is useful to define the density constrast at the point $\vec{r}$ and time t:

$$\delta(\vec{r}, t) \equiv \frac{\rho(\vec{r}, t) - \bar{\rho}(t)}{\bar{\rho}(t)} \tag{1.26}$$

where $\rho(\vec{r}, t)$ is the matter density at $\vec{r}$ at time t and $\bar{\rho}(t)$ is the average density of the Universe at time t. As time goes on Universe expands, but overdense regions expands slower with respect to underdense regions and the density contrast δ tends to increase. As far as $|\delta| \ll 1$ the perturbation is in the linear regime and it can be treated with the linear density evolution theory. At sufficiently large times $\delta \gtrsim 1$ and the perturbation is said to be in the non-linear regime. In the next Subsections these two regimes are studied.

Linear regime

As said above, I consider a non relativistic pressureless fluid with density $\rho = \bar{\rho}\,(1 + \delta)$ and velocity given by the Hubble flow plus peculiar velocity. Combining the Euler and continuity equations and neglecting all the non linear terms $\mathcal{O}(\delta^2)$, a dynamical equation for δ is obtained, reading:

$$\frac{\partial^2 \delta}{\partial t^2} + 2\,H\,\frac{\partial \delta}{\partial t} = 4\pi\,G\,\bar{\rho}\,\delta \tag{1.27}$$

Equation (1.27) is a linear ordinary differential equation, so the solution can be written in the form $\delta(\vec{x}, t) = D(t)\,\delta(\vec{x}, t_0)$, where $\vec{x} \equiv \vec{r}/a$ is the comoving coordinate, $D(t)$ is called growth factor and $\delta(\vec{x}, t_0)$ is the density contrast extrapolated at present time. In linear theory the spatial dependence of the density contrast does not change with time and only the amplitude evolves through the factor $D(t)$, whose value at present is $D(t_0) = 1$. Fixing the background cosmology, equation (1.27) can be solved for the growth factor. For a matter only Universe $D(t) = a(t)$, which can be considered a good approximation also for ΛCDM. Therefore in linear regime perturbations tend to grow at the same rate of the scale factor.

Non linear regime

As δ grows with time, it eventually reaches $\delta \gtrsim 1$ and it goes out of the linear regime. The non linear evolution can be determined numerically or through some analytical approximations. Here I briefly sketch the simplest analytical approximation: the spherical collapse model (see Lahav et al. 1991; Eke et al. 1996). The spherical collapse model takes into account a spherical region with constant density contrast δ, in the linear regime at the initial time t_i. As cosmic time goes on δ increases since the spherical region expands slower than the background up to a turn around time $t_{\rm ta}$ at which the spherical region stops expanding and start collapsing back. In the spherical collapse model this occurs when $1 + \delta(t_{\rm ta}) \simeq 5.55$. Extrapolating the linear theory up to this point the linear density constrast would have been $\delta_{\rm lin}(t_{\rm ta}) \simeq 1.062$.

The time of collapse of the spherical region is $t_{\rm coll} = 2\,t_{\rm ta}$ at which the density contrast diverge. In linear theory, instead, the density contrast at $t_{\rm coll}$ can be computed as $\delta_{\rm lin}(t_{\rm coll}) \simeq 1.686$, which is called critical overdensity for collapse δ_c. At a given cosmic time, only regions with linearly extrapolated density contrast $\delta_{\rm lin}(t) > \delta_c$ are collapsed. This implies that regions with higher initial density contrast collapsed earlier than lower density contrast regions. In order to compute the redshift of collapse for an overdensity with present day density contrast $\delta(t_0) > \delta_c$ it is sufficient to solve $\delta(t_0) = \delta_c/D(t)$ for redshift. For this reason the function $\delta_c(z) \equiv \delta_c/D(t)$ is usually defined.

Spherical collapse model assumes a matter only universe as background cosmology. However, its predictions are weakly dependent on cosmological parameters and, even in ΛCDM, matter dominates over other kind of energies for most of the time. Therefore results of the spherical collapse model can be extended to ΛCDM case to a good extent.

Though the spherical collapse model is useful, allowing to analytically estimate the collapse time of a given perturbation, overdensities, in general, are not uniform and the collapse is not spherical. DM particles undergo phase mixing and violent relaxation processes (Lynden-Bell 1967; Binney & Tremaine 2008) forming a virial system at equilibrium, called dark matter halo. The typical timescale of virial relaxation is $t_{\rm vir} \simeq 2\,t_{\rm ta}$ at which the system has a radius $r_{\rm vir} \simeq r_{\rm ta}/2$ and a density $\rho(t_{\rm vir})/\bar{\rho}(t_{\rm vir}) = 18\pi^2 \simeq 178$. This leads to the definition of the virial radius as the radius containing a density $\rho_{\rm vir} = \Delta_c\,\rho_c$. In a matter only Universe $\rho_c(t) = \bar{\rho}(t)$ and $\Delta_c \equiv 18\pi^2$ is called the critical overdensity for virialization. Relaxing the assumption of a matter only Universe, but still imposing $\Omega_{\rm M} + \Omega_{\rm DE} = 1$, Δ_c becomes a redshift dependent quantity that can be approximated as:

$$\Delta_c(z) \simeq 18\pi^2 + 82\,y - 39\,y^2 \tag{1.28}$$

with $y \equiv \Omega_{\rm M} - 1$. As said above, for a given Δ_c, it is possible to define the virial radius and, consequently, the virial mass as:

$$M_{\rm vir} \equiv \frac{4}{3}\pi\,\Delta_c\,\rho_c\,r_{\rm vir}^3 = \frac{\Delta_c(z)\,H^2(z)\,r_{\rm vir}^3}{2\,G} \tag{1.29}$$

and the virial velocity:

$$v_{\rm vir} \equiv \sqrt{\frac{G\,M_{\rm vir}}{r_{\rm vir}}} = (G\,M_{\rm vir}\,H(z))^{1/3}\left(\frac{\Delta_c(z)}{2}\right)^{1/6} \tag{1.30}$$

In the rest of the thesis I will refer to the halo mass M_H and radius R_H meaning

the virial mass and radius. Other commonly used definitions of these quantities are $M_{n\bar{\rho}}$ and $R_{n\bar{\rho}}$ where n indicates a specific overdensity with respect to the average density chosen to define the halo boundary. Typical choices are $n = 200$ and $n = 500$.

1.2.2 Halo mass function

In this Section I apply the main results of the spherical collapse model to theoretically derive the halo mass function $\mathrm{d}^2N/\mathrm{d}M_H/\mathrm{d}V$, i.e. the number density of halos with given mass M_H per unit comoving volume V, at given redshift. The statistics of DM halos is of fundamental importance for any theory of galaxy formation and evolution since halos provide the potential wells where baryons collapse, cool and form stars.

Observations of the halo mass function are extremely challenging (e.g., Castro et al. 2016; Dong et al. 2019; Li et al. 2019; Sonnenfeld et al. 2019; Cueli et al. 2021), given the nature of DM particles and the statistical and systematic uncertainties in the relations linking halo mass to observable galactic properties. The main way to derive the halo mass function in modern cosmology is via numerical N-body DM only simulations with volumes large enough to account for a good statistics (see Sheth & Tormen 1999b; Jenkins et al. 2001; Warren et al. 2006; Tinker et al. 2008; Crocce et al. 2010; Bhattacharya et al. 2011; Watson et al. 2013). However, simulations results can be limited in mass and redshift range and are dependent on the chosen algorithm to identify halos.

I sketch here the derivation of the halo mass function from theoretical basis, relying on the Press-Schechter formalism (Press & Schechter 1974) and its subsequent developments. The idea is that the initial density contrast field is a Gaussian random field and a DM halo collapses if it is in a sufficiently overdense region of such a field. However, since the overdensity around a point depends on the considered scale, it is useful to smooth the overdensity over a scale R, averaging out all the fluctuations at scales smaller than R. The variance of the smoothed density field $S(R)$ decreases increasing the scale R. Bond et al. 1991 developed the excursion set formalism (see also Lapi et al. 2013), demonstrating that an overdensity around a given location executes a random walk as a function of the variance S, or, equivalently, of the smoothing scale. The scale at which the smoothed density contrast first crosses the value $\delta_c(z)$ represent the scale of the collapsing region. It can be proven that the halo mass function is related to the distribution of first

crossing scales $f(S)$ as:

$$\frac{\mathrm{d}N}{\mathrm{d}M_H} = \frac{\bar{\rho}}{M_H^2} \left| \frac{\mathrm{d}\log S}{\mathrm{d}\log M_H} \right| S f(S) \tag{1.31}$$

where

$$f(S) = \frac{1}{\sqrt{2\pi}} \frac{\delta_c(z)}{S^{3/2}} \exp\left(-\frac{\delta_c(z)^2}{2S}\right) \tag{1.32}$$

is the first crossing distribution in the case of spherical collapse where collapse occurs whenever $\delta > \delta_c(z)$.

Successive models (Sheth et al. 2001; Sheth & Tormen 2002) refined the excursion set formalism, considering an ellipsoidal collapse and setting a mass dependent collapse threshold better in agreement with simulations. In Figure 1.4 I show an example of a random walk for the overdensity δ as a function of the variance. In the Figure are represented the threshold for collapse in the case of a spherical collapse and ellipsoidal collapse models, at $z = 0$ and $z = 2$. At smaller redshift the threshold for collapse decrease, leading overdensities with smaller variance (larger scales) to collapse, corresponding to the formation of a more massive halo.

1.2.3 Halo structure

In Sections 1.2.1 and 1.2.2 I have reviewed the overdensity evolution, giving the definition of dark matter halo and I have shown the formalism to theoretically derive the halo mass function. In this Section I focus on the internal structure of halos, in particular on their density profile, extensively relying on results of cosmological N-body DM only simulations, on their substructures and on their accretion rate.

Halo density profile

A nice property shared by all simulations is that the DM density profile does not significantly depend on the halo mass, meaning that every collapsed DM overdensity has almost the same radial distribution once virialised. A good fit for such a density distribution is given by the Navarro-Frank-White (NFW) profile (Navarro et al. 1996):

$$\rho(r) = \frac{4\,\rho_s}{(r/r_s)\,(1 + r/r_s)^2} \tag{1.33}$$

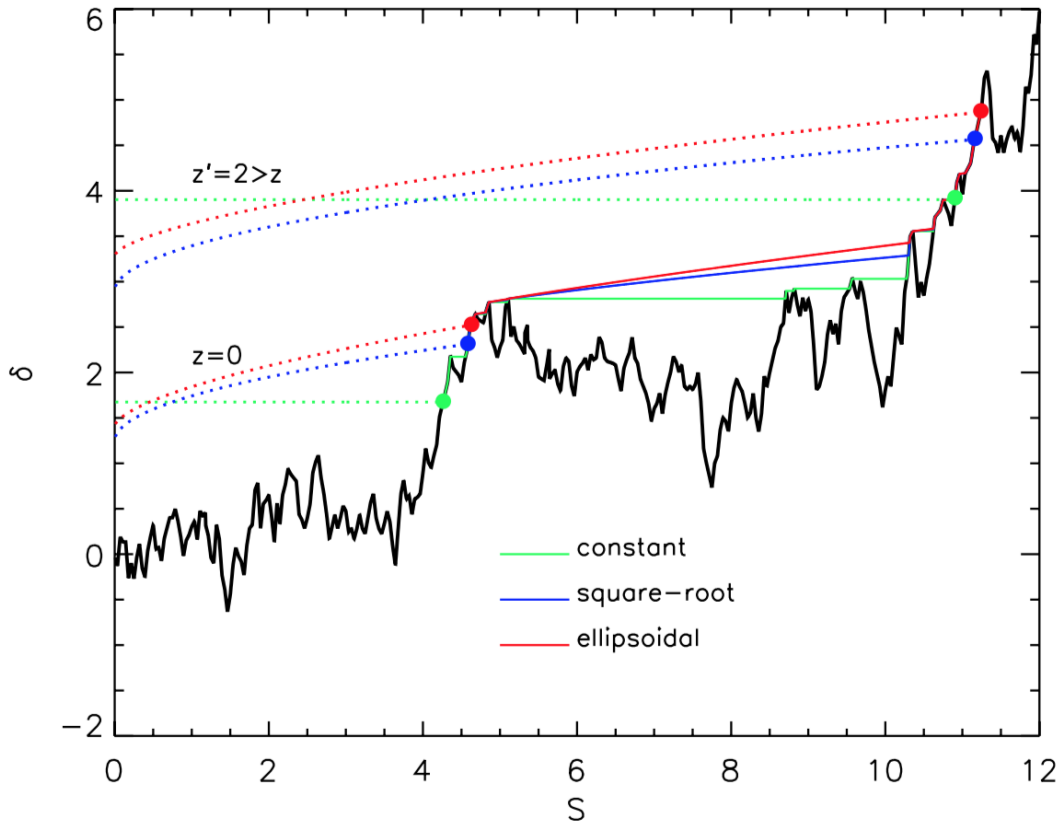

FIGURE 1.4: Example of a random walk executed by an overdensity δ around a given point as a function of the variance S. The black solid line represents the random walk. The dotted lines illustrate the constant (green), square-root (blue), and ellipsoidal barriers (red) at two redshifts $z = 0$ and $z' = 2$, with the dots indicating the locations of first crossing. Credits: Lapi et al. 2013.

where r_s is called scale radius and $\rho_s \equiv \rho(r_s)$. The mass inside radius r is given by:

$$M(r) = 4\pi \int_0^r \mathrm{d}r'\, r'^2\, \rho(r') = 16\pi\, \rho_s\, r_s^3 \left[\ln\left(1+\frac{r}{r_s}\right) - \frac{r/r_s}{1+r/r_s}\right] \tag{1.34}$$

Defining the concentration parameter $c \equiv r_{\rm vir}/r_s$ and $g(c) \equiv 1/(\ln(1+c) - c/(1+c))$, the NFW profile can be rewritten in terms of the virial radius and mass defined in Section 1.2.1:

$$\rho(r) = \frac{M_{\rm vir}}{4\pi\, r_{\rm vir}^3} \frac{c^2\, g(c)}{(r/r_{\rm vir})\,(1+c\, r/r_{\rm vir})} \tag{1.35}$$

with

$$M(r) = M_{\rm vir}\, g(c) \left[\ln\left(1+c\,\frac{r}{r_{\rm vir}}\right) - \frac{c\, r/r_{\rm vir}}{1+c\, r/r_{\rm vir}}\right] \tag{1.36}$$

The concentration parameter has a slight mass and redshift dependence; in particular it decreases at larger halo masses and at higher redshifts via power law relations. As an halo accretes mass over cosmic time, the concentration parameter tends to increase since matter is accumulated in the outskirt regions, increasing $r_{\rm vir}$, but leaving the central overdensity almost untouched.

Finally, I remark that, while NFW profile predicts a central logarithmic density slope $\gamma(r \simeq 0) \equiv \mathrm{d}\ln\rho/\mathrm{d}\ln r|_{r\simeq 0} \simeq -1$, observational data do not seem to favor such central cuspy profiles, but rather cored ones with $\gamma(r \simeq 0) \gtrsim 0.5$. This could be interpreted as the effect of gravitational interactions between DM particles and baryons which are not kept into account in DM only simulations.

Subhalos

Dark matter halos are not standalone entities, but are characterized by the presence of many substructures, called subhalos. Subhalos are smaller and less massive halos orbiting in the potential well of a larger halo and may host small satellite galaxies. The evolution of a subhalo is driven by many phenomena, such as tidal forces from the the host halo leading to tidal stripping, dynamical friction with respect to the background DM particles subtracting its energy and angular momentum and gravitational interactions with other subhalos. These processes may lead to destruction of many subhalos and the probability of surviving is related to the subhalo initial mass, density profile and orbit. For this reason it is usually defined an unevolved subhalo mass function in which subhalos are counted at the time of accretion and an evolved subhalo mass function in which subhalos are counted after a time

t. Both the unevolved and evolved subhalo mass functions can be described by the same functional form:

$$\frac{\mathrm{d}^2 N}{\mathrm{d}V\,\mathrm{d}\log\mu} \propto \gamma\,\mu^{\alpha}\,e^{-\beta\mu^{\omega}} \tag{1.37}$$

where $\mu \equiv M_{\rm sub}/M_{\rm host}$ is the mass ratio between the subhalo and the host halo and the set of parameters $(\gamma, \alpha, \beta, \omega)$ is different for the unevolved and the evolved case.

The subhalo mass function can be used to retrieve the average halo occupation number, i.e. the average number of subhalos in a host halo of given mass M_H at redshift z: $\langle N\rangle(M_H, z)$. Numerical simulations and halo occupation distribution models (Zehavi et al. 2005, 2011; Zheng et al. 2007, 2009; Tinker et al. 2013) suggest that the halo occupation distribution $P(N|\langle N\rangle)$ follow a Poisson distribution around the average number $\langle N\rangle$. The halo occupation distribution can be very important since it allows to obtain the galactic halo mass function (GHMF), i.e. the mass function of halos not containing subhalos and possibly hosting only a single galaxy (see Aversa et al. 2015):

$$\frac{\mathrm{d}^2 N_{GHMF}}{\mathrm{d}V\,\mathrm{d}\log M_H} = \frac{\mathrm{d}^2 N}{\mathrm{d}V\,\mathrm{d}\log M_H}\,P(<N=1|\langle N\rangle) \tag{1.38}$$

In Figure 1.5 it is shown the galactic halo mass function compared with the overall halo mass function at different redshifts.

Halo mergers and accretion

In ΛCDM growth of DM halos occurs bottom up, i.e. smaller structure are formed first and grow by merging with other DM halos or accreting not virialized matter in the surroundings. A merger is the coalescence of two virialized halos to form a new single virialized object. The process of growth of a DM halo through subsequent mergers with smaller systems is known as hierarchical merging, usually schematized in the famous merger tree. Mergers are divided in two categories depending on the merger mass ratio $\mu_H \equiv M'_H/M_H$ where M'_H is the less massive halo mass and M_H the most massive halo mass. Mergers with $\mu_H \lesssim 0.3$ are called minor mergers, while mergers characterized by $\mu_H \gtrsim 0.3$ are called major mergers. The merging rates per descendant halo per unit cosmic time and merger mass ratio are described by the fitting formula (Fakhouri & Ma 2008):

$$\frac{\mathrm{d}^2 N_{\rm merge}}{\mathrm{d}t\,\mathrm{d}\mu_H} = N\left(\frac{M_H}{10^{12}\,M_\odot}\right)^{a}\mu_H^{-b-2}\,e^{(\mu_H/\tilde{\mu}_H)^c}\,\frac{\mathrm{d}\delta_c(t)}{\mathrm{d}t} \tag{1.39}$$

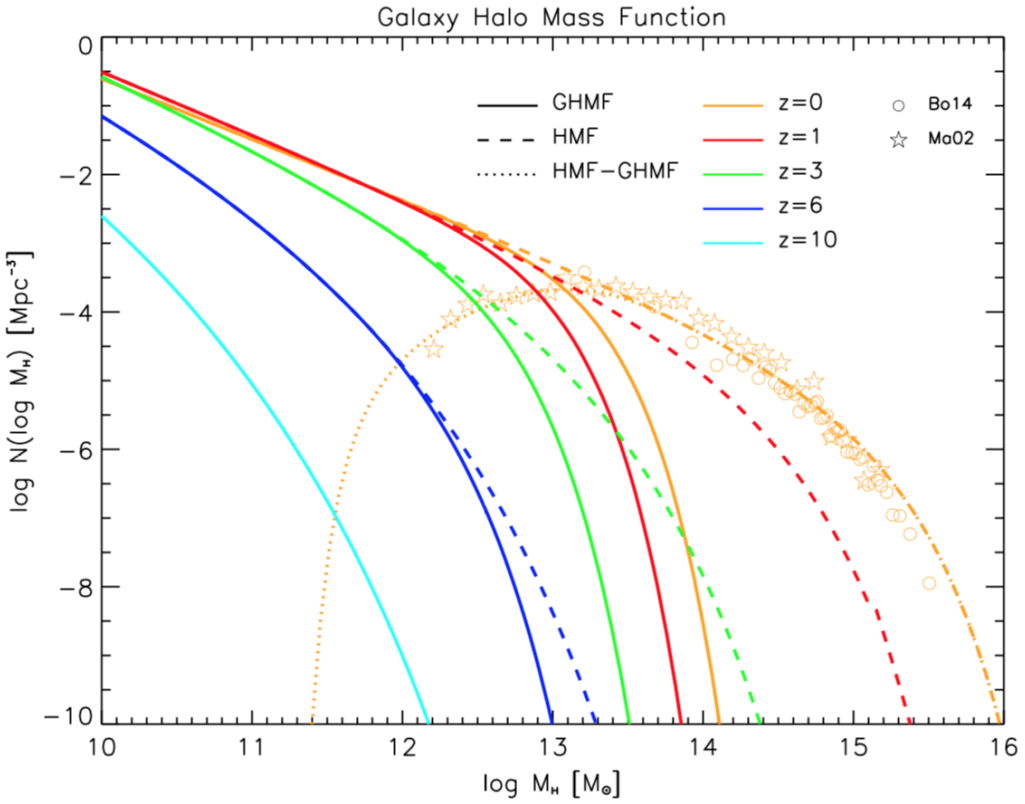

FIGURE 1.5: Solid lines represents the galactic halo mass function, dashed lines the total halo mass function at $z = 0$ (orange), $z = 1$ (red), $z = 3$ (green), $z = 6$ (blue), and $z = 10$ (cyan). The dotted line at $z = 0$ is the substraction of the two, i.e. the cluster and group halo mass function; this is compared with the determinations by Boehringer et al. 2014 (circles) from X-ray observations of groups and clusters and by Martinez et al. 2002 (stars) from optical observations of loose groups. Credits: Aversa et al. 2015.

The parameters of such a relation have been determined by Genel et al. 2010 comparing with results of the Illustris-Dark simulations, yielding: $N = 0.065\,\mathrm{Gyr}^{-1}$, $a = 0.15$, $b = -0.3$, $c = 0.5$, $\tilde{\mu}_H = 0.4$.

The other main mechanism driving the growth of DM halos is accretion from cosmic web. However, as many authors have pointed out (see Diemand et al. 2005; Cuesta et al. 2008; Diemer et al. 2013, 2017; Zemp 2014; More et al. 2015) such a growth should be interpreted carefully, remembering the definition of virial radius as the radius enclosing an overdensity $\Delta_c(z)\rho_c(z)$. Such a definition can lead to spurious evolution of the DM halo mass, due to the redshift evolution of the reference density $\rho_c(z)$. Since $\rho_c(z)$ decreases at larger cosmic times, the virial radius increases just because of its definition and, consequently, also the halo mass grows. This phenomenon is called

pseudo evolution and it is present even when other definitions of the halo mass are adopted, such as the commonly used $M_{200\bar{\rho}}$ and $M_{500\bar{\rho}}$. The authors cited above compared the mass evolution of DM halos using different definitions and showed that pseudo evolution is responsible for a large part of the observed halo mass increase with redshift. More et al. 2015 also proposed a formula to study the growth of halo mass inside a region of fixed physical size, typically $4\,r_s$, corresponding approximately to the initial virial radius. It's formula is useful to get rid of pseudo evolution and to keep into account only the physical evolution of the inner halo mass, which is more related to the central galaxy properties:

$$M_{\rm inner}(z) \simeq M_H(z)\,\frac{\ln(1+c_{\rm form}) - c_{\rm form}/(1+c_{\rm form})}{\ln(1+c) - c/(1+c)} \tag{1.40}$$

where $c_{\rm form}$ is the concentration parameter at formation time of the halo.

In Figure 1.6, I show the growth of halo mass as a function of cosmic time for halos of different descendant mass. It is shown the evolution of the mass defined as the DM mass contained in a region with spherical overdensity $200\,\bar{\rho}(z)$ (blue), which is similar to the usual definition of the virial radius and includes pseudo evolution, the evolution of the mass inside a fixed physical radius (red), defined as the virial radius at $z \sim 0$, which is depurated from pseudo evolution and the evolution of the mass inside a region with fixed spherical overdensity (orange), defined as $200\,\bar{\rho}(0)$, which seems to be scarcely affected by pseudo evolution.

1.3 Galaxy statistics and evolution

In Section 1.2 I reviewed the formation, the growth and the statistics of dark matter halos. They are extremely important for galaxy formation and evolution, since they provide the potential wells in which baryonic gas collapse, cool and forms stars, creating bound structures called galaxies. In this Section I summarize the main observational findings about galaxies, focusing on their statistical properties and on some scaling relations between different observables. I remark that this treatment is far from being complete since galaxy evolution is a wide field, still very open and rapidly evolving. The idea of this Section is to describe some basic elements and tools that will be used in the rest of the thesis.

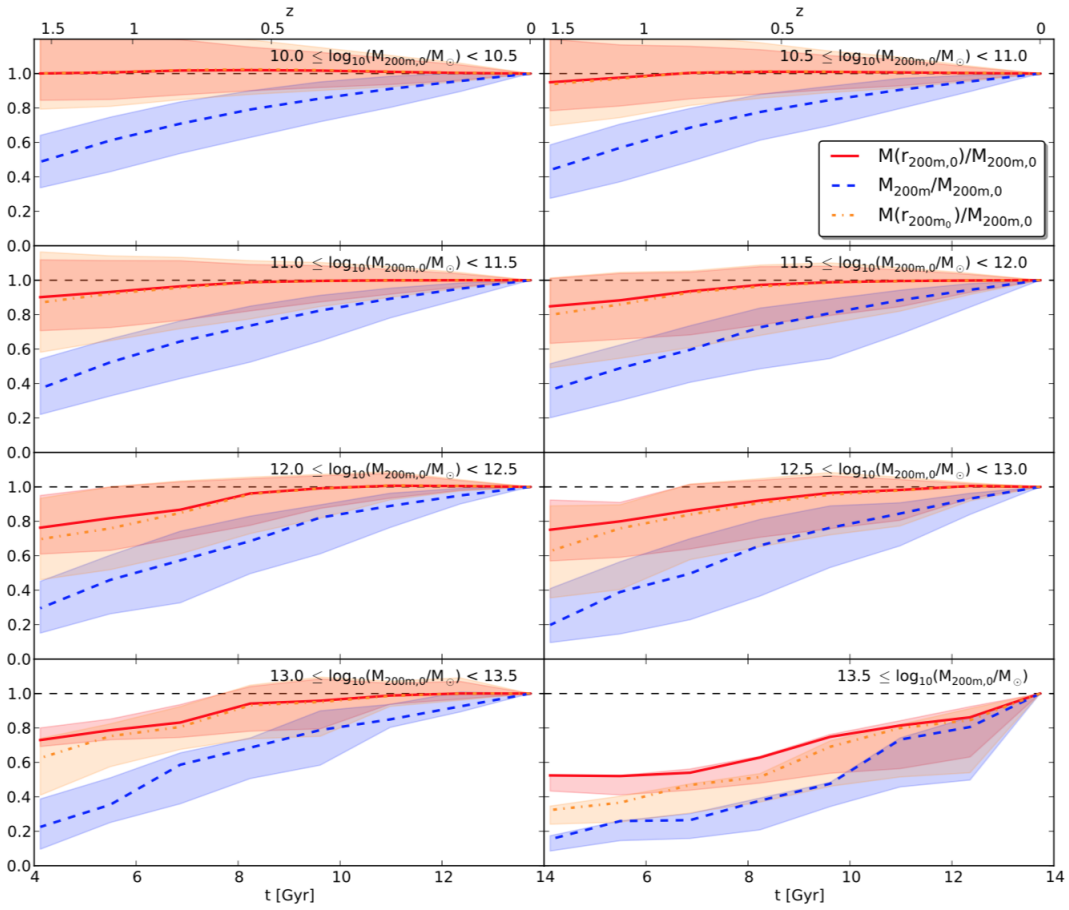

FIGURE 1.6: Mass evolution as a function of cosmic time for halos of different descendant mass. The blue curve shows the evolution of the mass contained in a region with spherical overdensity 200 $\bar{\rho}(z)$, the red curve the evolution of the mass inside a fixed physical radius, i.e. the virial radius at $z \sim 0$, the orange curve the evolution of the mass inside a region with fixed spherical overdensity, defined as 200 $\bar{\rho}(0)$. Shaded areas represent the 15th to 85th percentile ranges. Credits: Zemp et al. 2014

1.3.1 Galaxy classification

Galaxy classification is not an easy task even at $z \sim 0$ since galaxies are complex systems that can be made of different stellar populations and can show a vast variety of properties. Categorizing them by one specific attribute is limiting, since galaxies of the same group can behave differently with respect to other features that they have in common with galaxies of other groups. Moreover, since any classification is observationally based, it can be biased by degeneracies between parameters, by systematics of the observational

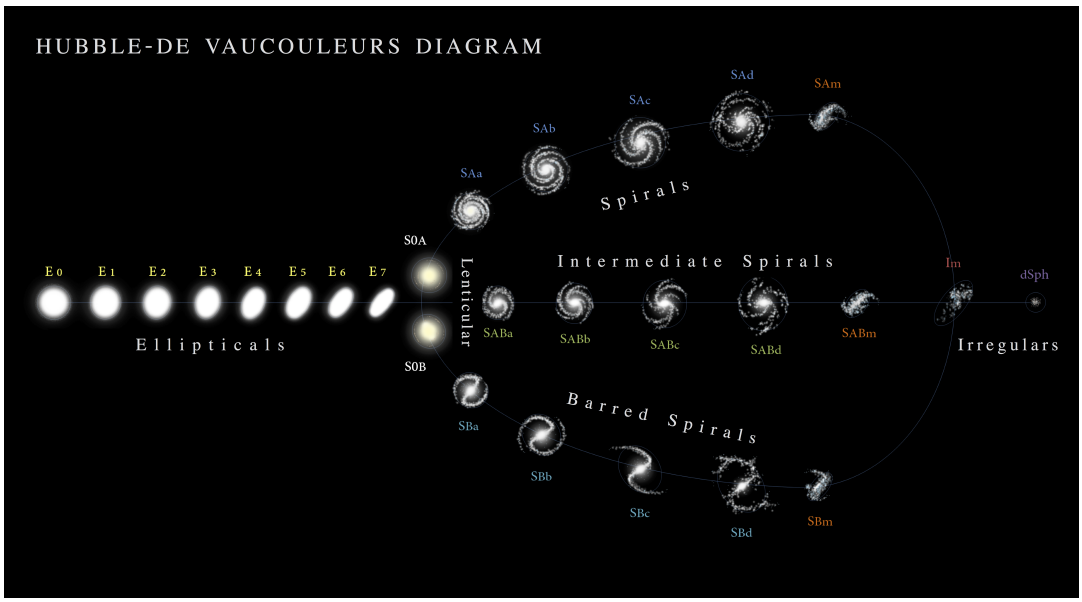

FIGURE 1.7: Morphological classification of galaxies by De Vaucouleurs.

instrument or even by the electromagnetic band chosen to perform the observation. At higher redshift the angular resolution of telescopes, especially ground-based ones, is another issue to take into account, not allowing for a detailed study of the galaxy on small scales.

The first type of classification at $z \sim 0$ was done by morphology by Hubble and then it has been extended by de Vaucouleurs (see Figure 1.7). On the left of the diagram there are elliptical galaxies going from E0 to E7 as the ellipticity grows. To the right of E7, galaxies start showing a central elliptical structure, called bulge, surrounded by a disk. In S0 galaxies, called lenticular galaxies, the disk component is extremely faint but it becomes more important going to the right part of the diagram containing S galaxies, also called spiral or disk galaxies. The subscript a-d indicates the importance of the disk component with respect to the bulge. The rightmost galaxies in the diagram, with subscript m, have irregular shapes. The 3 branches of the fork, specified by the letters A, B and AB, are for normal spiral galaxies, barred spirals and intermediate ones. Finally, galaxies with mass and luminosity $\sim$ 1 order of magnitude less than the Milky Way are called dwarfs. The morphological classification is one of the simplest, but I stress that even the morphological structure, especially the importance of disk with respect to bulge, depends on the observational wavelength, since stars with different ages and properties, and thus different colors, are typically located in different regions of the galaxy.

In order to further simplify the classification, galaxies are mainly grouped

in two classes: late-type galaxies (LTGs) and early-type galaxies (ETGs). LTGs are on the right part of the diagram, corresponding mainly to disk galaxies and irregulars. Since almost all the LTGs are forming stars in the local Universe they are also called star-forming galaxies (SFGs). ETGs are on the left part of the diagram, corresponding mainly to ellipticals and lenticulars. Since most of ETGs are not forming stars in the local Universe they are also called quiescent or passive galaxies. In the next Subsections I report the main observational properties of LTGs and ETGs.

Late-type galaxies (LTGs)

Late-type galaxies are the ensemble of disk galaxies and irregulars. Typically they have ongoing star formation, with a star formation rate (SFR) of the order of $\psi \sim 0.1 - 30\,\mathrm{M_\odot\,yr^{-1}}$ for spirals and $\psi \lesssim 1\,\mathrm{M_\odot\,yr^{-1}}$ for irregulars and a stellar mass in the range $10^9 - 10^{11}\,M_\odot$ for spirals and $\leq 10^9\,M_\odot$ for irregulars. Their stellar population is found to have a wide variety of ages, ranging from old stars ~ 10 Gyr to very young stars recently formed. From stellar archaeological analyses, consisting in the observation of single stars or in the fit of the full galactic spectra with composite stellar population models, it has been found that the star formation history (SFH) of LTGs can be thought to be almost flat or slowly evolving. They are usually described through an exponentially declining shape:

$$\psi(\tau) \propto e^{-\tau/\tau_\psi} \tag{1.41}$$

with a long star formation timescale $\tau_\psi \sim 6-8$ Gyr (see Chiappini et al. 1997; Courteau et al. 2014; Pezzulli & Fraternali 2016; Grisoni et al. 2017). Such a moderate and prolonged SFR is roughly consistent with their stellar masses: a typical galaxy with $\psi \sim 1\,M_\odot\,\mathrm{yr^{-1}}$ forming stars for ~ 10 Gyr will end up having a stellar mass $\sim 10^{10}\,M_\odot$.

Although the description above is valid on average, LTGs, especially disk galaxies, are composite systems with different stellar populations occupying different galactic regions. Generally speaking, an LTG can feature a galactic disk, a bulge or pseudo-bulge, a stellar bar and a stellar halo. Not all these elements are necessarily present and they can have various relative prominences, depending on the considered galaxy.

A rotationally supported stellar disk is present in all the spirals, with spiral arms extending from the center to the periferic regions. The stellar disks, especially the spiral arms, is where most of the star formation takes place and, due to the presence of young hot stars, it is typically very bright in the UV and optical band. The disk can have a variable extension in the range $1 - 10$ kpc, depending on the stellar mass, and disk stars are supported by

rotational velocity, with the ratio between tangential velocity and velocity dispersion $v/\sigma > 1$. This ratio regulates also the thickness of the disk: for $v/\sigma \sim 10$ the disk is thin, while for $v/\sigma \sim 1$ it is thicker. The surface brightness for a face-on disk galaxy can be well approximated by a Sersic profile (Sersic 1968):

$$I(r) = I_0 \exp\left[-b(n)\left(\frac{r}{R_e}\right)^{1/n}\right] \tag{1.42}$$

where R_e is the half light radius, n is the Sersic index and $b(n) \simeq 2n - 1/3 + 4/(405\,n)$. For disk galaxies $n \simeq 1$, so the surface brightness profile is a declining exponential with disk scale radius $R_d = R_e/b(1)$ in the range $1 - 10$ kpc.

Stellar bulges are instead spheroidal structures hosted at the center of disk galaxies. Their stellar population has properties more in common with ellipticals: they are older than stars in the disk, they are distributed following a Sersic profile with $2 \leq n \leq 4$ and they are supported by random motions with scarce or absent rotation. Pseudobulges are instead flatter than bulges, with lower Sersic indeces $n \leq 2$, higher rotation and a significant amount of star formation. Stellar bars are prolate structures with stellar population similar to the disk, but older on average. Bars are present in $\gtrsim 50\%$ of disk galaxies and they have similarities with pseudobulges. For these reasons it is thought that pseudobulges and bars are dynamically originated from disk evolution.

The stellar halo is constituted by stars which do not belong to the disk, bar or bulge. These stars do not lie on the disk plane, and can be diffuse stars or grouped in globular clusters or stellar streams. The stellar halo is present in almost all LTGs, a part for low mass ones.

LTGs hold a significant amount of interstellar medium, constituted by atomic neutral or ionised gas, molecular gas and dust. Gas can be classified as hot if $T \gtrsim 10^6$ K, warm if 10^3 K $\lesssim$ T $\lesssim 10^4$ K or cold if $T \lesssim 10^2$ K. Neutral atomic gas is mainly in the form of hydrogen (HI) with only $\sim 9\%$ of helium and a lesser percentage of metals. It can be observed via the 21 cm line of hydrogen, originated by the spin flip of the electron. HI mass depends on the galaxy type and the ratio between stellar and HI mass ranges from ~ 10 for massive spirals to $\lesssim 1$ for dwarf galaxies. HI radial distribution is shallower with respect to stars, with typical scale radius $\sim 1.5 - 2$ times larger than the stellar disk. Such a wide extension makes HI extremely important for rotation curves determinations and for studies of of DM distribution in galaxies. Neutral atomic gas is typically found in cold or warm phase.

Gas can be ionized by photons or by collisions. Photoionized gas can be found around massive stars which produce high energy ionizing photons

with $E_\gamma > 13.6$ eV able to break the hydrogen bond. Photoionized gas can be observed mainly via recombination lines, such as the Balmer or the Lyman series. The Balmer series, in particular the Hα line coming from the transition between the 3rd and 2nd hydrogen energy level, is often used for the estimation of the galaxies star formation rate, since it is connected to young hot stars. Photoionized regions also emit the so called forbidden lines, characterized by rather small Einstein coefficients and due to the de-excitation of ions such as O^+ (O[II]) and O^{2+} (O[III]), excited by electron collisions. These lines have been used to estimate the temperature of photoionized gas, finding $T \sim 10^4$ K. A fraction of ISM can also be collisionally ionized by shock and shock waves produced by stellar processes such as stellar winds and supernova explosions. Shocks are able to heat the gas up to very high temperatures $T \sim 10^6$ K and to ionize it. This form of energetic feedback injected by stars into the gas is extremely important in the regulation of the star formation process and must be kept into account in any galaxy evolution model.

Molecular gas is mainly in the form of molecular hydrogen and it is located in large molecular clouds with mass $\sim 10^7\, M_\odot$, high density $\gtrsim 10^2$ cm^{-3} and low temperatures $T \sim 10$ K. These cold and dense molecular clouds are the regions where most of the star formation occurs, therefore H_2 distribution traces the stellar distribution much better than neutral hydrogen and it is found to be more concentrated toward the inner galactic region and in the spiral arms.

Dust constitute only $\sim$ 1% of the ISM of LTGs but it plays a crucial role for galaxy evolution. First of all molecular hydrogen, fundamental for star formation, is formed on the surface of dust grains, second dust grains, absorbing UV radiation, are able to skirmish molecular hydrogen and prevent its photo dissociation. From the observational point of view the presence of dust must be kept into account in the estimation of the SFR of a galaxy. Indeed dust grains absorb UV and optical light and re-emit it in the mid and far-IR band, hampering the amount of escaping UV radiation used for SFR estimations. This phenomenon is called dust extinction and its importance, at different wavelengths, is characterized by the so called extinction curves, calibrated on local galaxies. Extinction curves can be different for different galaxies but, in general, the extinction magnitude scales as λ^{-1} from $\lambda \gtrsim 1000$ Å to far-infrared (FIR) wavelengths where there is no extinction.

Neutral and molecular gas are fundamental ingredients in star-forming

galaxies, since it has been shown that their surface density $\Sigma_{\rm gas}$ tightly correlates with SFR surface density $\Sigma_{\rm SFR}$. Such a correlation is called Schmidt-Kennicutt law (Schmidt 1959; Kennicutt 1998):

$$\Sigma_{\rm SFR} \simeq 10^{-4} \left(\frac{\Sigma_{\rm gas}}{M_\odot \, {\rm pc}^{-2}} \right)^{3/2} {\rm M}_\odot \, {\rm yr}^{-1} \, {\rm kpc}^{-2} \tag{1.43}$$

Equation (1.43) is thought to be originated by the fact that volume density of star formation rate can be thought to be proportional to volume density of gas divided by a typical star formation timescale. If such a timescale is the free-fall time $t_{\rm ff} \propto \rho_{\rm gas}^{-1/2}$ the volumetric relation $\rho_{\rm SFR} \propto \rho_{\rm gas}^{3/2}$ is obtained, which has the same scaling as equation (1.43). Since star formation is fed by cold gas, an important quantity usually estimated is the depletion time:

$$t_{\rm dep} \equiv \frac{M_{\rm gas}}{\psi} \tag{1.44}$$

which is the typical time during which a galaxy can form stars at a constant rate before exhausting its gas reservoir. For molecular gas in LTGs $t_{\rm dep} \sim 1$ Gyr, but this estimation can be altered by gas inflows and outflows and by the returned fraction of gas from stellar evolution. Inflows are due to gas accretion onto galaxies and can refurnish the gas supply, while outflows are due to galactic winds and supernova explosions, which expel gas from the galaxy. In regions containing associations of big O and B stars, SN explosions originate large expanding bubbles of gas which, reaching sizes comparable to the thickness of the disk, are able to expel huge amounts of gas (up to $\sim 10\%$) into the galactic halo. This material leave the star-forming region and fall back in another part of the disk. This phenomenon is usually called galactic fountain. The returned gas fraction is instead the result of the evolution of massive $M > 8\,M_\odot$ and intermediate $2\,M_\odot \leq M \leq 8\,M_\odot$ stars. Massive stars have a quick evolution $\lesssim 30$ Myr and return their gas to the ISM through stellar winds and core collapse supernova explosions, while intermediate mass stars have a slower evolution and return part of their material to the ISM during their giant and supergiant phases. This returned gas is metal enriched by stellar evolution processes (see Section 1.3.4) for further details.

Early-type galaxies (ETGs)

Early-type galaxies comprise ellipticals, lenticulars and dwarf ellipticals. Ellipticals feature very low or absent star formation in the present Universe, but they have huge stellar masses in the range 10^9–$10^{12}\,M_\odot$. Lenticulars have

almost comparable masses, while dwarf ellipticals are smaller $\leq 10^9\,M_\odot$. ETGs are redder than LTGs due to the presence of an older stellar population and/or higher stellar metallicities. Their color is found to correlate with their stellar mass, in particular redder galaxies are, on average, more massive, originating the so called red sequence.

In order to fully understand the properties of their stellar population an analysis of their spectral energy distribution (SED) is needed. Particularly important is the observation of the widths of some specific absorption lines in the optical band, called Lick indices, which are often used to maximize the sensitivity with respect to one parameter and to break the degeneracy between age and metallicity. Through this analyses it is found that stars inside ellipticals are old (> 5 Gyr) and almost coheval, with an age difference smaller at larger stellar masses. Moreover the stellar population follow 3 important scaling relations with the velocity dispersion, or with the total dynamical mass: the age-velocity relation, the metallicity-velocity relation and the α-enhancement-velocity relation. The age-velocity dispersion relation simply means that more massive ellipticals are older than less massive ones with stellar ages in the range $5 - 14$ Gyr. The metallicity-velocity dispersion relation states that more massive ellipticals are also more metal enriched with typical metallicities in the range $0.7 - 2.5\,Z_\odot$. Finally, the α-enhancement-velocity dispersion relation is a powerful indicator of star formation history. α-enhancement is the measure of the ratio of α-elements such as oxygen or magnesium against heavier elements such as iron, compared to the solar ratio. Since α-elements are produced by stellar winds and core collapse SNe while heavier elements are produced by type Ia SNe, α-elements enrichment occurs on shorter timescales. Therefore, if star formation is halted before type Ia SNe had time to explode and pollute the medium, the resulting stellar population will be more abundant in α-elements. α-enhancement in ETGs is usually positive and correlates with velocity dispersion and dynamical mass, with values of [Mg/Fe] in the range $0.05 - 0.4$. All these stellar archaeological results suggest 3 things:

- The coheval population of α-enhanced stars reveals that most of the stellar mass should have been built up in a rather short timescale $\tau_\psi \lesssim 0.5 - 1$ Gyr, especially in high mass ellipticals, with a main strong and short episode of star formation. More massive galaxies, being more α-enhanced, have had stronger and shorter SFHs.

- The metallicity growth, especially for α-elements has been very fast, reaching solar or even supersolar values at the end of the star formation episode.

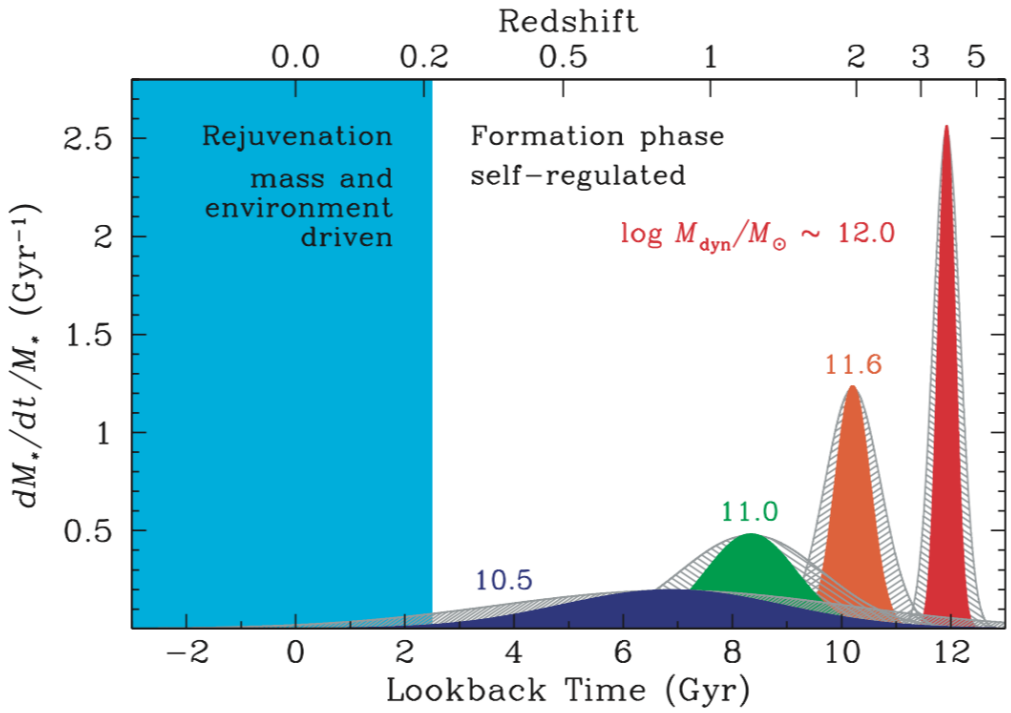

[h!]

FIGURE 1.8: Average specific SFR for ETGs as a function of the lookback time (bottom x axis) or redshift (top x axis). Color code indicates different dynamical masses. Credits: Thomas et al. 2010.

- More massive galaxies formed and evolved earlier and faster than lower mass ones. This is the so called downsizing scenario.

Such a scenario of ellipticals formation is well explained in Figure 1.8 from Thomas et al. 2010. It is shown the specific star formation rate sSFR $\equiv \psi/\mathrm{M}_\star$ as a function of the lookback time or redshift for galaxies of different dynamical mass, i.e. the total mass constituted by baryons and dark matter. More massive galaxies formed earlier and on a shorter timescale. It is worth noticing that the presented star formation histories are just a sketch of the typical formation history averaged over the entire galaxy population of a certain dynamical mass. Real star formation histories of individual galaxies are expected to be more bursty.

The shape of most ETGs is ellipsoidal with no stellar disk or spiral arms, except for the case of lenticular galaxies. Ellipticals, especially high mass ones, are triaxial systems, which tend to become oblate spheroids at lower masses. Their surface brightness is distributed according to a Sersic distribution with $2 \leq n \leq 10$, increasing as a function of the stellar mass and

$R_e \sim 1 - 10$ kpc. Since ellipticals are not planar as disk galaxies, it is useful to deproject the surface brightness profile, deriving the deprojected 3D Sersic profile, which, assuming that the baryonic mass distribution follows the light distribution, can be thought as the matter density profile in elliptical galaxies. Deprojection of equation (1.42) has been done in Prugniel & Simien 1997 and reads:

$$\rho(r) = A \left(\frac{r}{R_e}\right)^{-\alpha} \exp\left[-b\left(\frac{r}{R_e}\right)^{1/n}\right] \tag{1.45}$$

where A is a normalization constant and $\alpha = 1 - 1.188/(2n) + 0.22/(4n^2)$.

One of the most important structural scaling relations for ellipticals is the fundamental plane: a correlation identifying a 2D plane in the 3D parameter space defined by the half-light radius R_e, the velocity dispersion σ and the surface brightness $\langle I_e \rangle \equiv L/2\pi R_e^2$, which is followed by almost all ellipticals:

$$\log R_e = \alpha \log \sigma + \beta \log\langle I_e \rangle + \gamma \tag{1.46}$$

where $1 \lesssim \alpha \lesssim 1.4$, $-0.9 \lesssim \beta \lesssim -0.75$ and γ is a normalization constant.

Elliptical galaxies are mainly supported by velocity dispersion, with $v/\sigma \leq 1$, however, in some of them, especially the flatter ones, rotation is not completely absent and can play a role in flattening the ellipsoid. Systems flattened by rotation are called fast rotators, while systems with $v/\sigma \lesssim 0.2$ are called slow rotators and are flattened by orbital anisotropies.

Lenticular galaxies have instead a different shape and are more similar to spirals: they exhibit a central bulge surrounded by an extended disk with very faint or absent spiral arms.

As for the gas content, ETGs have a much less amount of gas with respect to LTGs and it is mainly in the form of hot ionised plasma emitting in the X-ray via bremsstrahlung or via collisionally excited lines from ionized metals. The exponential cut off in the X-ray spectrum allows to estimate the gas temperature that turns out to be almost comparable to the virial temperature $T \sim 10^6 - 10^7$ K. Despite with largely lower abundances also warm and cold gas are present in ETGs. Cold gas can be in the form of neutral atomic gas or molecular hydrogen. HI, in some cases, can be placed in an extended disk, as in the case of spiral galaxies, while H_2 is mostly present in the central regions in a various range of structures. Dust is also present and can be detected from the obscuration of optical stellar light and from its thermal emission.

Higher redshift galaxies

Observation of galaxies at high redshift $z > 1$ is challenging, especially for telescopes flux limits, and their search requires specifically designed surveys. However, after 1990 great progresses have been achieved in this field and the direct observation of galaxy evolution has become possible, even though still partial. In the following, I describe the main properties of galaxies at $z > 0$ selected at different wavelengths.

A commonly used technique to select high redshift galaxies in the optical band is through the Lyman break: UV photons with $\lambda_{\rm rest} < 1216\,$Å are typically absorbed by neutral hydrogen inside the galaxy and by the IGM along the line of sight. Therefore galaxies usually show a break in their spectrum at shorter wavelengths. Such a break is redshifted in the optical B band for galaxies at $z \sim 3$ and towards redder band for galaxies at $z > 3$; therefore, observing the Lyman break in the corresponding filter, allow to select high redshift galaxies. At $z < 3$ the drop is at wavelengths where the Earth atmosphere is opaque and other criteria must be used to select galaxies at $1 \leq z \leq 3$. Since Lyman break galaxies are selected from their rest frame UV spectra, they are star-forming systems with low dust attenuation. Their SFR is higher with respect to $z \simeq 0$ SFGs with $\psi \sim 10 - 30\,{\rm M}_\odot\,{\rm yr}^{-1}$, sometimes extending up to $\psi \lesssim 100\,{\rm M}_\odot\,{\rm yr}^{-1}$. They have stellar masses in the range $M_\star \sim 10^{10} - 5\times10^{10}\,{\rm M}_\odot$ and relatively high specific star formation rate sSFR $\equiv \psi/{\rm M}_\star \gtrsim 10^{-9}\,{\rm yr}^{-1}$, meaning that they are assembling a significant part of their stellar mass at that cosmic time. Morphologically, they are mainly irregulars and their sizes are smaller with respect to local SFGs, with typical half-light radii $R_e \sim 0.7 - 3\,$kpc and their ISM and stellar metallicity are in the range $0.1 - 1\,Z_\odot$.

Near infrared (NIR) surveys are also extremely important methods to detect high-z galaxies, since they attenuate the bias toward young star-forming galaxies selected in optical band. NIR samples allow to select also old galaxies with no ongoing star formation or dust reddened star-forming galaxies which were missed in optical surveys. Moreover NIR luminosity well traces the integrated light coming from evolved stars which constitute the bulk of the galaxies stellar mass. Therefore, this kind of selection is widely used to study galaxy stellar mass functions. Thanks to NIR surveys 2 important discoveries were added to the galaxy evolution picture:

- it was discovered a population of star-forming galaxies at $1 \leq z \leq 3$ with masses $M_\star \gtrsim 10^{11}\,{\rm M}_\odot$ larger than the SFGs detected in optical band. Their SFR $\psi \lesssim 100 - 200\,{\rm M}_\odot\,{\rm yr}^{-1}$ is also higher than the optically selected galaxies and their metallicity is around solar values.

- it was discovered a population of massive quiescent spheroidal galaxies which are the high redshift counterpart of local ETGs. Their abundance is comparable to SFGs at $1 \leq z \leq 3$, while it starts to decline at higher redshifts. As local ETGs, they have an old stellar population formed few Gyr before, with solar or supersolar metallicities and α-enhanced, indicating that their stellar mass has to be formed at $z > 3$ on very short timescales, in agreement with the downsizing scenario. Though, their size is different from local ETGs, with typical half light radii $R_e \lesssim 1$ kpc.

Also far-IR/(sub)mm surveys have a crucial role in the understanding of galaxy formation and evolution. Dust present in galaxies absorbs UV radiation produced by young massive stars and thermally re-emit it as a grey body spectrum with peak at $\lambda_{\rm rest} \simeq 100\,\mu$m. At high redshift this peak shifts toward submillimeter (submm) wavelengths. For this reason, increasing redshift, star-forming galaxies observed in the submm band become brighter rather than fainter. Far-IR/(sub)mm observations, with SCUBA, Hershel, Spitzer and ALMA, led to the discovery of a previously unknown population of high redshift $2 \leq z \leq 6$ star-forming galaxies, the so called submillimeter galaxies (SMGs). These galaxies feature extremely high SFR $\psi \sim 100 - 3000\,{\rm M}_\odot\,{\rm yr}^{-1}$, with a large molecular gas reservoir $M_{H_2} \sim 10^{10} - 10^{11}\,{\rm M}_\odot$ concentrated in a very compact spheroidal region characterized by $R_e \lesssim 1$ kpc. Their stellar mass can reach $M_\star \sim 10^{11}\,{\rm M}_\odot$ and their sSFR can be as high as $10^{-8}\,{\rm yr}^{-1}$ meaning that they are building most of their stellar mass through this huge star formation episode. For these reasons they are believed to be the progenitors of lower redshift ETGs, caught in the act of building up their stellar mass.

Let me now briefly summarize the picture of galaxy evolution from the observational point of view: galaxies can be divided in 2 main classes with very different histories of star formation and mass assembly: LTGs and ETGs. LTGs have ongoing star formation at a low or moderate rate $\psi \sim 0.1 - 10\,{\rm M}_\odot\,{\rm yr}^{-1}$. They have secular star formation histories over long ~ 10 Gyr timescales and their stellar population features different ages. Their metallicity depends on the mass and tend to decrease at high redshift, when the galaxy is younger. They are composite system constituted by an old central bulge and an extended star-forming disk rotationally supported. ETGs are instead quiescent galaxies of spheroidal shape with low or absent rotation. Their stellar population is almost coheval, old, metal rich and α-enhanced, indicating that their stellar mass has been built up on short timescales in the early Universe; in particular more massive galaxies should form earlier and faster. This scenario is confirmed by the detection of quiescent ellipticals

even at $z \sim 2$ and by the observation of SMGs at higher redshift featuring extreme star formation episodes.

1.3.2 Luminosity and mass functions

In Section 1.3.1 I have classified $z \sim 0$ galaxies based on their main observational features and I have discussed some properties of higher redshift galaxies. Now I deal with galaxy statistics, which provides a way to quantitatively classify and count galaxies with respect to one observational property such as stellar mass, luminosity or star formation rate.

Galaxy stellar mass function

The galaxy stellar mass function (GSMF) $\mathrm{d}^2N/\mathrm{d}M_\star/\mathrm{d}V$ is the number of galaxies per unit comoving volume per bin of stellar mass at different redshifts. It is constructed deriving the stellar mass mostly from NIR observations, dividing the mass range in bins and counting the galaxies in each bin in a given volume. Recent determinations of the GSMF at $z \sim 0$ are obtained in Baldry et al. 2012; Moustakas et al. 2013; Kelvin et al. 2014a; Moffett et al. 2016. In Figure 1.9 I show the determination by Moffett et al. 2016, in which the contributions of different morphological types are shown.

The overall GSMF is usually fitted via a single Schechter function (Schechter 1976):

$$\frac{\mathrm{d}^2N}{\mathrm{d}M_\star\,\mathrm{d}V} = \Phi^* \left(\frac{M_\star}{M^*}\right)^\alpha \exp\left(-\frac{M_\star}{M^*}\right) \tag{1.47}$$

which is characterized by a power-law behaviour at $M_\star \ll M^*$ with exponent α and an exponential cut-off at $M_\star \gg M^*$, hampering the presence of galaxies with extremely high masses. M^* is called the mass of the 'knee' and Φ^* is a normalization constant.

Since the mass function for LTGs and ETGs is substantially different (see Figure 1.10), it is customary to separately fit the disk-dominated and spheroid-dominated galaxies and to recover the mass function as the sum of these contribution, or to fit the mass function with a double Schechter profile, envisaging a separated exponential behaviour for the 2 types of galaxies, but a common knee mass M^*. From Figure 1.10 it can be see that disk-dominated galaxies are predominant at low masses $M_\star \lesssim 10^{10} - 10^{10.5}\,\mathrm{M}_\odot$, while spheroids at larger masses.

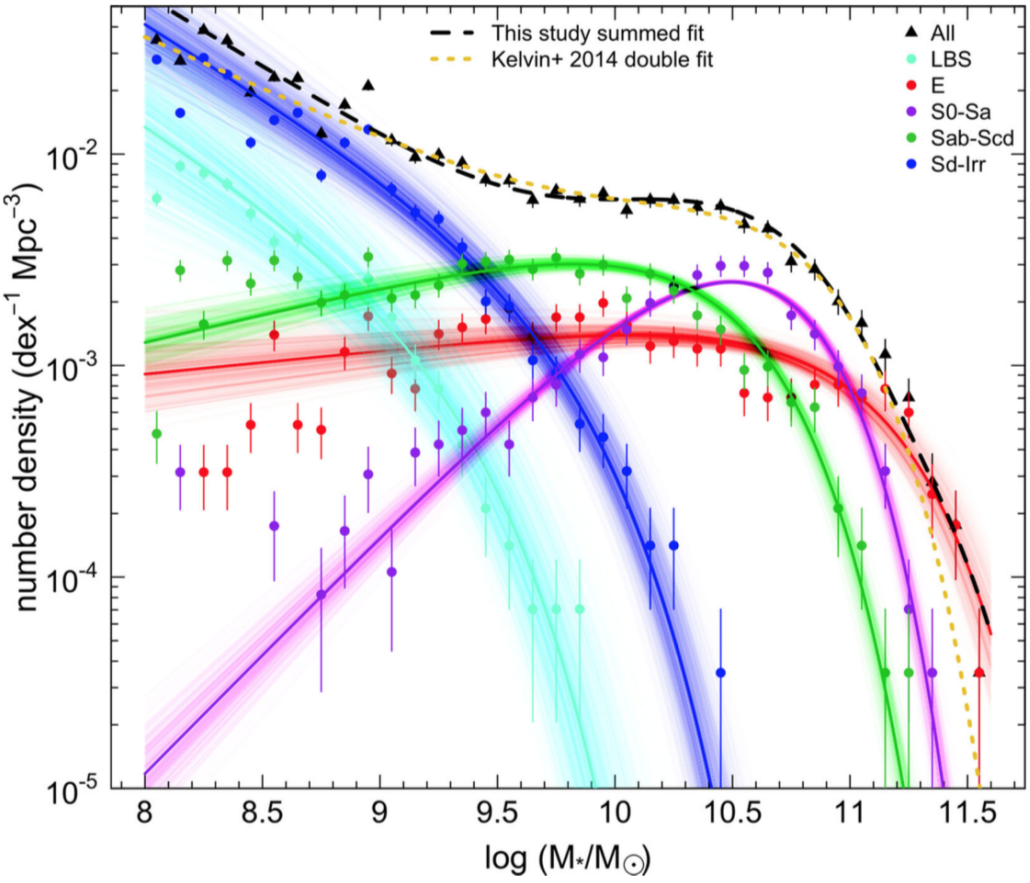

FIGURE 1.9: Contribution to the GSMF from different morphological types of galaxies: cyan are little blue spheroids, blue are Sd galaxies and irregulars, green are disk galaxies in the range Sab-Scd, purple are lenticulars S0 and Sa galaxies, red are ellipticals. Finally, black triangles are the overall GSMF data points, black dashed line is the fit performed in Moffett et al. 2016 and gold dashed line is the fit from Kelvin et al. 2014a. Credits: Moffet et al. 2016.

The total stellar mass density can be determined by integrating the GSMF multiplied by the stellar mass itself:

$$\rho_\star = \int \mathrm{d}M_\star \, M_\star \, \frac{\mathrm{d}^2 N}{\mathrm{d}M_\star \, \mathrm{d}V} \tag{1.48}$$

Separating the contribution of disks and spheroids it can be seen that spheroid-dominated galaxies account for $\sim$ 70% of the total stellar mass density, while disks for $\sim$ 30%, even though a disk component can be present in spheroid-dominated galaxies such as lenticulars or Sa galaxies. At higher

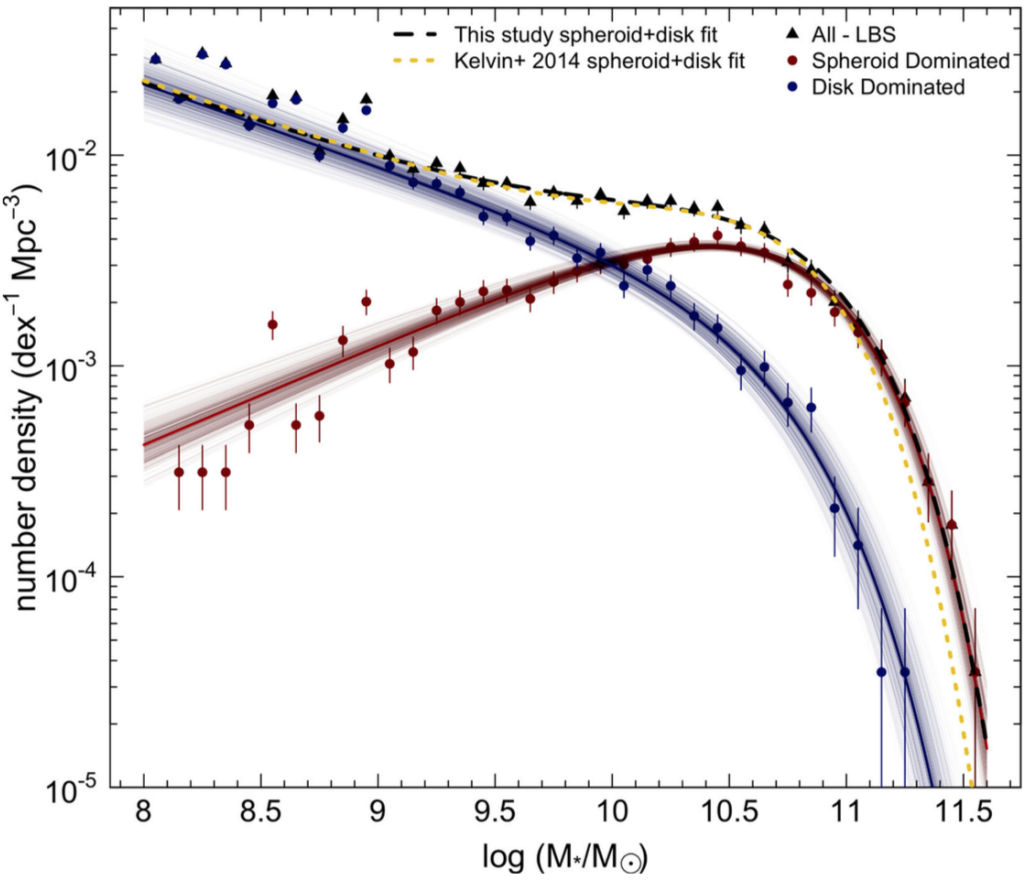

FIGURE 1.10: Contribution to the total GSMF from disk-dominated (blue) and spheroid-dominated (red) galaxies. Credits: Moffett et al. 2016

redshifts, recent determinations of the GSMF have been carried out by Ilbert et al. 2013; Muzzin et al. 2014; Tomczak et al. 2014; Davidzon et al. 2017, up to $z \sim 6$. In Figure 1.11 I report the GSMF by Davidzon et al. 2017, which can be splitted in SFGs stellar mass function and quiescent galaxy stellar mass function. The higher redshift GSMF can still be fitted by a double Schechter shape with redshift dependent parameters $\Phi_1^*(z), \Phi_2^*(z), \alpha_1(z), \alpha_2(z), M^*(z)$. GSMF determinations at $z > 6$ have been attempted by recent works by Song et al. 2016 and Bhatawdekar et al. 2019. However I caveat that determinations of GSMF, especially at high redshift, are still uncertain, mostly on the faint and bright end, with different studies presenting different results. Moreover, since different surveys with various levels of completeness and distinct selection effects are used at different redshifts, the transition between redshift bins of the GSMF may be not smooth.

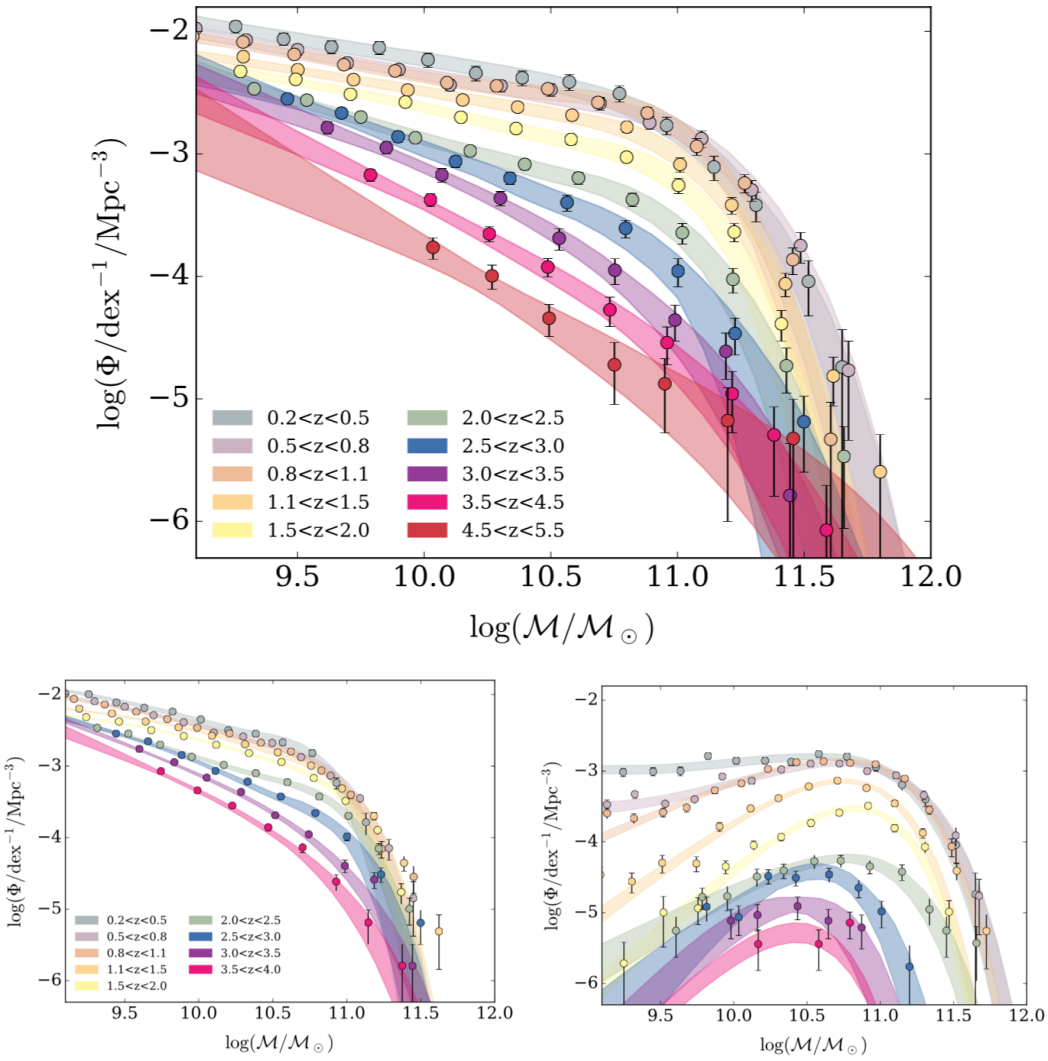

FIGURE 1.11: Top panel: Total GSMF in the redshift range $0 \leq z \leq 5.5$. Bottom panels: GSMF for star-forming galaxies (left) and quiescent galaxies (right) in the redshift range $0 \leq z \leq 4$. Credits: Davidzon et al. 2017.

Luminosity function

The galaxy luminosity function (LF) $\mathrm{d}^2N/\mathrm{d}L/\mathrm{d}V$ is the number of galaxies per unit comoving volume per luminosity bin. Since luminosity can be measured at different wavelengths, luminosity functions also change with wavelength. The bolometric luminosity function is computed considering the integrated luminosity of galaxies. Since luminosity is derived from the observed magnitude, luminosity functions are sometimes reported as a function of M_X i.e. the magnitude in a given observational band. In Figure 1.12 I

show the LF as a function of the magnitude in r-band determined by Kelvin et al. 2014b, with contributions coming from different morphological galaxy types. The luminosity function can also be fitted by a Schechter function:

$$\frac{\mathrm{d}^2 N}{\mathrm{d}L\,\mathrm{d}V} = \Phi^* \left(\frac{L}{L^*}\right)^{\alpha} \exp\left(-\frac{L}{L^*}\right) \tag{1.49}$$

with L^* being the luminosity at the knee, or by a double Schechter function separating the contribution from disk-dominated and spheroidal-dominated galaxies. As for the stellar mass density, the luminosity density

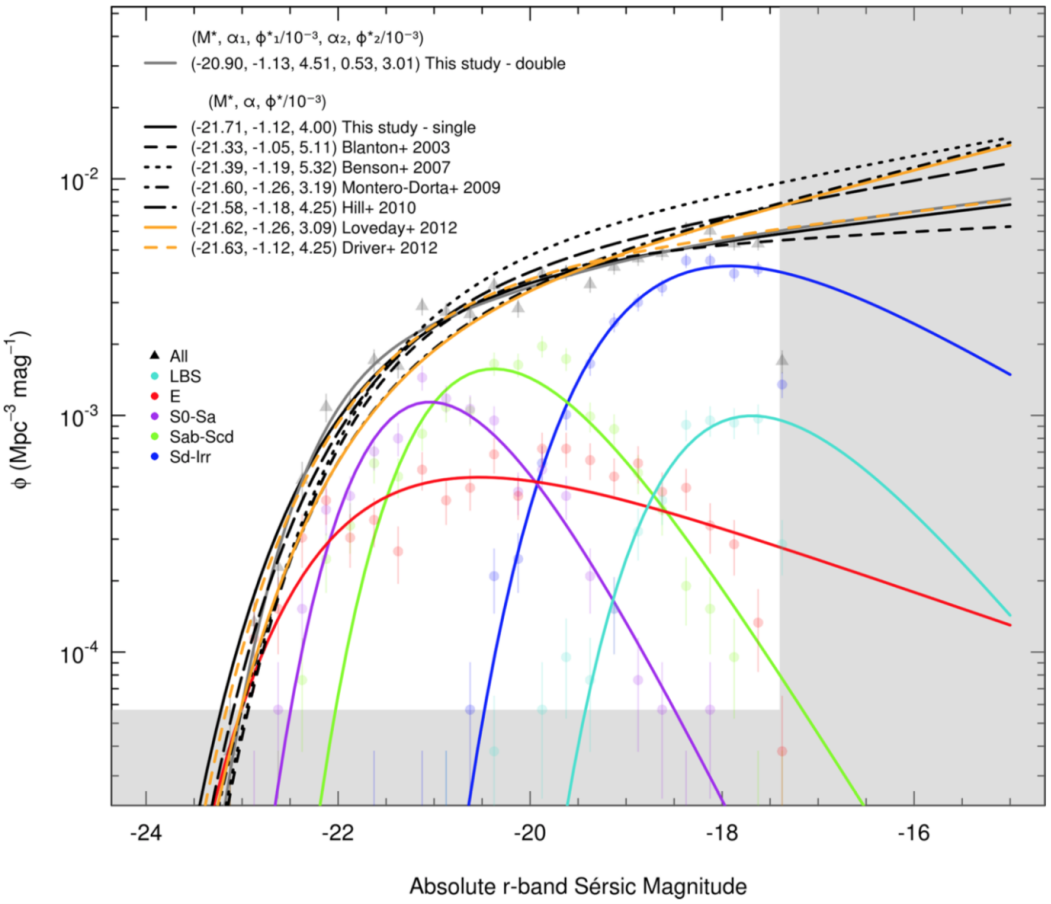

FIGURE 1.12: Contribution to the total r-band LF from different morphological types of galaxies: cyan are little blue spheroids (LBS), blue are Sd galaxies and irregulars, green are disk galaxies in the range Sab-Scd, purple are lenticulars S0 and Sa galaxies, red are ellipticals. Credits: Kelvin et al. 2014.

can be found via:

$$\rho_L = \int \mathrm{d}L\, L \frac{\mathrm{d}^2 N}{\mathrm{d}L\, \mathrm{d}V} \tag{1.50}$$

The most studied luminosity functions are the UV and the IR, since UV and IR emissions can be related to the galaxy SFR. UV LF have been studied via UV rest frame surveys by many authors over a wide redshift range $0 \leq z \leq 8$ (see e.g. Wyder et al. 2005; van der Burg et al. 2010; Oesch et al. 2010; Finkelstein et al. 2015; Alavi et al. 2016; Bouwens et al. 2016, 2017; Bhatawdekar et al. 2019). IR LF have been investigated mainly out to $z \sim 3$ due to the sensitivity limits of far-IR surveys (see e.g. Lapi et al 2011; Magnelli et al. 2013; Gruppioni et al. 2013, 2015) and only recently a determination of the IR LF has been extended out to $z \lesssim 6$ by Gruppioni et al. 2020, via ALMA serendipitous detections.

1.3.3 Main sequence and starbursts

The main sequence (MS) of star-forming galaxies is a well known relation between the stellar mass and the SFR of star-forming galaxies. Such a relation has been determined both observationally and theoretically (see e.g. Daddi et al 2007; Rodighiero et al. 2011, 2015; Whitaker et al. 2014; Speagle et al. 2014; Schreiber et al. 2015; Mancuso et al. 2016b; Dunlop et al. 2017; Bisigello et al. 2018; Pantoni et al. 2019; Lapi et al. 2020). Most of the studies report it as a power-law with exponent and normalization dependent on redshift or cosmic time, with a scatter $\sigma_{\mathrm{MS}} \sim 0.2 - 0.3$ dex.

In the remaining of this thesis I use the determination by Speagle et al. 2014:

$$\log \psi(M_\star, t) = (0.84 - 0.026t) \log M_\star - (6.51 - 0.11t) \tag{1.51}$$

where t is the cosmic time. Such a main sequence determination is shown in Figure 1.13. The normalization increases with redshift and the slope steepens from ~ 0.5 at $z \sim 0$ to ~ 0.84 at high-z. Both the normalization and slope evolution are rapid out to $z \lesssim 2$ but they become much slower at higher redshifts, as can be seen from the Figure. Though, I point out that the MS shape and evolution with redshift is still debated, with relevant differences among various works; in particular, its behaviour at large masses is very uncertain, with some authors advocating a possible flattening, although it may be effectively due to contamination from passive galaxies.

However, not all galaxies lie on the main sequence. A fraction of star-forming objects is found $\gtrsim 0.6$ dex above it, up to even ~ 1 dex. They are called starburst galaxies (SBGs) and their fraction with respect to the total number of galaxies is though to be minor $\sim 2 - 3\%$ (Rodighiero et al. 2011;

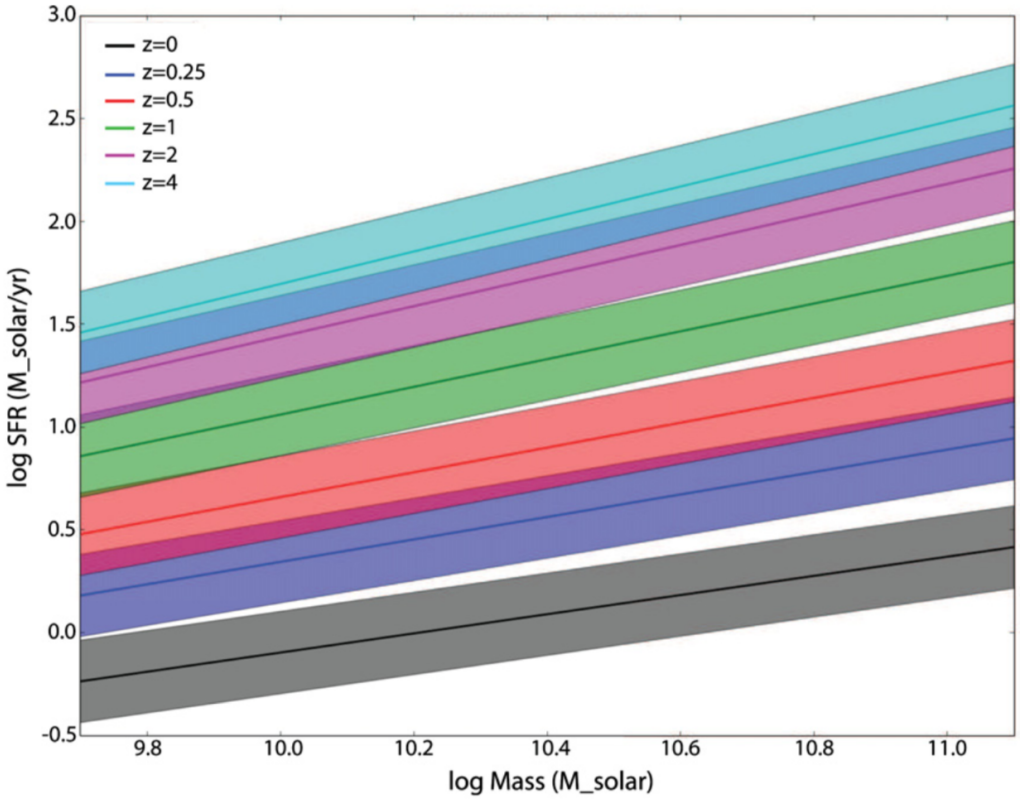

FIGURE 1.13: Main sequence of star-forming galaxies. Credits: Speagle et al. 2014.

Sargent et al. 2012; Bethermin et al. 2012; Ilbert et al. 2015; Schreiber et al. 2015), accounting up to $\sim$ 10% to the total star formation rate of the Universe. Still, recent works (Caputi et al. 2017; Bisigello et al. 2018), studying starbursts in a larger range of masses and redshifts, have pointed out that the starburst fraction tend to increase at lower masses and higher redshift, accounting for $\sim$ 15% of all galaxies at $2 \leq z \leq 3$ and so does their contribution to the total cosmic SFR. The discussion of this point is still open and I will come back to it in Section 2.1, when trying to interpret some discrepancies between different determinations of the cosmic SFR density and in Section 4.2, where I provide a brief overview of an ongoing project in which a varying starburst fraction is taken into account (Chruslinska et al. 2021).

It is worth stressing that, in principle, there is no net distinction between main sequence galaxies and starbursts. Some galaxies steadily evolve along the main sequence and may occasionally jump in the starburst branch due to an enhancement of their star formation activity; some others are located above the main sequence during their infancy and then evolve toward it, spending there most of their lifetime (e.g. Mancuso et al. 2016b; Rodighiero

et al. 2019).

Finally, there are also galaxies lying below the main sequence. These have very low sSFR and are considered quenched galaxies, meaning that they have formed all their stellar mass in the past and they are evolving passively. This is the case, for example, of ETGs at $z \sim 0$.

1.3.4 Metallicity evolution and scaling relations

The interstellar medium and the star-forming gas inside a galaxy are not only composed by hydrogen and helium, but also by a fraction of heavier elements, called metals (carbon, oxygen, magnesium, silicon and iron are among the most important). These elements are not coming from Big Bang Nucleosynthesis but are the result of stellar evolution and are returned to the ISM by stellar winds or supernova explosions.

Stellar metallicity and ISM metallicity will be crucial ingredients for this thesis and they will be extensively discussed in Section 2.2. Indeed stellar initial metallicity is, together with the initial mass, what determines the end-point of stellar evolution.

In this Section I present standard theoretical models for chemical enrichment in galaxies and I illustrate the main empirical scaling relations involving metallicity.

In order to build a model of chemical evolution it is convenient to consider just the evolution of one element i, an atom or an ion, and then sum over all the elements. The evolution equation for the gas mass $M_{\rm gas}\, Z_i$ of such element is:

$$\frac{\mathrm{d}(M_{\rm gas}\, Z_i)}{\mathrm{d}t} = Z_{i,\rm in}\, \dot{M}_{\rm in} - Z_{i,\rm out}\, \dot{M}_{\rm out} + \dot{M}_{i,\rm ret} - Z_i\, \psi \tag{1.52}$$

where $\dot{M}_{\rm in}$ is the mass inflow rate, $Z_{i,\rm in}$ the mass fraction of element i in the inflowing gas, $\dot{M}_{\rm out}$ the mass outflow rate, $Z_{i,\rm out}$ the mass fraction of element i in the outflowing gas and $\dot{M}_{i,\rm ret}$ the returned mass rate of element i from stellar evolution processes. The returned mass rate can be computed as the mass restituted to the ISM, i.e. the initial stellar mass minus the remnant mass $m_\star - m_{\rm rem}(m_\star)$, multiplied by the initial metallicity at the formation time of the star $t - \tau_{\rm MS}(m_\star)$ (where $\tau_{\rm MS}(m_\star)$ is the stellar main sequence lifetime), plus the so called stellar yield of newly formed atoms of type i ($p_{Z_i,\star}$), which depends on the initial stellar mass. Multiplying by the SFR at the time of formation and integrating over all the possible initial stellar masses, weighting the integral with the stellar initial mass function (IMF) $\phi(m_\star)$ (see

Section 1.3.6), it is obtained:

$$\dot{M}_{i,\mathrm{ret}}(t) = \int_{m_{\star,\mathrm{min}}}^{m_{\star,\mathrm{max}}} \mathrm{d}m_\star\, \phi(m_\star)\, \psi(t - \tau_{\mathrm{MS}}(m_\star)) \times \\ \times \left[(m_\star - m_{\mathrm{rem}}(m_\star))\, Z_i(t - \tau_{\mathrm{MS}}(m_\star)) + m_\star\, p_{Z_i,\star}(m_\star) \right] \tag{1.53}$$

In order to simplify this equation the instantaneous recycling approximation is often adopted. It consists simply in the assumption that there is no time delay between star formation and the time at which stars restitute metals to the ISM, $\tau_{\mathrm{MS}} \simeq 0$. Although this is a gradual process, occurring first through stellar wind, then through SN explosions and finally via type Ia SNe or NS mergers, the overall timescale of the process, at least for the first 2 steps, is much shorter with respect to the timescale of star formation, given the short lifetime $\tau_{\mathrm{MS}} \lesssim 30\,\mathrm{Myr}$ of massive stars. Under this assumption, equation (1.53) becomes:

$$\dot{M}_{i,\mathrm{ret}}(t) = \psi(t) \left[Z_i(t)\, \mathcal{R} + \int_{m_{\star,\mathrm{min}}}^{m_{\star,\mathrm{max}}} \mathrm{d}m_\star\, \phi(m_\star)\, m_\star\, p_{Z_i,\star}(m_\star) \right] \tag{1.54}$$

where $\mathcal{R} \equiv \int_{m_{\star,\mathrm{min}}}^{m_{\star,\mathrm{max}}} \mathrm{d}m_\star\, \phi(m_\star)\, (m_\star - m_{\mathrm{rem}}(m_\star))$ is the returned gas fraction. Now defining $y_{Z_i} \equiv \int_{m_{\star,\mathrm{min}}}^{m_{\star,\mathrm{max}}} \mathrm{d}m_\star\, \phi(m_\star)\, m_\star\, p_{Z_i,\star}(m_\star)/(1-\mathcal{R})$, equation (1.52) can be rewritten as:

$$\frac{\mathrm{d}(M_{\mathrm{gas}}\, Z_i)}{\mathrm{d}t} = Z_{i,\mathrm{in}}\, \dot{M}_{\mathrm{in}} - Z_{i,\mathrm{out}}\, \dot{M}_{\mathrm{out}} + (1 - \mathcal{R})\, (y_{Z_i} - Z_i)\, \psi \tag{1.55}$$

A further simplification consists in considering the metallicity of the outflows equivalent to the metallicity of the ISM $Z_{i,\mathrm{out}} \simeq Z_i$. Under this assumption, rewriting the outflow rate as a fraction ϵ_{out} of the SFR, $\dot{M}_{\mathrm{out}} = \epsilon_{\mathrm{out}}\, \psi$, it is obtained:

$$\frac{\mathrm{d}(M_{\mathrm{gas}}\, Z_i)}{\mathrm{d}t} = Z_{i,\mathrm{in}}\, \dot{M}_{\mathrm{in}} - \gamma\, \psi\, Z_i + (1 - \mathcal{R})\, y_{Z_i}\, \psi \tag{1.56}$$

where $\gamma \equiv 1 - \mathcal{R} + \epsilon_{\mathrm{out}}$. Finally, expliciting the derivative on the left hand side and considering that:

$$\frac{\mathrm{d}M_{\mathrm{gas}}}{\mathrm{d}t} = \dot{M}_{\mathrm{in}} - \epsilon_{\mathrm{out}}\, \psi + (1 - \mathcal{R})\, \psi \tag{1.57}$$

the following equation is obtained:

$$M_{\rm gas}\,\frac{{\rm d}Z_i}{{\rm d}t} = (Z_{i,{\rm in}} - Z_i)\,\dot{M}_{\rm in} + (1-\mathcal{R})\,y_{Z_i}\,\psi \tag{1.58}$$

representing the metallicity evolution of element i. From this last equation it can be clearly seen that new elements produced by stars, enclosed in the factor y_{Z_i} tend to increase the ISM metallicity, except elements with negative yields such as deuterium which are burnt in stars. The first term on the right hand side, instead, is typically negative, and it represents the dilution term due to the accretion of metal poor gas. These equation are useful to compute the growth in metals of a galaxy provided the knowledge of its star formation history and inflow rate. I just note that the restituted fraction $\mathcal{R}$ and the stellar yields y_{Z_i} are dependent on the chosen IMF and can vary by a factor $\sim$ 2 between different choices. An example of a galaxy evolution model self-consistently solving for metal enrichment is shown in Appendix A and used, in an approximated form, in Section 2.2.4.

As for the observational side, I report now the main scaling relations involving stellar and ISM metallicity. First I briefly illustrate the methods used to observationally infer stellar and gas-phase metallicity.

Stellar metallicity is measured from the observed galaxies spectra in the optical rest frame. Since metallicity is usually degenerate with the stellar population age, Lick indices (see Section 1.3.1) are often used to break the aforementioned degeneracy. Recently, comparisons between observed and synthetic spectra generated by a combination of input stellar populations have been exploited to derive the stellar metallicity. These methods use the whole information contained in the spectra to simultaneously derive chemical abundances, stellar ages and star formation histories. The main issues of this method is that the solution is not unique and there are model uncertainties due to stellar rotation and the presence of binary stars.

As for the gas-phase metallicity, there are various different methods to measure it, that might lead even to very different results with up to $\lesssim 0.7$ dex of difference. One of the principal techniques to infer ISM metallicity, also called direct method, is via measurements of electron temperature T_e in HII regions. Indeed ionized gas is usually very rich of collisionally excited emission lines. The flux of these metal lines depends on the abundance of the considered ion and on the electron temperature and density. Measuring electron temperature, through "auroral" lines, and comparing flux of metal lines to hydrogen recombination lines, it is possible to get the abundance of the considered element. The main limitation arises from the fact that auroral lines are very faint and their detection is limited to local galaxies,

with very sporadic detections at higher redshift with low signal to noise ratio. Moreover auroral lines are brighter in metal poor regions, biasing the result toward lower metallicities. Another direct method to infer ISM metallicity is through the comparison of specific recombination lines of metals and hydrogen in HII regions. Also this method is limited by the faintness of metal recombination lines with respect to hydrogen ones and can be applied only in very bright HII regions. The last primary method to infer metallicity is based on photoionization models. Detailed photoionization codes are used to generate a series of models with different metallicity and ionization parameter. These two parameters affect the flux ratio of some nebular lines than can be compared with observations. The main advantage of this approach is that the star-forming regions can be explored at all metallicities and even at high redshifts. On the other hand, many other parameters influence the strength of nebular lines and they cannot be directly inferred from observations. Moreover real HII regions are not characterized neither by a single value of ionization parameter nor by a single value of metallicity, but by a distribution of them. Therefore photoionization models assuming a single value for such parameters might be too simplistic. Methods illustrated up to now do not give the same results. In particular T_e-based methods tend to predict lower metallicities, while photoionization models give higher metallicities, and recombination line methods lie in between. The origin of these differences are still not very clear, even though some tentative explanations are given (see e.g. review by Maiolino & Mannucci 2019).

Given the limitations in observing the emission lines mentioned above, secondary methods for metallicity estimation have been developed. These methods are based on detection of strong emission lines ("strong line methods"), that can be calibrated, i.e. related to metallicity, via one of the direct techniques mentioned above. Strong lines can be calibrated empirically (via the direct methods), via photoionization models or with a mixture of the two. Strong line techniques can be extremely useful in extending metallicity measurements at high redshifts, but might suffer from degeneracies with other parameters or by contaminations from other excitation mechanisms independent on metallicity.

As for the stellar metallicity, the most important empirical scaling relation is the Mass Metallicity Relation (MZR). It envisages a correlation between stellar mass and stellar metallicity with, possibly, a flattening at the high mass end. The stellar MZR at $z \sim 0$ is shown in Figure 1.14. It can be seen that, on average, stars in quiescent galaxies have higher metallicities than stars in SFGs. At higher redshifts the MZR stays constant for quiescent galaxies (see Arrigoni et al. 2010; Spolaor et al. 2010; Gallazzi et al. 2014), since they are passive galaxies with no ongoing star formation processes,

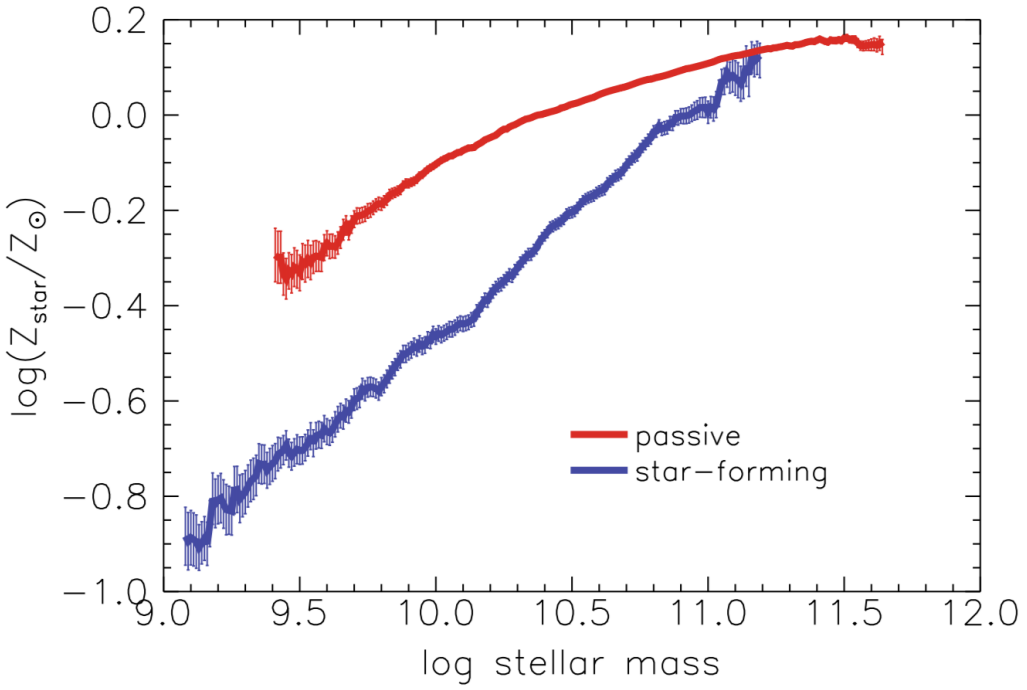

FIGURE 1.14: Stellar MZR for quiescent (red) and star-forming (blue) galaxies. Credits: Peng et al. 2015.

while it decreases in normalization for SFGs which were younger and poorer in metals (see Andrews & Martini 2013; Gallazzi et al. 2014; Zahid et al. 2014; de la Rosa et al. 2016; Onodera et al. 2016).

Even the ISM metallicity $Z_{\rm gas}$ of star-forming galaxies follow a Mass Metallicity Relation (see e.g. Kewley & Ellison 2008; Maiolino et al. 2008; Mannucci et al. 2009; Magnelli et al. 2012; Zahid et al. 2014; Genzel et al. 2015; Sanders et al. 2020), with more massive galaxies being more metal rich, even though its exact shape and normalization strongly depends on the specific method used to measure it (see Kewley & Ellison 2008). In Figure 1.15 it is shown the gas-phase MZR at different redshifts in the determination of Mannucci et al. 2009.[2]. The scatter around the MZR relation is $\sigma_{\rm MZR} \sim 0.15$ dex. In general, at fixed $M_\star$, the MZR predicts a decline in $Z_{\rm gas}$ towards higher redshifts, as for the case of stellar metallicity, but the level of redshift evolution is actively debated (Onodera et al. 2016; Sanders et al. 2020).

[2]As it can be seen from the Figure, the gas-phase metallicity is usually expressed in terms of oxygen abundance $12+\log(O/H)$; throughout the thesis I will often use this notation and I show the adopted convertion factor to overall metallicity in Section 2.2.

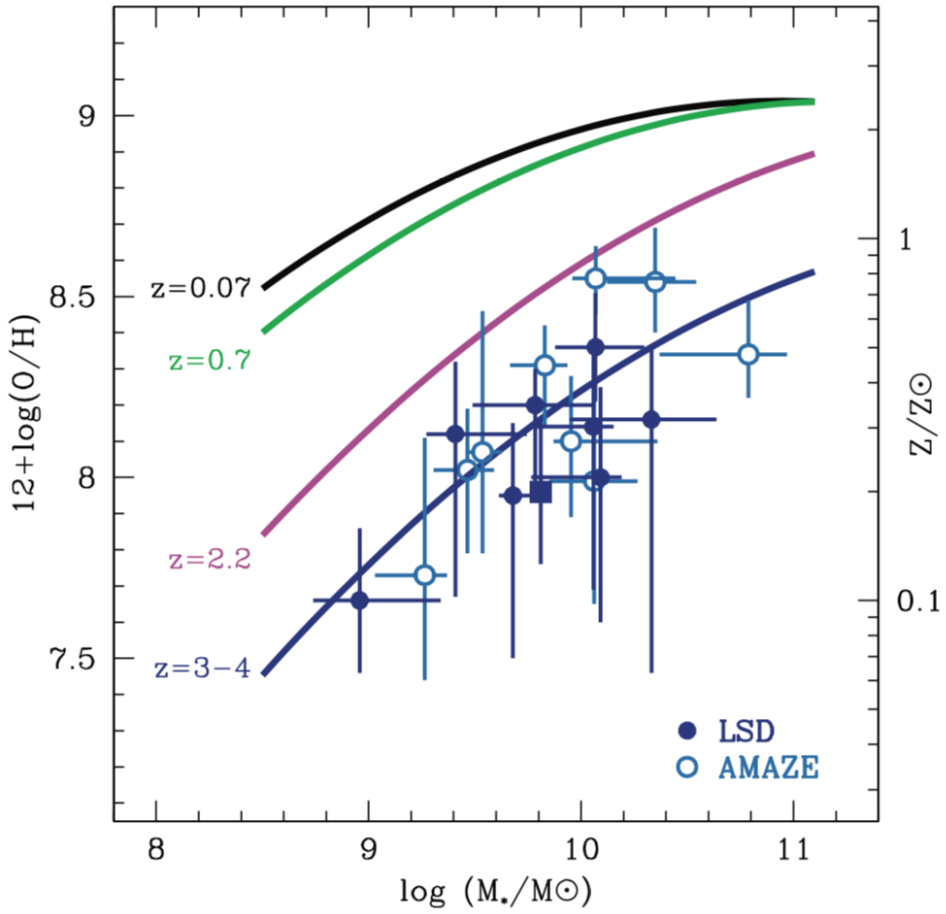

FIGURE 1.15: Gas-phase MZR at different redshifts. Credits: Mannucci et al. 2009.

Another important scaling relation for the ISM metallicity is the Fundamental Metallicity Relation (FMR), which is a 3 parameters relation between stellar mass, SFR and $Z_{\rm gas}$ (see e.g. Mannucci et al. 2010; Mannucci et al. 2011; Hunt et al. 2016; Curti et al. 2020). The FMR envisages a correlation between $Z_{\rm gas}$ and stellar mass, but an anti-correlation between $Z_{\rm gas}$ and SFR. However, the level of anti-correlation is dependent on the stellar mass itself with a stronger SFR dependence at low $M_\star$ and a weak or absent dependence at $M_\star \gtrsim 10^{10.5}\,{\rm M}_\odot$, as it can be clearly seen from Figure 1.16, dispaying the FMR derived by Mannucci et al. 2010. The inclusion of SFR is to account for the secondary dependence of metallicity on SFR initially observed in local SDSS galaxies (Mannucci et al. 2010) where $Z_{\rm gas}$ decreases increasing SFR at fixed stellar mass. This dependence has been also confirmed over larger data sets: galaxies with the same stellar mass at the same redshift can have different metallicities due to their different SFR, showing a clear anti-correlation

between $Z_{\rm gas}$ and sSFR (see e.g. Hunt et al. 2016). Such a relation has been found to be more tight than the MZR, with $\sigma_{\rm FMR} \sim 0.05$. The FMR is thought to be almost redshift independent and this is confirmed by observations out to $z \sim 3.5$ (Mannucci et al. 2010; Hunt et al. 2016). I will come back to the discussion on the relation between MZR and FMR and on the origin of redshift evolution of MZR in Section 2.2.

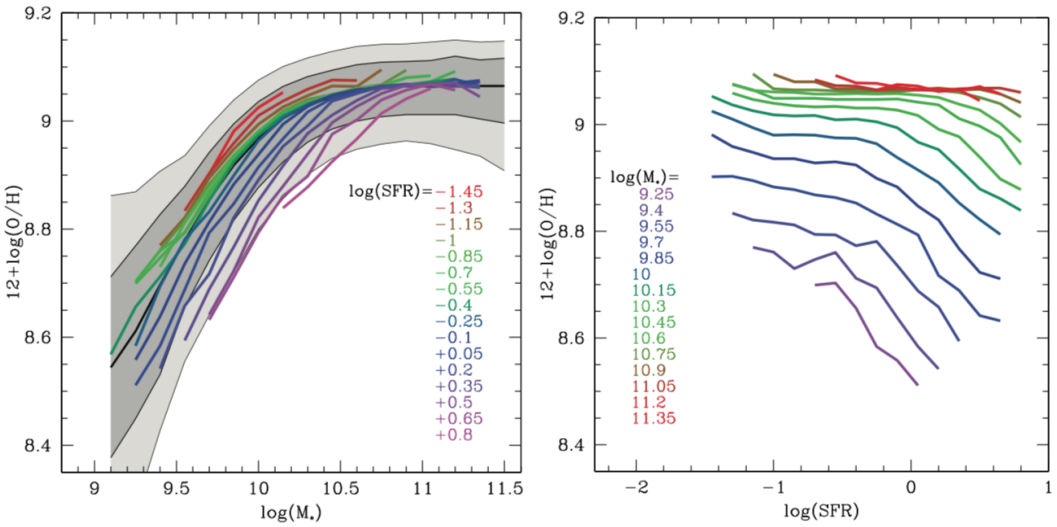

FIGURE 1.16: Left panel: FMR in the $Z_{\rm gas} - M_\star$ plane, different colors are for different SFR. Right panel: FMR in the $Z_{\rm gas} - \psi$ plane, different colors are for different $M_\star$. Credits: Mannucci et al. 2010.

1.3.5 Active galactic nuclei and supermassive black holes

A fraction of local and high redshift galaxies present radiative phenomena which cannot be explained just by stellar emissions, such as extremely high bolometric luminosities $L \sim 10^{48}\,{\rm erg\,s^{-1}}$, non stellar UV and optical radiation, strong X- and gamma-rays emissions, significant non-thermal radio activity and emission of relativistic jets of plasma. These galaxies are called Active Galactic Nuclei (AGN) and are usually classified in 4 categories depending on their features: Quasars, Seyfert galaxies, Radio galaxies and Blazars. It is thought that AGN activity is powered by a central supermassive black hole (SMBH) with mass $M_\bullet \sim 10^6 - 10^{10}\,{\rm M_\odot}$, surrounded by a disk of gas and stars which are accreted onto the black hole. The radiated energy is a fraction of the gas particles gravitational energy converted in radiation

and the AGN luminosity can be expressed as:

$$L \simeq \frac{\mathrm{d}M_{\mathrm{acc}}}{\mathrm{d}t}\,\eta \tag{1.59}$$

where $\mathrm{d}M_{\mathrm{acc}}/\mathrm{d}t$ is the SMBH accretion rate and $\eta \simeq 0.1$ is the fraction of gravitational energy radiated away (Shakura & Sunyaev 1973).

The effective existence of SMBH at the center of galaxies has been confirmed studying the motion of stars and ionized gas at the center of nearby galaxies. Kinematic data of the central galactic regions show that the central potential well cannot be explained by an extended mass distribution but requires a central massive compact object. It is now widely accepted that a SMBH is present at the center of each galaxy with a spheroidal component, such as ETGs or bulges. Moreover there is a famous correlation between the spheroid mass and the SMBH mass called Magorrian relation, shown in Figure 1.17 (see Kormendy & Ho 2013).

The SMBH mass correlates also with the galaxy velocity dispersion as well as with a number of galactic properties such as the number of globular clusters or the Sersic index of the density profile. Relations as the Magorrian can be interpreted as a sign of a common evolution between galaxy activity and SMBH accretion, usually referred to as galaxy-SMBH co-evolution. From equation (1.59) it can seen that if the AGN luminosity is known, it is possible to compute the SMBH accretion rate. Inferring the luminosity from analysis of the galactic spectra, it has been noticed that for main sequence galaxies the SMBH accretion rate correlates with the stellar mass, while starbursts and quiescent galaxies have respectively an enhanced and reduced AGN luminosity. Computing the accretion rate for galaxies at different redshifts it is possible to derive the cosmic SMBH accretion rate over the whole history of the Universe (see Figure 1.18), whose shape is remarkably similar to the cosmic SFR density (see Section 2.1 and Figure 2.3). Such a profound connection between SMBHs and galaxy evolution suggests that AGN energetic feedback should have played a crucial role in the evolution of the galaxy, for example quenching its star formation injecting enormous quantity of energy into the ISM. This is also confirmed by the numerous observations of star-forming galaxies at $z \geq 1$ showing outflows at $\sim$ kpc scales.

However, the galaxy-AGN relation is not the only mystery about SMBHs. Indeed, in recent years, an increasing number of high redshift quasars have been discovered, powered by active SMBHs with masses $M_\bullet \gtrsim 10^9\,\mathrm{M}_\odot$ at redshift up to $z \sim 7.5$ (e.g. Fan et al. 2006; Mortlock et al. 2011; Venemans et al. 2017a, 2017b, 2018; Banados et al. 2018). At those redshifts, the Universe was very young $\lesssim 0.8$ Gyr and, even if quasar hosts were formed very promptly, there would have been not enough time to accumulate those large masses

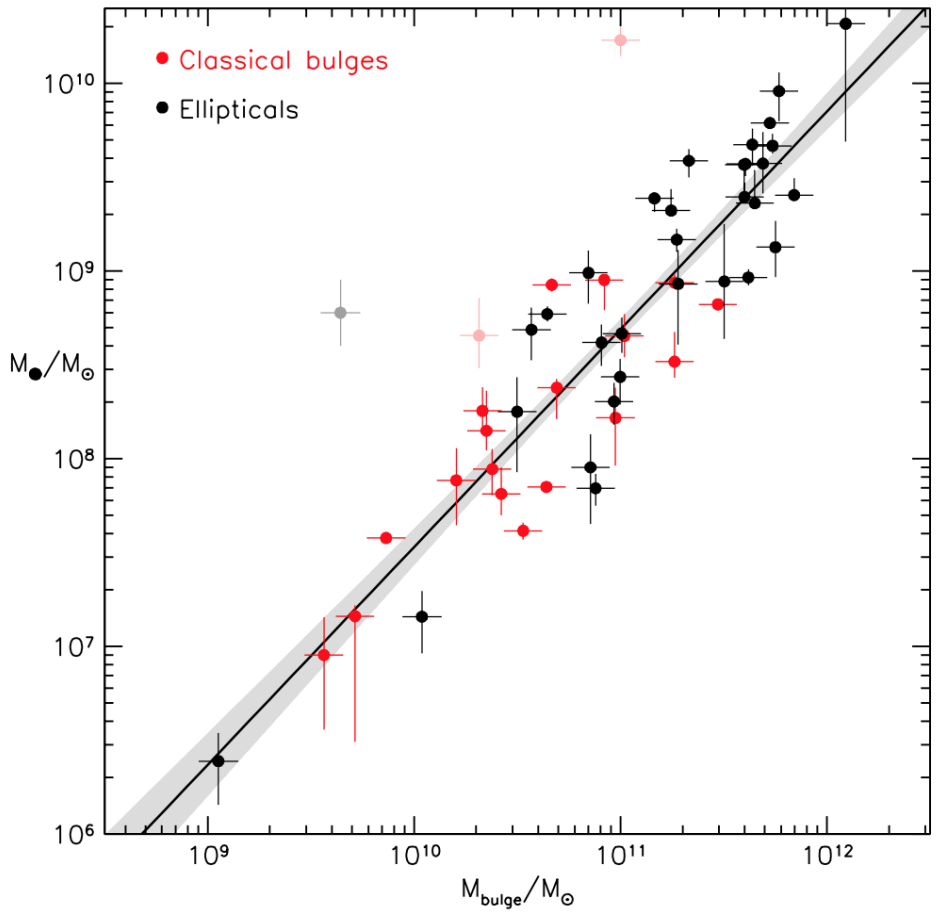

FIGURE 1.17: Relation between spheroid mass and SMBH mass for bulges (red dots) and ellipticals (black dots). Credits: Kormendy & Ho 2013.

in such a short timescale with standard Eddington accretion. I will deal with this problem and with the possible solutions in Chapter 3, where I propose a viable mechanism, alternative or complementary to others, to alleviate this tension.

1.3.6 IMF

I conclude the Chapter with a brief discussion about the stellar initial mass function $\phi(m_\star)$. The IMF characterizes the mass distribution of newly born stars and it plays a crucial role in any study involving stellar evolution. The IMF is the result of the star formation process and it is determined empirically observing single stars in young star clusters inside the Milky Way or in the Large Magellanic Cloud. Therefore, even if in many studies the IMF is

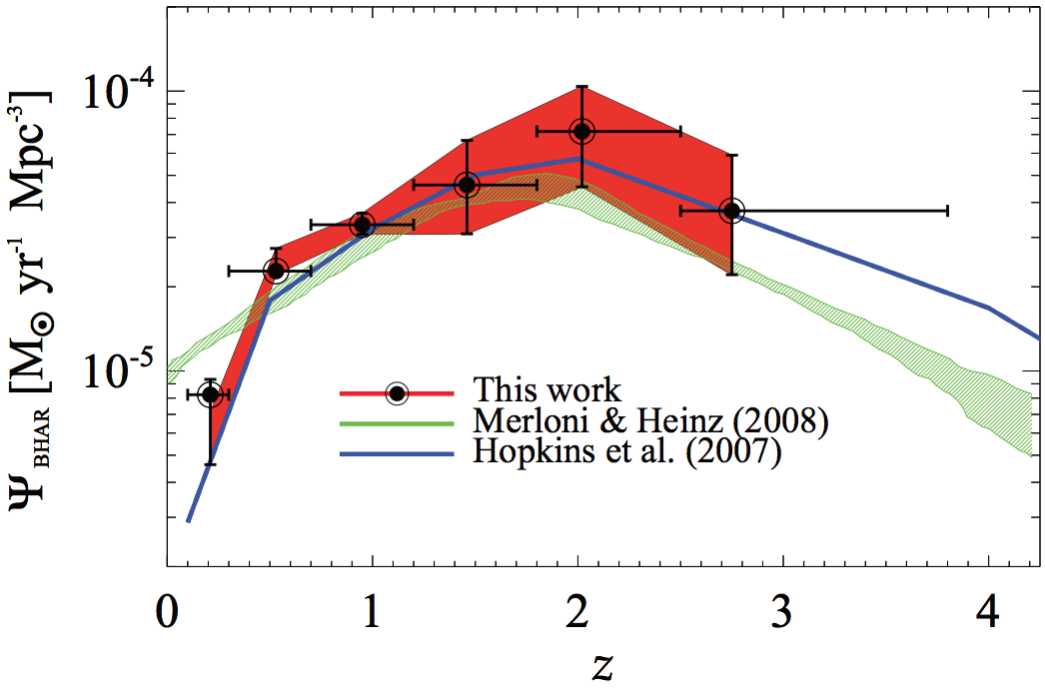

FIGURE 1.18: Black Hole Accretion Rate Density Ψ_{BHAR} as a function of redshift. Credits: Delvecchio et al. 2014.

usually taken as universal, this assumption is not proven and, in principle, it could vary in different galactic environments.

The IMF is not important only for stellar studies but also for galaxy evolution. Indeed, setting the mass ratio between stars belonging to different mass ranges, it enters in the estimation of the stellar mass and SFR. Indeed these quantities are usually derived from the observation of the light from certain kind of stars: in particular SFR stems from the UV light emitted by young massive stars, while stellar mass is evaluated from near-IR light emitted by older and less massive stars. Therefore setting the mass ratio between these stellar populations is a key step toward a correct estimation of SFR and stellar mass. Even the SFH and metallicity, derived via broadband SED fitting, rely on the assumption of a specific IMF. Typically, at given SFR, more top-heavy IMFs are proportionally richer in massive short-living stars, and yield a larger rest frame UV luminosity, a faster chemical enrichment, and a smaller stellar mass locked in long-living stars.

Throughout this thesis I adopt the Chabrier 2003 IMF, mainly because it constitutes a standard both in the galaxy formation and the stellar evolution communities (together with the Kroupa 2001 IMF, which anyway would

yield almost indistinguishable results), which has the form:

$$\phi(m_\star) \propto \begin{cases} \frac{3.58}{m_\star} \exp\left(-1.05 \left(\log\left(\frac{m_\star}{0.079}\right)\right)^2\right) & m_\star < 1\,\mathrm{M}_\odot \\ m_\star^{-2.3} & m_\star \geq 1\,\mathrm{M}_\odot \end{cases} \tag{1.60}$$

normalized such that the total mass formed in stars is equal to $1\,\mathrm{M}_\odot$:

$$\int \mathrm{d}m_\star \, m_\star \, \phi(m_\star) = 1\,\mathrm{M}_\odot \tag{1.61}$$

Chapter 2

Gravitational waves from compact object mergers: impact of galaxy evolution

In Chapter 1 I have summarized the main cosmological notions and reviewed the processes of halo and galaxy formation and evolution. Galaxies are the sites where stars form, evolve and die, eventually producing compact object (CO) remnants. Since merging of double compact object (DCO) binaries is the main mechanism though to originate the recently observed gravitational wave signals, it is important to well understand and correctly model the properties of galaxies, which provide the environment where compact binaries mergers take place. Though being extremely complex, a correct characterization of galactic properties has a twofold importance for the study of CO remnants and their mergers:

- On the context of theoretical astrophysics, the study of the galactic environment is needed for predictions on the number and properties of compact objects: SFR and metallicity, in particular, play an important role in determining the numbers and the masses of COs formed inside the galaxy. Therefore any work aimed at forecasting CO properties or their merging rates has to go through a modeling of the galaxy population. Moreover galactic properties, such as the stellar, gas and DM distributions, gas metallicity, total mass, velocity dispersion, can strongly affect the dynamics of stars and remnants and, consequently, the main CO merging channels might depend on galactic features.

- On cosmological context, understanding the link between GW signals and their host galaxy can lead to huge progresses in the field. Indeed host galaxy light provides an electromagnetic (EM) counterpart to the associated GW event opening the field to multimessenger studies, whose importance is unquestionable. Even few GW events with

detected EM counterpart can be a breakthrough both for cosmological parameter estimations and even for fundamental physics. However, given the practical difficulty in associating a single host galaxy to each GW event, even a simple likelihood for the host galaxy could be useful for statistical studies.

In this Chapter I focus on the isolated compact binary merging channel, i.e. I consider binaries of stars to evolve in isolation, without feeling any dynamical influence from other stellar systems. The main goal is to characterize the DCO population exploiting the notions of galaxy formation and evolution illustrated in Chapter 1 and to study the impact of galactic prescriptions on their properties and merging rates. Then I proceed on forecasting the GW detection rates from merging compact binaries as a function of redshift, in the perspective of the next AdvLIGO/Virgo observing runs and of the future Einstein Telescope and on the computation of the stochastic gravitational wave background (SGWB).

The merging rates per unit volume, as a function of the cosmic time, can be computed as (see Barrett et al. 2018 and Neijssel et al. 2019):

$$\frac{\mathrm{d}\dot{N}}{\mathrm{d}V}(t) = \int \mathrm{d}\mathcal{M}_{\bullet\bullet} \int \mathrm{d}t_\mathrm{d} \int \mathrm{d}Z \frac{\mathrm{d}^3 N}{\mathrm{d}M_\mathrm{SFR}\mathrm{d}\mathcal{M}_{\bullet\bullet}\mathrm{d}t_\mathrm{d}}(Z)\, \frac{\mathrm{d}^2 \dot{M}_\mathrm{SFR}}{\mathrm{d}V\,\mathrm{d}Z}(t - t_\mathrm{d}) \qquad (2.1)$$

where t is the cosmic time, equivalent to redshift, M_SFR is the star formed mass, $\mathcal{M}_{\bullet\bullet}$ is the chirp mass, defined as $\mathcal{M}_{\bullet\bullet} \equiv (m_{\bullet,1}\, m_{\bullet,2})^{3/5}/(m_{\bullet,1}+m_{\bullet,2})^{1/5}$, where $m_{\bullet,1}$ and $m_{\bullet,2}$ are the masses of the two merging objects, t_d is the delay time between the formation of the progenitor binary and the DCO merger, Z is the metallicity and V the comoving cosmological volume.

The first term in the integral $\mathrm{d}^3N/dM_\mathrm{SFR}/\mathrm{d}\mathcal{M}_{\bullet\bullet}/\mathrm{d}t_\mathrm{d}$ is related to stellar and binary evolution and represents the number of merging double compact objects per unit of star forming mass per bin of chirp mass and time delay. It can be evaluated via stellar and binary evolution simulations (see e.g. Dominik et al. 2012, 2015; de Mink et al. 2013; de Mink & Belczynski 2015; Belczynski et al. 2016; Spera & Mapelli 2017; Giacobbo & Mapelli 2018; Mapelli & Giacobbo 2018; Chruslinska et al. 2018; Spera et al. 2019; Santoliquido et al. 2021). Various processes involved in stellar and binary evolution depend on metallicity (e.g. radiation-driven stellar wind mass loss rates, core-collapse physics, mass transfer characteristics and stability, common envelope effects) and so the number of merging DCO binaries formed per unit mass in stars also varies with this quantity.

The second term $\mathrm{d}^2\dot{M}_\mathrm{SFR}/\mathrm{d}V/\mathrm{d}Z$ is instead related to galaxy evolution: it represents the star forming mass per units of time, comoving volume and metallicity, i.e. it is the cosmic star formation rate density per metallicity bin.

There are two main ways to estimate it: exploiting the results of cosmological simulations (e.g., Mapelli et al. 2017, 2018, 2019; O'Shaughnessy et al. 2017; Lamberts et al. 2018; Mapelli & Giacobbo 2018; Artale et al. 2019) or using empirical recipes concerning the cosmic SFR density and metallicity distributions inferred from observations (e.g., Belczynski et al. 2016; Lamberts et al. 2016; Cao et al. 2018; Elbert et al. 2018; Li et al. 2018; Boco et al. 2019, 2021; Chruslinska & Nelemans 2019; Neijssel et al. 2019; Santoliquido et al. 2021).

Throughout the Chapter, following Boco et al. 2021, I focus on explaining different approaches pursued to compute the galactic term, trying to quantify the impact of different choices and to understand their advantages and drawbacks. The methods discussed in the thesis to compute the galactic term are mainly based on observations and on empirically derived scaling relations, exploiting the wealth of observations (e.g., UV+far-IR/submillimeter/radio luminosity functions, stellar/gas/dust mass functions, broadband spectral energy distribution, mass metallicity relations) that in the recent years have brought to the estimation of the statistics of different galaxy populations as a function of their main physical properties across cosmic time, allowing also to shed light on the age dependent star formation and chemical enrichment histories of individual galaxies. These observational evidences have been presented in Section 1.3 and I will just briefly recap and extend them in this Chapter. Despite basing my analysis on empirical relations, in Section 2.2.4, following the lines of Boco et al. 2019, I also adopt an approximation of a chemical evolution model to compute the galactic term, using the theoretical formalism presented in Section 1.3.4 and in Appendix A. Then I study and evaluate the effects of different prescriptions for the galactic term computation on the merging rates and on the properties of merging binaries.

In particular, in Section 2.1 I present two empirical ways to compute the cosmic SFR density, in Section 2.2 I assign metallicity to galaxies via the two main empirical scaling relations presented in Section 1.3.4 (FMR and MZR) and via a chemical-enrichment model and I compute the galactic term $\mathrm{d}^2\dot{M}_{\rm SFR}/\mathrm{d}V/\mathrm{d}Z$ combining the different metallicity distributions with the two galaxy statistics. In Section 2.3 I explain the impact of metallicity on the stellar term and I describe the reference choice for its computation, taking the outcomes of the population synthesis code `STARTRACK`. In Section 2.4 I calculate the merging rates of DCO binaries combining galactic and stellar term. In Section 2.5 I forecast the GW detection rates for AdvLIGO/Virgo and ET and I compute the expected amount of lensed GW events and, finally, in Section 2.6 I compute the SGWB originated by DCO mergers.

2.1 Cosmic SFR and galaxy statistics

The first important ingredient in the computation of the factor $\mathrm{d}^2\dot{M}_{\rm SFR}/\mathrm{d}V/\mathrm{d}Z$ is constituted by the cosmic SFR density $\mathrm{d}\dot{M}_{\rm SFR}/\mathrm{d}V$, representing the average rate at which new stars are formed in the Universe at different redshifts per unit comoving volume. The cosmic SFR density has been estimated by many authors, using data at different wavelengths from various telescopes: dust-corrected UV observations (Schiminovich et al. 2005; Bouwens et al. 2015), ALMA submillimeter observations of UV-selected galaxies on the HUDF (Dunlop et al. 2017), VLA radio observations on the COSMOS field (Novak et al. 2017), multiwavelength determinations including UV, radio, Hα, and mid-IR 24 μm data (Hopkins & Beacom 2006), Herschel far-IR observations (Gruppioni et al. 2013), Herschel far-IR stacking (Rowan-Robinson 2016), far-IR/(sub)millimeter observations from super-deblended data on the GOODS field (Liu et al. 2018), far-IR ALMA serendipitous detections (Gruppioni et al. 2020), far-IR ALMA observations from the ALPINE survey (Khusanova et al. 2020) and estimates from long gamma ray burst rates (Kistler et al. 2009, 2013). One of the most famous fits to data has been provided in the review by Madau & Dickinson 2014.

A common choice to study the merging rates of DCO binaries is to take one of the determinations of the cosmic SFR density and convolve it with a standalone average cosmic metallicity distribution (see e.g. Belczynski et al. 2016; Cao et al. 2018; Li et al. 2018). In this approach, however, the link with the properties of star-forming galaxies and their evolution is lost and it is not easy to retrieve an accurate cosmic metallicity distribution without passing through a galaxy statistics; I discuss this approach at the beginning of Section 2.2. For these reasons, throughout the thesis, I exploit the SFR functions (Section 2.1.1) and the galaxy stellar mass functions (Section 2.1.2) as galaxy statistics and use them to compute the cosmic SFR density.

2.1.1 SFR/Luminosity functions

The most direct approach to compute the cosmic SFR density relies on the galaxy luminosity functions, which can be converted in star formation rate functions (SFRF) $\mathrm{d}^2N/\mathrm{d}V/\mathrm{d}\log\psi$, expressing the number density of galaxies per logarithmic bin of SFR at different redshifts.

Indeed luminosity, especially at UV and IR wavelengths, can be related to galaxies SFR (see e.g. Kennicutt 1998; Kennicutt & Evans 2012). In principle, SFRF can be determined both by UV and IR LFs, but both of them present some limitations in certain redshift and SFR ranges. Now I analyze

these limitations and I illustrate a mixed approach to derive the SFRF, referring the reader to Mancuso et al. 2016a for further details. As stated in 1.3.1 the SFR of a galaxy is directly proportional to its UV luminosity coming from young, blue stars. However, the latter can be significantly absorbed by even a modest amount of dust and re-radiated at far-IR/(sub)millimeter wavelengths; therefore SFR obtained only from UV luminosities can be substantially underestimated. Nevertheless, for galaxies with relatively low SFR, $\psi \lesssim 30 - 50\,M_\odot\,yr^{-1}$, dust attenuation is mild and the intrinsic SFR can be soundly estimated from UV data alone via standard corrections based on the observed correlation between UV continuum slope and FIR emission (see Meurer et al. 1999; Calzetti et al. 2000; Bouwens et al. 2015). As a consequence, the SFRF for $\psi \lesssim 30\,M_\odot\,yr^{-1}$ are rather well established by deep surveys in the rest-frame UV band mentioned in Section 1.3.2 and arriving up to $z \lesssim 8$. Contrarywise, in galaxies with high SFR $\psi \gtrsim 30 - 50\,M_\odot\,yr^{-1}$, dust absorption is heavier, and UV slope-based corrections are wildly dispersed and statistically fail (see Silva et al. 1998; Efstathiou et al. 2000; Howell et al. 2010; Coppin et al. 2015; Reddy et al. 2015; Fudamoto et al. 2017).

On the other hand, IR measurements trace the light thermally emitted from dust which has been heated by UV radiation. However, while IR light coming from molecular clouds is a good tracer of the SFR, diffuse dust (cirrus) can contaminate IR luminosities, reprocessing the light coming from less massive, older stars and leading to an overestimation of the SFR. Several studies (e.g., Hao et al. 2011; Clemens et al. 2013; Rowlands et al. 2014; Swinbank et al. 2014; da Cunha et al. 2015) have demonstrated that cold diffuse emission is relevant mainly for $\psi \lesssim 30\,M_\odot\,yr^{-1}$, but becomes less dominant at higher SFR $\psi \lesssim 100\,M_\odot\,yr^{-1}$. Consequently the SFRF at the bright end can be well traced by far-IR/(sub)millimeter wide-area surveys mentioned in Section 1.3.2 arriving up to $z \sim 3$.

Therefore, SFRF can be reconstructed up to $z \sim 3$ combining UV and far-IR data, respectively for the faint end and the bright end. For $z > 3$ and large SFRs $\psi \gtrsim 30 - 50\,M_\odot\,yr^{-1}$ the SFRF are more uncertain. However, relevant constraints have been obtained recently from deep radio surveys (Novak et al. 2017), from far-IR/(sub)millimeter stacking (see Rowan-Robinson et al. 2016; Dunlop et al. 2017) and super-deblending techniques (see Liu et al. 2018), and from targeted far-IR/(sub)millimeter observations of significant yet not complete samples of star-forming galaxies (e.g., Riechers et al. 2017; Marrone et al. 2018; Zavala et al. 2018) and quasar hosts (e.g., Venemans et al. 2017, 2018; Stacey et al. 2018). Moreover, very recently, Gruppioni et al. 2020 estimated the total IR luminosity functions up to redshift $z \sim 6$ from a sample of 56 galaxies serendipitously detected by ALMA in the COSMOS and ECDFS fields. Finally, at $z \gtrsim 8$ dust extinction plays a minor role and the

SFRF can be obtained from UV measurements at all SFR.

A fit to the observational data, keeping into account such considerations, has been performed by Mancuso et al. 2016a via a Schechter function:

$$\frac{\mathrm{d}^2 N}{\mathrm{d}\psi\,\mathrm{d}V} = \Phi^* \left(\frac{\psi}{\psi^*}\right)^{\alpha} \exp\left(-\frac{\psi}{\psi^*}\right) \tag{2.2}$$

with $\Phi^*(z)$ being the normalization, $\alpha(z)$ the power-law exponent and $\psi^*(z)$ the knee of the SFRF. The value of these redshift dependent parameters can be found in Table 1 of Mancuso et al. 2016a. This fit of the SFRF, together with observational data from surveys mentioned above is shown in Figure 2.1. Also the UV-only inferred SFRF is shown at $z \lesssim 1$ as dotted lines.

The SFRF normalization, as well as the knee of the SFRF tend to increase out to $z \sim 3$, receding back at higher redshifts. At $z \gtrsim 1$ the bright end of the SFRF turns out to be populated by heavily dust-obscured, strongly star-forming galaxies, which constitute the progenitors of local massive spheroids with masses $M_\star \gtrsim$ a few $10^{10}\,\mathrm{M}_\odot$; the faint end is instead mainly populated by mildly obscured star-forming galaxies, which will end up in spheroid-like objects with stellar masses $M_\star \lesssim 10^{10}\,\mathrm{M}_\odot$. On the other hand, disk-dominated galaxies with stellar masses $M_\star \lesssim$ several $10^{10}\,\mathrm{M}_\odot$ are found to be well traced by the UV-inferred SFRF at $z \lesssim 2$.

In Mancuso et al. 2016a, 2016b, 2017 and Lapi et al. 2017a, 2017b the SFRF have been validated against independent data sets, including integrated galaxy number counts at relevant far-IR/(sub)millimeter/radio wavelengths, counts/redshift distributions of strongly gravitationally lensed galaxies, and main sequence of star-forming galaxies. An additional, straight test for the SFRF, performed by Lapi et al. 2017b (see their Figure 4), is the computation of the stellar mass function via the continuity equation, directly connecting the star formation to the building up of the stellar mass in galaxies, and the comparison with statistical observations at different redshifts for both quiescent and star-forming objects (e.g., Davidzon et al. 2017).

The cosmic SFR density can be computed from the SFRF as:

$$\rho_\psi = \frac{\mathrm{d}\dot{M}_{\mathrm{SFR}}}{\mathrm{d}V} = \int \mathrm{d}\log\psi\,\psi\,\frac{\mathrm{d}^2 N}{\mathrm{d}\log\psi\,\mathrm{d}V} \tag{2.3}$$

The resulting determination is shown as a dot-dashed black line in Figure 2.3. It can be noticed that the cosmic SFR density computed in this way tends to be appreciably higher with respect to most of the previous determinations (e.g. Madau & Dickinson 2014) and tends to have a flatter peak toward

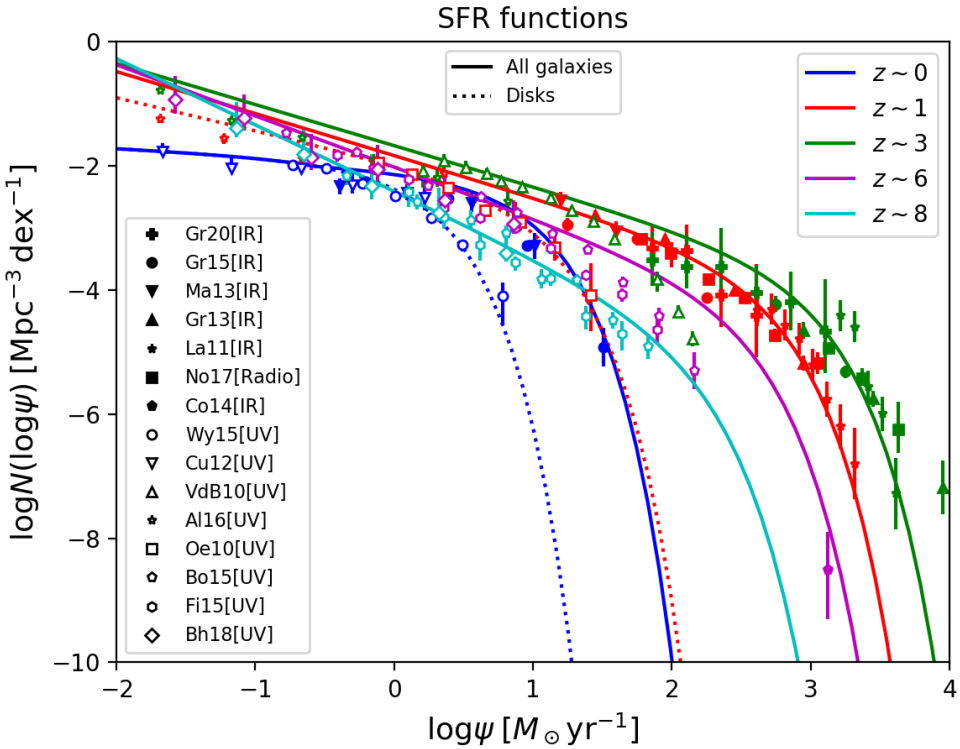

FIGURE 2.1: SFRF at redshifts $z = 0$ (blue), 1 (red), 3 (green), 6 (magenta), and 8 (cyan). Solid lines show the rendition from UV plus far-IR/(sub)millimeter/radio data, referring to the overall population of galaxies; dotted lines (only plotted at $z \simeq 0$ and 1) show the rendition from (dust-corrected) UV data, referring to disk galaxies. UV data (open symbols) are from van der Burg et al. 2010 (triangles), Bouwens et al. 2016, 2017 (pentagons), Finkelstein et al. 2015 (hexagons), Cucciati et al. 2012 (inverse triangles), Wyder et al. 2005 (circles), Oesch et al. 2010 (squares), Alavi et al. 2016 (stars), Bhatawdekar et al. 2018 (rhombus); far-IR/(sub)millimeter data (filled symbols) are from Gruppioni et al. 2020 (filled plus), Gruppioni et al. 2015 (circles), Magnelli et al. 2013 (inverse triangles), Gruppioni et al. 2013 (triangles), Lapi et al. 2011 (stars), and Cooray et al. 2014 (pentagons); radio data are from Novak et al. 2017 (squares).

slightly higher redshift. This can be traced back to to a more complete sampling of the dusty star-forming galaxy population thanks to the most recent wide-area far- IR/(sub)millimeter/radio surveys (see Gruppioni et al. 2013; Gruppioni & Pozzi 2019; Rowan-Robinson et al. 2016; Novak et al. 2017; Liu et al. 2018). Such dusty galaxies, featuring an extremely high level of star formation ($\sim 50 - 3000\,M_\odot$/yr), seem to have a significant impact on the total star formation at $2 \leq z \leq 6$ (see e.g. Wang et al. 2019; Gruppioni et al.

2020; Smail et al. 2021), flattening the cosmic SFR density peak out to high redshifts. Therefore, since the SFRF fit is based also on data coming from recent far-IR/(sub)mm surveys, the resulting cosmic SFR density is larger and more in agreement with the recent IR data (see e.g. Casey et al. 2018; Rowan-Robinson et al. 2016).

2.1.2 Stellar mass functions + main sequence

Another method to estimate the cosmic SFR density is convolving the stellar mass functions of star-forming galaxies at different redshifts with a distribution around the main sequence; this approach has been adopted in Chruslinska & Nelemans 2019 and Boco et al. 2021.

The GSMF is routinely estimated via near-IR data and broadband SED fitting (e.g., da Cunha et al. 2008; Boquien et al. 2019), as discussed in Section 1.3. The star-forming galaxy stellar mass function $\mathrm{d}^2N/\mathrm{d}V/\mathrm{d}\log M_\star$ has been determined at different redshifts by several authors (e.g. Ilbert et al. 2013; Muzzin et al. 2013; Tomczak et al. 2014; Davidzon et al. 2017). A good review of the different estimations can be found in Chruslinska & Nelemans 2019, where it is provided an average fit between many different determinations. In that work authors consider two possible variations of the GSMF, trying to account for the uncertainties on the faint end. In particular they analyze two extreme cases: (i) a fixed power-law slope at all redshifts and (ii) a slope increasing at higher redshift, making the GSMF steeper at high-z. In this thesis I adopt their fit, and, for simplicity, I only consider their prescription for a redshift independent slope at the faint end (see Figure 2.2 and Figure 3 in Chruslinska & Nelemans 2019, solid lines).

In order to compute the cosmic SFR density, the GSMF must be convolved with a distribution of SFR around the main sequence of star-forming galaxies. In this way, star-forming galaxies are parametrized and counted by their stellar mass and their SFR is determined by the MS, allowing the computation of the cosmic SFR density. However, as pointed out in Section 1.3.3, the MS is only an average relation between stellar mass and SFR, with the presence of outliers such as starbursts, lying even $\sim$ 1 dex above it.

Following some recent works on SBGs (see Sargent et al. 2012; Bethermin et al. 2012; Ilbert et al. 2015; Schreiber et al. 2015) star-forming galaxies with fixed mass at a given redshift tend to be distributed in SFR with a double gaussian shape. This bimodal distribution represents two populations: the dominant population of main sequence galaxies (MSGs), whose Gaussian distribution in SFR is centered around the MS value, and the subdominant population of starburst galaxies, whose Gaussian distribution is

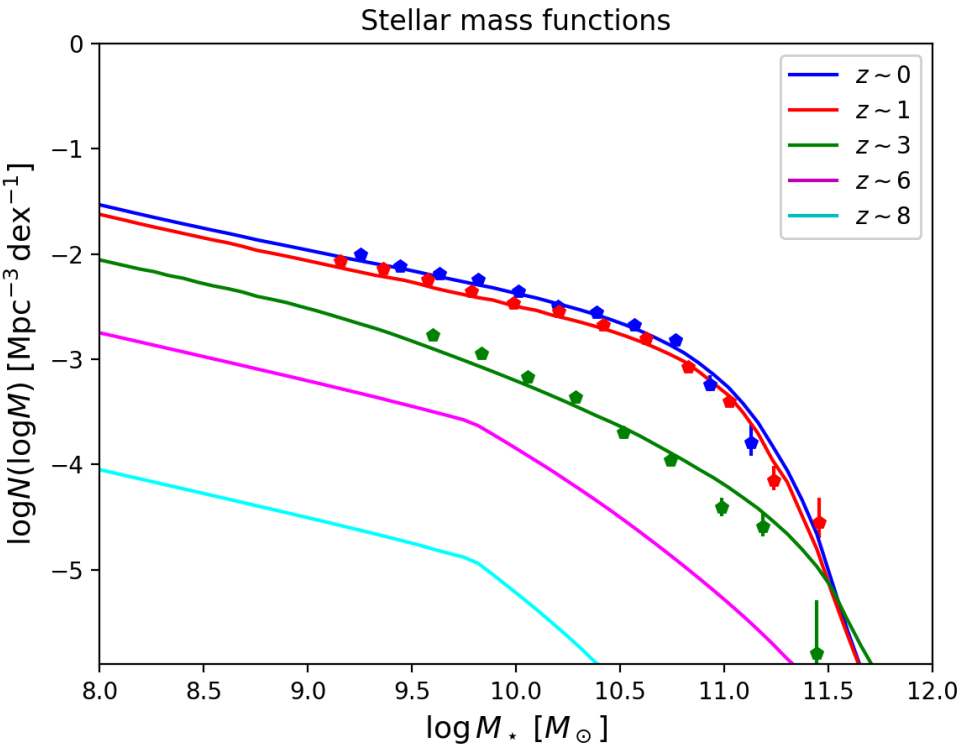

FIGURE 2.2: Right panel: Stellar mass functions for star-forming galaxies at redshifts $z = 0$ (blue), 1 (red), 3 (green), 6 (magenta), and 8 (cyan). Data points are taken from Davidzon et al. 2017.

centered around a SFR typically $\sim 3-4\sigma$ above the MS value. In the aforementioned works it is empirically found that the shape of the distribution is almost independent on the galaxy stellar mass and redshift. In the present thesis I take as fiducial the distribution in SFR found by Sargent et al. 2012 with the double Gaussian shape reported below:

$$\frac{\mathrm{d}p}{\mathrm{d}\log\psi}(\psi|z, M_\star) \propto A_{\mathrm{MS}} \exp\left[-\frac{(\log\psi - \langle\log\psi\rangle_{\mathrm{MS}})^2}{2\sigma^2_{\mathrm{MS}}}\right] + \\ + A_{\mathrm{SB}} \exp\left[-\frac{(\log\psi - \langle\log\psi\rangle_{\mathrm{SB}})^2}{2\sigma^2_{\mathrm{SB}}}\right] \tag{2.4}$$

where $A_{\mathrm{MS}} = 0.97$ is the fraction of MSGs, $A_{\mathrm{SB}} = 0.03$ the fraction of SBGs, $\langle\log\psi\rangle_{\mathrm{MS}}$ the value given by the MS and representing the central value for the first Gaussian, $\langle\log\psi\rangle_{\mathrm{SB}} = \langle\log\psi\rangle_{\mathrm{MS}} + 0.59$ the central value of the second

Gaussian, $\sigma_{\rm MS} = 0.188$ the one-sigma dispersion of the first Gaussian and $\sigma_{\rm SB} = 0.243$ the dispersion of the starburst population.

However, I caveat that, as mentioned in Section 1.3.3, other recent studies, probing the SFR distribution of galaxies around the MS in a more extended range of masses and redshifts, have found an increase of the starbursts fraction at low masses $M_\star \lesssim 10^9 M_\odot$ and at high redshifts $z \gtrsim 2-3$ (see Caputi et al. 2017; Bisigello et al. 2018). Computations of the cosmic SFR density varying the SBGs fraction according to these works have been performed in Chruslinska et al. 2021.

Convolving the distribution in equation (2.4) with the GSMF, one can reconstruct the SFRF of galaxies as:

$$\frac{\mathrm{d}^2 N_{\rm GSMF+MS}}{\mathrm{d}\log\psi\,\mathrm{d}V}(z,\log\psi) = \int \mathrm{d}\log \mathrm{M}_\star \frac{\mathrm{d}^2\mathrm{N}}{\mathrm{d}\log \mathrm{M}_\star\,\mathrm{dV}}(\mathrm{z},\log \mathrm{M}_\star)\,\frac{\mathrm{dp}}{\mathrm{d}\log\psi}(\log\psi|\mathrm{z},\mathrm{M}_\star) \tag{2.5}$$

In Sargent et al. 2012 and Ilbert et al. 2015 it is demonstrated that such a convolution yields a good reconstruction of the galaxy luminosity functions.

Integrating the reconstructed SFRF in the equation above over the whole range of star formation and multiplying by the SFR itself, as in equation (2.3), yelds the cosmic SFR density as a function of the cosmic time.

In Figure 2.3 I show the cosmic SFR density computed by integrating the SFRF directly fitted from the data (as in equation (2.2)) as a dot-dashed line, and the one derived from the GSMF as in equation (2.5) as a solid line. I find that the two determinations of the cosmic SFR density are in rather good agreement up to $z \sim 2$. At $z > 2$ the integration of the SFRF directly fitted from the luminosity data yields a larger cosmic SFR density, with the maximum difference being a factor ~ 2.5 at $z \sim 4.5$. These discrepancies, even if rather small, can be due to biases and selection effects arising respectively in the chosen determination of the SFRF and GSMF. For example, the shape of the faint end of the GSMF at high redshift is highly uncertain and, using a mass function whose shape steepens toward higher redshifts (see e.g. Figure 3, dashed lines in Chruslinska & Nelemans 2019), drastically reduce the differences. Other factors that can produce these discrepancies are possible biases in the determination of the SFR from the UV+IR luminosity, in the shape of the main sequence or in the relative contributions of the main sequence and starburst populations. As for the latter, in Caputi et al. 2017 and Bisigello et al. 2018, it is pointed out that the population of starburst galaxies tends to increase at $z \gtrsim 2$; keeping into account this trend can reduce the differences between the two cosmic SFR densities (Chruslinska et al. 2021). All in all, in Figure 2.3 I have shown that the two approaches yield a rather good agreement especially at $z \lesssim 2$, and I have quantitatively characterized

the differences toward higher redshifts.

The main advantage of an approach based on the SFRF is that it is rather direct. Indeed SFR is the main quantity of interest, since, provided an IMF, it gives the effective number of stars formed and so it provides a normalization for the DCO merging rates. Using the SFRF, a measure of the number density of galaxies with given SFR at a certain redshift is directly obtained. Instead, starting from the GSMF, the computation of the SFR requires a step more, involving the convolution with the main sequence and a correct modelization of the relative abundance of main sequence galaxies and starbursts.

On the other hand the GSMF provide a direct statistics of the star-forming galaxies stellar masses and, as shown above, the distribution of SFRs at fixed stellar mass and redshift is well established in literature. Therefore, once the stellar mass is known, it is easy to associate a SFR and to use a scaling relation, such as the MZR or FMR, to infer its metallicity. Contrariwise, fixing the SFR and redshift, the association of a stellar mass is not straightforward from an empirical point of view, and some assumptions about the galaxy star formation history should be made, as I will show in Subsection 2.2.2. It is therefore trickier to use a scaling relation to assign metallicity. Still, starting from the SFRF, it is possible to follow the chemical enrichment of a galaxy using a model of galaxy evolution, as done e.g. in Boco et al. 2019 and as I will show in Section 2.2.4.

A final comparison concerns the possibility of disentangling different galactic populations using the two mentioned statistics. From the SFRF it can be determined the contribution to the total cosmic SFR density coming from late type disk galaxies (mainly traced by UV data) and star-forming progenitors of local early type galaxies (mainly traced by far-IR/(sub)mm data), as explained in Subsection 2.1.1. From the GSMF, instead, it is possible to separate between main sequence galaxies and starburts. Understanding the contribution to the total SFR and the metallicities of different galactic populations can be important also for the association of a host galaxy to a GW event.

2.2 Metallicity distribution

Along with stellar mass and star formation rate, the metal content of the gas-phase of the ISM (i.e. the gas-phase metallicity, $Z_{\rm gas}$) is one of the key physical quantities that has to be considered in statistical galaxy evolution studies (for a review, see Maiolino & Mannucci 2019).

As it can be seen in equation (2.1), metallicity is a crucial ingredient also to compute the merging rates of DCOs, since many aspects of stellar and

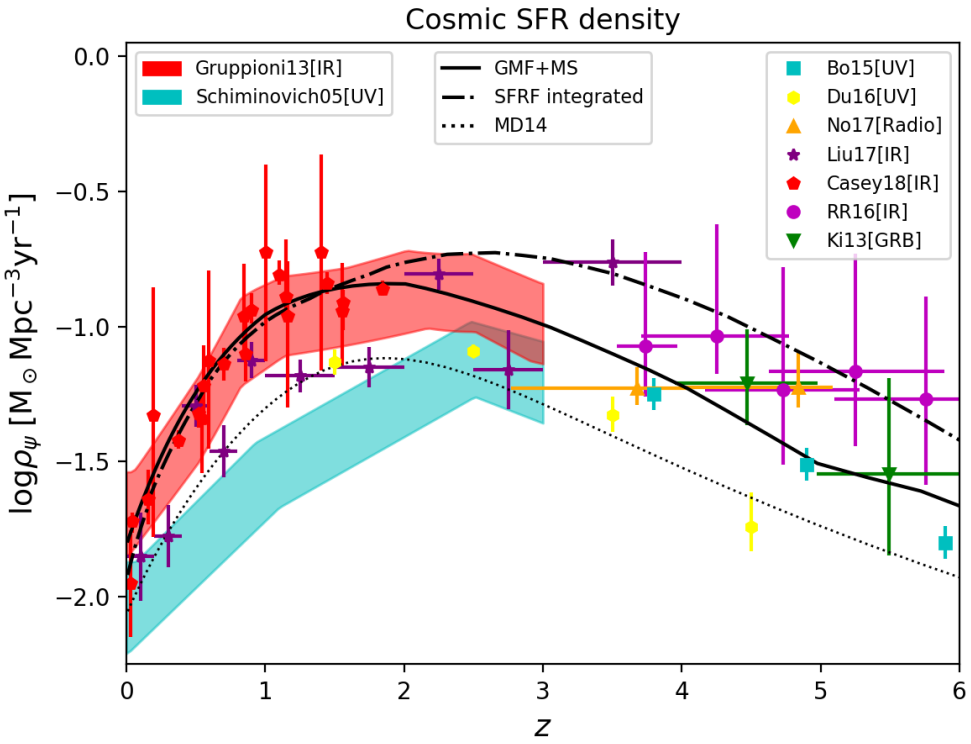

FIGURE 2.3: Cosmic SFR density as a function of redshift. The black solid line shows the result obtained integrating the SFR functions reconstructed from the stellar mass functions plus the main sequence (equation (2.5)). The black dot dashed line shows, instead, the result of the integration of the SFRF directly derived from the luminosity functions (equation (2.2)). For reference, the dotted line illustrates the determination by Madau & Dickinson 2014. Data are from (dust-corrected) UV observations by Schiminovich et al. 2005 (cyan shaded area) and Bouwens et al. 2015 (cyan squares); ALMA submillimeter observations of UV-selected galaxies on the HUDF by Dunlop et al. 2017 (yellow hexagons); VLA radio observations on the COSMOS field by Novak et al. 2017 (orange triangles); Herschel far-IR observations by Gruppioni et al. 2013 (red shaded area) and Casey 2018 (red pentagons); Herschel far-IR stacking by Rowan-Robinson 2016 (magenta circles); far-IR/(sub)millimeter observations from super-deblended data on the GOODS field by Liu et al. 2018 (purple stars); and estimates from long GRB rates by Kistler et al. 2009, 2013 (green reversed triangles).

binary evolution depend on it (stellar winds, supernova kicks, direct collapse, common envelope effects, etc.). As for single stellar evolution, metallicity and mass of the zero-age-main-sequence (ZAMS) star are the key ingredients to determine its fate and, in particular, its final mass. Indeed at high metallicities stellar mass loss from radiation driven winds is more efficient, due to the presence of heavier elements in the stellar atmosphere which have a larger scattering cross section with photons. Low metallicity stars, instead, experience much weaker stellar winds and smaller mass losses. Therefore stars in metal poor environments finish their evolution being more massive with respect to stars with the same initial mass in metal rich environments, yielding more massive compact remnants. As for binary evolution, metallicity has a strong effect on the survival of the binary. In particular, compact objects as black holes and neutron stars are originated from massive stars which can undergo supernova explosions at the end of their life. These explosions, if asymmetric, can imprint a velocity in a certain direction to the newly born compact object. Such a phenomenon is usually referred to as natal kick, with kick velocity that can be as high as $\lesssim 500\,\mathrm{km\,s^{-1}}$ which can lead to the disruption of the binary. However, more massive remnants, produced at lower metallicities, receive, on average, smaller kick due to their higher mass and to a larger fallback fraction (i.e. the mass fraction of stellar material falling back onto the compact remnant), reducing the kick momentum. For very high stellar masses ($M_{\mathrm{ZAMS}} \gtrsim 40\,\mathrm{M}_{\odot}$) it is even possible to have a fallback fraction ~ 1, meaning that the star directly collapses to a BH without undergoing a supernova explosion. No natal kick is present in this case. Therefore binaries born at low metallicity have higher probability to form compact remnants with larger masses and to remain bound after stellar evolution, eventually reaching the merging phase, via GW emission. For a detailed discussion on the effects of metallicity on stellar and binary evolution I refer the reader to Belczynski et al. 2010a; Dominik et al. 2012; Chruslinska et al. 2018. For these reasons, in order to investigate the properties and the merging rates of DCOs, a determination of the gas-phase metallicity in different galaxies at different redshift is essential.

The easiest way to estimate the gas-phase metallicity at a given redshift is via the average cosmic metallicity approach, which has been adopted in several works (e.g. Belczynski et al. 2016; Cao et al. 2018; Li et al. 2018). The average cosmic metallicity can be computed as:

$$\langle Z(z)\rangle = \frac{y_Z\,(1-\mathcal{R})}{\rho_b}\int_z \mathrm{d}z'\,\frac{\mathrm{d}\dot{M}_{\mathrm{SFR}}}{\mathrm{d}V}(z')\left|\frac{\mathrm{d}t}{\mathrm{d}z'}\right| \tag{2.6}$$

where the star formation rate of the universe is integrated over all the redshift range from the beginning of the universe to the considered redshift z. This quantity is then multiplied by the stellar metal yield and divided by the background baryon density ρ_b. The rationale behind the formula is that, integrating the cosmic SFR over the cosmic time and multiplying it by the metal yield, it is obtained an estimate of the metal mass density produced in the Universe up to a certain redshift z, and, dividing by the background baryon density, a metallicity is obtained.

However, such a metallicity is an average over the whole background baryon density, which does not keep into account the different environmental conditions inside galaxies where star formation occurs. Indeed, at early times, the cosmic metallicity resulting from this formula would stay rather low just because only few DM halos collapsed and few galaxies were formed with respect to the totality of cosmic baryons, but the metallicity inside such galaxies could, in principle, be high. So, smoothing over the whole baryon content of the universe, can bias the value of metallicity at which star formation takes place. Indeed the cosmic metallicity determined in this way is in rather good agreement with IGM measurements, but it is not able to reproduce neither the metallicity of high redshift damped Lyman-alpha systems (DLAs), nor the metallicity of star-forming galaxies (see e.g. Figure 14 in Madau & Dickinson 2014). Therefore, in order to overcome this underestimation, some authors (e.g. Belczynski et al. 2016; Cao et al. 2018) adopted a shift of 0.5 dex toward higher metallicities. Though, even with this prescription, this formula still yields low metallicity values, in partial agreement with the metallicity in DLAs, but that falls short with respect to the metallicities of massive star-forming galaxies. Usually, in literature, a log-normal distribution $\mathrm{d}p/\mathrm{d}Z$ with a scatter of $\sigma_{\log Z} = 0.5$ around this mean value has been adopted.

The approach described here is functional because it promptly associate a metallicity at each redshift and, convolving a cosmic SFR density determination with the average cosmic metallicity, it is possible to directly compute the galactic term as:

$$\frac{\mathrm{d}^2 \dot{M}_{\mathrm{SFR}}}{\mathrm{d}V\,\mathrm{d}Z}(t) = \frac{\mathrm{d}\dot{M}_{\mathrm{SFR}}}{\mathrm{d}V}(t) \times \frac{\mathrm{d}p}{\mathrm{d}Z}(t) \tag{2.7}$$

treating the cosmic SFR density and the metallicity distribution as independent. However, a part from the bias toward low metallicities described above, this approach is too simplistic for the purposes of this thesis, in which I aim at being able to associate a metallicity to each single star-forming galaxy parametrized by its stellar mass or SFR.

The gas-phase metallicity of a galaxy can be estimated via different methods: using empirical scaling relations such as the MZR (e.g. Kewley & Ellison 2008; Maiolino et al. 2008; Mannucci et al. 2009; Magnelli et al. 2012; Zahid et al. 2014; Genzel et al. 2015; Sanders et al. 2020) and the FMR (e.g. Mannucci et al. 2010; Mannucci et al. 2011; Hunt et al. 2016; Curti et al. 2020) or using some theoretical models of chemical evolution. A discussion about theoretical models and empirical scaling relations has been carried out in Section 1.3.4. In the next Subsections I first focus on empirical methods, deepening the study of the MZR and FMR and comparing their predictions (Section 2.2.1), then I use these empirical scaling relations in combination with the galaxy statistics described in Section 2.1 to calculate the galactic term (Sections 2.2.2 and 2.2.3). Finally, I briefly describe the theoretical model adopted throughout this thesis and I exploit its results to compute the galactic term (Section 2.2.4).

Since many metallicity scaling relations are given in terms of oxygen abundance ratio $12 + \log(O/H)$, I will often use it when reporting metallicity values and to express my results. However I also convert it to the overall metallicity $Z_{\rm gas}$ assuming solar abundances to be representative of the whole star-forming gas: $\log(Z_{\rm gas}/Z_\odot) = \log(O/H) - \log(O_\odot/H_\odot)$. I take as solar metallicity and oxygen abundance ratio the values reported in Caffau et al. 2011: $Z_\odot \simeq 0.0153$ and $12 + \log(O_\odot/H_\odot) \simeq 8.76$, yielding the conversion relation $\log Z \simeq 12 + \log(O/H) - 10.575$. However, I caveat that this relation might be biased in the case of strong α-enhancement.

2.2.1 MZR and FMR comparison

As already seen in Section 1.3.4, the MZR is a correlation between $Z_{\rm gas}$ and $M_\star$ (see Figure 1.15). The shape is thought to be almost linear up to $M_\star \lesssim 10^{10}\,{\rm M}_\odot$, with a bending at larger masses. The overall normalization of the relation decreases at higher redshift, but different studies finds different rates of redshift evolution. Some earlier works (e.g. Maiolino et al. 2008; Mannucci et al. 2009; Magnelli et al. 2012) found a slow evolution of the MZR out to $z \sim 2$, but a very sharp decline in $Z_{\rm gas}$ of about $\sim 0.4 - 0.5$ dex between $z \sim 2.5$ and $z \sim 3.5$, suggesting a huge drop in $Z_{\rm gas}$ in the early universe and creating somewhat tensions with the modern cosmological simulations of massive galaxy formation (e.g. Davé et al. 2017; Torrey et al. 2018). The problem of accurately determining $Z_{\rm gas}$ becomes strongly pronounced for high-z ($z > 3$) massive, dusty galaxies (see e.g. discussions in Tan et al. 2014; Liu et al. 2019; Tacconi et al. 2020), where the MZR should be extrapolated. Indeed, if a linear extrapolation of a sharply declining MZR is performed,

very low values of metallicities ($12 + \log(\mathrm{O/H}) < 8.0$) are found at $z > 3$ even for massive systems.

The FMR, instead, is a relation among three parameters $M_\star$, SFR, and $Z_{\rm gas}$, envisaging a correlation between $Z_{\rm gas}$ and $M_\star$ and an anti-correlation between $Z_{\rm gas}$ and SFR, with the strength of the anticorrelation dependent on the stellar mass (see Figure 1.16). The FMR is thought to be redshift independent and z is not a parameter directly entering in the relation. From the FMR perspective, the metallicity evolution with redshift at fixed stellar mass can be traced back to the redshift evolution of the SFR (or sSFR), described by the main sequence. Indeed, at fixed stellar mass and higher redshift, SFR inferred from the main sequence are larger, sampling a different region of the FMR, with higher SFR and, therefore, lower $Z_{\rm gas}$. The FMR redshift independence is proven out to $z \sim 3.5$, but, following this interpretation, it can be extrapolated at $z > 3.5$ using the redshift evolution of the main sequence, which is determined out to $z \sim 6$. This originates a rather shallow decline of metallicity with redshift, given the slow redshift evolution of the main sequence at $z > 2$.

Thus, while the level of redshift evolution for the FMR and MZR at $z \lesssim 2$ is somewhat comparable, the evolution of the two relations becomes completely different at $z \gtrsim 3$. To explicitly show these differences I first put the two relations on the same ground computing an averaged MZR from the FMR at different redshifts. I do this, at fixed stellar mass and redshift, averaging the metallicity given by the FMR over the distribution of SFR around the MS in equation (2.4):

$$\langle \mathrm{Z_{MZR}} \rangle (\mathrm{z}, \mathrm{M}_\star) = \int \mathrm{d}\log\psi \frac{\mathrm{dp}}{\mathrm{d}\log\psi}(\psi|\mathrm{z}, \mathrm{M}_\star)\, \mathrm{Z_{FMR}}(\mathrm{M}_\star, \psi) \tag{2.8}$$

In Figure 2.4 I show this averaged MZR (solid lines), computed from the Mannucci et al. 2011 FMR. In the Figure, for comparison, it is also reported the MZR of Mannucci et al. 2009 (dashed lines), linearly extrapolated at $z > 3.5$. It can be noticed that, while at low redshifts ($z \lesssim 2$) the two relations give comparable results, at high redshifts ($z \gtrsim 3$) the MZR evolution is very rapid yielding values of metallicity much lower than those obtained from the FMR.

Trying to solve this tension is crucial, since, as seen in Section 2.1, the amount of SFR at $z > 3$ is not negligible. However, the quest is rather challenging, because on the one hand at those redshifts optical/near-IR spectroscopy suffers from large dust attenuation, on the other hand the statistics of sources that have been spectroscopically studied through fine structure lines with ALMA is still limited (Boogard et al. 2019).

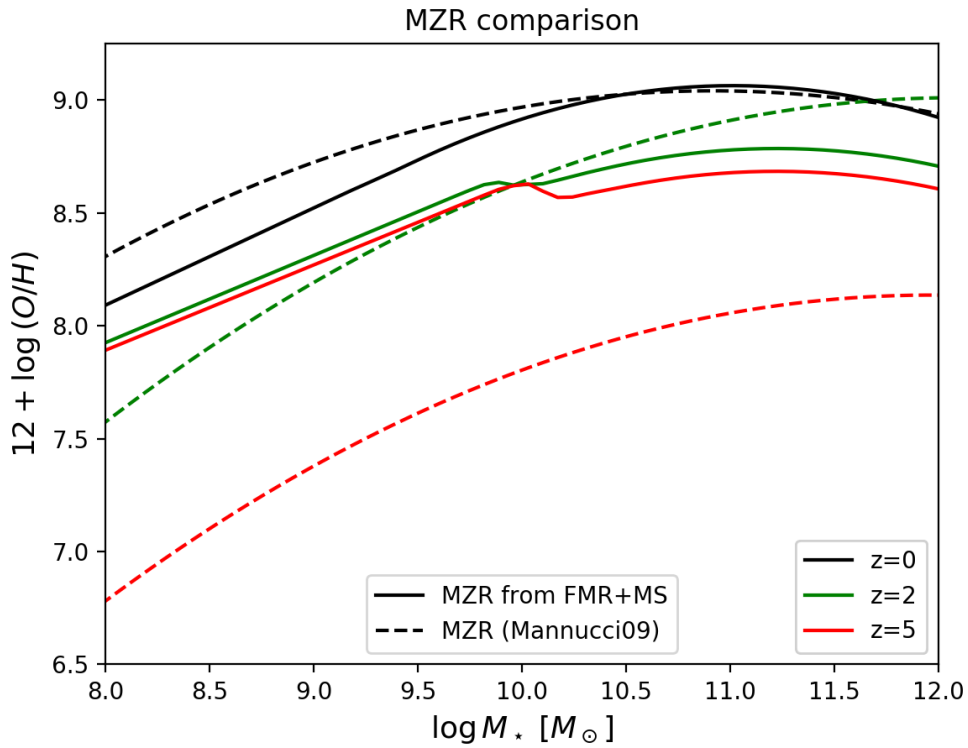

FIGURE 2.4: The average MZR relation $\langle Z_{\rm MZR} \rangle$ computed convolving the FMR of Mannucci et al 2011 with the MS at different redshifts (solid lines), compared with the MZR determination of Mannucci et al. 2009 at different redshifts (dashed lines).

Nonetheless, very recent studies obtained a great agreement between the FMR and a smoothly evolving MZR. Sanders et al. 2021 retrieved MOSDEF spectroscopy of a large sample of massive galaxies at $z > 3$, and significantly improved the statistics upon past studies over the same redshift range. By employing a novel dust-correction method, they found a much slower evolution of MZR observing a very shallow metallicity decline of only 0.11 dex between $2.5 < z < 3.5$. This result greatly supports FMR and slowly evolving MZRs calibrated from UV+IR data (Genzel et al. 2015).

On top of that, an important evidence of a significant metal enrichment in the early Universe came from the novel dust mass ($M_{\rm dust}$) estimates in distant galaxies at $z > 3-6$ (e.g. da Cunha et al. 2015, Donevski et al. 2020; Ginolfi et al. 2020). For instance, by analysing a large sample of 300 massive ($M_\star > 10^{10}\ M_\odot$) dusty galaxies in the COSMOS field observed with ALMA over a wide redshift range ($0.5 < z < 5.25$), Donevski et al. 2020 show that, in order to explain the observed $M_{\rm dust}$, their $Z_{\rm gas}$ are, on average, close to solar

(12+log(O/H)=8.64 and 12+log(O/H)=8.52 for MS and SB galaxies, respectively). These values are in great agreement with recent direct $Z_{\rm gas}$ measurements through [NII]λ6584/Hα ratio by Shapley et al. 2020 for dusty galaxies within the same mass range at $z \sim 2$.

All of this complements classical arguments from stellar archaeology, discussed in Section 1.3.1, suggesting a fast metal enrichment of galaxies even at high-z. Indeed the study of stellar emission in local massive ETGs can place very good constraints on their metallicity evolution: stars observed in these galaxies, formed typically at high redshifts, are found to be almost coheval and α-enhanced, indicating a short ($<$ 1 Gyr) burst of high star formation stopped by some form of energetic feedback (e.g., Romano et al. 2002; Thomas et al. 2005, 2010; Gallazzi et al. 2006; Johansson et al. 2012). Their stellar metallicity ranges from $0.5\,Z_{\odot} - 2\,Z_{\odot}$ (see Thomas et al. 2010, Gallazzi et al. 2014; Maiolino & Mannucci 2019) implying that their chemical enrichment should have been very rapid. Such a fast metallicity growth has been confirmed even by SED studies of high redshift quiescent galaxies revealing solar and supersolar stellar metallicities even at early times. For example in Morishita et al. 2019 a sample of 24 quiescent galaxies at $z \sim 2$ has been studied finding average stellar metallicities of $Z \sim 1.5 - 2\,Z_{\odot}$ (see also Saracco et al. 2020); in particular, authors find that the relation between stellar mass and stellar metallicity of their sample shows no evolution with respect to the same relation for $z \sim 0$ galaxies in Gallazzi et al. 2014.

Finally, a direct measure of metallicity through $[\mathrm{OIII}]_{88\mu\mathrm{m}}/[\mathrm{NII}]_{122\mu\mathrm{m}}$ line ratio in high redshift quasar hosts (up to $z \sim 7.5$) has been performed by several authors, showing solar and supersolar metallicity values with no signs of redshift evolution (see e.g. Juarez et al. 2009; Novak et al. 2019; Onoue et al. 2020; Li et al. 2020).

These numerous findings point towards the need of a rapid metal enrichment in the distant Universe, a scenario that has recently been proposed theoretically by several authors (Asano et al. 2013; Béthermin et al. 2015; Popping et al. 2017; Vijayan et al. 2019; Pantoni et al. 2019; Lapi et al. 2020). I have also explored predictions on the metallicity evolution from state-of-the-art cosmological simulations (Davé et al. 2019) that self-consistently model gas and dust under standard IMF. By looking at different snapshots over the redshift range $0 < z < 5$ for the most massive objects ($10^{10}\,\mathrm{M}_{\odot} < \mathrm{M}_{\star} < 10^{11}\,\mathrm{M}_{\odot}$) it is found a very shallow $Z_{\rm gas}$ evolution of only ~ 0.3 dex drop from $z \sim 0$ to $z \sim 5$. This further strengthen the above cited observational findings that can suffer of selection biases.

Evidence for substantial metal content is also found for less massive galaxies ($10^9 < M_{\star} < 10^{9.5}\,M_{\odot}$) in the epoch of re-ionization ($6 < z < 9$, Jones et al. 2020; Strait et al. 2020). These studies claimed that the observed

$Z_{\rm gas}$ can be achieved by extrapolating FMR or slowly evolving MZRs.

All these reasons motivate me to apply prescriptions based on FMR as a reference scaling relation to infer the metal properties of galaxies at high-z (see the next Section). However, given the substantial uncertainties, in Section 2.2.3 I also show the case in which a MZR with a rapid decrease in $Z_{\rm gas}$ with redshift (e.g., Mannucci et al. 2009) is assumed as representative for the whole population of galaxies at $z > 3$.

2.2.2 The galactic term computed through a FMR

Given all the arguments above I compute the galactic term $\mathrm{d}^2\dot{M}_{\rm SFR}/\mathrm{d}V/\mathrm{d}Z$ using the FMR presented in Mannucci et al. 2011, assuming that I can extrapolate the FMR in the same form even at $z > 3.5$, as said in Section 2.2.1. Since the FMR is a relation between stellar mass, SFR and metallicity ($Z_{\rm FMR} = Z_{\rm FMR}(M_\star, \psi)$) I can use both the GSMF and the SFRF as galaxy statistics to perform the computation.

GSMF + FMR

Fixing redshift and stellar mass, I can derive a distribution in SFR as in equation (2.4); therefore the factor $\mathrm{d}^2\dot{M}_{\rm SFR}/\mathrm{d}V/\mathrm{d}Z$ can be computed as:

$$\frac{\mathrm{d}^2\dot{M}_{\rm SFR}}{\mathrm{d}V\,\mathrm{d}Z}(Z|z) = \int \mathrm{d}\log M_\star \frac{\mathrm{d}^2N}{\mathrm{d}V\,\mathrm{d}\log M_\star}(\log M_\star|z)\times \\ \times \int \mathrm{d}\log\psi\,\psi\frac{\mathrm{d}p}{\mathrm{d}\log\psi}(\psi|z,M_\star)\left.\frac{\mathrm{d}p}{\mathrm{d}Z}\right|_{\rm FMR}(Z|Z_{\rm FMR}(M_\star,\psi)) \tag{2.9}$$

where

$$\left.\frac{\mathrm{d}p}{\mathrm{d}\log Z}\right|_{\rm FMR}(Z|Z_{\rm FMR}(M_\star,\psi)) \propto \exp\left[-\frac{(\log Z - \log Z_{\rm FMR}(M_\star,\psi))^2}{2\sigma^2_{\rm FMR}}\right] \tag{2.10}$$

is just a log-normal distribution around the logarithmic metallicity value set by the FMR at fixed stellar mass and SFR, the factor $\mathrm{d}^2N/\mathrm{d}V/\mathrm{d}\log M_\star$ represents the GSMF, and the factor $\mathrm{d}p/\mathrm{d}\log\psi$ is the distribution in SFR around the MS computed as in equation (2.4). Notice that, using the FMR, there is not an explicit redshift dependence on the value of the metallicity; the redshift dependence enters only indirectly through the GSMF and the distribution of SFR $\mathrm{d}p/\mathrm{d}\log\psi$, which accounts for the MS redshift evolution.

In Figure 2.5 (top panel), I show the result of equation (2.9), using the Mannucci et al. 2011 FMR and the GSMF from Chruslinska & Nelemans 2019. The redshift dependence of the cosmic SFR density reflects the black solid line in Figure 2.3, as expected since the GSMF is used as starting point. As for the metallicity dependence, notice that its redshift evolution is very mild: there is not net evidence of a strong decrease with redshift of the metallicity at which star formation occurs, as expected looking at Figure 2.4. In fact, while at $z \lesssim 2$ most of the star formation takes place around solar values, at $z \sim 4-5$ the typical metallicities at which star formation occurs are $Z \sim 0.4-0.5\,Z_{\odot}$. The bottom left and bottom right panels show, respectively, the contribution of main sequence galaxies and starbursts. It can be noticed that the metallicity at which starbursts form stars tends to be slightly lower. This is natural, since, at fixed mass, the FMR predicts lower metallicities increasing SFR.

SFRF + FMR

The FMR can be used to assign metallicities even if the SFRF are chosen as galaxy statistics. The main difficulty is that, while at fixed redshift and stellar mass the SFR distribution can be easily constructed as in equation (2.4), it is not clear how to derive a distribution of galaxies stellar masses at fixed redshift and SFR; there are no works in literature facing the issue of deriving a stellar mass distribution from empirical data. This is why, in order to roughly estimate such stellar mass distribution, I must assume a star formation history for galaxies.

The method proceed as follows. Since I am considering only star-forming galaxies, the value of masses that they can assume at fixed redshift and SFR is less or equal than the mass given by the main sequence $M_{\star,\mathrm{MS}}(z,\psi)$; all the values of mass larger than $M_{\star,\mathrm{MS}}$ are below the MS and represent quenched galaxies which are no more forming stars. Actually I do not sharply cut all the stellar masses above $M_{\star,\mathrm{MS}}$, rather I put a Gaussian tail for masses $M_{\star} \geq M_{\star,\mathrm{MS}}$. As for the mass distribution for stellar masses smaller than the MS mass ($M_{\star} < M_{\star,\mathrm{MS}}$) I should make some assumption on the galaxies SFH.

For ETG progenitor galaxies, SED-modeling studies (e.g., Papovich et al. 2011; Smit et al. 2012; Moustakas et al. 2013; Steinhardt et al. 2014; Cassará et al. 2016; Citro et al. 2016) suggest to describe the SFH with a truncated power-law shape:

$$\psi(\tau) \propto \tau^{\kappa}\,\Theta_{\mathrm{H}}(\tau-\tau_{\psi}) \tag{2.11}$$

where $\kappa \lesssim 0.5$ controls the slow power law rise and $\Theta_{\mathrm{H}}(\tau-\tau_{\psi})$ is the Heaviside theta function specifying the star formation duration τ_{ψ}, which is of the

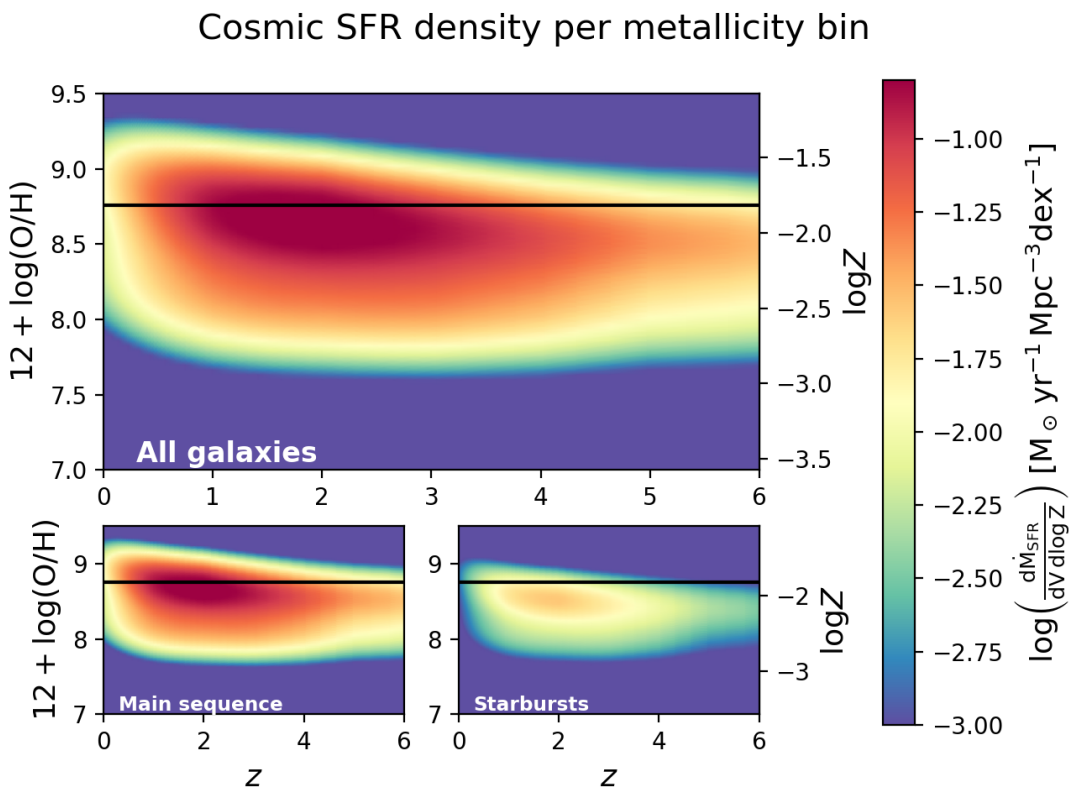

FIGURE 2.5: Top panel: The factor $\log(\mathrm{d}^2\dot{M}_{\rm SFR}/\mathrm{d}V/\mathrm{d}\log Z)$ computed convolving the GSMF with the FMR of Mannucci et al. 2011 (color coded) as a function of redshift on the x axis and gas-phase metallicity $12+\log(\mathrm{O/H})$ on the left y axis; on the right y axis it is plotted the logarithm of the metallicity $\log Z$ and the solar value is plotted as a black solid line. Bottom left panel: Contribution to the cosmic SFR density coming from main sequence galaxies. Bottom right panel: Contribution to the cosmic SFR density coming from starburst galaxies.

order of $\tau_\psi \leq 1$Gyr for massive and highly star-forming ETG progenitors and longer $\tau_\psi \sim$ few Gyr in low-mass spheroidal galaxies.

On the other hand, late type disk dominated galaxies, as mentioned in Section 1.3.1, tend to have, on average, a SFH exponentially declining $\psi(\tau) \propto e^{-\tau/\tau_\psi}$, over rather long star formation timescales $\tau_\psi \sim$ several Gyr (see Chiappini et al. 1997; Courteau et al. 2014; Pezzulli & Fraternali 2016; Grisoni et al. 2017; Lapi et al. 2020).

Even if the star formation timescales are very different, the SFRs in both cases can be considered as nearly constant with time: for ETG progenitors the SFR range is not larger than a factor ~ 1.5 for most of their lifetime, while for LTGs the SFR changes only of a factor ~ 2.5 over $\sim 8-9$ Gyr. Given that,

for the sake of simplicity, I assume a constant SFH for the galaxies considered in this thesis. Under this assumption, the stellar mass of a galaxy increases linearly with time, with a slope set by its SFR. The logarithmic distribution of masses smaller than the MS mass $M_\star < M_{\star,\mathrm{MS}}$, at fixed redshift and SFR, is therefore proportional to the mass itself $\mathrm{d}p/\mathrm{d}\log M_\star \propto M_\star$. At $M_\star \geq M_{\star,\mathrm{MS}}$, as already said, I adopt a gaussian tail to keep into account the scatter around the MS. The overall stellar mass distribution at fixed z and SFR can be written as:

$$\frac{\mathrm{d}p}{\mathrm{d}\log M_\star}(\mathrm{M}_\star|\mathrm{z},\psi) \propto \begin{cases} \mathrm{M}_\star & M_\star < M_{\star,\mathrm{MS}} \\ \mathrm{M}_{\star,\mathrm{MS}} \times \exp\left(-\frac{(\log \mathrm{M}_\star - \log \mathrm{M}_{\star,\mathrm{MS}})^2}{2\sigma_{\mathrm{M}_\star}}\right) & M_\star \geq M_{\star,\mathrm{MS}} \end{cases} \tag{2.12}$$

normalized to unity. Actually, this is a crude approximation of what has been done in Mancuso et al. 2016b, where authors are able to theoretically reproduce the MS starting from the SFRF and similar prescriptions for the galaxies SFHs.

Using the SFRF as a starting point and equation (2.12) as stellar mass distribution at given z and ψ, I can assign a metallicity to galaxies with the FMR and compute the factor $\mathrm{d}^2\dot{M}_{\mathrm{SFR}}/\mathrm{d}V/\mathrm{d}Z$ as:

$$\frac{\mathrm{d}^2\dot{M}_{\mathrm{SFR}}}{\mathrm{d}V\,\mathrm{d}Z}(Z|z) = \int \mathrm{d}\log\psi\,\psi\,\frac{\mathrm{d}^2N}{\mathrm{dV}\,\mathrm{d}\log\psi}\times \\ \times \int \mathrm{d}M_\star \frac{\mathrm{d}p}{\mathrm{d}M_\star}(M_\star|z,\psi)\left.\frac{\mathrm{d}p}{\mathrm{dZ}}\right|_{\mathrm{FMR}}(Z|Z_{FMR}(M_\star,\psi)) \tag{2.13}$$

where $\mathrm{d}p/\mathrm{d}\log Z|_{\mathrm{FMR}}\,(Z|Z_{\mathrm{FMR}}(M_\star,\psi))$ is the same log-normal distribution around the central logarithmic value of metallicity set by the FMR appearing in equation (2.10).

The result of the computation in equation (2.13) is shown in Figure 2.6. It can be noticed that the redshift dependence of the SFR density reflects the shape of the cosmic SFR density derived by the integration of the SFRF (dot-dashed lines in Figure 2.3), with a broader peak slightly shifted towards $z \sim 2.5-3$, as expected, since the employed galaxy statistics is the same. The metallicity dependence on redshift is similar to Figure 2.5, since they share the same prescription to assign metallicity (the FMR). In particular the redshift decrease is mild also in this case, with most of the star formation occurring at solar metallicities for $z \lesssim 2$ and at $Z \sim 0.4-0.5\,Z_\odot$ for $z \sim 4-5$. In case the SFRFs are used as a starting point, it is more difficult to disentangle the contribution of main sequence galaxies with respect to starbursts. On

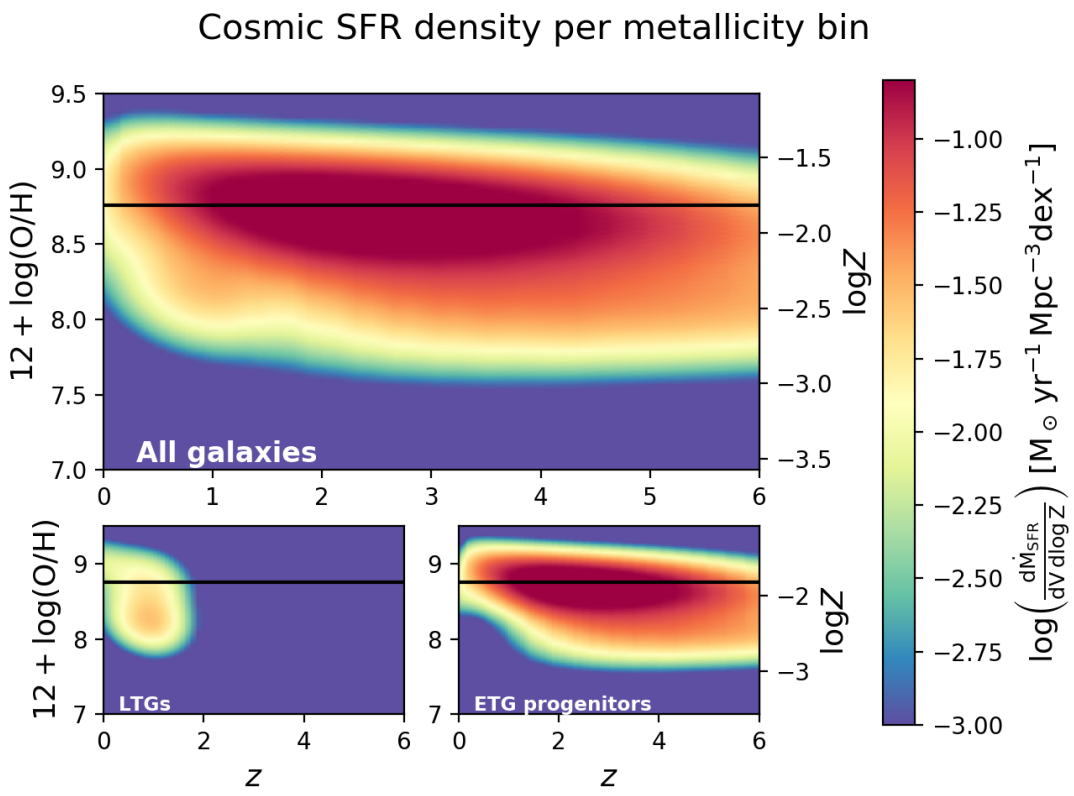

FIGURE 2.6: Top panel: The factor $\log(\mathrm{d}^2\dot{M}_{\rm SFR}/\mathrm{d}V/\mathrm{d}\log Z)$ computed convolving the SFRF with the FMR of Mannucci et al. 2011 (color coded) as a function of redshift on the x axis and gas-phase metallicity $12+\log(\mathrm{O/H})$ on the left y axis; on the right y axis it is plotted the logarithm of the metallicity $\log Z$ and the solar value is plotted as a black solid line. Bottom left panel: Contribution to the cosmic SFR density coming from LTGs. Bottom right panel: Contribution to the cosmic SFR density coming from ETG progenitors.

the other hand, it is easier to look at the contribution to the total SFR density given by LTGs and ETG progenitors, as explained in Section 2.1. These contributions are shown, respectively, in the bottom left and bottom right panels of Figure 2.6. It can be noticed that LTGs, having on average a lower stellar mass, tend to produce a tail of lower metallicity star formation even at low redshift. However, the bulk of the SFR density occurs at $z \gtrsim 1$ and it is given by ETG progenitors.

2.2.3 The galactic term computed through a MZR

In Subsection 2.2.2 I have computed the galactic term using a FMR which, as shown in the results, imply a shallow decrease of metallicity with redshift. Now I compute the same factor $\mathrm{d}^2\dot{M}_{\rm SFR}/\mathrm{d}V/\mathrm{d}Z$ using instead a sharply declining MZR (Mannucci et al. 2009), linearly extrapolated at $z > 3.5$ to see how much this choice will impact on the final results.

The factor $\mathrm{d}^2\dot{M}_{\rm SFR}/\mathrm{d}V/\mathrm{d}Z$ can be computed convolving the MZR with the stellar GSMF at a given redshift and using the distribution around the main sequence to assign a SFR to a galaxy with given stellar mass and redshift:

$$\frac{\mathrm{d}^2\dot{M}_{\rm SFR}}{\mathrm{d}V\,\mathrm{d}Z}(Z|z) = \int \mathrm{d}\log \mathrm{M}_\star \frac{\mathrm{d}^2\mathrm{N}}{\mathrm{dV}\,\mathrm{d}\log \mathrm{M}_\star}(\log \mathrm{M}_\star|\mathrm{z})\times \\ \times \left.\frac{\mathrm{d}p}{\mathrm{d}Z}\right|_{\rm MZR}(Z|Z_{\rm MZR}(z,M_\star)) \int \mathrm{d}\log\psi\,\psi\,\frac{\mathrm{dp}}{\mathrm{d}\log\psi}(\psi|\mathrm{z},\mathrm{M}_\star) \tag{2.14}$$

where $\mathrm{d}p/\mathrm{d}\log Z|_{\rm MZR}\,(Z|Z_{\rm MZR}\,(z,M_\star)) \propto \exp\left[-(\log Z - \log Z_{\rm MZR}(z,M_\star))^2/2\sigma^2_{\rm MZR}\right]$ is a log-normal distribution around the logarithmic value given by the MZR ($\log Z_{\rm MZR}$).

In Figure 2.7 I show the resulting $\mathrm{d}^2\dot{M}_{\rm SFR}/\mathrm{d}V/\mathrm{d}Z$ (color code) as a function of redshift and metallicity. As for the redshift dependence of the cosmic SFR, it reflects the shape presented in Figure 2.3 (solid lines) obtained using the GSMF as galaxy statistic, with a peak of star formation around $z \sim 2$. As for the metallicity dependence, at lower redshifts $z \lesssim 2$ the metallicity stays rather high, similarly to the FMR cases, with most of the star formation occurring at slightly supersolar values, while at higher z metallicity starts to decline rapidly, with most of the star formation occurring at $Z \leq 0.1\,Z_\odot$ at $z \gtrsim 4$, in contrast with the FMR cases in which the metallicity stays around $\sim 0.4\,\mathrm{Z}_\odot$, reaching values of $\sim 0.1\,Z_\odot$ only in the less massive systems. I stress that the differences between the two approaches are rather small at low redshifts $z \leq 2.5$ and start to be significant at higher redshifts, mainly in the regions where both the relations have been extrapolated. The main message here is that extrapolating the FMR, which is a redshift independent relation, can yield higher metallicity values with respect to a sharply declining MZR, more in agreement with the arguments discussed at the beginning of this Section.

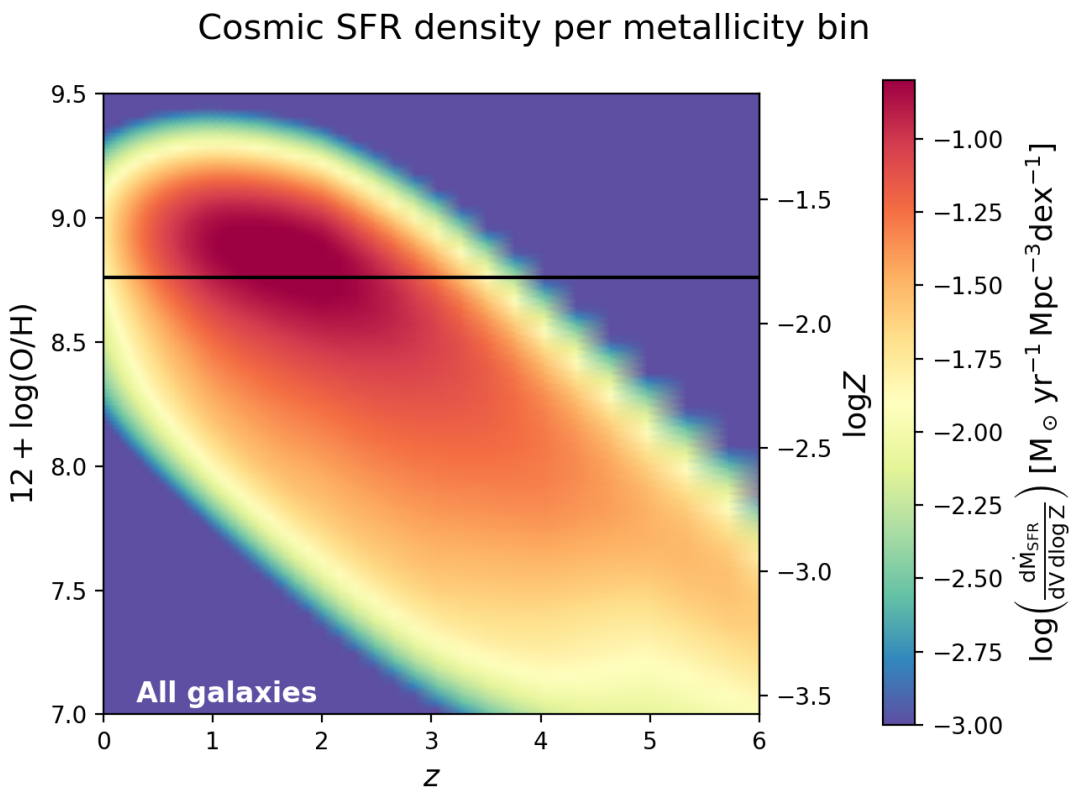

FIGURE 2.7: The factor $\log(\mathrm{d}^2\dot{M}_{\mathrm{SFR}}/\mathrm{d}V/\mathrm{d}\log Z)$ computed convolving the GSMF with the MZR of Mannucci et al. 2009 (color coded) as a function of redshift on the x axis and gas-phase metallicity $12+\log(\mathrm{O/H})$ on the left y axis; on the right y axis it is plotted the logarithm of the metallicity $\log Z$ and the solar value is plotted as a black solid line.

2.2.4 The galactic term computed through a chemical evolution model

In order to theoretically estimate metallicity I make use of the simple chemical evolution model presented in Section 1.3.4 under the instantaneous recycling approximation. In particular, the metallicity growth as a function of time can be determined using equation (1.56) and a model of galaxy evolution able to predict the evolution of stellar and gas mass as well as of the SFR.

The galaxy evolution model I adopt in this thesis is based on Pantoni et al. 2019 and Lapi et al. 2020. In these works authors consider galaxies as open, one-zone systems mainly constituted by 3 interlinked components: (1) infalling halo gas that is able to cool quickly, subject to condensation toward the central regions, and refurnished by outflows via wind recycling;

(2) cold star-forming gas fed by infall and depleted by star formation and stellar feedback; and (3) stellar mass, partially restituted to the cold phase by stellar evolution. Authors find analytic solutions for the evolution of the aforementioned quantities as a function of the halo mass and the formation redshift of the galaxy and are able to reproduce important observed scaling relations such as the main sequence or the gas fraction as a function of the stellar mass. Moreover they self-consistently derive an analytical evolution for the gas-phase and stellar metallicity. For an overview of the model, see Appendix A

Even though the full equation is complex, the general behaviour is such that at early times metallicity grows almost linearly up to a certain value $Z_{\rm sat}$ at which it saturates. Both the saturation value and the time spent on the linearly increasing phase are dependent on the galaxy features. In Boco et al. 2019, authors have found an expression to roughly approximate the metallicity behaviour and to express it as a function only of the galaxy SFR, considered approximately constant for the same considerations reported in Section 2.2.2. Such a metallicity evolution can be expressed as:

$$Z(\tau) \simeq \begin{cases} Z_{\rm sat}\, \frac{\tau}{\Delta\, \tau_\psi} & \frac{\tau}{\tau_\psi} \leq \Delta \\ \\ Z_{\rm sat} & \frac{\tau}{\tau_\psi} > \Delta \end{cases} \tag{2.15}$$

i.e., it increases from $Z = 0$ almost linearly with the galactic age, and then after a time $\tau = \Delta\, \tau_\psi$ it saturates to the value $Z_{\rm sat}$, with τ_ψ being the star formation timescale.

The saturation value $Z_{\rm sat}$ and the fraction of time spent in the linearly increasing phase Δ can be parametrized as a function of the SFR, of the stellar yields y_Z and of the recycling fraction $\mathcal{R}$ as:

$$Z_{\rm sat} \simeq \frac{y_Z\, (1-\mathcal{R})}{\gamma - 0.75\, \epsilon_{\rm out}} \tag{2.16}$$

$$\Delta \simeq \frac{3}{\gamma - 0.75\, \epsilon_{\rm out}} \tag{2.17}$$

for LTGs and as:

$$Z_{\rm sat} \simeq \frac{y_Z\, (1-\mathcal{R})}{\gamma} \tag{2.18}$$

$$\Delta \simeq \frac{1}{\gamma} \tag{2.19}$$

for ETG progenitors. The factor $\gamma \equiv 1 - \mathcal{R} + \epsilon_{\rm out}$ has been already defined

in Section 1.3.4 and $\epsilon_{\rm out} \simeq 2(\psi\,\tau_\psi/10^{10}\,M_\odot)^{-0.25}$ is the mass-loading factor of galactic outflows from stellar winds and SN explosions. Here I adopt the stellar yields and the recycling fraction from Romano et al. 2010 for a Chabrier IMF: $y_Z \simeq 0.06$ and $\mathcal{R} \simeq 0.44$. As a result, typical values $Z_{\rm sat} \sim 0.3 - 1.5\,Z_\odot$ are obtained for galaxies with final stellar masses in the range $M_\star \sim 10^9$–10^{11} M$_\odot$ respectively; the related quantity $\Delta \sim 0.2 - 0.5$ specifies how quickly the metallicity saturates to such values as a consequence of the interplay between cooling, dilution, and feedback processes. Note that several chemical evolution codes present in the literature, reproducing comparably well observations on the chemical abundances in galaxies of different stellar masses, also share a similar age-dependent metallicity behaviour.

A metallicity distribution can be derived from the metallicity evolution within individual galaxies expressed by equation (2.15), taking into account the fractional time spent by the galaxy in a given metallicity bin:

$$\frac{{\rm d}p}{{\rm d}Z}(Z|\psi,z) = \frac{\Delta}{Z_{\rm sat}}\,\Theta_{\rm H}(Z - Z_{\rm sat}) + (1-\Delta)\,\delta(Z - Z_{\rm sat}) \tag{2.20}$$

This expression is constituted by 2 terms: the first assigns equal probability to all the metallicities between 0 and $Z_{\rm sat}$, while the second is a Dirac delta centered on $Z_{\rm sat}$. The first term is weighted by the fractional time spent in the linearly increasing phase Δ and the second by its complementary $1 - \Delta$. Actually, I convolve the above distribution with a Gaussian-in-log kernel featuring a dispersion of 0.15 dex.

The galactic term can be computed as:

$$\frac{{\rm d}^2\dot{\rm M}_{\rm SFR}}{{\rm d}V\,{\rm d}Z}({\rm Z}|{\rm z}) = \int {\rm d}\log\psi\;\psi\;\frac{{\rm d}^2{\rm N}}{{\rm dV\,d}\log\psi}\;\frac{{\rm dp}}{{\rm dZ}}({\rm Z}|\psi,{\rm z}) \tag{2.21}$$

In Figure 2.8 I show the resulting ${\rm d}^2\dot{M}_{\rm SFR}/{\rm d}V/{\rm d}Z$ (color code) as a function of redshift and metallicity. Also in this case, as for the SFRF+FMR case, the redshift dependence of the SFR density reflects the shape of the cosmic SFR density derived by the integration of the SFRF (dot-dashed lines in Figure 2.3). The metallicity dependence on redshift is somewhat similar to the FMR cases, characterized by a mild redshift decrease, with most of the star formation occurring at solar metallicities for $z \lesssim 2$ and at $Z \sim 0.4$–$0.5\,Z_\odot$ for $z \sim 4$–5, even though with a pronounced tail toward low metallicities, representing young metal poor galaxies which have just started their star formation process. In the bottom panels are shown the contributions from LTGs (left) and ETG progenitors (right). It can be noticed that LTGs, having on average a slower stellar mass growth, tend to produce a tail of lower metallicity even at low redshift. However, the bulk of the SFR density occurs at $z \gtrsim 1$

and it is given by ETG progenitors.

The overall agreement between the model predictions and the FMR results is remarkable, since on the one hand it provides observational support for the model at $z \leq 3.5$ where there are solid determinations of the FMR, on the other hand it shows that an extrapolation of the FMR at $z \geq 3.5$ is in agreement with an ab initio model, suggesting that such a relation might be valid at all redshifts, at least to some extent.

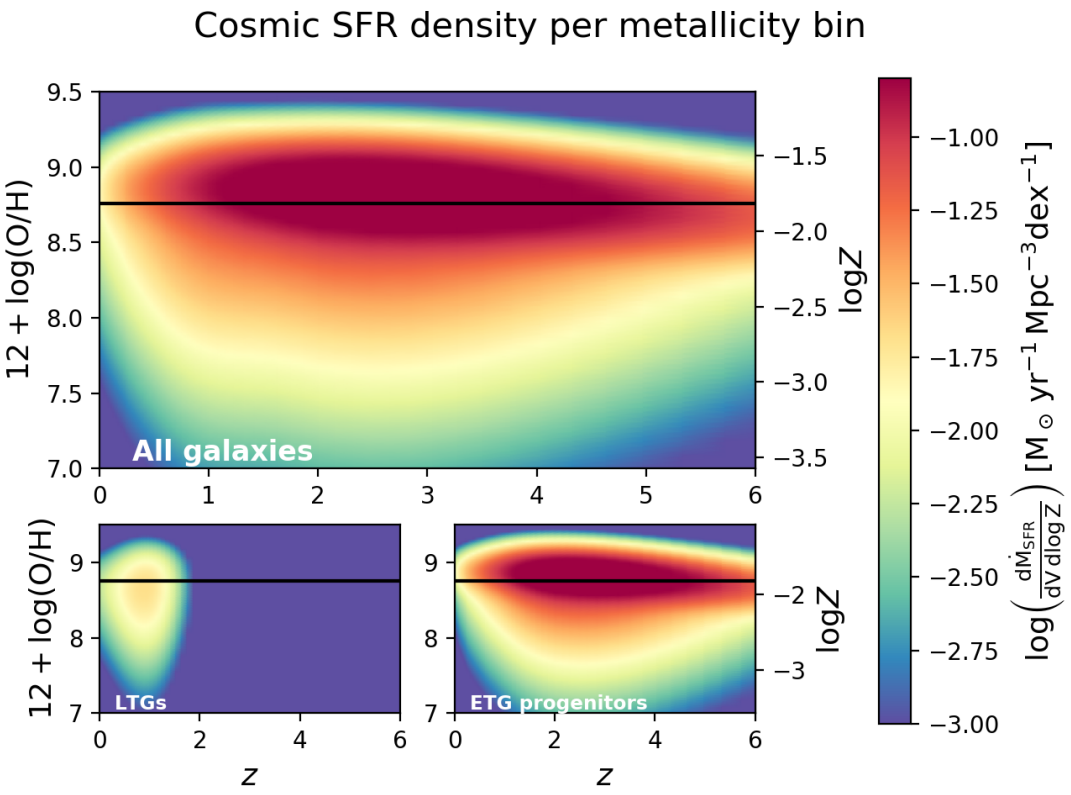

FIGURE 2.8: Top panel: The factor $\log(\mathrm{d}^2\dot{M}_{\rm SFR}/dV/d\log Z)$ computed convolving the SFRF with the metallicity computed through a chemical evolution model as a function of redshift on the x axis and gas-phase metallicity $12 + \log(\mathrm{O/H})$ on the left y axis; on the right y axis it is plotted the logarithm of the metallicity $\log Z$ and the solar value is plotted as a black solid line. Bottom left panel: Contribution to the cosmic SFR density coming from LTGs. Bottom right panel: Contribution to the cosmic SFR density coming from ETG progenitors.

Before proceeding to the estimation of the stellar term and the merging rates, I stress that the formalism to derive the galactic term developed in this Chapter is not only useful for merging rates computations, but also for the study of any other metallicity-dependent astrophysical process. For example, in Sicilia et al. 2021 in preparation, we are exploiting the galactic term

derived here to compute the stellar BH mass function over the whole cosmic history, see Section 4.2 and Appendix C for further details.

2.3 The stellar term

In Section 2.2 I have shown different ways to estimate the galactic term, i.e. the amount of star formation occurring at different redshifts and metallicities. The second important ingredient to control in order to compute the DCO merging rates, is the stellar term $\mathrm{d}^3N/\mathrm{d}M_{\rm SFR}/\mathrm{d}\mathcal{M}_{\bullet\bullet}/\mathrm{d}t_d$, representing the number of DCO systems with characteristics apt to allow merging of the companions within a Hubble time per unit of star formed mass per bin of chirp mass and time delay. Within the isolated binary evolution scenario leading to the formation of merging DCOs considered in this Chapter, the stellar term is commonly obtained from binary population synthesis simulations (e.g. Belczynski et al. 2016, Eldridge et al. 2017, Mapelli et al. 2017, Stevenson et al. 2017).

The outcome of those simulations (and therefore also the stellar term) depends on a number of assumptions made in order to describe the evolution of massive stars and binary interactions. Many of those are highly uncertain (e.g. common envelope evolution, core-collapse physics and the related natal kicks) and are known to strongly affect the properties of the simulated populations of merging DCO (e.g. Portegies Zwart & Yungelson 1998, Dominik et al. 2012, Chruslinska et al. 2018).

As already mentioned in Section 2.2, stellar evolution depends on metallicity, which affects, for instance, stellar winds and radii, also impacting the nature and outcome of binary interactions (e.g. Maeder 1992; Hurley et al. 2000; Vink et al. 2001; Belczynski et al. 2010b). Therefore metallicity have an impact both on the final masses and on the survival of the DCO system. The effect on the remnant masses can be seen in Figure 2.9, which is a realization of the binary evolution code `SEVN`, presented in Spera et al. 2019. In the Figure the relation $m_{\rm ZAMS} - m_{\bullet}$ between the ZAMS mass and the remnant mass is shown for both the objects in DCOs (left column), for primaries (middle column) and secondaries (right column) at different metallicities: $Z = 0.02$ (top row), $Z = 0.006$ (middle row), $Z = 0.0001$ (bottom row). Comparing the different rows of the Figure it is evident that stars in metal poor environments tend to form larger mass compact remnants.

The effect of metallicity on DCO merging efficiency is instead shown in Figure 2.10 displaying the number of DCOs able to merge in an Hubble time per unit star formed mass as a function of metallicity for different DCO types. While for NS-NS the dependence on metallicity is weak, featuring a slow rise,

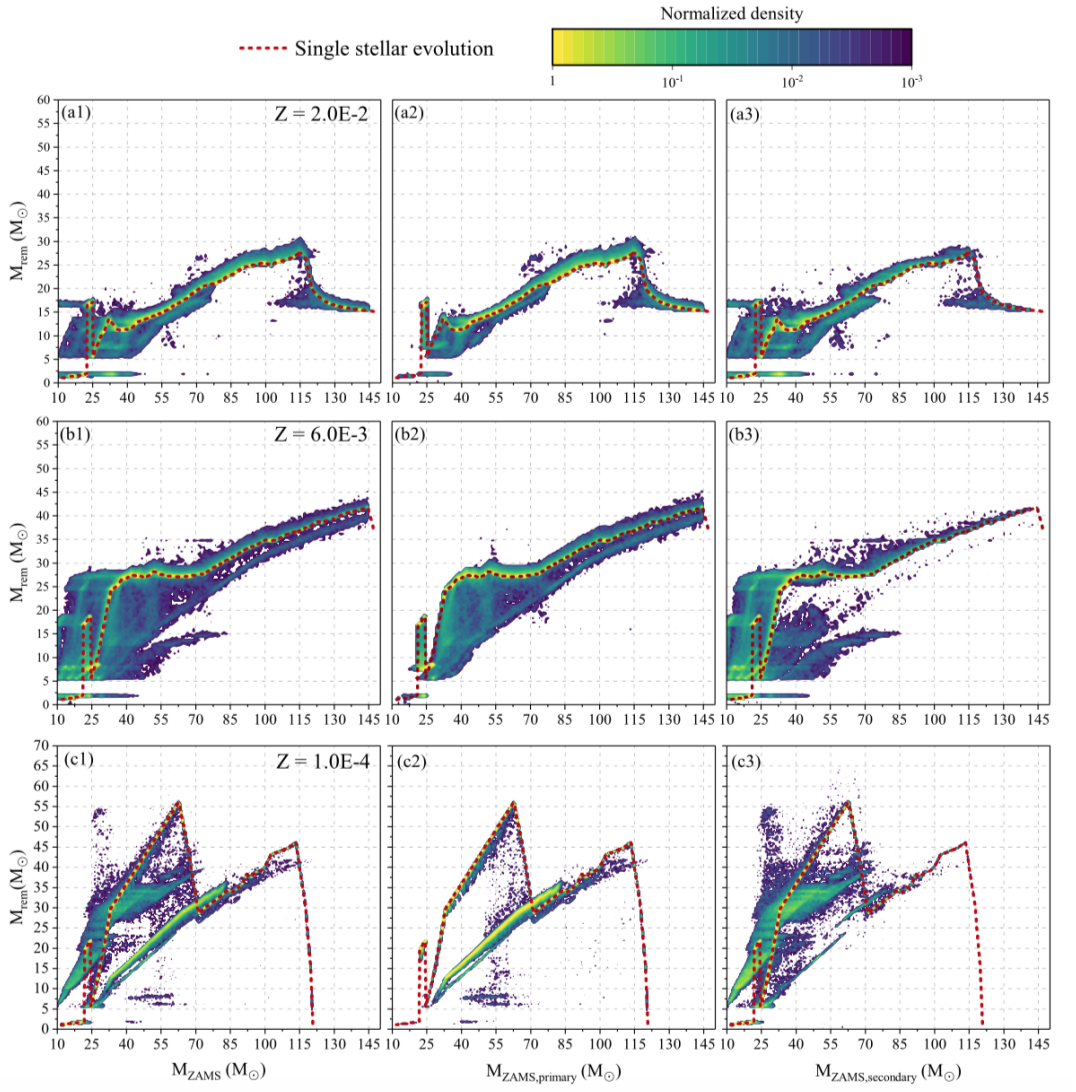

FIGURE 2.9: Example of the distribution of $m_\bullet$ as a function of $m_{\rm ZAMS}$ and metallicity: $Z = 0.02$ top row, $Z = 0.006$ middle row, $Z = 0.0001$ bottom row. Left column: all binary COs, middle column: primaries, right column: secondaries. Credits: Spera et al. 2019.

the BH-BH merging efficiency is typically found to show a strong low metallicity preference (e.g. Belczynski et al. 2010a; Dominik et al. 2012; Eldridge & Stanway 2016; Stevenson et al. 2017; Klencki et al. 2018; Giacobbo et al. 2018; Spera et al. 2019) with an approximately constant behaviour only up to $Z \lesssim 0.002$, followed by a rather sharp drop of ~ 2 order of magnitudes at higher metallicities. For BH-NS the efficiency decrease is instead of just ~ 1 order of magnitude.

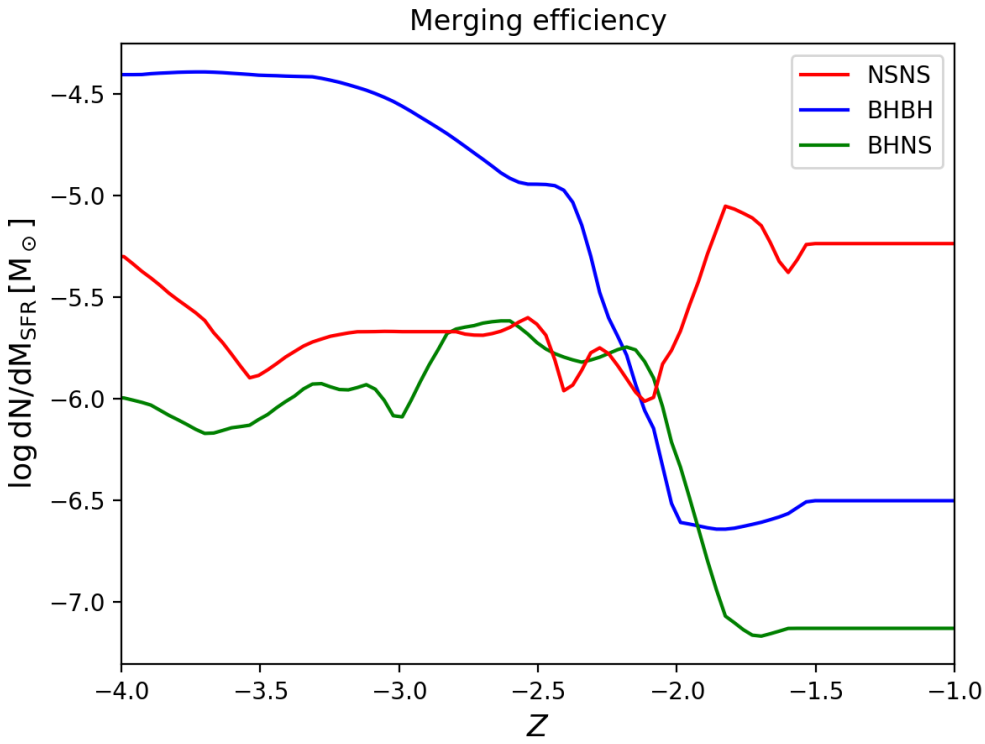

FIGURE 2.10: Example of merging efficiency as a function of metallicity. Adaptation from Chruslinska et al. 2019.

I caveat that Figures 2.9 and 2.10 are meant just to represent some general features of stellar and binary evolution as a function of metallicity, but the details, such as the exact $m_{\rm ZAMS} - m_{\bullet}$ relation and the drop at high metallicities in the merger efficiency are largely dependent on the population synthesis code adopted and on the parameter choice for the simulation. Still, the crucial role of metallicity on the outcomes is unquestionable.

In the computation of the stellar term, I make the simplifying assumption of splitting the overall stellar term in 3 independent distributions:

$$\frac{\mathrm{d}^3 N}{\mathrm{d}M_{\rm SFR}\,\mathrm{d}\mathcal{M}_{\bullet\bullet}\,\mathrm{d}t_d}(Z) = \frac{\mathrm{d}N}{\mathrm{d}M_{\rm SFR}}(Z) \times \frac{\mathrm{d}p}{\mathrm{d}\mathcal{M}_{\bullet\bullet}}(Z) \times \frac{\mathrm{d}p}{\mathrm{d}t_d} \tag{2.22}$$

where $\mathrm{d}N/\mathrm{d}M_{\rm SFR}$ is the number of DCO merging in an Hubble time per unit mass formed in stars at metallicity Z (merging efficiency, shown in Figure 2.10), $\mathrm{d}p/\mathrm{d}\mathcal{M}_{\bullet\bullet}$ is the metallicity dependent chirp mass distribution and $\mathrm{d}p/\mathrm{d}t_d$ is the distribution of delay times between the formation of the progenitor binary and the DCO merger.

The delay time distribution resulting from binary population synthesis is commonly found to be well described with a simple inverse proportionality $\mathrm{d}p/\mathrm{d}t_d \propto t_d^{-1}$, almost independent of the DCO type or metallicity. I assume $\mathrm{d}p/\mathrm{d}t_d \propto t_d^{-1}$ with the minimum $t_{d,\mathrm{min}} = 50$ Myr. The distribution is normalized to unity between $t_{d,\mathrm{min}}$ and the age of the Universe. It is important to notice that, as for the remaining terms, even the time delay distribution could be retrieved from population synthesis simulations and be dependent on the choice of stellar and binary evolution parameters entering in the simulation as well as on the properties of the binary itself, such as the mass of the stars, or of the environment, such as metallicity. In particular, in Giacobbo & Mapelli 2018 and Mapelli et al. 2019, it is found that the simulation results are well fitted with a $\propto t_d^{-1}$ distribution for $t_d \gtrsim 500$ Myr, but slight deviations from such a distribution are required at smaller delay times. These deviations are strongly dependent on parameters such as the common envelope ejection efficiency or the strength of SN natal kicks (Giacobbo & Mapelli 2018) or on the mass of the binary components (Mapelli et al. 2019). In the present treatment, to ease the computation, I simply use the t_d^{-1} distribution, but I caveat that those deviations might clearly affect the merger rates: for example a behaviour flatter than t_d^{-1} would enhance the the overall amount of mergers, while a steeper t_d distribution would reduce the merger rates.

I base the remaining two factors on the results of population synthesis calculations, using the model 'reference B' from Chruslinska et al. 2018 [1]. The factor $\mathrm{d}N/\mathrm{d}M_{\mathrm{SFR}}$ as a function of metallicity for the chosen evolutionary model is shown in Figure 2.10 (see also Figure 1 in Chruslinska et al. 2019, thin lines). Metallicity dependence of the chirp mass distribution is to large extent a consequence of the metallicity dependence of the maximum mass of the stellar remnant resulting from single stellar evolution. As a result, a population of DCO containing a higher fraction of objects originating from low metallicity progenitors will result in a chirp mass distribution with a more extended high mass tail (e.g. Figure 4 in Chruslinska et al. 2019).

I caveat that this choice is taken just as an example. The exact results concerning the populations of merging DCO presented in Section 2.4 would generally be affected by the choice of the population synthesis model (e.g. Chruslinska et al. 2019). However, the main focus of this Chapter is on the galactic term and a more in-depth discussion of the uncertainties related to stellar and binary evolution is beyond the scope of this thesis. Therefore this choice has to be intended just as a reference model useful to proceed with the computation of the merging rates and to highlight the effects of different

[1] I use the simulation data publicly available under this url: https://www.syntheticuniverse.org/

galactic terms at fixed stellar term, but not as a precise presentation of the DCO population.

2.4 Merging rates computation

The DCO merging rates as a function of redshift are computed as in equation (2.1) for the three types of merging binaries: BH-BH, NS-NS and BH-NS. I use the stellar term described in Section 2.3 and the 4 different galactic terms computed in Section 2.2. To simplify the notation I name the 4 galactic terms as GSMF+FMR, SFRF+FMR, GSMF+MZR and MODEL. Figures 2.11, 2.12, 2.13 and 2.14 show, respectively, the results.

In the top panels are plotted the merging rates redshift distributions, highlighting the contribution of starburst galaxies in the GSMF+FMR case and the contribution of LTGs in the cases adopting the SFRF. The local ($z \sim 0$) merging rates determinations by LIGO/Virgo for BH-BH (15.3 – 38.8 $\mathrm{Gpc^{-3}\,yr^{-1}}$), NS-NS (80 – 810 $\mathrm{Gpc^{-3}\,yr^{-1}}$) and BH-NS ($\leq$ 610 $\mathrm{Gpc^{-3}\,yr^{-1}}$) are also reported (see Abbot et al. 2021b). The NS-NS merging rates fall inside the LIGO/Virgo interval for all the cases considered, while the BH-BH merging rates are above the LIGO/Virgo interval for the GSMF+FMR, GSMF+MZR and MODEL cases, while they fall inside for the SFRF+FMR case[2]. Comparing the top panels of Figure 2.11 and 2.13, referring to the GSMF+FMR and GSMF+MZR cases, which use the same galaxy statistics as a starting point (GSMF) and differ only in the metallicity prescriptions, it can be noticed that the merging rates of NS-NS and BH-NS are similar, since they are less dependent on metallicity. On the other hand, the BH-BH merging rates, which are strongly dependent on metallicity, are substantially different: at low redshift ($z < 1.5$) they are similar due to the comparable behaviour of the metallicity distribution, while at high redshift ($z \geq 1.5$) they are larger for the MZR case (by a maximum factor of ~ 10) due to the strong decrease of metallicity at high redshift in the MZR case (see Figures 2.5 and 2.7), favoring a large merging effciency. As for the SFRF+FMR case (Figure 2.12) the BH-BH merging rates lies in between. In fact, even if the metallicity, assigned through the FMR, stays rather high suppressing BH-BH mergers, this fact is partially compensated by the higher cosmic SFR density at high redshift obtained when the SFRF are employed as galaxy statistics (see Figure 2.3). This is also reflected on the larger merging rates for NS-NS and

[2] I stress again that the agreement/disagreement with the LIGO/Virgo determinations can be due to the modelization of the stellar term. Moreover this is only one of the many constraint that a galactic or stellar model should be able to satisfy. So, the local rate alone does not represent a proof of the goodness of a model with respect to the others.

BH-NS in the SFRF+FMR case. On the other hand, for the MODEL case the BH-BH merging rates are a factor ~ 2 larger than the other cases at $z < 1$ due to the long tail at low metallicity of young star-forming galaxies. In this case the merging rates reach a peak at $z \sim 1-2$ and they sharply decrease at higher redshift due to the very shallow evolution of metallicity at high-z.

The bottom panels of Figures 2.11, 2.12 , 2.13 and 2.14 are also rather informative. They show the redshift and chirp mass distribution of the BH-BH merging rates. In the GSMF+MZR case (Figure 2.13) the chirp mass distribution extends up to $\mathcal{M}_{\bullet\bullet} \gtrsim 30\,\mathrm{M}_\odot$ at high redshift ($z \geq 2$) where the metallicity tends to drop at subsolar values. This high chirp mass tail is reduced for the cases in which the FMR is used (Figure 2.11 and 2.12), since metallicity never drops too much, even at high redshifts, producing remnants with lower masses on average. In the MODEL case, instead, it is present a long tail toward high chirp massses $\mathcal{M}_{\bullet\bullet} \gtrsim 30\,\mathrm{M}_\odot$ even at low redshift, originated by the low metallicity tail of Figure 2.8.

Notice that none of the four cases analyzed is able to reproduce the high chirp mass events ($\mathcal{M}_{\bullet\bullet} \gtrsim 30\,\mathrm{M}_\odot$) recently observed at $z < 1$ by the LIGO/Virgo collaboration (see Abbott et al. 2021a, 2021b). This is not an issue, since even the chirp mass distribution, as well as the total rates of DCOs mergers, is strongly dependent on the selected model of stellar and binary evolution, whose discussion is out of the scope of the current thesis. The comparisons shown here are useful just to understand the general trend of DCOs mergers for different galactic prescriptions, but are not meant to reproduce the real chirp mass distribution. However, I stress that, in the four cases shown here, events with $\mathcal{M}_{\bullet\bullet} \gtrsim 30\,\mathrm{M}_\odot$ are still produced, simply their rate is much less than the rate of $\mathcal{M}_{\bullet\bullet} < 30\,\mathrm{M}_\odot$ events. A GW detector as AdvLIGO/Virgo would mainly detect high chirp mass events since they produce stronger GW signals, so that the chirp mass distribution of detected DCOs may substantially be altered by selection effects. In addition, other channels of GW emission should not be excluded: dynamical formation and merger of compact object binaries (e.g. Di Carlo et al. 2019, 2020; Rodriguez et al. 2015, 2021; Antonini & Rasio 2016; Kumamoto et al. 2019; Arca-Sedda et al. 2020; Boco et al. 2020, 2021; Banerjee 2021; Mapelli et al. 2021a, 2021b) as well as primordial black holes mergers (e.g. Scelfo et al. 2018; Franciolini et al. 2021) could somewhat contribute to the GW detections and change the detected chirp mass distribution.

In the small plots on the bottom right of Figures 2.11, 2.12 and 2.14 it is shown the contribution of main sequence galaxies and starbursts, for the GSMF+FMR case (Figure 2.11), and the contribution of LTGs, ETGs and their star-forming progenitors, for the SFRF+FMR and MODEL cases (Figures 2.12

and 2.14). Between main sequence galaxies and starbursts, no evident difference can be found, it is clear just that main sequence galaxies are the main contributors to the BH-BH merging rates. This is clearly dependent on the way I have chosen to model starbursts: I have fixed their fraction to be $\sim$ 3% for all the stellar masses at all redshifts; it would be interesting to see how this would change treating the starburst fraction in a more detailed way (Chruslinska et al. 2021). Instead, the contribution of LTGs and ETGs is substantially different: LTGs contribute to the merging rates only at low redshift ($z \leq 2$) while only ETG progenitors are present at higher redshifts. At $z \leq 2$ the relatively longer tail towards larger chirp masses of LTGs can be explained by the fact that they have, on average, lower metallicities (see Figure 2.6 and 2.8).

2.4.1 Chirp mass and time delay

The differential merging rates as a function of chirp mass and time delay explicits how the time delays and chirp masses are distributed for the merging events. They can be very helpful even for host galaxy association, since, given the chirp mass of the signal, they give information on the average age of the stellar population producing the merger.

They can be computed as:

$$\frac{\mathrm{d}^3\dot{N}}{\mathrm{d}V\,\mathrm{d}\mathcal{M}_{\bullet\bullet}\,\mathrm{d}t_d}(t,\mathcal{M}_{\bullet\bullet},t_d) = \int \mathrm{d}Z \frac{\mathrm{d}^3 N}{\mathrm{d}M_{\mathrm{SFR}}\,\mathrm{d}\mathcal{M}_{\bullet\bullet}\,\mathrm{d}t_d}(Z)\frac{\mathrm{d}^2\dot{M}_{\mathrm{SFR}}}{\mathrm{d}V\,\mathrm{d}Z}(t-t_d) \quad (2.23)$$

I present results only for BH-BH mergers at $z \sim 0$, but in principle this treatment could be applied to all kind of sources at all redshifts. The results are shown in Figures 2.15, 2.16, 2.17 and 2.18 for the four different ways to compute the galactic term.

The top panels illustrate the merging rates per units of time delay $\mathrm{d}^2\dot{N}/\mathrm{d}V/\mathrm{d}t_d$, meaning that equation (2.23) has been integrated over the chirp mass. In the GSMF+FMR case I show the contribution of starburst galaxies, while in the SFRF+FMR and MODEL cases I show the contribution of LTGs. In all the Figures it is clearly visible a double peak distribution: the peak at low delay times is due to the shape of the intrinsic t_d distribution $\mathrm{d}p/\mathrm{d}t_d \propto t_d^{-1}$ favoring short time delays, while the peak at $t_d \sim 10-12$ Gyr is due to the huge amount of star formation happening at redshift $z \sim 2-3$ that compensates for the intrinsic time delay distribution: a small fraction of the many objects formed at $z \sim 2-3$ can be seen through GW emission at $z \sim 0$.

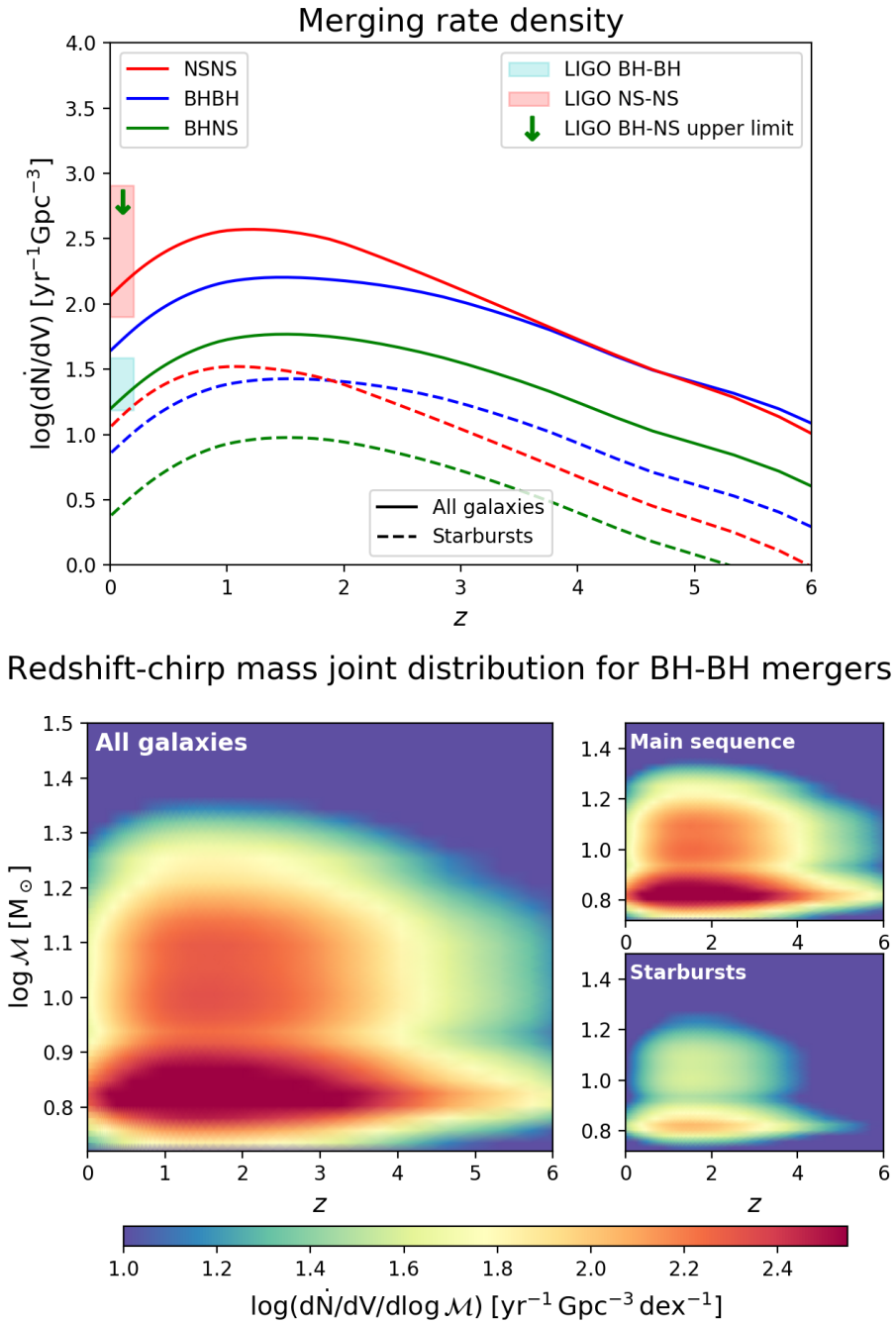

FIGURE 2.11: Top panel: merging rate density of double compact objects binaries as a function of redshift, computed using the GSMF as galaxy statistics and the FMR, following equation (2.9). Blue lines refers to BH-BH, red lines to NS-NS, green lines to BH-NS events. Solid lines represents mergers happening in all the galaxies (main sequence and starbursts), while the dashed lines highlight the contribution of starbursts. The red and blue patches and the green arrow at $z \sim 0$ represents the LIGO/Virgo 90% confidence intervals on the local rates for NS-NS and BH-BH and the upper limit for BH-NS after the O1, O2 and first half of O3 runs (Abbott et al. 2021b). Bottom panels: differential merging rates $\log(\mathrm{d}^2\dot{N}/dV/d\log\mathcal{M}_{\bullet\bullet})$ for the BH-BH case (color code) as a function of redshift and chirp mass. Contribution coming from all the galaxies (left panel), from main sequence galaxies (top right panel) and starbursts (bottom right panel).

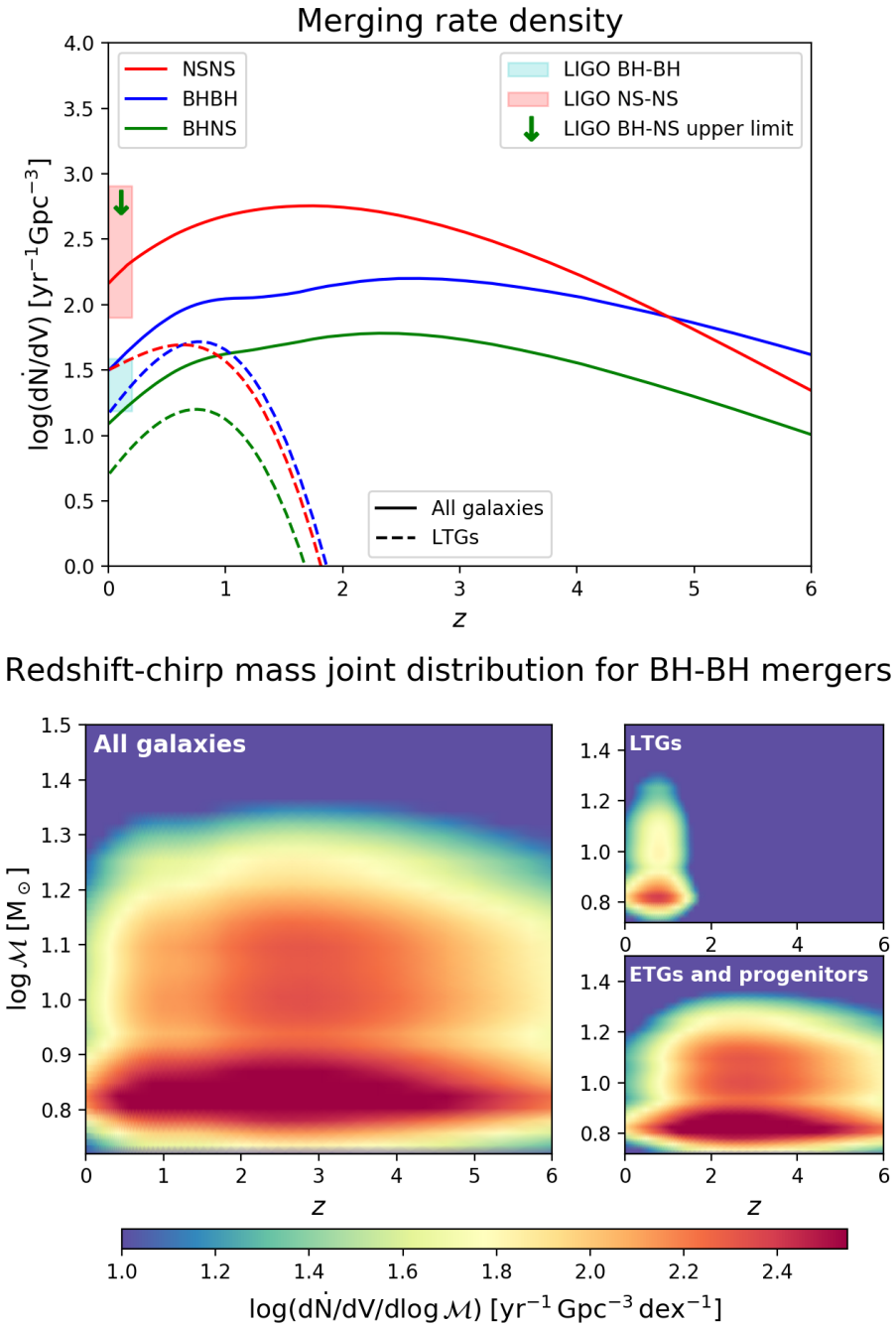

FIGURE 2.12: Top panel: same as Figure 2.11 but for the SFRF+FMR case. Bottom panels: differential merging rates $\log\left(\mathrm{d}^2\dot{N}/dV/d\log\mathcal{M}_{\bullet\bullet}\right)$ for the BH-BH case (color code) as a function of redshift and chirp mass. Contribution coming from all the galaxies (left panel), from LTGs (top right panel) and ETGs and their progenitors (bottom right panel).

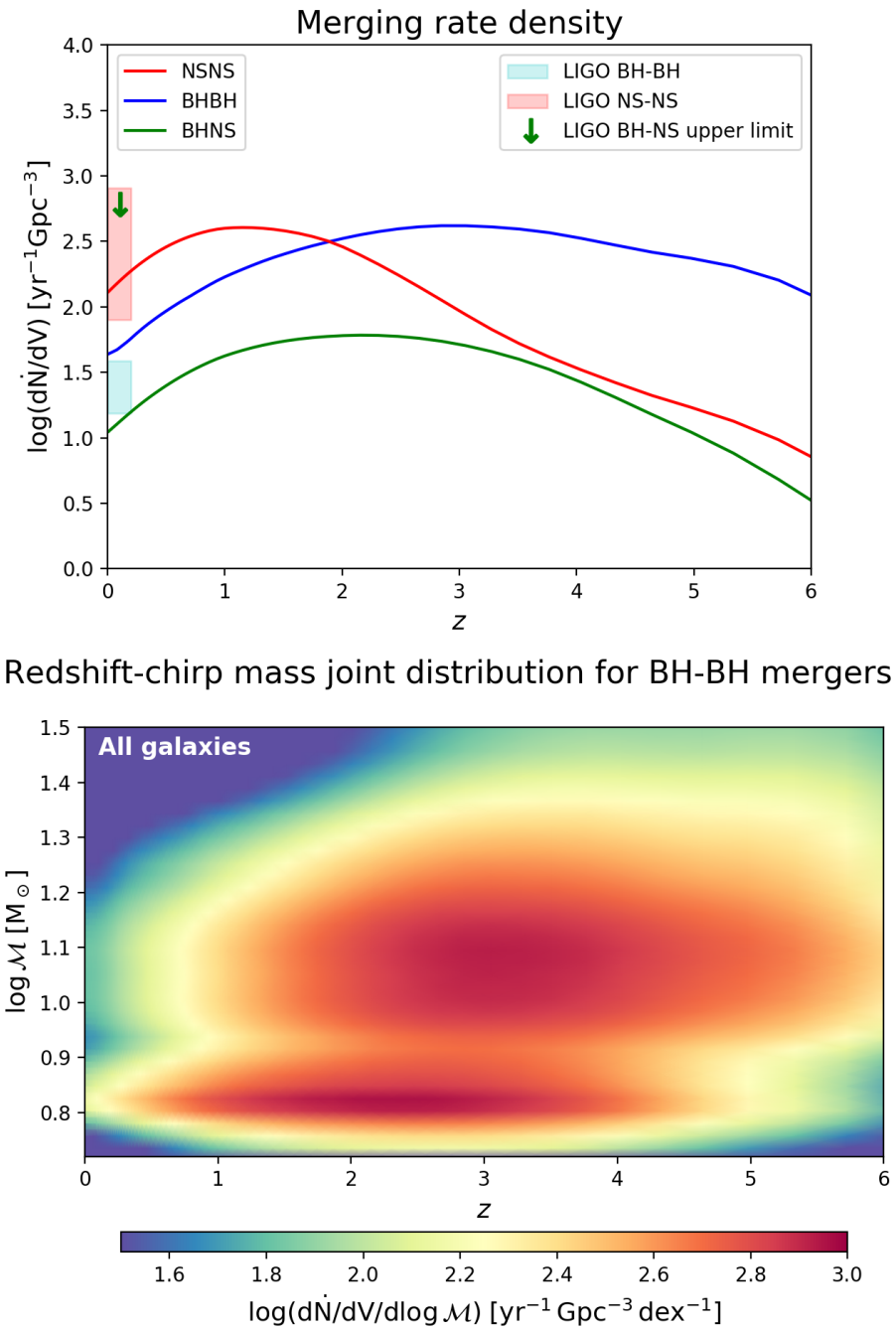

FIGURE 2.13: Top panel: same as Figure 2.11 but for the GSMF+MZR case. Bottom panel: differential merging rate $\log\left(\mathrm{d}^2\dot{N}/dV/d\log\mathcal{M}_{\bullet\bullet}\right)$ for the BH-BH case (color code) as a function of redshift and chirp mass. Notice the change in the color code scale due to the larger number of BH-BH mergers occurring in this case.

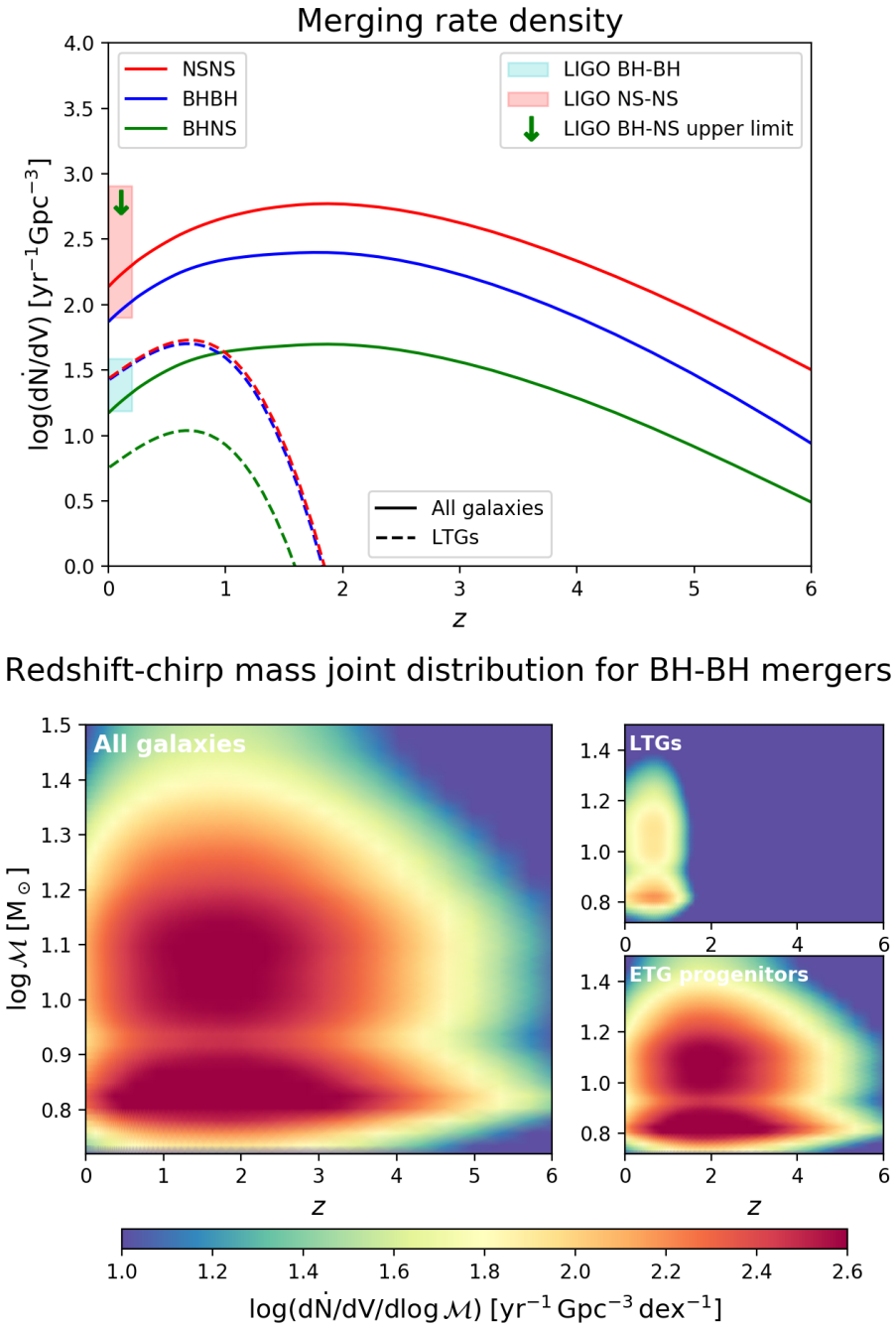

FIGURE 2.14: Top panel: same as Figure 2.11 but for the MODEL case. Bottom panels: differential merging rates $\log(\mathrm{d}^2\dot{N}/dV/d\log\mathcal{M}_{\bullet\bullet})$ for the BH-BH case (color code) as a function of redshift and chirp mass. Contribution coming from all the galaxies (left panel), from LTGs (top right panel) and ETGs and their progenitors (bottom right panel).

Apart from this shape shared by all the four cases, there are some differences among them that I explain in the following. In the cases where the GSMF is used as statistics (Figures 2.15 and 2.17) the NS-NS time delay distribution is similar since NS-NS mergers are almost independent on metallicity. The BH-BH time delay distribution is instead rather different: while for the GSMF+FMR case (Figure 2.15) the time delay distribution is flatter, with $\sim$ 50% of the BH-BH merging with $t_d \leq 6$ Gyr, for the GSMF+MZR case the second peak is more pronounced, with only $\sim$ 20% of BH-BH merging with $t_{\rm d} \leq 6$ Gyr and many events with $t_{\rm d} \geq 9-10$ Gyr. This is due to the fact that, as already seen, in the MZR case the metallicity is much lower at high redshift, increasing the contribution to the $z \sim 0$ merging events from BHs formed at high redshift. For the BH-NS mergers the same effect, even if milder, can be seen. The starbursts contribution, shown only in the GSMF+FMR case, is subdominant. Comparing the NS-NS and BH-BH mergers in starbursts it can be noticed a slight difference with respect to the all galaxies case. In fact, while the NS-NS contribution is always larger than the BH-BH one in the all galaxies case, restricting to starbursts the two contribution are roughly comparable, with BH-BH events being even dominant with respect to NS-NS for $t_d > 11$ Gyr; this is due to the average lower metallicities of starbursts that slightly enhances the occurrence of BH-BH mergers.

In the SFRF+FMR case (Figure 2.16) NS-NS have a similar shape to the other cases for $t_d \leq 9-10$ Gyr, while there is an enhancement at larger time delays, due to the higher cosmic SFR at $z \geq 2$. The contribution of LTGs to the NS-NS merging rates follows the relative abundance of LTGs with respect to ETGs with the cosmic time. For the BH-BH mergers the shape is in between the GSMF+FMR and GSMF+MZR case: it can be seen a decrease at $1 \leq {\rm t_d} \leq 6$ Gyr and a moderate enhancement at $t_d \geq 10$ Gyr, with a resulting $\sim$ 37% of the BH-BH mergers having $t_d < 6$ Gyr. The behaviour at small time delays can be explained by the rather high metallicity at low redshift, and the enhancement at large time delays is due to the larger amount of cosmic SFR, even if the metallicity remains pretty high. The contribution at low time delays comes almost exclusively from LTGs, which are less metallic, as seen in Figure 2.6, while events with large time delays come from ETGs that formed stars at higher redshifts, producing the second peak at $t_d > 10$ Gyr. In the MODEL case, instead, the NS-NS time delay distribution is similar to the SFRF+FMR case since the galaxy statistics used (SFRF) is the same and the NS-NS merger efficiency is weakly dependent on metallicity. The BH-BH time delay distribution is instead more similar to the GSMF+FMR case with $\sim$ 50% of events $z \sim 0$ mergers having $t_d < 6$ Gyr. Again, this is due to the fact that the metal rich star formation is present even at high redshift, as in the FMR case.

The bottom panels show also the dependence on the chirp mass. It can be seen that in the GSMF+MZR case high chirp mass events tend to have long time delays, while the distribution for the GSMF+FMR case is smoother. This means that in the GSMF+MZR case the GW events at $z \sim 0$ with $\mathcal{M}_{\bullet\bullet} \geq 20\,M_{\odot}$ can be clearly linked to long delay times ($\gtrsim 10$ Gyr) and so to an older stellar population, while in the GSMF+FMR case the association between chirp mass and time delay is much less clear. The SFRF+FMR case lies in between, while the MODEL case is more similar to the GSMF+FMR case. In the bottom right small panels of Figure 2.15 it is shown the contribution of main sequence galaxies and starbursts, while in the bottom right small panels of Figures 2.16 and 2.18 the contribution of LTGs and ETGs. Between main sequence and starburst galaxies differences are not so evident, due to my treatment of the starburst population, while between LTGs and ETGs the difference is marked, especially in the SFRF+FMR case: as already seen ETGs clearly contribute mostly to events with large time delays ($t_d > 9$ Gyr) and LTGs to the events with $t_d < 9$ Gyr. High chirp mass events can come from both the populations.

2.5 Detection rates and GW lensing

In this Section I turn to computing and discussing the GW detection rates from merging binaries, selecting as a case study only the merging rates forecast from the MODEL case.

Since the Chapter is focused on DCO mergers, I consider ground based detectors such as AdvLIGO/Virgo at its design sensitivity and ET, adopting the formalism to compute the detection rates by Taylor & Gair 2012 (see references therein and discussions in Boco et al. 2019, 2020). Such a formalism, even if very handy, is not up to date and in future works it will be updated in light of more recent software developed for AdvLIGO/Virgo and ET.

The GW events rates per unit redshift, chirp mass $\mathcal{M}_{\bullet\bullet}$, and signal-to-noise ratio (S/N) ρ can be computed as:

$$\frac{\mathrm{d}^3\dot{N}}{\mathrm{d}\mathcal{M}_{\bullet\bullet}\,\mathrm{d}\rho\,\mathrm{d}z} = \frac{1}{1+z}\frac{\mathrm{d}V}{\mathrm{d}z}\frac{\mathrm{d}^2\dot{N}}{\mathrm{d}\mathcal{M}_{\bullet\bullet}\,\mathrm{d}V}\frac{\mathrm{d}p}{\mathrm{d}\rho}(\rho|\mathcal{M}_{\bullet\bullet}, z) \tag{2.24}$$

where $\mathrm{d}^2\dot{N}/\mathrm{d}\mathcal{M}_{\bullet\bullet}/\mathrm{d}V$ is the merging rate per unit chirp mass, $\mathrm{d}V/\mathrm{d}z$ the differential comoving cosmological volume, the factor $1/(1+z)$ takes into account the cosmological time dilation and $\mathrm{d}p/\mathrm{d}\rho$ is the distribution of S/N at given chirp mass and redshift.

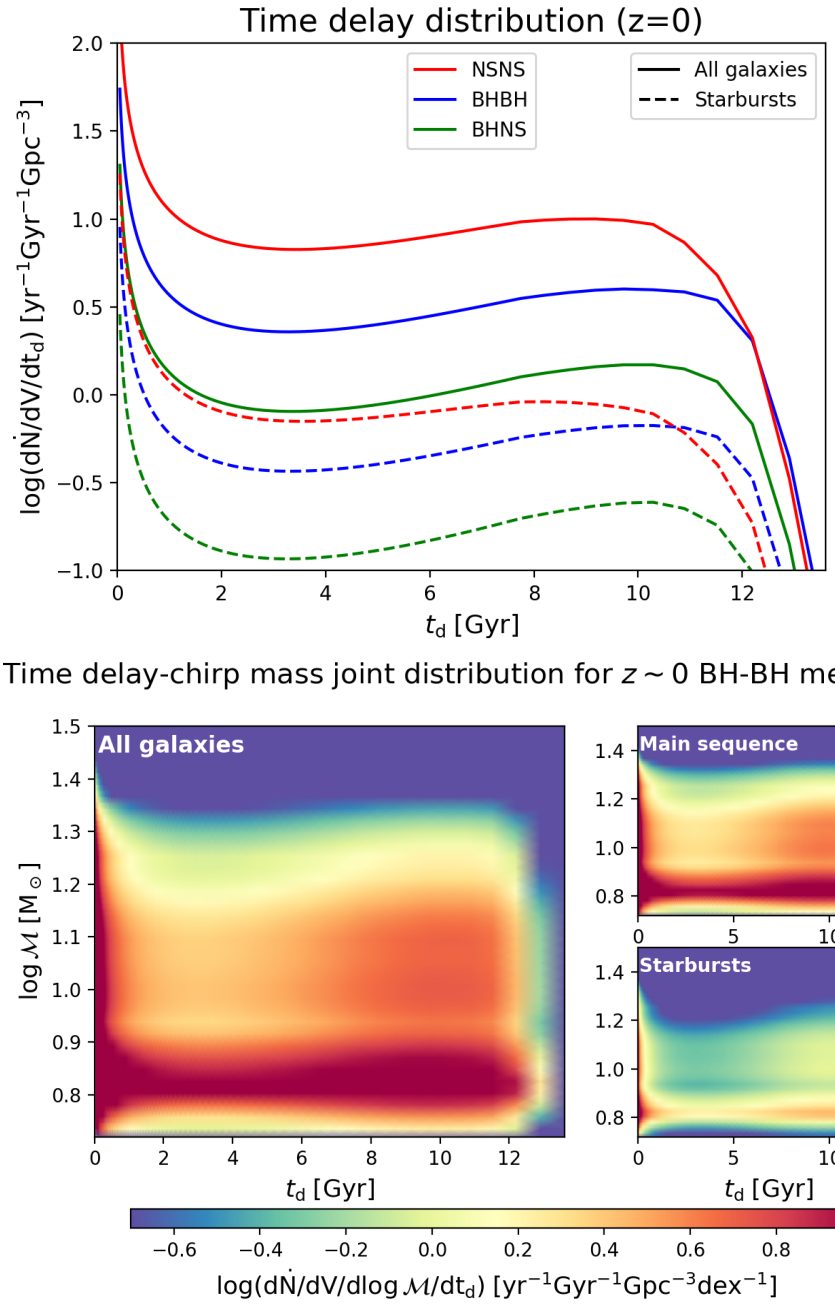

FIGURE 2.15: Top panel: differential merging rate $\log(\mathrm{d}^2\dot{N}/\mathrm{d}V/\mathrm{d}t_d)$ at $z \sim 0$ for BH-BH as a function of the time delay between the formation of the binary and the merger, computed using the GSMF as galaxy statistics and the FMR, following equation (2.9). Bottom panels: differential merging rates $\log(\mathrm{d}^3\dot{N}/\mathrm{d}V/\mathrm{d}\log\mathcal{M}_{\bullet\bullet}/\mathrm{d}t_d)$ at $z \sim 0$ for BH-BH as a function of the chirp mass and time delay. On the x axis there is the time delay, on the y axis the chirp mass and the color code represents the logarithmic number density of merging events. Contribution coming from all the galaxies (left panel), from main sequence galaxies (top right panel) and starbursts (bottom right panel).

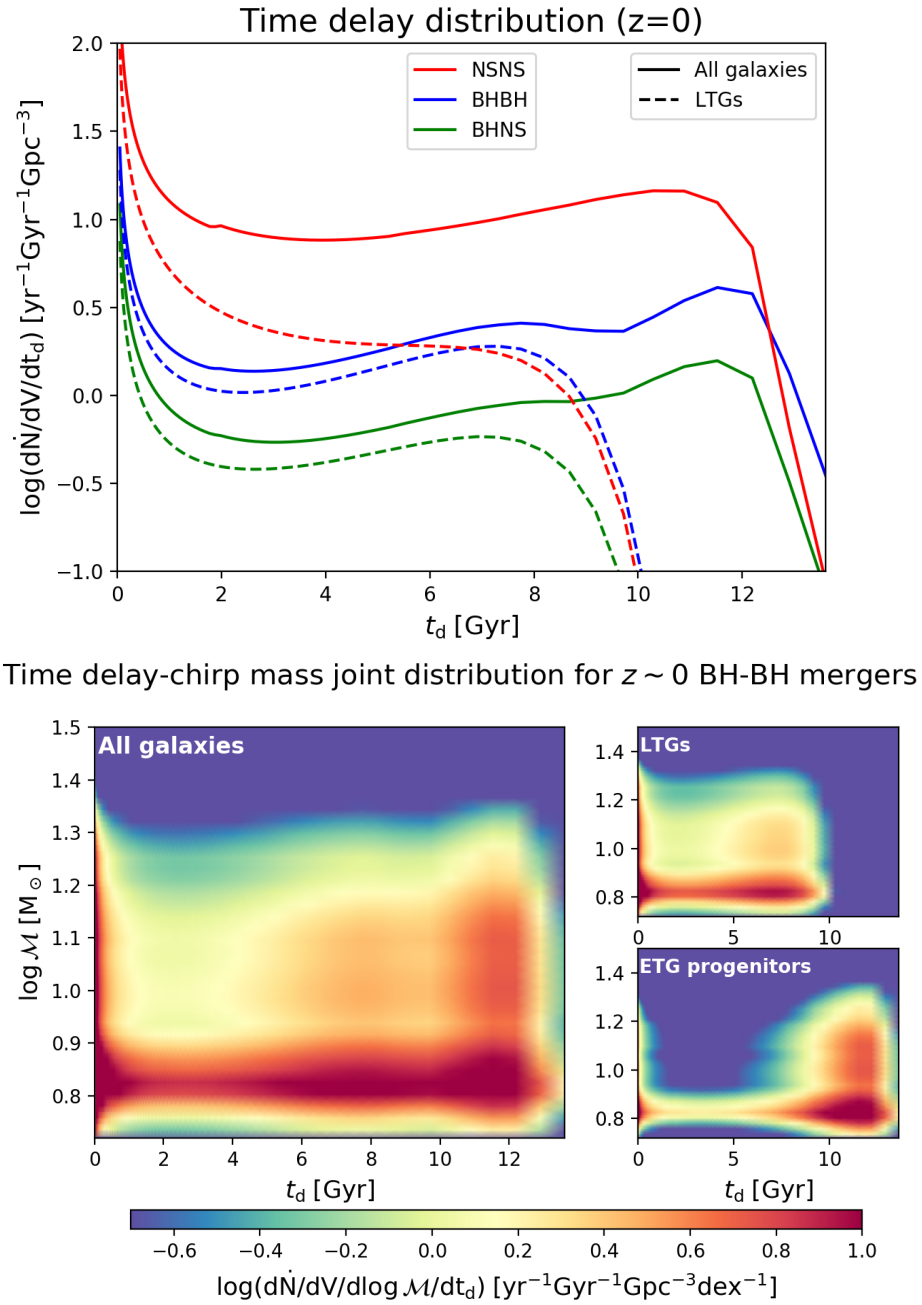

FIGURE 2.16: Top panel: same as Figure 2.15 but for the SFRF+FMR case. Bottom panels: differential merging rate $\log(\mathrm{d}^3\dot{N}/\mathrm{d}V/\mathrm{d}\log\mathcal{M}_{\bullet\bullet}/\mathrm{d}t_d)$ at $z \sim 0$ for BH-BH as a function of the chirp mass and time delay. On the x axis there is the time delay, on the y axis the chirp mass and the color code represents the logarithmic number density of merging events. Contribution coming from all the galaxies (left panel), from LTGs (top right panel) and ETG progenitors (bottom right panel).

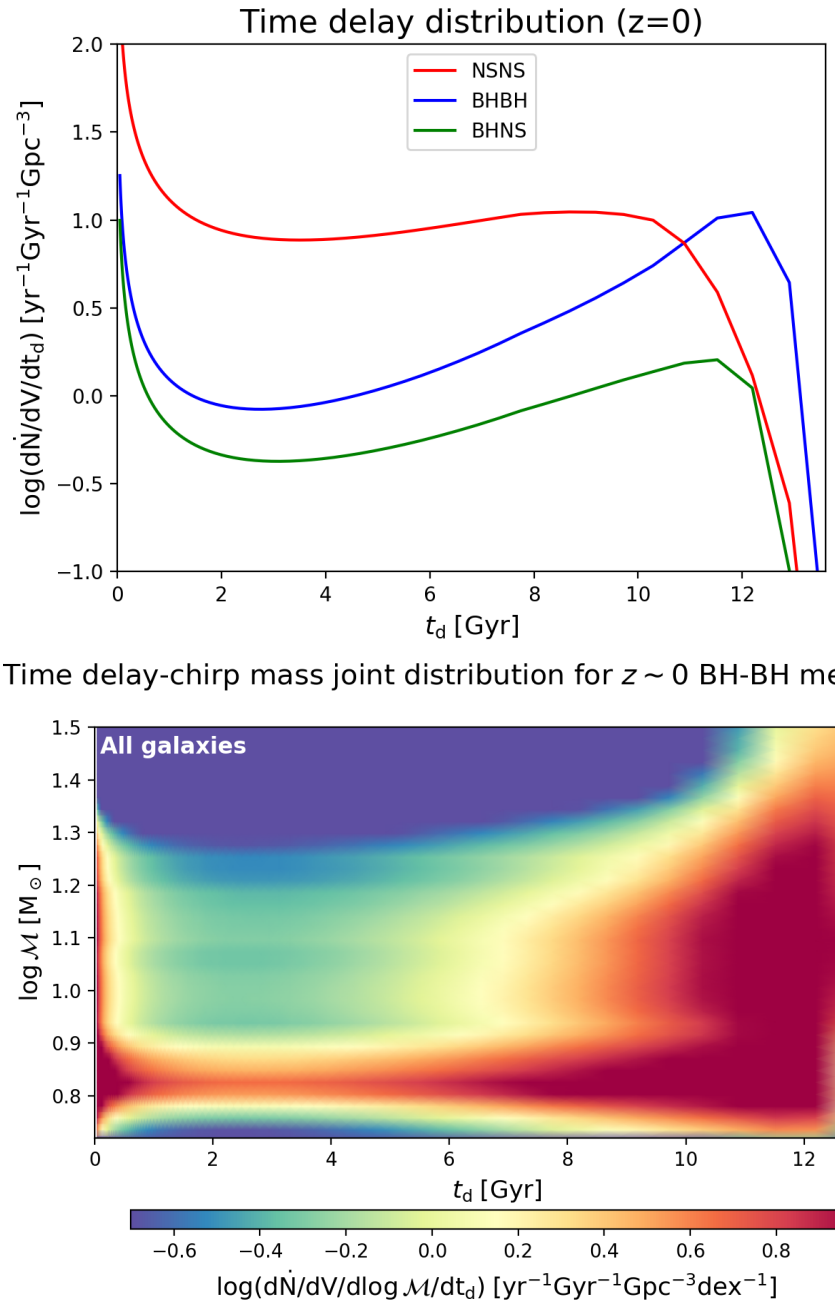

FIGURE 2.17: Top panel: same as Figure 2.15 but for the GSMF+MZR case. Bottom panel: differential merging rate $\log(\mathrm{d}^3\dot{N}/\mathrm{d}V/\mathrm{d}\log\mathcal{M}_{\bullet\bullet}/\mathrm{d}t_d)$ at $z \sim 0$ for BH-BH as a function of the chirp mass and time delay. On the x axis there is the time delay, on the y axis the chirp mass and the color code represents the logarithmic number density of merging events.

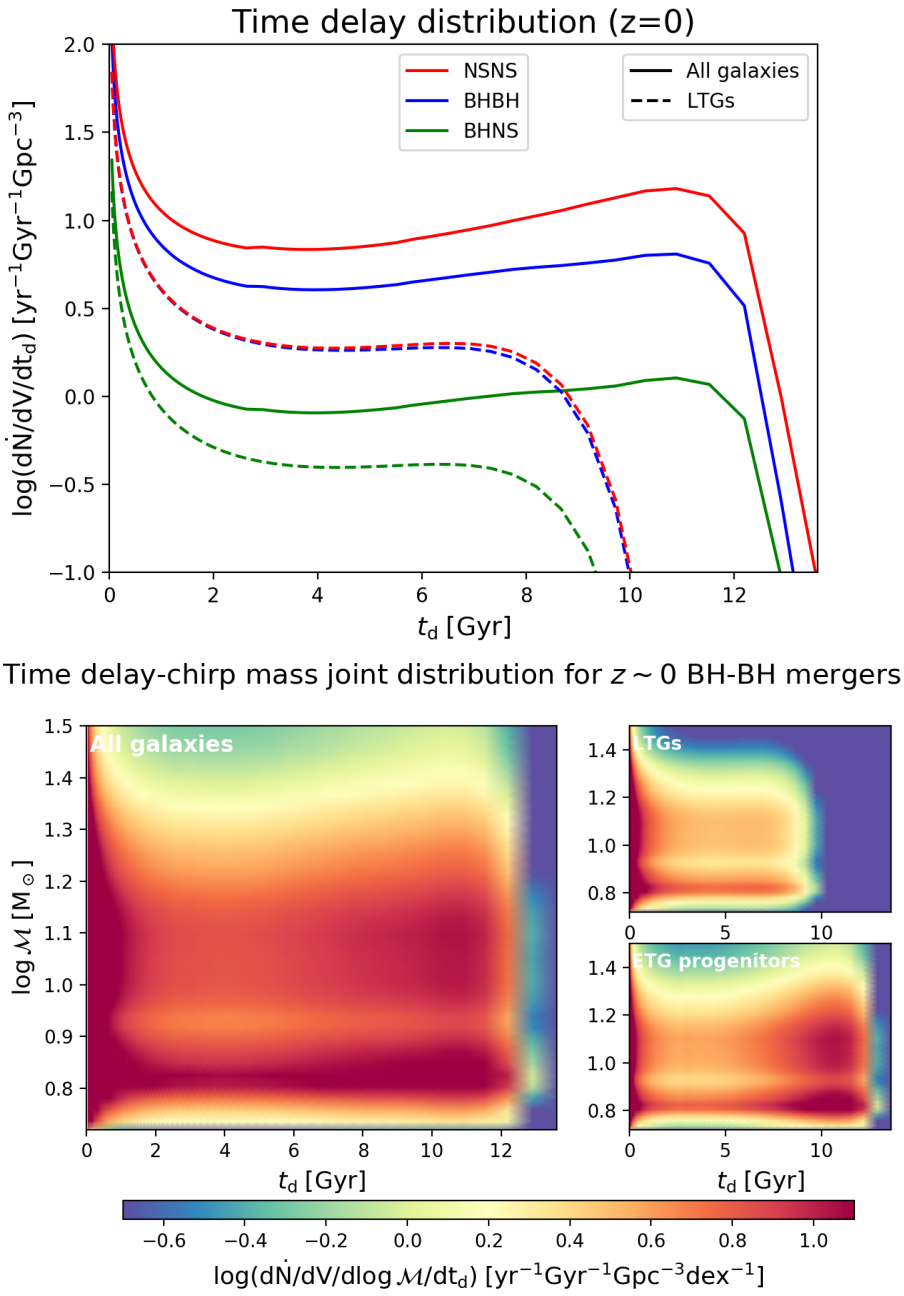

FIGURE 2.18: Top panel: same as Figure 2.15 but for the MODEL case. Bottom panels: differential merging rate $\log(\mathrm{d}^3\dot{N}/\mathrm{d}V/\mathrm{d}\log\mathcal{M}_{\bullet\bullet}/\mathrm{d}t_d)$ at $z \sim 0$ for BH-BH as a function of the chirp mass and time delay. On the x axis there is the time delay, on the y axis the chirp mass and the color code represents the logarithmic number density of merging events. Contribution coming from all the galaxies (left panel), from LTGs (top right panel) and ETG progenitors (bottom right panel).

The sky-averaged S/N for a GW signal is related to redshift and chirp mass as:

$$\sqrt{\bar{\rho}^2} = 8\sqrt{\frac{2}{25}}\left(\frac{20}{3}\right)^{5/6}\frac{R_0}{D_L(z)}\left[\frac{\mathcal{M}_{\bullet\bullet}\,(1+z)}{M_\odot}\right]^{5/6}\sqrt{\zeta(\mathcal{M}_{\bullet\bullet}, q, \Delta t_{\rm obs}, z)} \quad (2.25)$$

In the above $D_L(z)$ is the luminosity distance from the GW source at redshift z, while R_0 is the detector characteristic distance parameter; this is commonly written as

$$R_0^2 = \frac{25\,M_\odot^2}{192\,\pi\,c^3}\left(\frac{3\,G}{20}\right)^{5/3} x_{7/3} \quad (2.26)$$

in terms of the auxiliary quantity

$$x_{7/3} = \frac{1}{(\pi\,M_\odot)^{1/3}}\int_0^\infty \frac{{\rm d}f}{f^{7/3}\,S(f)}\,. \quad (2.27)$$

Here $S(f) = R(f)\,P_n(f) + S_c(f)$ represents the total sensitivity curve, that includes the sky and polarization averaged response function $R(f)$ of the instrument, the instrumental noise $P_n(f)$, and the confusion noise $S_c(f)$. For ground-based detectors like AdvLIGO/Virgo and ET, which are the ones of interest in this Chapter, $S_c(f)$ is usually neglected and $R(f) \simeq 5$ holds independently of the frequency (in some previous works $x_{7/3}$ is defined in terms of $P_n(f)$ and the quantity $1/R(f) \approx 1/5$ is included in the prefactor of equation (2.26) defining R_0^2). For a detector as LISA, instead, $R(f)$ is a complex frequency dependent function and $S_c(f)$, mainly due to unresolved galactic binaries, must be taken into account.

Finally, coming back to equation (2.25), the function $\zeta \equiv \zeta_{\rm isco} + \zeta_{\rm insp} + \zeta_{\rm merge} + \zeta_{\rm ring}$ specifies the overlap of the waveform with the observational bandwidth during the inspiral ($\zeta_{\rm isco} + \zeta_{\rm insp}$), merger ($\zeta_{\rm merge}$) and ringdown ($\zeta_{\rm ring}$) phases of the merger event (see also Ajith et al. 2008). The expressions

for the different components of ζ are the following:

$$\zeta_{\rm isco} = \frac{1}{(\pi\, M_\odot)^{1/3} x_{7/3}} \int_{f_{\rm in}}^{2\, f_{\rm isco}} \frac{df}{S(f)} \frac{1}{f^{7/3}} \tag{2.28}$$

$$\zeta_{\rm insp} = \frac{1}{(\pi\, M_\odot)^{1/3} x_{7/3}} \int_{2\, f_{\rm isco}}^{f_{\rm merge}} \frac{df}{S(f)} \frac{1}{f^{7/3}} \tag{2.29}$$

$$\zeta_{\rm merge} = \frac{1}{(\pi\, M_\odot)^{1/3} x_{7/3}} \int_{f_{\rm merge}}^{f_{\rm ring}} \frac{df}{S(f)} \frac{1}{f^{4/3}\, f_{\rm merge}} \tag{2.30}$$

$$\zeta_{\rm ring} = \frac{1}{(\pi\, M_\odot)^{1/3} x_{7/3}} \int_{f_{\rm ring}}^{f_{\rm cut}} \frac{df}{S(f)} \frac{1}{f_{\rm merge}\, f_{\rm ring}^{4/3}} \left[1 + \left(\frac{f - f_{\rm ring}}{\sigma/2}\right)^2\right]^{-2} \tag{2.31}$$

The different frequencies appearing in these expressions are the initial GW frequency when the detector is switched-on $f_{\rm in}$, the frequency of the innermost stable circular orbit $f_{\rm isco}$, the merging frequency $f_{\rm merge}$, the ringdown frequency $f_{\rm ring}$ and the frequency at which the GW signal is suppressed $f_{\rm cut}$. The exact expressions for these quantities and for σ can be found in Ajith et al. 2008: they depend on redshift, on the total binary mass $M_{\rm bin} \equiv m_{\bullet,1} + m_{\bullet,2}$ and on the symmetric mass ratio $\eta \equiv m_{\bullet,1}\, m_{\bullet,2}/M_{\rm bin}^2$, but they can be recasted in terms of chirp mass $\mathcal{M}_{\bullet\bullet}$ and mass ratio q as $M_{\rm bin} = \mathcal{M}_{\bullet\bullet}\,(1+q)^{6/5}\, q^{-3/5}$ and $\eta = q/(1+q)^2$. However, since the dependence on η is rather weak and the range of η values spanned by DCO binaries is limited, I make the approximation of $\eta \sim 0.25$ to simplify the computations.

The lower limit of integration in equation (2.28) is the initial GW frequency $f_{\rm in}$ that takes into account the evolution during the observation time. For ground-based instrument like AdvLIGO/Virgo and ET, probing high frequency regimes, the frequency shift is very rapid and one can approximately take $f_{\rm in} \simeq 0$, so that the S/N in equation (2.25) is independent of $\Delta t_{\rm obs}$. Contrariwise, for LISA the frequency evolution is quite slow, and one can determine $f_{\rm in}$ by integrating the orbital averaged equations (see Peters 1964) to obtain:

$$f_{\rm in} \simeq f_{\rm isco} \left[1 + \frac{1}{5}\left(\frac{2}{3}\right)^4 \frac{q^{8/5}}{(1+q)^{16/5}} \frac{c^3\, \Delta t_{\rm obs}}{G\mathcal{M}_{\bullet\bullet}\,(1+z)}\right]^{-3/8} \tag{2.32}$$

Under the assumptions mentioned above ($\eta \simeq 0.25$, $f_{\rm in} \simeq 0$), the S/N is

only dependent on z and $\mathcal{M}_{\bullet\bullet}$ and the distribution $\mathrm{d}p/\mathrm{d}\rho(\rho|z,\mathcal{M}_{\bullet\bullet})$ is simply a Dirac delta function[3]:

$$\frac{\mathrm{d}p}{\mathrm{d}\rho}(\rho|z,\mathcal{M}_{\bullet\bullet}) = \delta\left(\rho - \sqrt{\bar{\rho}^2(\mathcal{M}_{\bullet\bullet},z)}\right) \tag{2.33}$$

The GW event detection rates per unit redshift are then obtained by integrating equation (2.24) over chirp mass $\mathcal{M}_{\bullet\bullet}$ and S/N ρ, selecting only the events above a certain S/N threshold for detection ρ_0, chosen to be $\rho_0 = 8$ for both AdvLIGO/Virgo and ET. The resulting expression is the following:

$$\begin{aligned}\frac{\mathrm{d}\dot{N}}{\mathrm{d}z}(>\rho_0,z) =& \frac{1}{1+z}\frac{\mathrm{d}V}{\mathrm{d}z}\int \mathrm{d}\mathcal{M}_{\bullet\bullet}\,\frac{\mathrm{d}^2\dot{N}}{\mathrm{d}\mathcal{M}_{\bullet\bullet}\,\mathrm{d}V}\int \mathrm{d}\rho_{\rho_0}\,\frac{\mathrm{d}p}{\mathrm{d}\rho}(\rho|\mathcal{M}_{\bullet\bullet},z) = \\ & \frac{1}{1+z}\frac{\mathrm{d}V}{\mathrm{d}z}\int \mathrm{d}\mathcal{M}_{\bullet\bullet}\,\frac{\mathrm{d}^2\dot{N}}{\mathrm{d}\mathcal{M}_{\bullet\bullet}\,\mathrm{d}V}\,\Theta_{\mathrm{H}}\left(\sqrt{\bar{\rho}^2(\mathcal{M}_{\bullet\bullet},z)} - \rho_0\right)\end{aligned} \tag{2.34}$$

where the innermost integral is equivalent to an Heaviside theta function enforcing the condition for detectability $\bar{\rho} > \rho_0$.

In Figure 2.19 I report the results for AdvLIGO/Virgo (top panel) and for the ET (bottom panel). Blue lines refer to BH-BH events, red lines to NS-NS and green lines to BH-NS. Although the intrinsic merging rates are larger for NS-NS than for BH-BH (see Section 2.4), the detector response makes GW detection rates from BH-BH to overcome those from NS-NS toward increasing redshift; the crossover occurs at $z \sim 0.05$ for AdvLIGO/Virgo and at $z \sim 0.9$ for ET. The increasing dependence of detectability on the chirp mass implies that GW event rates from BH-BH mergers peak at $z \sim 0.4 - 0.6$ and then falls off rapidly at $z \gtrsim 1$ for AdvLIGO/ Virgo, while they have a broad shape peaking around $z \sim 1.5$ with an extended tail out to very high redshift for ET. GW event rates from NS-NS mergers can be practically detected only within a few hundred megaparsecs for AdvLIGO/Virgo while out to $z \lesssim 2$ with ET and GW event rates from BH-NS mergers peak at $z \sim 0.2$ and then steeply fall off for AdvLIGO/Virgo, while they have a more extended redshift distribution for ET, somewhat mirroring the shape of BH-BH with a peak at smaller redshifts and a more rapid fall off. The contribution to the BH-BH detection rates from LTGs is also shown as a blue dashed line.

I remark that, even if the quantities I displayed are cosmic-integrated,

[3]Notice that, in principle, the S/N for a GW signal, would also be a function of the orientation function $\Theta \equiv 2[F_+^2\,(1+\cos^2\iota)^2 + 4F_\times^2\,\cos^2\iota]^{1/2}$, dependent on the inclination angle of the source ι and on the detector pattern functions F_+ and $F_\times$. In this thesis I have applied the sky-averaged approximation, averaging out this dependence; a more accurate and detailed treatment can be found in Boco et al. 2019.

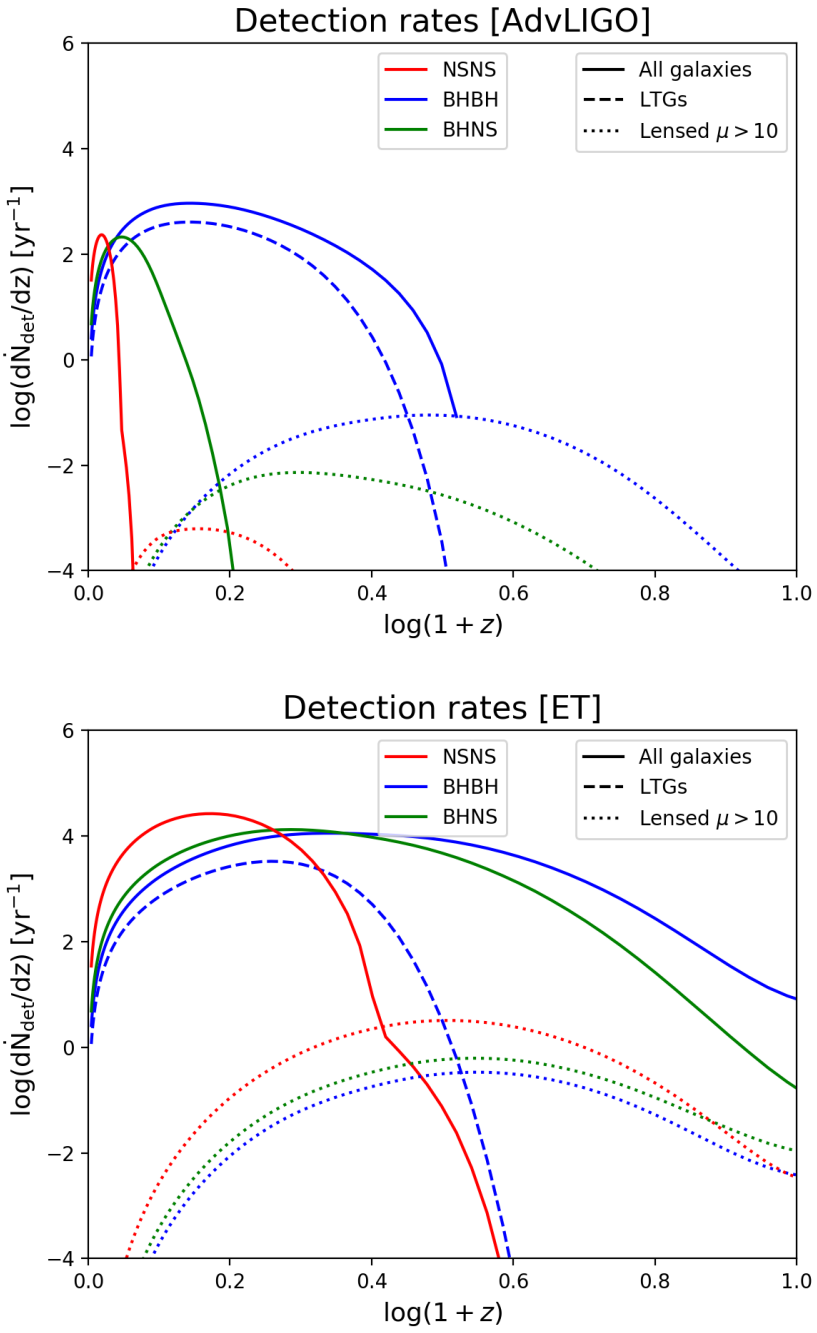

FIGURE 2.19: GW event rate per unit redshift expected for the AdvLIGO/Virgo (top panel) and ET (bottom panel) with S/N threshold $\rho_0 = 8$. Solid lines refer to all the events, the dashed line to the contribution from LTGs. The red line corresponds to NS-NS events, the blue lines to BH-BH and the green line to BH-NS. The dotted lines refer to galaxy-scale gravitational lensing of GWs with magnification $\mu > 10$.

the formalism developed in this Chapter would allow to easily retrieve information about single galaxies. Since they are counted and statistically weighted by SFR or stellar mass, avoiding the integration over these observables would result, respectively, in SFR- and mass-dependent merging or detection rates. An example of this is shown in Scelfo et al. 2020 (see also Appendix B of this thesis), where cross-correlations between galaxies and GWs are performed for different bins of SFR. Such information on the SFR of the host galaxy is also used in order to produce an estimation of the bias parameter for GWs, associating the bias of the GW event to a weighted average of the biases of possible host galaxies (see Appendix B).

2.5.1 GW number counts

The GW count rate $\dot{N}(> \rho_0)$ can be obtained integrating equation (2.34) over redshift. The redshift integrated Euclidean-normalized GW counts are shown in Figure 2.20, for both AdvLIGO/Virgo and ET. Here I just notice that for electromagnetic signals the counts of a uniform distribution of sources with a smooth distribution of luminosities (Euclidean counts) obey the scaling $N(> S) \propto S^{-3/2}$ in terms of the flux S (e.g., Weinberg 2008); this is basically because $N(> S) \propto V \propto D_L^3$ and $S \propto D_L^{-2}$ hold. In the case of GWs, the relation between S/N and distance is inverse linear $\rho \propto D_L^{-1}$, implying the Euclidean behaviour $N(> \rho) \propto \rho^{-3}$ or in differential terms $\mathrm{d}N/\mathrm{d}\rho \propto \rho^{-4}$. When this dependence is normalized out, the counts are flat at high S/Ns, which are mainly contributed by local sources, while the decrease toward lower S/Ns mainly reflects the rapid evolution in the number density of increasingly distant galaxies. The sharp drop at large S/N $\rho \gtrsim 100$ for AdvLIGO/Virgo for NS-NS and BH-NS is simply due to the fact that there are no sources of that type with such an high S/N.

2.5.2 Galaxy-scale Gravitational Lensing of GW

High-redshift $z \gtrsim 2$ star-forming galaxies have a non negligible probability of being gravitationally lensed by other galaxies (mostly low $z \lesssim 1$ early-type galaxies) and by galaxy groups/clusters intervening between the source and the observer (e.g., Blain 1996; Perrotta et al. 2002; Negrello et al. 2007, 2010; Lapi et al. 2012). The GW emission from merging binaries in these sources can be gravitationally lensed too, thus enhancing the detectability of high redshift GW sources (see Li et al. 2018; Ng et al. 2018; Oguri 2018). The effect of a gravitational lensing event with magnification μ on the GWs emitted by a compact source is to enhance the S/N $\rho \propto \sqrt{\mu}$ without changing

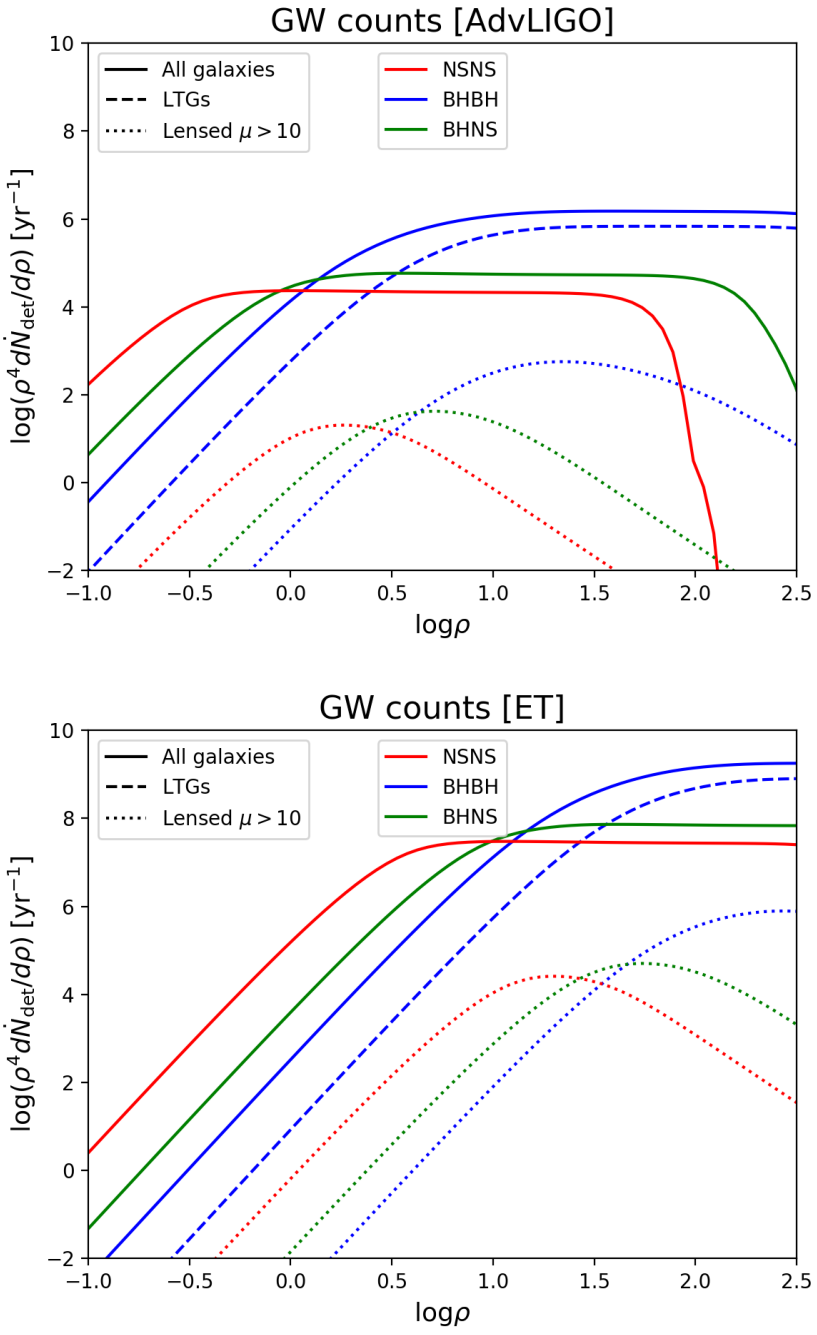

FIGURE 2.20: Euclidean-normalized counts of GW event rate as a function of the S/N for AdvLIGO/Virgo (top panel) and ET (bottom panel). Line styles and color-code are the same as in Figure 2.19.

the observed frequency structure of the waveform (due to the achromaticity of lensing in the geometrical-optics limit; see Takahashi & Nakamura 2003).

In the following I focus on galaxy-scale gravitational lensing, which is the most efficient for intermediate to high redshift sources, close to the peak of the cosmic star formation history (see Lapi et al. 2012). The rate of gravitationally lensed events can be computed as:

$$\frac{\mathrm{d}^2\dot{N}_{\rm lensed}}{\mathrm{d}\rho\,\mathrm{d}z} = \int_{\mu_{\rm min}} \mathrm{d}\mu\,\frac{\mathrm{d}^2\dot{N}}{\mathrm{d}\rho\,\mathrm{d}z}(\rho/\sqrt{\mu},z)\,\frac{\mathrm{d}p}{\mathrm{d}\mu}(\mu,z) \tag{2.35}$$

where $\mathrm{d}^2\dot{N}_{\rm lensed}/\mathrm{d}\rho/\mathrm{d}z$ is the unlensed statistics obtained integrating equation (2.24) over chirp mass and $\mathrm{d}p/\mathrm{d}\mu$ is a probability distribution of amplification factors that depends on the redshift of the GW source and on the properties of the intervening galaxies acting as lenses. The minimum amplification $\mu_{\rm min}$ defines the strength of the lensing events under consideration.

I use the amplification distribution derived by Lapi et al. 2012, which takes into account the redshift dependent statistics of galactic halos, their inner radial distribution of dark matter and baryons, and possible non axisymmetric structure. The redshift distribution of GW events above a detection threshold ρ_0 is:

$$\frac{\mathrm{d}\dot{N}_{\rm lensed}}{\mathrm{d}z}(>\rho_0) = \int_{\rho_0} \mathrm{d}\rho\,\frac{\mathrm{d}^2\dot{N}_{\rm lensed}}{\mathrm{d}\rho\,\mathrm{d}z} \tag{2.36}$$

and the lensed counts are instead obtained by integrating equation (2.35) over redshift.

The results concerning the lensed GW redshift distribution and counts are shown as dotted lines in Figures 2.19 and 2.20; for clarity I illustrate the case $\mu_{\rm min} = 10$ to better highlight the overall impact of strong lensing events. Plainly, strongly lensed events have a redshift distribution shifted toward high redshift. GWs from NS-NS mergers, which in the unlensed case are detectable only locally with AdvLIGO/Virgo and to intermediate redshifts with ET, can in principle be revealed out to $z \lesssim 1$ for AdvLIGO/Virgo and out to high-z with ET; however, the lensed rates are very small for AdvLIGO/Virgo $\lesssim 10^{-3}$ events yr^{-1} , while they attain even $\sim$ 3 events yr^{-1} with ET. The lensed rate of GW events from BH-BH mergers detectable by AdvLIGO/Virgo has a maximum value around $z \sim 2$ attaining ~ 0.1 events yr^{-1}, overwhelming the unlensed events for $z > 2$; for ET instead the lensed BH-BH rates are a factor $\sim 3-4$ smaller than the lensed NS-NS ones, and factors $\gtrsim 10^3$ below the unlensed BH-BH. The lensed BH-NS rates feature a similar behaviour to the lensed BH-BH ones.

I stress that the detection of high-redshift, strongly lensed events can be

particularly important for cosmological studies, related to the detection of multiple images and to the characterization of GW time delay distributions (e.g., Lapi et al. 2012; Eales 2015). This is especially true if there is an accompanying electromagnetic emission (e.g., from BH-NS or NS-NS mergers) that can provide independent measurement of the source redshift and thus help in removing the well-known degeneracy $\rho \propto \sqrt{\mu}\,(\mathcal{M}_{\bullet\bullet}\,(1+z))^{5/6}/D_L(z)$ among chirp mass, redshift and lensing magnification.

2.6 Stochastic GW background

The incoherent superposition of weak, undetected GW sources originates a stochastic background (see Abbott et al. 2017, 2018). In this Section I aim at estimating the contribution to such a background by mergers of compact binaries in galaxies, using the MODEL case as a reference.

I compute the overall background energy density produced by all DCO binaries at given observed frequency $f_{\rm obs}$ as:

$$\Omega_{\rm GW}(f_{\rm obs}) = \frac{8\,\pi\,G\,f_{\rm obs}}{3\,H_0^3\,c^2}\int \frac{{\rm d}z}{h(z)\,(1+z)}\int d\mathcal{M}_{\bullet\bullet}\,\frac{{\rm d}^2\dot{N}}{{\rm d}\mathcal{M}_{\bullet\bullet}\,{\rm d}V}\,\frac{{\rm d}E}{{\rm d}f}(f|\mathcal{M}_{\bullet\bullet},z) \tag{2.37}$$

with $h(z)\equiv[\Omega_M\,(1+z)^3+1-\Omega_M]^{1/2}$. The GW energy spectrum dE/df emitted by a single binary at given redshift and with given chirp mass is taken as (e.g. Zhu et al. 2011):

$$\frac{{\rm d}E}{{\rm d}f} \simeq \frac{(\pi\,G)^{2/3}\mathcal{M}_{\bullet\bullet}{}^{5/3}}{3}\times\begin{cases} f^{-1/3} & f<f_{\rm merge}\\ f_{\rm merge}^{-1} & f_{\rm merge}\le f<f_{\rm ring}\\ \dfrac{f_{\rm merge}^{-1}\,f_{\rm ring}^{-4/3}\,f^2}{\left[1+\left(\frac{f-f_{\rm ring}}{\sigma/2}\right)^2\right]^2} & f_{\rm ring}\le f<f_{\rm cut}\end{cases} \tag{2.38}$$

in terms of the same parameters $f_{\rm merg}$, $f_{\rm ring}$, $f_{\rm cut}$ and σ appearing in equations (2.28), (2.29), (2.30) and (2.31).

Equation (2.37) gives the overall SGWB produced by all the sources in the

sky. However, to compute the residual SGWB originated only by the undetected sources, it has to be modified as:

$$\Omega_{\rm GW}(f_{\rm obs}) = \frac{8\,\pi\,G\,f_{\rm obs}}{3\,H_0^3\,c^2}\int \frac{{\rm d}z}{h(z)\,(1+z)}\times \\ \times \int {\rm d}\mathcal{M}_{\bullet\bullet}\,\frac{{\rm d}^2\dot{N}}{{\rm d}\mathcal{M}_{\bullet\bullet}\,{\rm d}V}\,\frac{{\rm d}E}{{\rm d}f}(f|\mathcal{M}_{\bullet\bullet},z)\int_{\rho<\rho_0}{\rm d}\rho\,\frac{{\rm d}p}{{\rm d}\rho}(\rho|\mathcal{M}_{\bullet\bullet},z) \tag{2.39}$$

with the innermost integral selecting only the sources below a certain S/N threshold.

The results for the SGWB originated by BH-BH, NS-NS, and BH-NS mergers are shown in Figure 2.21 for both AdvLIGO/Virgo and ET as a function of the observed frequency. Solid lines indicate the total background energy produced by all the mergers, while dashed lines represent the residual background after subtracting the detected events. The residual SGWB for AdvLIGO/Virgo is of the same order of the total SGWB, especially for NS-NS and BH-NS since the detection rates are very low, with a factor ~ 1.5 of difference only for BH-BH. For ET, instead, it is present a substantial damping of the residual SGWB given the high detection rates, even of a factor ~ 30 for BH-BH. The general behaviour features an increase scaling as $f_{\rm obs}^{2/3}$ generated by the inspiral phase of DCO binaries, a peak typically broader for BH-BH with respect to NS-NS which is originated by the mergers of different binaries which might occur at different frequencies and then a sharp decline originated by the ringdown phases of binaries that have merged. The frequency of the peak shifts towards higher frequencies for lighter remnants, yielding ~ 200 Hz for BH-BH, ~ 600 Hz for BH-NS and ~ 2000 Hz for NS-NS. The thick cyan lines report the 1σ sensitivity curves for 1 yr of observation and colocated detectors (Thrane & Romano 2013; Abbott et al. 2017; Crocker et al. 2017). The stochastic background due to BH-BH may only marginally be revealed by AdvLIGO/Virgo, while that from all kinds of compact binary mergers should be detected with, and possibly characterized by, ET.

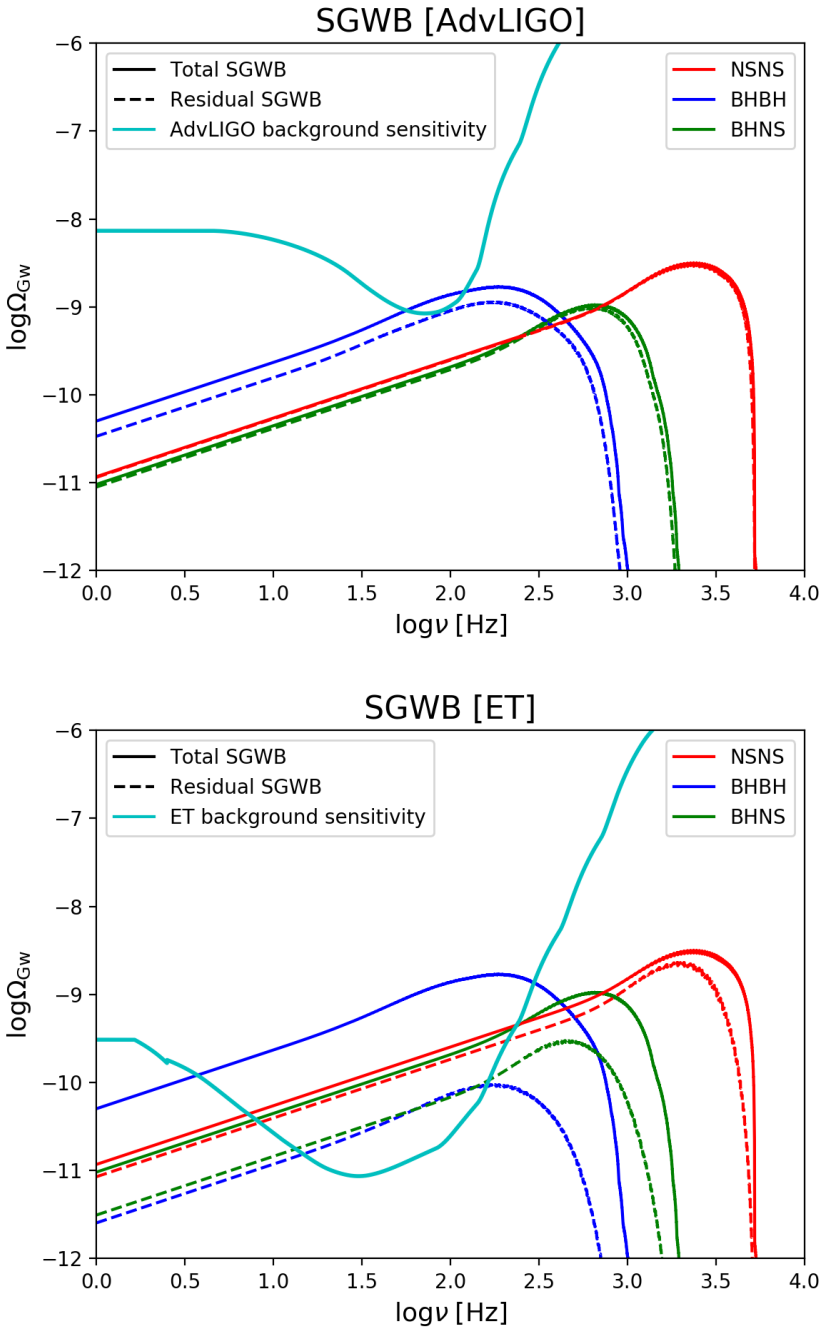

FIGURE 2.21: Energy density of the GW background as a function of the observed frequency for AdvLIGO/Virgo (top panel) and ET (bottom panel). Color code is the same as in Figure 2.19. Solid lines represents the total SGWB, dashed lines the residual after the subtraction of detected events. The thick cyan lines illustrate 1σ sensitivity curves for 1 yr of observations and colocated detectors.

Chapter 3

Growth of SMBH seeds in ETG progenitors

While in Chapter 2 I have investigated the influence of the galactic environment on the mergers of compact objects binaries which were assumed to be isolated, in this Chapter I take inspiration from the dense environment of the central regions of ETG progenitors to propose a new scenario for SMBH heavy seed formation via multiple mergers of stellar compact objects and I suggest a way to test it via GW observations with future detectors. The rationale behind the proposal of such a scenario is to try to alleviate the high redshift quasar tension, that I am going to briefly summarize in the following.

As mentioned in Section 1.3.5, the discovery of an increasing number of active SMBHs with masses $M_\bullet \gtrsim 10^9\,M_\odot$ at very high redshift $z \gtrsim 7$ in gas- and dust-rich host galaxies (e.g., Fan et al. 2006; Mortlock et al. 2011; Banados et al. 2018; Venemans et al. 2017a,b, 2018), when the age of the Universe was shorter than $\lesssim 0.8$ Gyr, rekindles the longstanding issue on how these huge masses can be accumulated within such short timescales. If the increase in BH mass is mainly driven by gas disk (Eddington-like) accretion, the characteristic $e-$folding timescale $\tau_{\rm ef}$ for the BH exponential mass growth $M_\bullet(\tau) \propto e^{\tau/\tau_{\rm ef}}$ amounts to:

$$\tau_{\rm ef} = \frac{\eta}{(1-\eta)\,\lambda}\,t_{\rm Edd} \approx \frac{4.5\times10^7}{\lambda}\,{\rm yr} \tag{3.1}$$

here $\lambda \equiv L/L_{\rm Edd}$ is the Eddington ratio, i.e. the ratio between the actual to the Eddington luminosity $L_{\rm Edd} \approx 1.4\times10^{38}\,M_\bullet/M_\odot$ erg s^{-1}, while $t_{\rm Edd} = M_\bullet\,c^2/L_{\rm Edd} \approx 0.4$ Gyr is the Eddington timescale, and $\eta \equiv L/\dot{M}_\bullet\,c^2$ is the radiative efficiency that in the last equality of the equation above has been set to the reference value $\eta \sim 10\%$ appropriate for a thin disk (Shakura & Sunyaev 1973).

If the BH featured light seed masses of order $\sim 100\,M_\odot$ as expected from

an early generation of stars (e.g., Bromm & Larson 2004; Greif et al. 2010; Hirano et al. 2014) and the Eddington ratios were close to $\lambda \sim 1$, a number of $\gtrsim 17\,\tau_{\rm ef} \gtrsim 0.75$ Gyr would be required to grow the BH to the measured few billion solar masses, which is critically close to the age of the Universe at the observation redshifts $z \gtrsim 7$.

In order to possibly relieve this tension, two main classes of solutions have been proposed in literature:

- The first invokes super-Eddington accretion rates (e.g., Li 2012; Madau et al. 2014; Aversa et al. 2015; Volonteri et al. 2015; Lupi et al. 2016; Regan et al. 2019). The Eddington limit constitutes the limiting luminosity at which the BH gravitational force is balanced by radiation pressure and, therefore, the Eddington ratio is usually assumed $\lambda \leq 1$. However this is true only in the spherical isotropic accretion case, and extremely large accretion rates, overshooting the Eddington limit, can be reached in other accretion models. Even with moderately slim-disk conditions allowing $\lambda \sim$ a few, the radiative efficiency η can get substantially reduced to values of a few percent (almost independently of the BH spin), shortening the $e-$folding time to appreciably less than 10^7 yr, allowing for the rapid growth of SMBHs.

- The second way-out involves mechanisms able to rapidly produce BHs heavier than ones originated by standard stellar evolution, with typical masses $m_\bullet \gtrsim 10^3 - 10^5\,M_\odot$, called BH seeds, so reducing somewhat the time required to attain the final billion solar masses by standard Eddington accretion (see Mayer & Bonoli 2019 for a recent review).

As for the BH seeds class, a vast variety of mechanisms to produce such objects has been proposed in literature. The issue is complex since all the possible information on the initial BH seed mass and properties are washed out by the subsequent exponential mass growth due to standard gas accretion.

Still, a lot of theoretical and numerical work has been done in this direction and the progressive discovery of SMBHs at high redshift, together with the study of the properties of their host galaxies, can place interesting constraints on their origin. The most accredited seed formation models can be further divided into 3 classes:

- The first assumes that BH seeds are the stellar remnants of Population III stars (see Volonteri 2012; Hosokawa et al. 2012, 2013), i.e. the first generation of stars which could reach masses up to $m_\star \sim 100-1000\,{\rm M}_\odot$ due to the extremely metal poor environment of the first virialized DM mini halos, where only molecular hydrogen cooling was possible. Because of the seed BH masses $m_\bullet \lesssim 10^3\,{\rm M}_\odot$ this scenario is also referred

to as "light seeds" scenario. Given the relatively low mass of these light seeds, these models struggle in reproducing the most massive SMBHs observed at high redshift and at least a partial super Eddington accretion must be present to alleviate the tension.

- The second class contains the direct collapse models, able to produce "heavy seeds" with masses $m_\bullet \gtrsim 10^4$ yr. These models envisage the prompt formation of a BH seed from the direct collapse of a gaseous cloud which was prevented from fragmentation. Different models achieve this condition in various ways. The most straightforward way to suppress fragmentation is to assume that direct collapse occurs in metal free small protogalaxies at high redshift ($z \gtrsim 15$) where star formation has still not started (e.g. Choi et al. 2013, 2015; Latif et al. 2013, 2015). However such a scenario is prone to some criticism mainly related to the mechanism to suppress molecular hydrogen cooling and to the low gas inflow rate in such small high-z halos ($M_H \sim 10^8 - 10^9\,\mathrm{M}_\odot$). For these reasons in Mayer et al. 2010, 2015 it has been proposed a model for direct collapse in massive star-forming galaxies with $M_H \sim 10^{11} - 10^{12}\,\mathrm{M}_\odot$ where fragmentation of the central gaseous cloud is avoided not by suppressing eventual cooling processes but by the high inflow rate toward the central region, triggered by a galaxy major merger, which ensures an high surface density and makes the gas optically thick.

- The third class of solutions foresee that the formation of BH seeds may be driven by the efficient mergers of stars or stellar mass black holes inside globular clusters (e.g., Portegies Zwart et al. 2004; Devecchi et al. 2012; Latif & Ferrara 2016; Mapelli 2016), though so far no intermediate mass BH has been clearly detected at the center of local stellar systems. This class of models leads to seeds of masses $\sim 10^3\,\mathrm{M}_\odot$ in between the Population III and the direct collapse scenarios.

The issue about the SMBH origin is also of some relevance at lower redshifts $z \sim 2 - 7$. This is because in the local Universe the most massive relic BHs with $M_\bullet \gtrsim$ several $10^8 - 10^9\,M_\odot$ are typically hosted in massive galaxies with bulge mass $M_\star \gtrsim 10^{11}\,M_\odot$ (e.g., McConnell & Ma 2013; Kormendy & Ho 2013), and there are extreme instances in brighter cluster galaxies where the BH mass can even exceed $M_\bullet \sim 10^{10}\,M_\odot$ (e.g., Mehrgan et al. 2019). Given that the hosts of these monsters are early-type galaxies most of their old stellar component must have been accumulated during a quite short main star formation episode lasting some 10^8 yr at $z \gtrsim 1$, as demonstrated by astro archaeological measurements of their stellar ages and α-enhanced metal

content (see Section 1.3.1; Thomas et al. 2005, 2010; Gallazzi et al. 2006, 2014; Johansson et al. 2012). Moreover, the well established correlations between BH and galaxy properties (e.g., McConnell & Ma 2013; Kormendy & Ho 2013; Shankar et al. 2016) and the parallel evolution of the cosmic SFR density for galaxies and of the luminosity density for bright quasars (see Section 1.3.5; Madau & Dickinson 2014; Aird et al. 2015; Kulkarni et al. 2019) strongly suggest that the BH and stellar mass must have been accumulated over comparably short timescales, thought to be ultimately determined by the energy feedback from the BH itself (see Silk & Rees 1998; Fabian 1999; King 2005; Lapi et al. 2006, 2014; for a recent review, see King & Pounds 2015). To grow billions solar masses in some 10^8 yr is somewhat challenging if disk accretion starts from a light seed $\sim 10^2\,M_\odot$ and proceeds with the typical Eddington ratios $\lambda \lesssim 0.3$ estimated out to $z \lesssim 4$ (see Vestergaard & Osmer 2009; Kelly & Shen 2013; Vestergaard 2019); as a matter of fact, an heavy seed may help in speeding up the BH growth and in explaining huge masses $M_\bullet \gtrsim 10^9\,M_\odot$ accumulated over short timescales $\lesssim$ Gyr even at these intermediate redshifts.

In this Chapter I submit a new scenario to form heavy BH seeds, alternative or complementary to the aforementioned mechanisms, and I suggest a way to test it via future gravitational wave observations, following the lines of Boco et al. 2020. Specifically, I propose BH seeds to be formed in the inner, gas-rich regions of ETG progenitors via multiple mergers of stellar compact remnants, that are driven to sink toward the centre by gaseous dynamical friction.

The idea was inspired by the wealth of recent observational evidences concerning the population of submillimeter galaxies discovered thanks to wide-area far-IR/(sub)mm/radio surveys, that are thought to be the progenitors of local ETGs and to be responsible for the bulk of the cosmic star formation history out to $z \lesssim 6$ (e.g., Lapi et al. 2011; Gruppioni et al. 2013, 2015; Weiss et al. 2013; Koprowski et al. 2014, 2016; Strandet et al. 2016; Novak et al. 2017; Riechers et al. 2017; Schreiber et al. 2018; Zavala et al. 2018; Wang et al. 2019). As mentioned in Section 1.3.1, interferometric, high-resolution observations with ALMA have allowed to reveal large SFRs $\psi \gtrsim 10^2 - 10^3\,M_\odot\,\mathrm{yr}^{-1}$ in these galaxies, considerable dust amounts $M_{\rm dust} \gtrsim 10^8 - 10^9\,M_\odot$ and huge molecular gas reservoirs $M_{\rm gas} \sim 10^{10} - 10^{11}\,M_\odot$ within a central compact region of a few kiloparsecs (e.g., Scoville et al. 2014, 2016; Ikarashi et al. 2015; Simpson et al. 2015; Barro et al. 2016; Spilker et al. 2016; Tadaki et al. 2017a,b, 2018; Talia et al. 2018; Lang et al. 2019). Ensuing optical/near-IR/mid-IR followup measurements and broadband SED modeling have highlighted that these objects already comprise large stellar masses $M_\star \gtrsim 10^{11}\,M_\odot$, implying typical star formation timescales $\tau_\psi \sim$

a few to several 10^8 yr, as also inferred from the so called galaxy main sequence (e.g., Elbaz et al. 2007; Rodighiero et al. 2011, 2015; Speagle et al. 2014; Popesso et al. 2019; Boogaard et al. 2019; Wang et al. 2019). Finally, targeted X-ray observations have started to reveal the early growth of a supermassive BH by disk accretion in their nuclear regions, before it attains a high enough mass and power to manifest as a quasar, and to likely quench star formation and evacuate gas and dust from the host (e.g., Mullaney et al. 2012; Page et al. 2012; Delvecchio et al. 2015; Rodighiero et al. 2015, 2019; Stanley et al. 2015, 2017; Massardi et al. 2018).

Such observational evidences reveal that in the nuclear regions of ETG progenitors a considerable amount of stars, and consequently of stellar compact remnants (neutron stars and BHs), is being formed rapidly in a very dense gaseous environment; I will show that such conditions are apt for efficient gaseous dynamical friction to occur and to drive the sinking of compact objects toward the nuclear regions (see schematics in Figure 3.1).

The model presented in Boco et al. 2020 has been complemented and extended in Boco et al. 2021 under 2 respects:

- Primordial black holes (pBHs) have been added into the game. If pBHs are present and constitute a fraction $f_{\rm pBH}$ of the dark matter mass, they will undergo the gaseous dynamical friction process as well, especially in the central galactic region where the gas is more concentrated. Therefore they could contribute to the growth of the central BH seed; moreover, their mergers with said seed could produce GW signals with specific properties. However I stress that, despite the possibility of considering pBHs as contributors to the central seed growth is interesting, the model presented is general and not related to their existence. For this reason I present results varying the fraction of pBHs in the range $0.01 \leq f_{\rm pBH} \leq 1$, where the lower limit $f_{\rm pBH} = 0.01$ should be intended as an effective absence of such kind of black holes.

- Predictions regarding the stochastic gravitational wave background produced by all the unresolved merger events, both for stellar compact remnants and for pBHs, have been performed. I will show that the detection of the SGWB over an extended frequency spectrum could constitute a crucial test for this scenario of seed formation.

Throughout the Chapter I present such a model, trying to address the following issues: what are the typical timescales of the gaseous dynamical friction process? How this process may concur with standard disk accretion in providing an heavy BH seed and in growing the central supermassive BH? Is it possible to test this scenario via the detection of GWs emitted by the merging events between the migrating compact remnants/pBHs

and the accumulating central BH? If so, what are the marking features of these GW emissions with respect to that coming from the compact binary mergers already detected by the LIGO/Virgo team? Is this process going to produce a detectable stochastic gravitational wave background? Is this background distinguishable from the SGWB originated by other astrophysical/cosmological processes?

The Chapter is organized as follows: in Section 3.1 I quantitatively characterize the properties of the considered galaxies and the nature of the dynamical friction force; in Section 3.2 I put the precedent results together to compute the compact objects orbital decay and the gaseous dynamical friction timescales; in Section 3.3 I compute the ensuing merging rates of the stellar compact remnants and of the primordial black holes as a function of the fraction $f_{\rm pBH}$; in Section 3.4 I infer the induced time evolution of the central BH mass via dynamical friction and disk (Eddington-like) accretion; in Section 3.5 I discuss the GW emission associated to the process of seed formation proposed here, and its detectability with future ground-based (ET and DECIGO) and space-based (LISA) detectors; in Section 3.6 I predict the SGWB originated by the incoherent superposition of unresolved merging events. Finally, in Section 3.7, I critically discuss the main assumptions of my treatment.

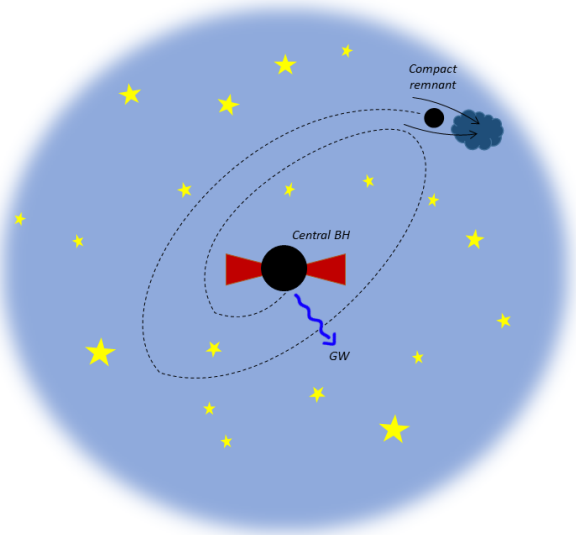

FIGURE 3.1: Schematics (not to scale) depicting the migration of a compact object due to gaseous dynamical friction toward the galaxy center, and its merging with the central BH (possibly also accreting matter via disk Eddington-like accretion) with ensuing emission of GWs.

3.1 Gaseous dynamical friction in ETG progenitors

Generally speaking, dynamical friction consists in the gravitational interaction between a moving object (dubbed perturber) and its gravitationally-induced wake, which generates a reduction in the energy and angular momentum of the perturber, and hence its progressive orbital decay. In the literature more emphasis has been given to the dynamical friction process against a sea of background collisionless particles such as stars or dark matter (e.g., Chandrasekhar 1943; Binney & Tremaine 1987; Lacey & Cole 1993; Hashimoto et al. 2003; Fujii et al. 2006; Boylan-Kolchin et al. 2008; Jiang et al. 2008). For example, this is a leading mechanism thought to drive the formation of a supermassive BH binary after a galaxy merger (see Begelman et al. 1980; Mayer et al. 2007; Barausse 2012; Chapon et al. 2013; Antonini et al. 2015; Tamburello et al. 2017; Katz et al. 2020); the binary can eventually coalesce and emit GWs if stalling around the hardening radius (the so called 'final parsec problem') is avoided by some mechanism like gas dynamics, triple BH interactions, circum-nuclear disk migration, etc. (see Yu 2002; Escala et al. 2004; Merritt & Milosavljevic 2005; Kulkarni & Loeb 2012; Bonetti et al. 2019).

In the considered context of driving stellar compact remnants and pBHs to the center of gas-rich ETG progenitors, dynamical friction against collisionless matter is of minor relevance. This is because I am mainly interested in the buildup of an heavy BH seed before standard disk (Eddington-like) accretion becomes the dominant channel for the BH growth. At these early stages, an ETG progenitor is still poor in stellar content though extremely rich in molecular gas; moreover, such gas reservoir is expected to strongly dominate the inner gravitational potential (see next Section 3.1.1). Therefore gaseous rather than stellar or dark matter dynamical friction should constitute the relevant process to drive the compact remnants toward the nucleus, prevent stalling, and enforce coalescence with the accumulating central BH mass.

The efficiency of gaseous dynamical friction and its timescales assume a crucial role for the viability of the seed formation process. In order to estimate typical dynamical friction timescales I need to model three basic ingredients: (i) the gas density distribution and the gravitational potential in the central regions of ETG progenitors; (ii) the dynamical friction force acting on a compact object during its orbit in the galactic potential well; (iii) the accretion of gas onto compact objects during the orbital decay. These will be now discussed in turn in Sections 3.1.1, 3.1.2 and 3.1.3 respectively.

3.1.1 Gas density profile and compact objects distribution

Resolved interferometric observations of ETG progenitors (see discussion at the beggining of the Chapter) show that these objects feature a central region of size $\sim$ kpc containing huge gas masses $\gtrsim$ some $10^{10}\,\mathrm{M}_\odot$ and undergoing heavy star formation at rates $\psi \gtrsim 10^2 - 10^3\,\mathrm{M}_\odot\,\mathrm{yr}^{-1}$; these SFRs will lead to accumulate stellar masses $M_\star \gtrsim 10^{10}\,\mathrm{M}_\odot$ over a timescale of some 10^8 yr.

The molecular gas mass is typically found to be distributed like a Sersic profile with index $n \sim 1.5$ and half-mass radius $R_e \sim$ kpc, strongly dominating the inner gravitational potential well (the dark matter contribution is negligible out to a few tens kpcs; see van Dokkum et al. 2015; Genzel et al. 2017; Teklu et al. 2018). On such observational basis, I adopt a 3-D Sersic gas distribution (see also equation (1.45) in Chapter 1):

$$\rho(r) = \frac{M_{\rm gas}}{4\pi\,R_e^3}\,\frac{b^{n\,(3-\alpha)}}{n\,\Gamma[n\,(3-\alpha)]}\,\left(\frac{r}{R_e}\right)^{-\alpha}\,e^{-b\,(r/R_e)^{1/n}} \tag{3.2}$$

where R_e is the half-mass radius, n is the Sersic index, and α is the inner density slope. In the classic 3-D Sersic profile (see Prugniel & Simien 1997) $\alpha = 1 - 1.188/2n + 0.22/(4n^2)$ is related to n, yielding $\alpha \approx 0.6$ for $n = 1.5$ that I adopt as fiducial case. However, in the nuclear region, α can deviate somewhat from this value due to the local environment, so I will explore the impact on my results of freely varying this parameter. The corresponding mass distribution writes:

$$M(<r) = M_{\rm gas}\,\left\{1 - \frac{\Gamma[n\,(3-\alpha), b\,(r/R_e)^{1/n}]}{\Gamma[n\,(3-\alpha)]}\right\} \tag{3.3}$$

in terms of the incomplete Gamma function $\Gamma(t,a) \equiv \int_a^\infty \mathrm{d}t\,t^{x-1}\,e^{-t}$; the parameter b can be determined numerically by the consistency condition $M_{\rm gas}(<R_e) = M_{\rm gas}/2$, which readily implies the equation $\Gamma[n\,(3-\alpha), b] = \Gamma[n\,(3-\alpha)]/2$. Finally, the associated gravitational potential is given by:

$$\phi(r) = -\frac{G\,M_{\rm gas}}{R_e}\,\left\{\frac{1}{r} - \frac{\Gamma[n\,(3-\alpha), b\,(r/R_e)^{1/n}])}{\Gamma[n\,(3-\alpha)]} + b^n\,\frac{\Gamma[n\,(2-\alpha), b\,(r/R_e)^{1/n}]}{\Gamma[n\,(3-\alpha)]}\right\} \tag{3.4}$$

For comparison with previous works, I will also explore other two classic density distributions: (i) the singular isothermal sphere or SIS model, for

which:

$$\rho(r) = \frac{M_{\rm gas}}{2\pi\, R_e^3} \left(\frac{r}{R_e}\right)^{-2} \tag{3.5}$$

$$M(<r) = M_{\rm gas}\, \frac{r}{2\, R_e} \tag{3.6}$$

$$\phi(r) = \frac{G\, M_{\rm gas}}{2\, R_e} \left[\log\left(\frac{r}{2\, R_e}\right) - 1\right] \tag{3.7}$$

(ii) the Hernquist 1990 profile for which:

$$\rho(r) = \frac{M_{\rm gas}}{2\pi\, R_e^3}\, (\sqrt{2}-1) \left(\frac{r}{R_e}\right)^{-1} \left(\sqrt{2}-1+\frac{r}{R_e}\right)^{-3} \tag{3.8}$$

$$M(<r) = M_{\rm gas} \left(\frac{r}{R_e}\right)^{2} \left(\sqrt{2}-1+\frac{r}{R_e}\right)^{-2} \tag{3.9}$$

$$\phi(r) = -\frac{G\, M_{\rm gas}}{R_e} \left(\sqrt{2}-1+\frac{r}{R_e}\right)^{-1} \tag{3.10}$$

In the next Subsections, I try to estimate the initial positions and velocities of stellar compact remnants and primordial black holes in the environment described above.

Stellar compact remnants

I assume stars, and hence stellar compact remnants, to be created following the gas distribution in equation (3.2); specifically, I prescribe that:

$$\frac{{\rm d}p}{{\rm d}r} \propto \frac{{\rm d}M(<r)}{{\rm d}r} \propto r^2 \rho(r) \tag{3.11}$$

is the probability that a star was born at a radius r. After a timescale $\lesssim$ a few 10^7 yr stars more massive than $m_\star \gtrsim 7-8\, M_\odot$ will explode as supernovae leaving a compact remnant, i.e. a neutron star or a stellar mass BH. I assume that the compact remnant inherits the same velocity of the progenitor star, in turn being related to that of the star-forming molecular gas cloud; in particular, I take the distributions of radial and tangential velocities:

$$\frac{{\rm d}p}{{\rm d}v_{r,\theta}}(v_{r,\theta}|r) \propto e^{-v_{r,\theta}^2/2\,\sigma^2} \tag{3.12}$$

to be Gaussians with null mean and a dispersion equal to the isotropic velocity dispersion at the radius r:

$$\sigma^2(r) = \frac{1}{\rho(r)} \int_r^\infty \mathrm{d}r' \frac{\rho(r')\, M(<r')}{r'^2} \tag{3.13}$$

found by self-consistently solving the isotropic Jeans equation in the aforementioned potential well. To provide some definite values useful in the sequel, consider that for $R_e \sim 1$ kpc and $M_{\rm gas} \sim 10^{11}\, M_\odot$, one finds $\sigma(r) \approx 150 - 300$ km s^{-1} for initial radii $r \sim 10 - 100$ pc.

These prescriptions are used to initialize the position and velocity of the compact remnants that, in turn, determine their initial energy and angular momentum, needed for computing the dynamical friction timescales as detailed below.

Primordial black holes

Primordial black holes, if they exist, would also undergo the dynamical friction process and sink towards the nuclear galactic region, contributing to the growth of the central BH seed. I quantify the total number of pBHs, $N_{\rm pBH}$, present in a galaxy with overall halo mass M_H via:

$$N_{\rm pBH} \approx \frac{f_{\rm pBH}\, M_{\rm H}}{\int \mathrm{d}m_\bullet\, m_\bullet \frac{\mathrm{d}p}{\mathrm{d}m_\bullet}} \tag{3.14}$$

In the above $M_{\rm H}$ is the dark matter (halo) mass of the galaxy, $f_{\rm pBH}$ is the fraction of halo mass $M_{\rm H}$ constituted by pBHs, and $\mathrm{d}p/\mathrm{d}m_\bullet$ is the pBH mass distribution in terms of the individual pBH mass $m_\bullet$. The pBH mass function is theoretically determined by the pBHs formation mechanism (e.g. Carr et al. 2017; Sasaki et al. 2018), but largely unconstrained by even indirect observations. Stringent upper limits have been placed on $f_{\rm pBH}$, yet in turn still somewhat dependent on the mass function. In the present thesis I adopt a log-normal distribution of pBH masses with central value of 30 $M_\odot$ and dispersion $\sigma_{\log m_\bullet} = 0.3$ dex. These have been selected to fall in a region of the parameter space where $f_{\rm pBH}$ is still poorly constrained (see Carr et al. 2017), so as to allow maximal flexibility.

The initial spatial distribution of pBHs is assumed to follow the DM density profile, in terms of a Navarro-Frank-White 1996 distribution $\rho_{\rm H}(r) \propto 1/r/(r+r_s)^2$. As in the compact remnant case, the probability for a pBH to be born at a distance r from the center is $\mathrm{d}p/\mathrm{d}r \propto r^2\, \rho_{\rm H}(r)$ and I assume the radial and tangential velocities distributions to be Gaussians with dispersion

computed as in equation (3.13) keeping into account the total density profile.

3.1.2 Gaseous dynamical friction force

Dynamical friction of massive perturbers in a smooth gaseous medium has been extensively investigated in a series of classic literature works (e.g., Dokuchaev 1964; Ruderman & Spiegel 1971; Bisnovatyi-Kogan et al. 1979; Rephaeli & Salpeter 1980; Ostriker 1999). These concurrently found that, when the motion of the perturber is supersonic, gaseous dynamical friction is as efficient as that occurring in a collisionless medium; contrariwise, when the motion of the perturber is subsonic, gaseous dynamical friction gets strongly suppressed. All in all, the gaseous dynamical friction force $F_{\rm DF}$ can be generally described by the expression:

$$F_{\rm DF} = -\frac{4\pi\, G^2\, m_\bullet^2\, \rho}{v^2}\, f(\mathcal{M}) \tag{3.15}$$

where $m_\bullet$ is the mass of the perturber, v is its velocity, and $f(\mathcal{M})$ is a function of the Mach number $\mathcal{M} \equiv v/c_s$, namely the ratio of the perturber velocity to the sound speed c_s of the background medium. The latter, in turn, can be related $c_s \equiv \sqrt{\gamma\, k_B\, T/\mu\, m_p}$ to the gas temperature T in terms of the Boltzmann constant k_B, of the mean molecular weight $\mu \sim 0.6$ and of the adiabatic index $1 \lesssim \gamma \lesssim 5/3$. In the environment of a gas-rich ETG progenitor, the typical temperatures of the molecular gas are found to be around $T \lesssim 10 - 100$ K, as estimated from the far-IR/(sub)mm observations of the dust emission, that is in rough thermal equilibrium with the gas (e.g., Silva et al. 1998; Pearson et al. 2013; Casey et al. 2014; da Cunha et al. 2015; Boquien et al. 2019); these values yield modest sound speeds $c_s \sim 0.3 - 3$ km s^{-1} and, given the initial velocity distributions discussed in Section 3.1.1, strongly supersonic motions with $\mathcal{M} \gtrsim 100$ apply for the majority of the compact remnants, at least for most of their orbital evolution.

For point-like perturbers in straight motion, Ostriker 1999 derived the approximate expression:

$$f(\mathcal{M}) = \begin{cases} \dfrac{1}{2}\ln\left(\dfrac{1+\mathcal{M}}{1-\mathcal{M}}\right) - \mathcal{M} & \mathcal{M} \leq 1 \\ \\ \dfrac{1}{2}\ln\left(1 - \dfrac{1}{\mathcal{M}^2}\right) + \ln\Lambda & \mathcal{M} > 1 \end{cases} \tag{3.16}$$

where $\ln\Lambda \equiv \ln(r_{\rm max}/r_{\rm min})$ is the so called Coulomb logarithm, defined in terms of the maximum and minimum 'impact' parameters $r_{\rm max}$ and $r_{\rm min}$ (see discussion below), pointing out that for supersonic motion the gaseous dynamical drag is more efficient than in the collisionless case, especially in the transonic regime $\mathcal{M} \gtrsim 1$, and that for subsonic motion the dynamical drag does not vanish, even though it is somewhat reduced. These results have been also confirmed numerically (Sanchez-Salcedo & Brandenburg 2001; Escala et al. 2004), extending the analysis to extended perturbers on non-straight trajectories. They studied the orbital decay of a moving object in a uniform gaseous medium and found a pleasant agreement with the analytical formula of Ostriker 1999, apart for an overestimation of the dynamical drag for perturbers in transonic motion. In Escala et al. 2004 it is proposed a new parametric formula to correct for this overestimation. However, the exact value of the gaseous dynamical friction force in the transonic regime is still debated, with the more recent numerical simulations of Chapon et al. 2013 being more in agreement with the analytical expression of Ostriker 1999, pointing toward a stronger drag at $\mathcal{M} \gtrsim 1$. In the present thesis I adopt the analytical expression for $f(\mathcal{M})$ provided by Tanaka & Haiman 2009 and Tagawa et al. 2016, which is a refinement of Escala et al. 2004 prescription and thus represent a conservative estimate for the dynamical friction force:

$$f(\mathcal{M}) = \begin{cases} \dfrac{1}{2}\ln\Lambda\left[\mathrm{erf}\left(\dfrac{\mathcal{M}}{\sqrt{2}}\right) - \sqrt{\dfrac{2}{\pi}}\,\mathcal{M}\,e^{-\mathcal{M}^2/2}\right] & 0 \le \mathcal{M} \le 0.8 \\ \dfrac{3}{2}\ln\Lambda\left[\mathrm{erf}\left(\dfrac{\mathcal{M}}{\sqrt{2}}\right) - \sqrt{\dfrac{2}{\pi}}\,\mathcal{M}\,e^{-\mathcal{M}^2/2}\right] & 0.8 \le \mathcal{M} \le \mathcal{M}_{\rm eq} \\ \dfrac{1}{2}\ln\left(1 - \dfrac{1}{\mathcal{M}^2}\right) + \ln\Lambda & \mathcal{M} > \mathcal{M}_{\rm eq} \end{cases} \tag{3.17}$$

where $\mathcal{M}_{\rm eq}$ is set so that $f(\mathcal{M})$ is a continuous function. I stress again that for most of the perturber's orbital evolution the $\mathcal{M} > \mathcal{M}_{\rm eq}$ case is relevant.

A subtle issue concerns the values of the Coulomb logarithm $\ln\Lambda \equiv \ln(r_{\rm max}/r_{\rm min})$, which brings about a considerable (though logarithmic) uncertainty for both stellar and gaseous dynamical friction. Some authors (e.g., Lacey & Cole 1993; van den Bosch et al. 1999; Tanaka & Haiman 2009; Tamburello et al. 2017) leave it constant during the evolution of the perturber, some others (e.g., Ostriker 1999; Tagawa et al. 2016) make it to evolve with time; moreover, the adopted values differ appreciably from author to author,

though there is a general consensus for it to be $\ln\Lambda \gtrsim 1$. As to the minimum impact parameter $r_{\rm min}$, it can be identified with the accretion radius $2\,G\,m_\bullet/v^2$ if this is much larger than the softening radius of the perturber, namely the Schwartzschild radius $2\,G\,m_\bullet/c^2$ of the compact object in this context (see Kim & Kim 2009; Bernal & Sanchez-Salcedo 2013; Thun et al. 2016). The maximum impact parameter $r_{\rm max}$ is more controversial (see Binney & Tremaine 1987), and it is often taken to be the typical scale R_e of the gas distribution in which the perturber is moving (e.g., Rephaeli & Salpeter 1980; Lacey & Cole 1993; Silva 2016)[1]; other authors commonly assume $r_{\rm max} = v\,t$ that for a straight motion (or equivalently highly eccentric orbits) would correspond to the length of the wake behind the perturber (e.g., Ostriker 1999; Tagawa et al. 2016), or a direct proportionality $r_{\rm max} = 2\,r$ to the orbital radius r for perturbers in nearly circular and supersonic motion (Kim & Kim 2007).

Given this spectrum of possible choices, in this thesis I will explore the effect of three different prescriptions. The first one, inspired by Lacey & Cole 1993, is to adopt $r_{\rm max} = R_e$ and $r_{\rm min} = G\,m_\bullet/v^2$ in terms of the initial velocity v and mass $m_\bullet$ of the perturber, yielding a constant Coulomb logarithm $\ln\Lambda = \ln[R_e\,v^2/G\,m_\bullet]$. The second is to maintain the expression $\ln\Lambda = \ln[R_e\,v(t)^2/G\,m_\bullet(t)]$ but to use in it the running velocity $v(t)$ and mass $m_\bullet(t)$ of the perturber; the velocity changes along the orbit and on the average tends to decrease due to dynamical friction, while the mass can increase due to accretion of diffuse gas during the orbital evolution (see next Section). The third prescription, which will actually constitute my fiducial one, employs $r_{\rm max} = v\,t$ and $r_{\rm min} = G\,m_\bullet/v^2$, yielding $\ln\Lambda = \ln[v^3(t)\,t/G\,m_\bullet(t)]$; I also check that this prescription brings about very similar results to that based on $r_{\rm max} = 2\,r$ and $r_{\rm min} = G\,m_\bullet/v^2$, corresponding to $\ln\Lambda = \ln[v^2(t)\,r(t)/G\,m_\bullet(t)]$

3.1.3 Mass accretion onto perturbers

While the compact object, aka the perturber, is moving through the sea of gaseous particle, it can increase its mass by accretion (e.g., Bondi & Hoyle 1944; Edgar 2004; Cantó et al. 2013; Sanchez-Salcedo & Chametla 2018). Note that in this context the perturber is a compact remnant or a pBH in supersonic motion and the gain in mass by accretion is expected to be slow, so that I can safely neglect tidal debris effects on the orbit evolution.

[1] As a specific example, Lacey & Cole 1993 considered the dynamical friction force on perturbers orbiting in a SIS gravitational potential of collisionless matter; they choose $\ln\Lambda = \ln(v^2\,M_{\rm tot}/V_c^2\,m_\bullet)$ where $V_c = \sqrt{GM_{\rm tot}/R_e}$ is the circular velocity and $M_{\rm tot}$ the total mass; so their prescription is formally equivalent to take $r_{\rm min} \approx G\,m_\bullet/v^2$ and $r_{\rm max} \approx R_e$.

Mass accretion causes a net deceleration:

$$a_{\rm acc} = -\frac{\dot{m}_\bullet\, v(t)}{m_\bullet(t)} \tag{3.18}$$

and a simultaneous increase of the dynamical friction force $F_{\rm DF}$, which is proportional to the time-dependent mass $m_\bullet^2(t)$ after equation (3.15). In order to compute the mass accretion rate for a compact object moving through a gaseous medium, I use the recipe by Lee & Stahler 2011, 2014 (see also Tagawa et al. 2016):

$$\frac{{\rm d}m_\bullet}{{\rm d}t} = 4\pi G^2\, m_\bullet^2\, \frac{\rho}{c_s^3}\, \frac{\sqrt{\lambda^2+\mathcal{M}^2}}{(1+\mathcal{M}^2)^2}\,, \tag{3.19}$$

where $\lambda = 1.12$. Since in the present context the motion is largely supersonic, including this mass accretion is of minor relevance for what concerns the estimate of the dynamical friction timescales.

3.2 Perturbers dynamics

Now I put together the 3 ingredients examined in the previous Section to investigate the orbital evolution of a perturber in the central regions of submillimeter galaxies (Subsection 3.2.1) and I finally arrive to the computation of the dynamical friction timescale as a function of the compact object properties (initial mass $m_\bullet$, energy and angular momentum) and of the considered galactic environment (parametrized by gas mass $M_{\rm gas}$, half-mass radius R_e, Sersic parameters n and α) (Subsection 3.2.2).

3.2.1 Orbital decay by gaseous dynamical friction

The total energy ϵ and angular momentum j per unit mass of a compact object in orbit around the galactic center can be computed from its total velocity $v = \sqrt{v_r^2 + v_\theta^2}$, its tangential component v_θ and its distance r from the center as:

$$\begin{cases} \varepsilon = \dfrac{v^2}{2} + \phi(r) \\ \\ j = r\, v_\theta\,, \end{cases} \tag{3.20}$$

These are the basic quantities to follow the orbital evolution. The dynamical friction force $|F_{\rm DF}|$ dissipates both energy and angular momentum according to the evolution equations:

$$\begin{cases} \dfrac{\mathrm{d}\varepsilon}{\mathrm{d}t} = -v\dfrac{|F_{\rm DF}|}{m_\bullet} \\ \\ \dfrac{\mathrm{d}j}{\mathrm{d}t} = -\dfrac{j}{v}\dfrac{|F_{\rm DF}|}{m_\bullet} \end{cases} \tag{3.21}$$

I use the orbit-averaged approximations (e.g., Lacey & Cole 1993; Tonini et al. 2006), consisting in evaluating the total energy and angular momentum lost during the entire orbit, yielding:

$$\begin{cases} \langle\dot{\varepsilon}\rangle = -\dfrac{\int_{r_-}^{r_+}\mathrm{d}r\,(v/v_r)\,|F_{\rm DF}|/m_\bullet}{\int_{r_-}^{r_+}\mathrm{d}r/v_r} \\ \\ \langle\dot{j}\rangle = -j\,\dfrac{\int_{r_-}^{r_+}\mathrm{d}r\,(1/v_r)\,(1/v)\,|F_{\rm DF}|/m_\bullet}{\int_{r_-}^{r_+}\mathrm{d}r/v_r} \end{cases} \tag{3.22}$$

where $v_r = \sqrt{2\,[\varepsilon - \phi(r)] - j^2/r^2}$ is the radial velocity component, and r_- and r_+ are the pericenter and apocenter radial positions determined by the condition $v_r = 0$; the corresponding orbital eccentricity can be computed as:

$$e = \frac{r_+ - r_-}{r_+ + r_-} \tag{3.23}$$

Notice that when in the Coulomb logarithm $\ln\Lambda = \ln r_{\rm max}/r_{\rm min}$ a time-dependent $r_{\rm max}(t) = v\,t$ is adopted, the above equation must be modified somewhat. I recall that this choice of $r_{\rm max}$ was justified by Ostriker 1999 as the displacement of a perturber travelling on a straight line after a time t, so it represents a lengthscale of the wake. In the case of elliptical orbits, such a quantity depends on the perturber position and, since at the apocenter and pericenter the direction of motion is reversed, the wake cannot be longer than half of the orbit. Thus I divide the above orbit-averaged integral into two halves, taking into account that when the perturber is at apocenter or pericenter the time appearing into the expression for $r_{\rm max} \propto t$ must be reset

to zero. Writing $F_{\rm DF}(\ln\Lambda)$ as a function of the Coulomb logarithm, I use:

$$\begin{cases} \langle\dot{\varepsilon}\rangle = -\dfrac{\int_{r_-}^{r_+} \mathrm{d}r\,(v/v_r)|F_{\rm DF}(\ln\Lambda_-)| + \int_{r_+}^{r_-} \mathrm{d}r\,(v/v_r)|F_{\rm DF}(\ln\Lambda_+)|}{2m_\bullet \int_{r_-}^{r_+} \mathrm{d}r/v_r} \\ \\ \langle\dot{j}\rangle = -j\,\dfrac{\int_{r_-}^{r_+} \mathrm{d}r\,(1/v_r v)|F_{\rm DF}(\ln\Lambda_-)| + \int_{r_+}^{r_-} \mathrm{d}r\,(1/v_r v)|F_{\rm DF}(\ln\Lambda_+)|}{2m_\bullet \int_{r_-}^{r_+} \mathrm{d}r/v_r} \end{cases} \tag{3.24}$$

where $\ln\Lambda_\pm = \ln(v\,t_\pm/r_{\rm min})$ in terms of the time $t_\pm(r) = \int_{r_\pm}^{r} \mathrm{d}r/v_r$ elapsed at distance r from/to pericenter/apocenter.

A couple of consequences found by computing the above terms are the following. First, the points which contribute more to the dynamical friction force $F_{\rm DF} \propto \rho/v^2$ turn out to be the pericenter and apocenter; the former is the innermost point of the orbit where the gas density ρ is higher, while the latter is the outermost point of the orbit where the velocity v of the perturber is smaller. Second, gaseous dynamical friction is much more efficient in dissipating angular momentum than energy; as a consequence, the apocenter r_+ evolves slowly, being mainly determined by the orbital energy, while the pericenter r_- decays much rapidly, being directly related to the centrifugal barrier, and the overall orbit eccentricity increases. In fact, this process is of runaway type since as j decreases, higher density regions are reached at pericenter while the velocity lowers near apocenter, to imply enhanced dynamical friction force and further angular momentum loss.

I numerically integrate the orbit-averaged equations $\mathrm{d}\varepsilon/\mathrm{d}t = \langle\dot{\varepsilon}\rangle$ and $\mathrm{d}j/\mathrm{d}t = \langle\dot{j}\rangle$ to determine the timescale $\tau_{\rm DF}$ needed for the compact remnant to migrate to the galaxy center. Actually, I halt the computation when the pericenter attains a value below $r_- \sim 10^{-5}$ pc, since in these nuclear region the migrating compact remnant feels the potential of the growing central BH, and rapid energy and angular momentum losses eventually take place due to emission of GWs; the orbit-averaged loss rates (see Peters 1964) $\langle\dot{\varepsilon}_{\rm GW}\rangle \propto (1-e^2)^{-7/2}$ and $\langle\dot{j}_{\rm GW}\rangle \propto (1-e^2)^{-2}$ are very efficient since the remnant tends to reach such inner regions with high eccentricity $e \approx 1$, enforced by the gaseous dynamical friction on larger scales; subsequently, the orbit shrinks rapidly and merging between the central BH and the migrating compact object can occur. I stress that the runaway nature of the pericenter decay makes of minor relevance the choice of the minimum radius where the computation of the dynamical friction evolution is stopped and $\tau_{\rm DF}$ is evaluated.

In Figure 3.2 I show the evolution of the potential and total energy, of the

pericenter and apocenter, and of the orbital eccentricity, for two representative cases with nearly circular $e \lesssim 0.1$ (left column) and mildly eccentric $e \sim 0.5$ (right column) initial orbits; reference values $M_{\rm gas} = 10^{11}\,{\rm M}_\odot$, $R_e = 1$ kpc and $m_\bullet = 100\,M_\odot$ have been adopted. It can be easily appreciated the runaway decrease of the pericenter r_-; this is mainly driven by the loss in angular momentum, which reduces the centrifugal barrier and hence flattens the shape of the effective potential at small radii. Contrariwise, the apocenter r_+ is mainly determined by the decrease in total energy and decays slowly; as a consequence, the orbital eccentricity increases with time. Less eccentric initial conditions imply longer overall dynamical timescales, but a more rapid evolution of the apocenter (somewhat parallel to the pericenter), since the system remain quite close to a circular orbit, with the total energy hovering around the minimum of the effective potential; correspondingly, the eccentricity stays low for most of the evolution, and then rises abruptly close to the pericenter runaway.

3.2.2 Gaseous dynamical friction timescales

The resulting dynamical friction timescale $\tau_{\rm DF}$ depends on the properties of the background gas mass distribution (half-mass radius R_e, total mass $M_{\rm gas}$ and shape parameters n and α), and on the initial mass $m_\bullet$, energy ε and angular momentum j of the compact object.

Actually it is convenient to express the dependence on energy through the circular radius $r_c(\varepsilon)$ that the compact remnant would have if it were on a circular orbit at given energy ε; this is computed just by solving $\varepsilon = G\,M(<r_c)/2\,r_c + \phi(r_c)$. On the same footing $j_c(\varepsilon) = \sqrt{G\,M(<r_c)/r_c}$ will be the angular momentum associated to that circular orbit, and so the ratio $j/j_c(\varepsilon)$ constitutes a measure of the (non-)circularity of the motion.

In terms of these quantities, the dynamical friction timescale can be expressed as:

$$\tau_{\rm DF} = \mathcal{N}\left(\frac{m_\bullet}{100 M_\odot}\right)^a \left(\frac{M_{\rm gas}}{10^{11}\,M_\odot}\right)^b \left(\frac{R_e}{1\,{\rm kpc}}\right)^c \left(\frac{j}{j_c(\varepsilon)}\right)^\beta \left(\frac{r_c(\varepsilon)}{10\,{\rm pc}}\right)^\gamma \tag{3.25}$$

where $\mathcal{N}$ is a normalization constant.

When the mass accretion onto the perturber is neglected and the Coulomb logarithm $\ln\Lambda = \ln[R_e\,v^2/G\,m_\bullet]$ in the dynamical friction force is taken to be constant in time (see Section 3.1.2), one obtains the exponents $a \approx -1$, $b \approx 1/2$, $c = (\alpha-3)/2$, $\beta \approx 2$, and $\gamma \approx 3-\alpha/2$. The dependencies on $m_\bullet$ and $M_{\rm gas}$ are somewhat trivial and can be derived basing on a simple dimensional analysis of the orbital equations (e.g., Lacey & Cole 1993; Tamburello

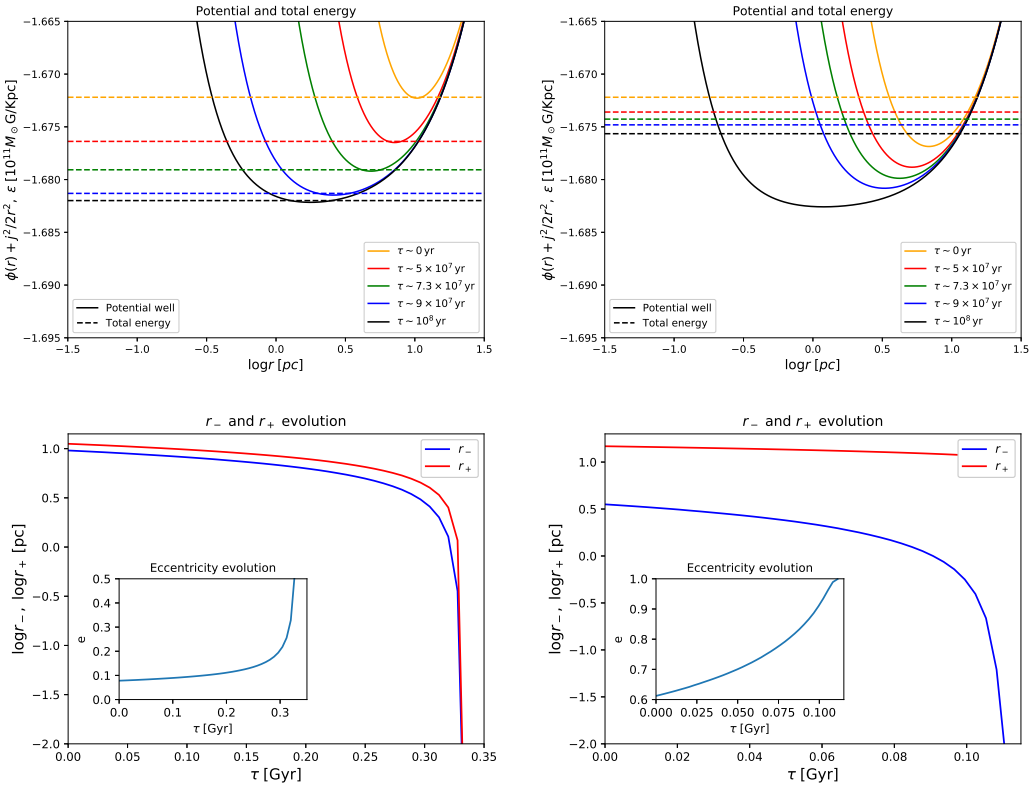

FIGURE 3.2: Top panels: effective potential $\phi(r) + j^2/2\,r^2$ (solid lines) and total energy ε (dashed lines) at different times τ (color coded as in legend) for a perturber of $m_\bullet = 100\,M_\odot$ experiencing dynamical friction against a gaseous medium of mass $M_{\rm gas} = 10^{11}\,M_\odot$ distributed with a Sersic profile with index $n = 1.5$ and half-mass radius $R_e = 1$ kpc; the initial configuration of the perturber is such that the circularity $j/j_c(\varepsilon)$ amounts to 1 (nearly circular orbit) in the left panels and to 0.5 (mildly eccentric orbit) in the right panels, with the same total energy. Bottom panels: evolution of the pericenter r_- (blue line), of the apocenter r_+ (red line) and of the eccentricity e (cyan line in the inset), for the same configurations as above.

et al. 2017). In addition, the dependencies on R_e and on $r_c(\varepsilon)$ are controlled by the inner slope of the density profile α, independently on the Mach number (and actually being the same also for dynamical friction against a collisionless background). Indeed a remarkable agreement has been found between equation (3.25) and other literature formula for dynamical friction in a collisionless medium, adopting specific gas density shapes. For example, adopting a SIS profile with $\alpha = 2$ as in Lacey & Cole 1993 yields $c \approx -1/2$ and $\gamma \approx 2$, in agreement with their result, while adopting a Hernquist profile with $\alpha = 1$ yields $c \approx -1$ and $\gamma \approx 5/2$ as in Tamburello et al. 2017. Finally,

Gaseous dynamical friction timescale: parameter dependence

Profile	n	α	$\ln\Lambda$	$\mathcal{N}/10^8$ yr	a	b	c	β	γ
Sersic	1.5	0.6	$\ln[v^3(t)t/Gm_\bullet(t)]$	3.4	−0.95	0.45	−1.2	1.5	2.5
Sersic	1.5	1	$\ln[v^3(t)t/Gm_\bullet(t)]$	5.9	−0.95	0.45	−1	1.5	2.4
Sersic	4	0.6	$\ln[v^3(t)t/Gm_\bullet(t)]$	13.6	−0.95	0.45	−1.2	1.5	2.4
Sersic	1.5	0.6	$\ln[R_e v^2(t)/Gm_\bullet(t)]$	2.5	−0.95	0.45	−1.2	1.8	2.6
Sersic	1.5	0.6	$\ln[R_e v^2/Gm_\bullet]$ = const	2.2	−1	0.5	−1.2	2	2.7
Hernquist	–	1	$\ln[R_e v^2/Gm_\bullet]$ = const	5.7	−1	0.5	−1	2	2.5
SIS	–	2	$\ln[R_e v^2/Gm_\bullet]$ = const	21.4	−1	0.5	−0.5	2	2

TABLE 3.1: Gaseous dynamical friction timescale: parameter dependence

the exponent β is found to be independent of the profile, but to depend crucially on the Mach number of the perturber during its motion in the background gaseous atmosphere; in particular, if the motion is supersonic like in the present case then $\beta \approx 2$ applies, while for (sub)sonic motion (or when the medium is collisionless) the dependence is found to be much shallower $\beta \approx 0.78$, as in Lacey & Cole 1993.

When the mass accretion onto the perturber is switched on and a time-dependent Coulomb logarithm $\ln\Lambda = \ln[R_e\, v^2(t)/G\, m_\bullet(t)]$ is considered, the exponents in equation (3.25) change into $a \approx -0.95$, $b \approx 0.45$, $c \approx (\alpha-3)/2$, $\gamma \approx 3-\alpha/2+\epsilon_0(n,\alpha)$, and $\beta \approx 1.8$; here $\epsilon_0(n,\alpha)$ is a small correction dependent on the shape parameter of the density profile, with typical values $\epsilon_0(n,\alpha) \sim 10^{-1}$.

Finally, when the fiducial expression for the Coulomb logarithm $\ln\Lambda = \ln[v^3(t)\, t/G\, m_\bullet(t)]$ is implemented, one finds the exponents $a \approx -0.95$, $b \approx 0.45$, $c \approx (\alpha-3)/2$, $\gamma \approx 3-\alpha/2+\epsilon_1(n,\alpha)$, and $\beta \approx 1.5+\epsilon_2(j/j_c)$. Thus in this case not only γ gets a correction $\epsilon_1(n,\alpha) \sim 10^{-1}$ dependent on the shape of the density profile, but also β acquires a weak dependence on the circularity $j/j_c(\varepsilon)$ via the quantity $\epsilon_2(j/j_c)$ that spans the range –0.3 to 0 to 0.3 when j/j_c increases from 0 to 0.5 to 1. In Table 3.1 I report the values of the exponents and of the normalization constant $\mathcal{N}$ appearing in equation (3.25) for some representative cases. Variations of the Coulomb logarithm, of Sersic indeces and of the gas density profile are reported.

In Table 3.2 I present specific examples of the resulting dynamical friction timescales. The Table refers to the reference Sersic density profile with $n = 1.5$, $\alpha = 0.6$, and time-dependent Coulomb logarithm $\ln[v^3(t)t/Gm_\bullet(t)]$ with mass accretion onto the perturber switched on. For different values of the initial physical radius r, velocities $v_{r,\theta}/\sigma(r)$ and perturber mass $m_\bullet$, I report the circular radius $r_c(\varepsilon)$, circularity $j/j_c(\varepsilon)$ and the dynamical friction

Gaseous dynamical friction timescale: examples

r/pc	$v_r/\sigma(r), v_\theta/\sigma(r)$	r_c/pc	j/j_c	$\tau_{\rm DF}$/Gyr			
				$m_\bullet = 1.5\,M_\odot$	$m_\bullet = 10\,M_\odot$	$m_\bullet = 40\,M_\odot$	$m_\bullet = 100\,M_\odot$
5	1, 1	30	0.18	–	4.1	1.1	0.46
5	1, 0.1	18	0.041	0.75	0.12	0.033	0.014
5	0.1, 1	18	0.41	–	4.0	1.0	0.44
5	0.1, 0.1	4	0.55	0.75	0.12	0.033	0.014
15	1, 1	50	0.31	–	–	9.4	3.9
15	1, 0.1	33	0.064	6.4	1.0	0.28	0.12
15	1, 0.025	33	0.016	0.80	0.13	0.035	0.015
30	1, 1	76	0.41	–	–	–	–
30	1, 0.1	50	0.080	–	4.1	1.1	0.46
30	1., 0.01	50	0.0081	0.79	0.13	0.035	0.015
50	1, 1	100	0.49	–	–	–	–
50	1, 0.1	70	0.089	–	–	3.0	1.2
50	1, 0.01	70	0.0090	2.1	0.35	0.093	0.039
50	1, 0.005	70	0.0045	0.75	0.12	0.033	0.014
150	1, 1	200	0.64	–	–	–	–
150	1, 0.1	150	0.10	–	–	–	10
150	1, 0.01	150	0.010	–	2.8	0.75	0.31
150	1, 0.001	150	0.0010	0.55	0.091	0.024	0.010
300	1, 0.1	26	0.10	–	–	–	–
300	1, 0.01	26	0.010	–	–	3.0	1.2
300	1, 0.001	26	0.0010	2.0	0.33	0.088	0.037
300	1, 0.0005	26	0.00050	0.72	0.12	0.032	0.013

TABLE 3.2: Gaseous dynamical friction timescale: some examples. A dash (–) indicates a timescale longer than 10 Gyr.

timescales $\tau_{\rm DF}$. It is found that dynamical friction timescales smaller than 1 Gyr are allowed for a variety of initial conditions and remnant masses, implying that the process can be relevant for the formation of heavy BH seeds.

The dependence of the dynamical friction timescale on initial conditions is easily explained. At given initial radius, raising v_r increases the energy so enhancing r_c but at the same time it decreases the circularity, so that the overall dependence on v_r is weak; this is why in the Table v_r is changed only in the case referring to $r = 5$ pc, but the behaviour for other radii stays put. The impact of v_θ is significant, since decreasing it both reduces the energy and the circularity, so shortening $\tau_{\rm DF}$. Increasing the initial radius r basically enhances the energy so raising $r_c(\varepsilon)$, making $\tau_{\rm DF}$ longer.

In Table 3.2 I also highlight that at larger radii the dynamical friction timescale can still be appreciably smaller than 1 Gyr if v_θ is sufficiently small. Given the Gaussian shape of the tangential velocity distribution (see equation (3.12)), this implies that a lower fraction of the compact remnants produced at larger radii can reach the nuclear region and contribute to the

growth of the central BH seed. On the other hand, given the inner power-law shape of the gas density profile $\propto r^{-\alpha}$, the number of compact remnants produced in larger radial shells increases as $\propto r^{2-\alpha}$ (see equation (3.11)). All in all, I find that these two effects partially compensate, so as to cause a similar overall contribution to the central BH mass growth from remnants formed at different radii, at least out to $r \sim 300$ pc where the exponential cutoff of the density profile progressively takes over drastically reducing the number of available remnants.

3.3 Merging rates

In this Section I make use of the expression for the dynamical friction timescale derived in the previous Section to compute the merging rates of compact remnants and of pBHs at different galactic ages, so evaluating the contribution of this process to the growth of the central supermassive BH seed; in the next Section I will discuss how the efficiency of BH growth by dynamical friction compares and couples with that due to standard disk (Eddington-like) accretion.

Throughout all the Section I express the merging rates as a function of the redshift and of the spatially-integrated SFR of the host galaxy. Parametrizing galaxies in terms of SFR is necessary since in the next Sections I am going to compute the cosmic integrated merging rates via the SFR function statistics.

Stellar compact remnants

For stellar compact remnants, the merging rates per unit mass due to dynamical friction at a galactic age τ inside a galaxy with spatially-integrated SFR ψ at redshift z can be written as:

$$\frac{\mathrm{d}\dot{N}_{\mathrm{DF},\star}}{\mathrm{d}m_\bullet}(m_\bullet,\tau|\psi,z) = \int \mathrm{d}r \frac{\mathrm{d}p}{\mathrm{d}r}(r) \int \mathrm{d}v_\theta \frac{\mathrm{d}p}{\mathrm{d}v_\theta}(v_\theta|r)\times \\ \times \int \mathrm{d}v_r \frac{\mathrm{d}p}{\mathrm{d}v_r}(v_r|r)\, \frac{\mathrm{d}\dot{N}_{\mathrm{birth}}}{\mathrm{d}m_\bullet}(m_\bullet,\tau-\tau_{\mathrm{DF}}|\psi,z) \tag{3.26}$$

here $\mathrm{d}p/\mathrm{d}r$ and $\mathrm{d}p/\mathrm{d}v_{r,\theta}$ are the probability distributions of initial radii and velocities given in equations (3.11) and (3.12); $\mathrm{d}\dot{N}_{\mathrm{birth}}/\mathrm{d}m_\bullet(m_\bullet,\tau|\psi,z)$ is the birthrate for a stellar compact remnant of mass $m_\bullet$ at a galactic age τ and $\tau_{\mathrm{DF}}[m_\bullet,\varepsilon(r,v_\theta,v_r),j(r,v_\theta)]$ is the dynamical friction timescale (see equation

(3.25)) for a compact remnant of mass $m_\bullet$, formed at radius r with initial velocities $v_{r,\theta}$, or equivalently with energy ε and angular momentum j. The underlying rationale of this expression is that the merging rate at the galactic age τ depends directly on the birthrate $\mathrm{d}\dot{N}_{\rm birth}/\mathrm{d}m_\bullet$ at a galactic age $\tau - \tau_{\rm DF}$ (plainly I require that $\tau_{\rm DF}$ for a compact remnant is longer than the progenitor star's lifetime); the resulting quantity turns out to be a function of the initial radius and velocities, that are averaged over the associated distributions.

As already shown, both the dynamical friction timescale $\tau_{\rm DF}$ and the distributions of initial radii and velocities depend on the gas density profile, and in particular on the initial total gas mass $M_{\rm gas}$. I compute $M_{\rm gas}$ for a given value of ψ by first estimating the stellar mass from the galaxy main sequence by Speagle et al. 2014, and then inferring the initial gas mass from the redshift-dependent $M_\star/M_{\rm gas} - M_\star$ relation by Lapi et al. 2017 (see also Moster et al. 2013; Aversa et al. 2015; Shi et al. 2017; Behroozi et al. 2019) based on abundance matching techniques.

Coming back to equation (3.26) the birthrate $\mathrm{d}\dot{N}_{\rm birth}/\mathrm{d}m_\bullet$ is computed as follows (e.g., Dvorkin et al. 2016; Cao et al. 2018; Li et al. 2018; Boco et al. 2019):

$$\frac{\mathrm{d}\dot{N}_{\rm birth}}{\mathrm{d}m_\bullet}(m_\bullet, \tau|\psi, z) = \psi \int_{m_{\star,\rm min}} \mathrm{d}m_\star \, \phi(m_\star) \, \frac{\mathrm{d}p}{\mathrm{d}m_\bullet}(m_\bullet|m_\star, Z(\tau|\psi, z)) \quad (3.27)$$

the quantity $\mathrm{d}p/\mathrm{d}m_\bullet$ represents the probability distribution of producing a compact remnant of mass $m_\bullet$ given the initial star mass $m_\star$ and metallicity Z. Following Boco et al. 2019 this probability distribution is taken to be a log-normal:

$$\frac{\mathrm{d}p}{\mathrm{d}\log m_\bullet}(m_\bullet|m_\star, Z) = \frac{1}{\sqrt{2\pi}\,\sigma_{\log m_\bullet}} \exp\left\{-[\log m_\bullet - \log m_\bullet(m_\star, Z)]^2/2\,\sigma^2_{\log m_\bullet}\right\} \quad (3.28)$$

centered around the average relationship $m_\bullet(m_\star, Z)$ obtained by Spera & Mapelli 2017 (see also Spera et al. 2015 for details) via the SEVN stellar evolutionary code including pair-instability and pair-instability pulsational supernovae (causing a 'failed' explosion and a direct collapse to BH), and with a dispersion of $\sigma_{\log m_\bullet} = 0.1$ dex that takes into account plausible astrophysical uncertainties and intrinsic scatter.

The Spera relation $m_\bullet(m_\star, Z)$, relating the mass of the compact remnant to that of the progenitor star, depends crucially on the gas metallicity $Z(\tau|\psi, z)$; I compute the latter as a function of the galactic age τ using the chemical evolution model described in Chapter 2 and Appendix A.

In equation (3.27) the remnant distribution $\mathrm{d}p/\mathrm{d}m_\bullet$ is then integrated over the star masses $m_\star$, weighting by the IMF $\phi(m_\star)$ from the lower limit $m_{\star,\mathrm{min}} \sim 8\,M_\odot$ required to produce a compact remnant (i.e., neutron star or BH). Finally, the result is multiplied by the SFR ψ acting as a normalization factor, just specifying that galaxies with larger SFRs will produce more numerous compact remnants.

In Figure 3.3 I illustrate the merging rate $\mathrm{d}\dot{N}_\mathrm{DF}/\mathrm{d}\log m_\bullet$ per unit logarithmic bin of compact remnant mass $m_\bullet$, for a galaxy at redshift $z \sim 2$ and spatially-integrated SFR $\psi \sim 300\,M_\odot/\mathrm{yr}$, at different galactic ages τ; this SFR is a typical value for a star-forming ETG progenitor at $z \sim 2$, that characterizes galaxies at the knee of the SFR function (e.g., Gruppioni et al. 2013; 2015; Mancuso et al. 2016; Lapi et al. 2017, 2018). At early times (say 10^7 yr, which are anyway needed for the most massive stars to explode as supernovae) only the most massive compact remnants with $m_\bullet \gtrsim 30\,M_\odot$ contribute to the merging rate, since the dynamical friction timescale is shorter for them (see equation (3.25) and Table 3.2). At later stages, compact remnants of all masses progressively enter into the game. After some 10^7 yr the shape of the merging rate becomes stationary, with some relevant characteristic features: (i) a peak at around $m_\bullet \sim 1.5$–$2\,M_\odot$ representing the contribution from neutron stars, which are much more abundant than BHs for the standard Chabrier IMF adopted here; (ii) a rise toward more massive remnants due to the increased efficiency of the dynamical friction process for larger $m_\bullet$; (iii) a second peak for masses in the range $m_\bullet \sim 40 - 60\,M_\odot$, which are created more frequently according to the birthrate mass spectrum; (iv) a subsequent decline for remnants with $m_\bullet \gtrsim 60\,M_\odot$, that is due to the strong suppression in the birthrate for these masses by pair-instability and pair-instability pulsational supernovae.

As the galaxy age increases, the overall merging rate grows in normalization just because even compact remnants with larger τ_DF can reach the galaxy center. At galactic ages $\tau \gtrsim 10^8$ yr the aforementioned second peak tends to shift toward lower masses, and the drop kicks in for masses $m_\bullet \geq 40\,M_\odot$; this occurs because the metallicity increases with the galactic age, up to a value $Z \gtrsim 0.1\,Z_\odot$ when very massive BH remnants are no more efficiently produced according to the relation $m_\bullet(m_\star, Z)$, due to stronger stellar winds (see Section 2.2).

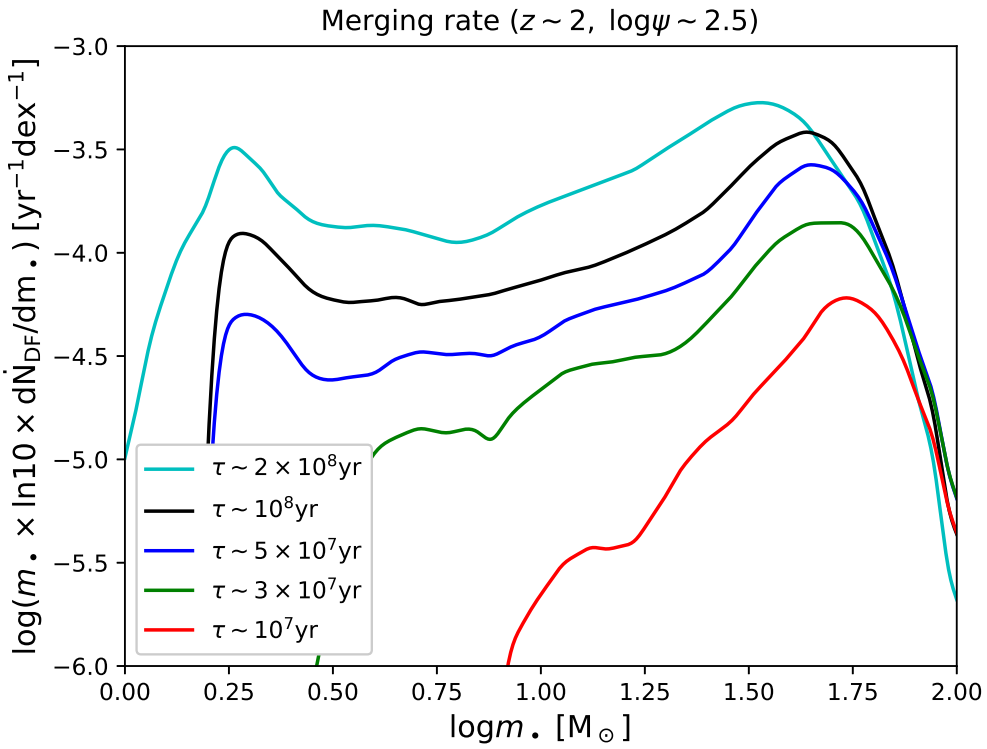

FIGURE 3.3: Merger rate due to gaseous dynamical friction per unit logarithmic bin of stellar compact remnant mass at different galactic ages (color-coded as in legend), for a typical ETG progenitor located at $z \sim 2$ and featuring a SFR $\psi \sim 300\, M_\odot$ yr^{-1}.

Primordial black holes

The merging rates per unit pBH mass in a galaxy with average SFR ψ at redshift z is written:

$$\frac{\mathrm{d}\dot{N}_{\mathrm{DF,pBH}}}{\mathrm{d}m_\bullet}(m_\bullet,\tau|\psi,z) = N_{\mathrm{pBH}}\frac{\mathrm{d}p}{\mathrm{d}m_\bullet}\int \mathrm{d}r\,\frac{\mathrm{d}p}{\mathrm{d}r}(r)\int \mathrm{d}v_\theta\,\frac{\mathrm{d}p}{\mathrm{d}v_\theta}(v_\theta|r)\times \\ \times\int \mathrm{d}v_r\,\frac{\mathrm{d}p}{\mathrm{d}v_r}(v_r|r)\,\delta_{\mathrm{D}}(\tau-\tau_{\mathrm{DF}}) \tag{3.29}$$

Since pBHs are not continuously created as stellar compact remnants, but are a component of the dark matter halo, the birthrate appearing in equation (3.26) is replaced here by a Dirac delta distribution $\delta_{\mathrm{D}}(\cdot)$ selecting only the pBHs with dynamical friction timescale equal to the galaxy age $\tau_{\mathrm{DF}} = \tau$.

As for the stellar remnants case, also the pBHs merging rate is parametrized in terms of SFR. The dependence on the galaxy SFR enters in the dynamical friction timescale through M_{gas} and in the total number of pBHs N_{pBH}. Indeed, as seen in equation (3.14), N_{pBH} is proportional to the halo mass, which, in turn, can be related to SFR via abundance matching techniques (see Aversa et al. 2015; Scelfo et al. 2020; Capurri et al. 2021).

3.4 Central mass growth

The overall merging rate at galactic age τ due to dynamical friction migration of stellar compact remnants and pBHs can be found by integrating equations (3.26) and (3.29) over the remnant masses:

$$\dot{N}_{\mathrm{DF},\star/\mathrm{pBH}}(\tau) = \int \mathrm{d}m_\bullet\,\frac{\mathrm{d}\dot{N}_{\mathrm{DF},\star/\mathrm{pBH}}}{\mathrm{d}m_\bullet}(m_\bullet,\tau|\psi,z) \tag{3.30}$$

while the growth rate of the central BH mass is given by:

$$\dot{M}_{\bullet,\mathrm{DF},\star/\mathrm{pBH}}(\tau) = \int \mathrm{d}m_\bullet\,m_\bullet\,\frac{\mathrm{d}\dot{N}_{\mathrm{DF},\star/\mathrm{pBH}}}{\mathrm{d}m_\bullet}(m_\bullet,\tau|\psi,z) \tag{3.31}$$

Clearly, further integrating the latter equation over time provides the contribution of dynamical friction to the growth of the central BH as a function of galactic age:

$$M_{\bullet,\mathrm{DF},\star/\mathrm{pBH}}(\tau) = \int_0^\tau \mathrm{d}\tau'\,\dot{M}_{\bullet,\mathrm{DF},\star/\mathrm{pBH}}(\tau'|\psi,z) \tag{3.32}$$

To ease the notation I have dropped from the quantities on the left hand side the explicit dependence on the galaxy SFR ψ and redshift z, but the reader should keep track of that for use in the next Sections.

Note that, for the sake of simplicity, I am assuming that the migrating remnants accumulate their mass in a single, or at least dominant, central BH; actually, in the early stages multiple of such sinks could originate but dynamical friction, being stronger for more massive perturbers, should enforce rapid merging among them.

Once the central BH mass starts to accumulate, standard disk accretion becomes an additional source for the hole growth. In a gaseous-rich environment like the nuclear region of ETG progenitors, the disk accretion is typically demand-limited. For the sake of definiteness, I assume an Eddington-like accretion rate (i.e., proportional to the BH mass) with a given Eddington ratio $\lambda \equiv L/L_{\rm Edd}$ in terms of the Eddington luminosity $L_{\rm Edd} \approx 1.4 \times 10^{38}\, M_\bullet/M_\odot$ erg s^{-1}, and a radiative efficiency $\eta \equiv L/\dot{M}_\bullet\, c^2$ of order 10% (see Davis & Laor 2011; Raimundo et al. 2012; Wu et al. 2013; Aversa et al. 2015). The resulting growth rate due to accretion onto the disk is:

$$\dot{M}_{\bullet,\rm acc} = \frac{M_\bullet}{\tau_{\rm ef}} \tag{3.33}$$

where the e–folding time amounts to $\tau_{\rm ef} \approx 4.5 \times 10^7\, \lambda^{-1}$ yr.

Thus the central mass growth, including both dynamical friction and disk accretion, can be computed simply by integrating the linear differential equation $\dot{M}_\bullet = \dot{M}_{\bullet,{\rm DF},\star}(\tau) + \dot{M}_{\bullet,{\rm DF,pBH}}(\tau) + \dot{M}_{\bullet,\rm acc}(M_\bullet(\tau)$, which yields:

$$M_\bullet(\tau) = M_\bullet(0)\, e^{\tau/\tau_{\rm ef}} + \int_0^\tau {\rm d}\tau' e^{-(\tau'-\tau)/\tau_{\rm ef}}\, (\dot{M}_{\bullet,{\rm DF},\star}(\tau') + \dot{M}_{\bullet,{\rm DF,pBH}}(\tau')) \tag{3.34}$$

Since $\dot{M}_{\bullet,\rm acc}$ is proportional to the central BH mass, at early times disk accretion is expected to be subdominant with respect to dynamical friction, and to dominate at late times.

In the top panel of Figure 3.4 I illustrate the growth of the central BH, and the contribution from dynamical friction and Eddington accretion ($\lambda = 1$) for a galaxy at redshift $z \approx 7$ with SFR $\psi \sim 100\, M_\odot$ yr^{-1}, apt for the typical hosts and progenitors of the most distant quasars (e.g., Venemans et al. 2017a,b, 2018). The red line is the contribution from stellar compact remnants that have been funnelled toward the center via dynamical friction; it starts to become somewhat relevant at $\tau \gtrsim 10^6$ yr which is the typical lifetime of the most massive stars. Through this channel, the central BH seed can attain a mass of $\gtrsim 10^4\, M_\odot$ in a timescale of $\sim 3 \times 10^7$ yr, effectively being able to provide an heavy seed for the future SMBH growth.

The green patch represents the contribution to the central BH mass from migrating pBHs. The edge solid line refers to $f_{\rm pBH} \approx 1$ while the dashed to $f_{\rm pBH} \approx 0.01$, and the area in between to values of $f_{\rm pBH}$ within this interval. pBHs can be driven toward the nuclear region more rapidly than stellar compact remnants and hence can provide the dominant contribution to the growth of the central BH seed in its initial phases. Then the contribution from stellar compact remnants takes over at a galactic age $\tau \gtrsim 10^6 - 3 \times 10^7$ yr, depending on the value of $f_{\rm pBH} \approx 0.01 - 1$. This behaviour is expected since pBHs are already distributed throughout the galaxy and can immediately undergo dynamical friction, while the formation of stellar compact remnants requires some time dictated by stellar evolution processes. Nevertheless, the growth of the central BH mass by migrating pBH is rather slow, since they are distributed over all the DM halo associated to the galaxy, so that their number in the central region, where the total mass density is indeed dominated by the baryonic component, is limited. This explains why, when stellar compact remnants start to migrate toward the center, their contribution promptly overcomes that of the pBHs. These considerations are generally true but quantitatively dependent on the pBH fraction $f_{\rm pBH}$; when $f_{\rm pBH} \gtrsim 0.3$, pBHs are still able to grow the central BH seed to masses $M_\bullet \gtrsim 10^3\,M_\odot$ before other processes take over. However, even in the absence of pBHs $f_{\rm pBH} = 0.01$, stellar compact remnants alone are still able to grow a central heavy seed.

The cyan patch is instead the contribution to the growth of the central BH by gas accretion, for different $f_{\rm pBH} \sim 0.01 - 0.1$ as above. As expected, gas accretion progressively takes over at later times $\tau \gtrsim 3 \times 10^7$ yr, when the central BH mass is $M_\bullet \gtrsim 10^4\,M_\odot$, and it rapidly leads the central BH to $M_\bullet \sim 10^9\,{\rm M}_\odot$ in a timescale of $\lesssim 300$ Myr. This is made possible thanks to the dynamical friction process, that was able to grow a heavy seed of $M_\bullet \sim 10^4 - 10^5\,M_\odot$ in first place, making very efficient the subsequent gas accretion onto it.

Finally, the black patch represents the sum of the three aforementioned contributions. Notice that, already at intermediate times $\sim 10^7$ yr, differences in $f_{\rm pBH}$ are partly suppressed by the contribution of stellar compact remnants and at late times they are completely washed out by the last phase of nearly exponential mass growth via gas accretion. Therefore I conclude that the existence of pBHs can have an important role in building up a BH seed in the very early stages. The mass of the seed so originated depends critically on the pBH mass fraction $f_{\rm pBH}$; the latter, however, cannot be probed by looking at the BH mass at late times, which is practically independent of the pBH contribution.

I compare this evolutionary track to the ones for pure disk accretion

(without dynamical friction) with Eddington ratios $\lambda = 1$ (dashed grey line) and $\lambda = 3$ (dotted grey line). It is seen that to obtain final BH masses of a few $10^9\,M_\odot$ within some 10^8 yr, super-Eddington accretion with $\lambda = 3$ is required if dynamical friction is switched off, while $\lambda = 1$ can be retained if dynamical friction enters into the game to build up an heavy seed at early stages. As discussed at the beginning of the Chapter this is particularly relevant at $z \gtrsim 7$, where an age of the Universe shorter than 0.8 Gyr is a demanding constraint. Although a mildly super-Eddington accretion with $\lambda \sim$ a few is not implausible at these early cosmic times (e.g., Li 2012; Madau et al. 2014; Aversa et al. 2015; Volonteri et al. 2015; Lupi et al. 2016; Davies et al. 2019; Regan et al. 2019), the formation of an heavy seed by dynamical friction as proposed here may constitute an alternative explanation or a complementary process.

In the bottom panel of the same Figure 3.4 I show the mass growth of a BH, in a galaxy at $z \approx 2$ with SFR $\psi \sim 300\,M_\odot\,\mathrm{yr}^{-1}$, representative of a typical ETG progenitor at the peak of the cosmic star formation history and at the knee of the SFR function. In this case the evolutionary track with dynamical friction (black patch) is obtained using an Eddington ratio $\lambda = 0.3$ and it is compared to that for pure disk accretion, without dynamical friction, with $\lambda = 1$ (grey dashed line). This is to show that, even at these intermediate redshifts, the dynamical friction mechanism allows to effectively create heavy seeds within $\tau \sim$ some 10^7. These may help to attain BH masses in excess of several $10^8 - 10^9\,M_\odot$ within a time $\tau_\psi \sim$ some 10^8 yr (the typical duration of the star formation and BH accretion in massive ETG progenitors), even with Eddington ratios $\lambda \sim 0.3$ appreciably smaller than 1, that are on the average suggested by single-epoch measurements in quasars out to $z \lesssim 4$ (see Vestergaard & Osmer 2009; Kelly & Shen 2013; Vestergaard 2019).

3.5 GW emission and detection

3.5.1 Rates and properties of GWs from dynamical mergers

The contribution to the early BH growth from migration of compact remnants and pBHs by gaseous dynamical friction in high-z ETG progenitors could hardly be probed via standard electromagnetic observations; even if it were present, luminous emission would be too weak and likely strongly dimmed by the very gas and dust-rich environment to be ever detected. However, I will show that the repeated mergers of the compact objects with the accumulating central BH mass can originate detectable GW signals (e.g., Barausse 2012; Barack et al. 2019). Specifically, in this Section I aim at computing the cosmic integrated GW rate density of these events as a function

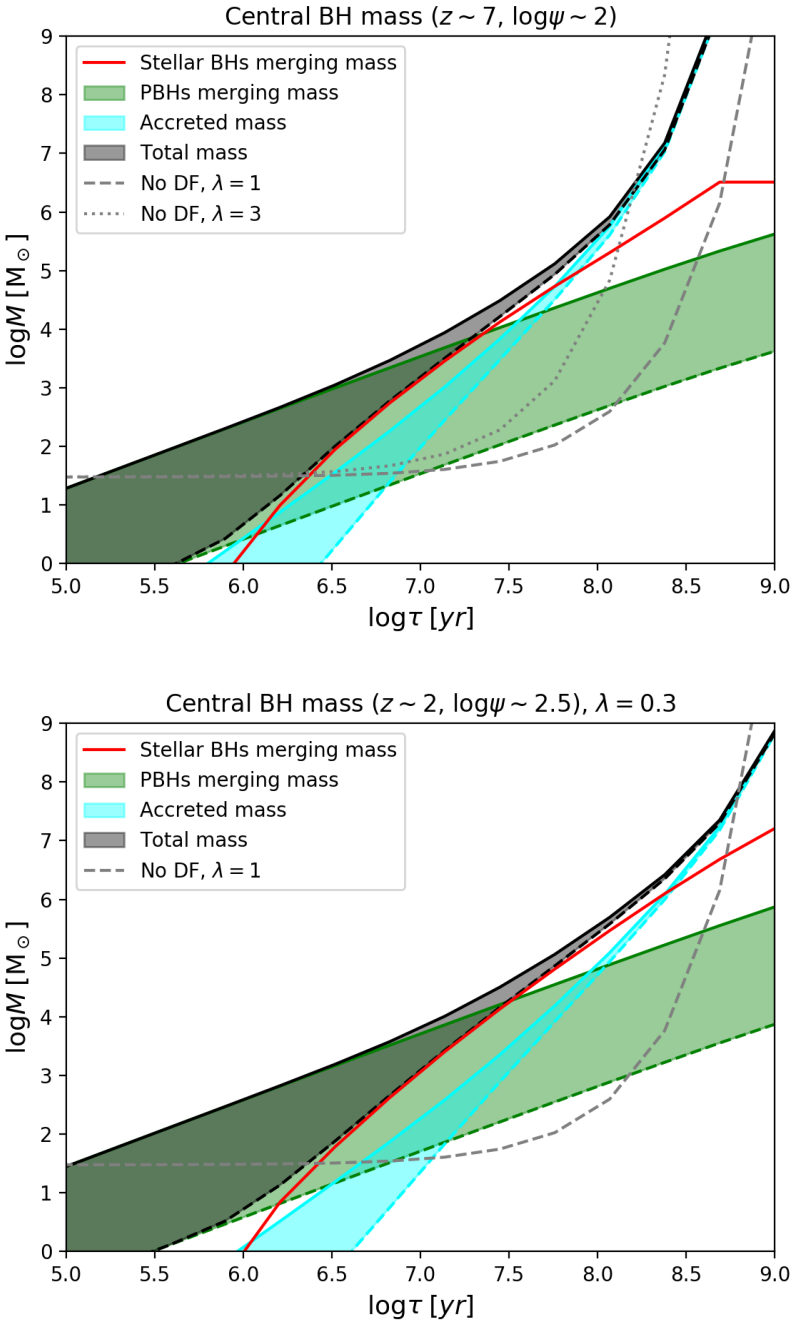

FIGURE 3.4: Growth of the central BH mass $M_\bullet$ as a function of the galactic age τ, due to the gaseous dynamical friction process discussed in this Chapter. Red line illustrates the contribution to the growth from migrating stellar compact remnants, green shaded area from migrating pBHs, cyan shaded area from gas accretion onto the central BH, and black shaded area refers to the the total mass. Both shaded areas show the effect of varying the pBH-to-DM fraction $f_{\rm pBH}$ from 0.01 (dashed edge lines) to 1 (solid edge lines). Top panel: host galaxy with average SFR $\psi \sim 100\,M_\odot$ yr^{-1} at redshift $z \approx 7$, the dashed grey line represents pure disk accretion with $\lambda = 1$, the dotted grey line represents pure disk accretion with $\lambda = 3$. Bottom panel: Eddington factor set to $\lambda = 0.3$. Host galaxy with average SFR $\psi \sim 300\,M_\odot$ yr^{-1} at redshift $z \approx 2$, the dashed gray line represents pure disk accretion with $\lambda = 1$.

of redshift, and their detectability with the future ET, DECIGO and LISA detectors.

Equation (3.34) establishes a one-to-one correspondence between the galaxy age τ and the value of the central BH mass $M_\bullet(\tau|\psi,z)$; moreover, the latter can be combined with a given mass $m_\bullet$ of the migrating compact object to construct the chirp mass $\mathcal{M}_{\bullet\bullet} = (M_\bullet\, m_\bullet)^{3/5}/(M_\bullet + m_\bullet)^{1/5}$, which determines the strength of the GW signal associated to each merging event. Thus the rate of mergers due to dynamical friction per bin of chirp mass is obtained easily from equations (3.26) and (3.29) by a change of variable, in the form:

$$\frac{\mathrm{d}\dot{N}_{\rm DF}}{\mathrm{d}\mathcal{M}_{\bullet\bullet}}(\mathcal{M}_{\bullet\bullet},\tau|\psi,z) = \frac{\mathrm{d}\dot{N}_{\rm DF}}{\mathrm{d}m_\bullet}(m_\bullet,\tau|\psi,z)\,\frac{\mathrm{d}m_\bullet}{\mathrm{d}\mathcal{M}_{\bullet\bullet}} \tag{3.35}$$

Note that here I have dropped the subscripts $\star/pBH$ to simplify the notation, but the reader should keep in mind that these equations refer to both the types of compact objects.

Noe I can compute the cosmic rate density of merging events due to dynamical friction per unit chirp mass $\mathcal{M}_{\bullet\bullet}$ and comoving cosmic volume V as a function of redshift z (or equivalently cosmic time t_z) as:

$$\frac{\mathrm{d}^2\dot{N}_{\rm DF}}{\mathrm{d}V\,\mathrm{d}\mathcal{M}_{\bullet\bullet}}(\mathcal{M}_{\bullet\bullet},z) = \int \mathrm{d}\psi\,\frac{\mathrm{d}^2N}{\mathrm{d}V\,\mathrm{d}\psi}(\psi,z)\int_{t_z-\tau_\psi}^{t_z}\mathrm{d}t_{\rm form}\,\frac{\mathrm{d}p}{\mathrm{d}t_{\rm form}}(t_{\rm form}|\psi)\times$$

$$\times\,\frac{\mathrm{d}\dot{N}_{\rm DF}}{\mathrm{d}\mathcal{M}_{\bullet\bullet}}(\mathcal{M}_{\bullet\bullet},t_z-t_{\rm form}|\psi,z)\,\Theta_{\rm H}(t_z-t_{\rm form}\le t_{\rm max}) \tag{3.36}$$

Here the contribution of different galaxies is weighted by the SFR function $\mathrm{d}N/\mathrm{d}V/\mathrm{d}\psi$, expressing the number density of galaxies per bin of SFR and comoving volume at different redshifts. Moreover, $t_{\rm form}$ is the formation time of the galaxy and $\mathrm{d}p/\mathrm{d}t_{\rm form}$ is the related probability distribution, that I take as flat for simplicity. Other relevant quantities are the star formation timescale τ_ψ and the maximum time $t_{\rm max}$ over which the dynamical friction process is active, as specified in terms of the Heaviside step function $\Theta_{\rm H}(\cdot)$.

The above equation can be understood along the following lines. The merging rates in a galaxy with given SFR ψ at redshift z are computed at the galactic age $\tau = t_z - t_{\rm form}$, averaging over all the possible formation times. Then the result is summed over all the galaxies with different SFR, weighted by their statistics. The meaning of the star formation timescales τ_ψ and of the activity timescale $t_{\rm max}$ for dynamical friction is more subtle. It is well established that, when the central BH mass has grown to substantial values $M_\bullet \gtrsim$ some $10^8\,M_\odot$, feedback in the form of energy and momentum from the active nucleus will affect the host galaxy, removing gas and quenching

the star formation; this typically occurs on a timescale τ_ψ which depends on the SFR and redshift, but typically amounts to several 10^8 yr. At this point, the gas reservoir is substantially reduced even on large scales and the dynamical friction process is also stopped, to imply $t_{\rm max} \sim \tau_\psi$. This will be my fiducial choice here, but I caveat that the BH feedback can be effective in depleting the gas reservoir from the nuclear regions, even before the galaxy-wide SFR is quenched, to imply $t_{\rm max} \lesssim \tau_\psi$; a strict lower limit to $t_{\rm max}$ could be some 10^7 yr, which is the timescale when the dynamical friction contribution to the growth of the central seed mass becomes subdominant with respect to gas accretion. I illustrate this case in Appendix D.

Integrating equation (3.36) over the chirp mass yields the cosmic rate density of merging events due to dynamical friction during BH seed formation:

$$\frac{{\rm d}\dot{N}_{\rm DF}}{{\rm d}V}(z) = \int {\rm d}\mathcal{M}_{\bullet\bullet} \frac{{\rm d}^2\dot{N}_{\rm DF}}{{\rm d}V\,{\rm d}\,\mathcal{M}_{\bullet\bullet}}(\mathcal{M}_{\bullet\bullet}, z) \tag{3.37}$$

valid both for stellar compact remnants and pBHs. I show the outcome as a function of redshift in Figure 3.5. The contribution of stellar compact remnants, which does not depend on $f_{\rm pBH}$, is shown as a solid red line. Their number density is comparable to that for the merging of isolated BH binaries, see e.g. Section 2.4. The pBH contribution is instead represented by the green patch for $f_{\rm pBH}$ ranging between 0.01 (dashed green edge line) and 1 (solid green edge line). Plainly, the number density of pBHs migrating toward the center grows with $f_{\rm pBH}$ but is always substantially lower with respect to that of stellar compact remnants.

The chirp mass distribution ${\rm d}^2\dot{N}_{\rm DF}/{\rm d}V/d\mathcal{M}_{\bullet\bullet}$ of equation (3.36) at a reference redshift $z \sim 2$ is shown in Figure 3.6. The red patch refers to stellar compact remnants, while the green patch to pBHs; solid edge lines are for $f_{\rm pBH} \approx 1$ and dashed edge lines for $f_{\rm pBH} \approx 0.01$. Notice that while the overall number density of stellar compact remnants mergers is independent of $f_{\rm pBH}$ (see Figure 3.5), their chirp mass distribution instead does depend on it. In fact, as seen in Section 3.4, pBHs migrate toward the galactic center earlier than stellar compact remnants and contribute to the initial growth of the central BH seed. A larger number of pBHs implies a faster growth of the central BH in the initial stages, so increasing the chirp mass of the subsequent merging events with stellar compact remnants. This explains why the chirp mass distribution for stellar compact remnants shifts towards higher chirp masses for larger values of $f_{\rm pBH}$.

The shape of the curves is mainly determined by the evolution of the central BH mass which grows by continuous mergers due to gaseous dynamical friction and by disk accretion. In the early stages the dynamical friction

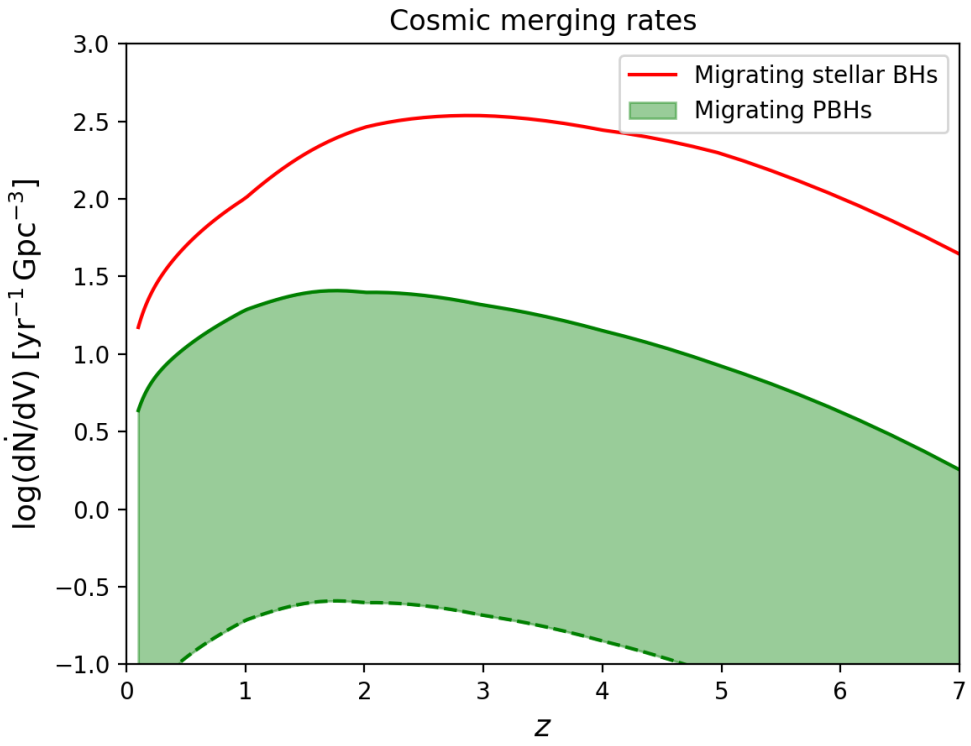

FIGURE 3.5: Cosmic merging rate density as a function of redshift, due to the gaseous dynamical friction process discussed in this thesis. Red solid line refers to migrating stellar compact remnants, green shaded area to migrating pBHs, for different pBH-to-DM fraction $f_{\rm pBH}$ ranging from 0.01 (dashed edge line) to 1 (solid edge line).

process dominates, and the time spent by the central BH in a given (logarithmic) mass bin increases with the BH mass; this in turn originates an increasing behaviour of the chirp mass distribution at low $\mathcal{M}_{\bullet\bullet}$. In the late evolution, the disk Eddington-like accretion takes over, and the time spent by the central BH in a given (logarithmic) mass bin is independent of the BH mass; thus the chirp mass distribution flattens at large $\mathcal{M}_{\bullet\bullet}$; the final drop at $\mathcal{M}_{\bullet\bullet} \gtrsim 10^5\,M_\odot$ is related to the absence of such huge chirp mass events since this extreme value would correspond to the coalescence of a central BH of $M_\bullet \approx 3\times10^9\,M_\odot$ with a stellar remnant of $m_\bullet \approx 100\,M_\odot$.

A useful quantity for the detection rates estimation is the probability distribution of mass ratios $q \equiv m_\bullet/M_\bullet$ at given chirp mass $\mathcal{M}_{\bullet\bullet}$, averaged over the galaxy population. To this purpose I relate each galactic age τ to the central BH mass $M_\bullet$ via equation (3.34), and then I express both

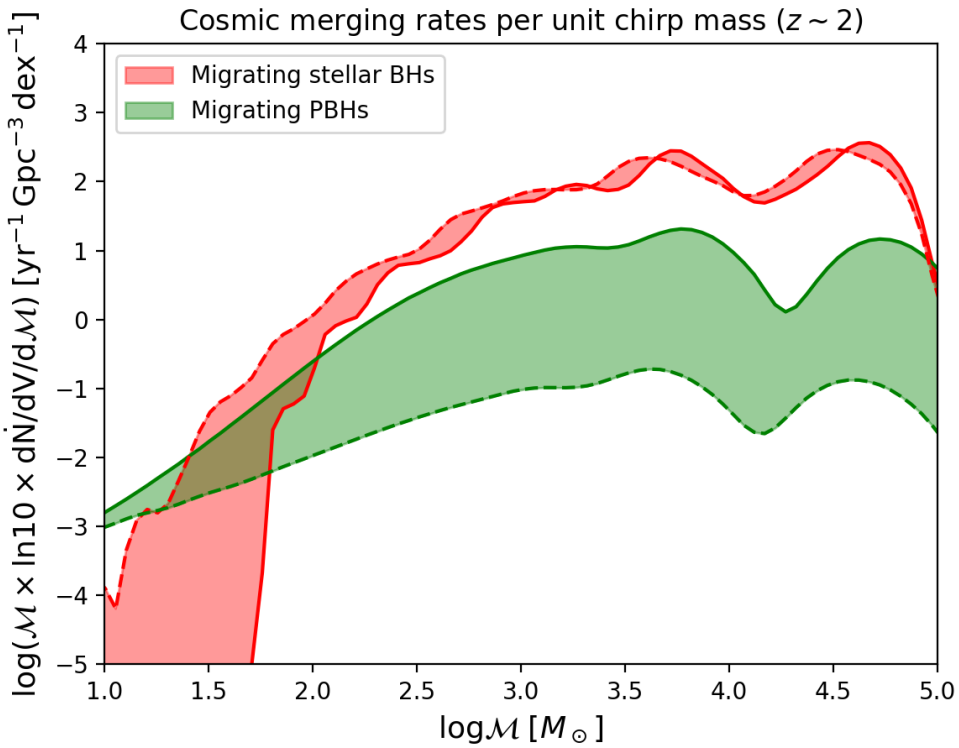

FIGURE 3.6: Cosmic chirp mass distribution at a reference redshift $z \sim 2$. Red shaded area refers to migrating stellar compact remnants, green shaded area to migrating pBHs, for different pBH-to-DM fraction $f_{\rm pBH}$ ranging from 0.01 (dashed edge lines) to 1 (solid edge lines).

$M_\bullet = \mathcal{M}_{\bullet\bullet}\, q^{-3/5}\,(1+q)^{1/5}$ and the merging compact remnant mass $m_\bullet = \mathcal{M}_{\bullet\bullet}\, q^{2/5}\,(1+q)^{1/5}$ in terms of $\mathcal{M}_{\bullet\bullet}$ and of q themselves. The mass ratio distribution from the dynamical friction process is then given by

$$\frac{\mathrm{d}p_{\rm DF}}{\mathrm{d}q}(q|\mathcal{M}_{\bullet\bullet},z) \propto \int \mathrm{d}\psi\, \frac{\mathrm{d}N}{\mathrm{d}V\,\mathrm{d}\psi}(\psi,z)\, \frac{\mathrm{d}m_\bullet}{\mathrm{d}q}\, \frac{\mathrm{d}\dot{N}_{\rm DF}}{\mathrm{d}m_\bullet}(m_\bullet(\mathcal{M}_{\bullet\bullet},q),\tau(\mathcal{M}_{\bullet\bullet},q)|\psi,z) \tag{3.38}$$

with the normalization constant determined by the condition $\int \mathrm{d}q\, \mathrm{d}p_{\rm DF}/\mathrm{d}q = 1$.

3.5.2 Rates and properties of detectable GWs

I now investigate the detectability of the merging events associated to the BH growth via dynamical friction and disk accretion by the future ground and space-based instruments, and in particular the ET, DECIGO and LISA. Given

their diverse frequency sensitivity bands, these detectors provide complementary information; specifically, ET will preferentially pinpoint the early stages of the process when the central BH has still a comparable mass to the migrating stellar remnants, while LISA will probe the subsequent phase when the central BH has already accumulated a mass much larger than that of the remnants, so as to originate intermediate to extreme mass ratio inspirals. The large frequency band and the exquisite sensitivity of DECIGO will allow it to probe both the phases of the process described in this Chapter.

I am interested in estimating the rate of detected events from redshift z with a sky-averaged signal-to-noise ratio $\sqrt{\bar{\rho}^2}$ exceeding a given threshold ρ_0 (standard values of $\rho_0 = 8$ for ET and DECIGO and $\rho_0 = 30$ for LISA are chosen). The procedure is similar to Section 2.5, with the S/N computed as in equation (2.34), but with some differences. First of all, in this case, the S/N dependence on the mass ratio q cannot be neglected, since q can span a large range of values during the whole process of seed growth. Moreover, as already explained in Section 2.5, the initial binary frequency when the detector is switched on, $f_{\rm in}$, cannot be approximated to $f_{\rm in} \simeq 0$ for LISA and it should be computed as in equation 2.5, so that also the dependence of S/N on $\Delta t_{\rm obs}$ must be kept into account. Finally, I stress that in the S/N computation, for simplicity, I consider only the inspiral phase up to the ISCO frequency, so that $\zeta = \zeta_{\rm ISCO}$.

All in all the detection rates per unit redshift and chirp mass can be written as:

$$\frac{\mathrm{d}^2\dot{N}}{\mathrm{d}z\,\mathrm{d}\mathcal{M}_{\bullet\bullet}}(z,\mathcal{M}_{\bullet\bullet},>\rho_0) = \frac{1}{1+z}\frac{\mathrm{d}V}{\mathrm{d}z}\frac{\mathrm{d}^2\dot{N}_{\rm DF}}{\mathrm{d}V\,\mathrm{d}\mathcal{M}_{\bullet\bullet}}(\mathcal{M}_{\bullet\bullet},z)\int \mathrm{d}q\,\frac{\mathrm{d}p_{\rm DF}}{\mathrm{d}q}(q|\mathcal{M}_{\bullet\bullet},z)\times$$
$$\times\int \mathrm{d}\Delta t_{\rm obs}\,\frac{\mathrm{d}p}{\mathrm{d}\Delta t_{\rm obs}}\,\Theta_{\rm H}\left(\sqrt{\bar{\rho}^2(\mathcal{M}_{\bullet\bullet},q,\Delta t_{\rm obs},z)}-\rho_0\right) \tag{3.39}$$

where $\mathrm{d}V/\mathrm{d}z$ is the comoving volume per unit redshift interval, the factor $1/(1+z)$ takes into account cosmological time dilation, $\mathrm{d}\dot{N}_{\rm DF}/\mathrm{d}V/\mathrm{d}\mathcal{M}_{\bullet\bullet}$ is the cosmic merging rate density from equation (3.36), $\mathrm{d}p_{\rm DF}/\mathrm{d}q$ is the mass ratio distribution from equation (3.38), $\mathrm{d}p/\mathrm{d}\Delta t_{\rm obs}$ is the probability distribution of observing the inspiral phase for a time interval $\Delta t_{\rm obs}$, and finally the Heaviside step function $\Theta_{\rm H}(\cdot)$ specifies that only events with sky-averaged S/N $\sqrt{\bar{\rho}^2}$ (that depends on all these variables) in excess of the threshold ρ_0 must be considered in the detection rate estimation.

Integrating equation (3.39) over the chirp mass yields the detected GW rates as a function of redshift for stellar compact remnants and pBHs. The

results for ET, DECIGO and LISA are shown in Figure 3.7; red patches are for stellar compact remnants, green patches for pBHs. The edge lines refer to $f_{\rm pBH} \approx 1$ (solid) and to $f_{\rm pBH} \approx 0.01$ (dashed). All in all, the outcomes mirror the intrinsic merging rates (see Figure 3.5).

In the ET case (top left panel) a larger value of $f_{\rm pBH}$ increases the detected GWs from pBHs and correspondingly decrease those from stellar compact remnants. Again this is due to the fact that pBHs contribute mainly to the initial growth of the central BH mass. If the number of pBHs increase, the central mass grows faster, and the migrating stellar compact remnants tend to merge with an already massive central BH seed; this will in turn make the GW signal to exit the ET observational window, which is sensible only to events with relatively low chirp mass $\mathcal{M}_{\bullet\bullet} \lesssim 500\,M_{\odot}$. This can be seen also from Figure 3.6, where for larger $f_{\rm pBH}$ the number of merging stellar compact remnants is the same, but their chirp mass distribution is shifted towards higher masses, so reducing the GW frequency and, consequently, the number of events detectable by ET. The ET detection rates of stellar compact remnants and pBHs are of the same order for $f_{\rm pBH} \sim 0.3$. I stress that, for any value of $f_{\rm pBH}$, the number of detected events are strongly suppressed with respect to the overall number of emitted GWs due to the frequency sensitivity band of ET and they are always lower than detected GW events associated to isolated compact binary mergers, described in Chapter 2. This can be seen from the dotted black line in the top panel of Figure 3.7, representing the forecast for the ET BH-BH detection rate done by Boco et al. 2019, which is $\gtrsim 2$ order of magnitude above the detected rates from the dynamical friction process.

To disentangle the events related to dynamical friction, one possibility is to rely on those with chirp masses much larger than expected from isolated binary mergers. To this purpose, in Figure 3.7 (top right panel) I also plot the rates of GW signals associated to the dynamical friction process with chirp mass $\mathcal{M}_{\bullet\bullet} \gtrsim 200\,M_{\odot}$. Plainly the detected rates are reduced somewhat, especially the ones for stellar compact remnants with $f_{\rm pBH} \sim 0.01$, but their number is still sizeable; a detection of these high-chirp mass event could could be a marking feature of the BH seed formation process by gaseous dynamical friction invoked in this thesis.

For DECIGO (bottom left panel) and LISA (bottom right panel), although the detected GW rates from pBH mergers are still strongly dependent on $f_{\rm pBH}$, those from stellar compact remnants are not. This is because the GW events entering in the DECIGO and LISA observational bands are extreme mass ratio inspirals between a migrating compact remnant and an already large central BH mass $10^5 - 10^8\,M_{\odot}$. This occurs at galactic ages when the growth of the central BH is mainly dominated by migrating stellar compact remnants or gas accretion; thus the possible effects of pBHs, and the related

dependence on $f_{\rm pBH}$, is almost completely washed out (see also Figure 3.4). The detected rate for LISA peaks around $z \sim 1$ and then declines steeply because the S/N falls below threshold, while DECIGO would be the best detector to probe the proposed mechanism, with an extremely high number of detected GW per year, thanks to the frequency range at which it is designed and to its planned deep sensitivity curve.

Figure 3.8 shows the contribution to the detected rates at $z \sim 2$ from different chirp masses, associated to stellar compact remnants (top panel) and pBHs (bottom panel). The black patch represents the intrinsic chirp mass distribution, while the blue, green and orange patches refer to the chirp mass distribution detected by ET, DECIGO and LISA, respectively; the edge lines refer to $f_{\rm pBH} \approx 1$ (solid) and to $f_{\rm pBH} \approx 0.01$ (dashed). ET and LISA are almost complementary: ET will detect events with chirp mass $\mathcal{M}_{\bullet\bullet} \sim 10 - 500\,M_\odot$ corresponding to central BH masses up to $M_\bullet \sim 10^5\,\mathrm{M}_\bullet$ and occurring in the initial stages of the seed growth; LISA will detect events with chirp mass $\mathcal{M}_{\bullet\bullet} \sim 1000 - 5000\,M_\odot$ corresponding to central BH masses $M_\bullet \sim 10^5 - 10^8\,M_\odot$ and occurring in the late stages of central BH growth. On the other hand, the large frequency band and exquisite sensitivity of DECIGO will allow to probe a vast range of the chirp mass distribution $10 \lesssim \mathcal{M}_{\bullet\bullet}\,[\mathrm{M}_\odot] \lesssim 5000$.

3.6 Stochastic GW background

The mechanism discussed in this Chapter, emitting a large number of GWs, but relatively few detections (at least for ET and LISA), would naturally produce a strong stochastic gravitational wave background amplitude. In this Section I characterize the SGWB energy and its frequency range.

The SGWB originated by the incoherent superposition of the undetected GW signals can be computed as:

$$\Omega_{\rm GW}(f_{\rm obs}) = \frac{8\pi G\, f_{\rm obs}}{3\,H_0^3\,c^2} \int \frac{\mathrm{d}z}{(1+z)\,E(z)} \int \mathrm{d}\mathcal{M}_{\bullet\bullet}\, \frac{\mathrm{d}^2\dot{N}}{\mathrm{d}V\,\mathrm{d}\mathcal{M}_{\bullet\bullet}} \int \mathrm{d}q \frac{\mathrm{d}p}{\mathrm{d}q}(q|\mathcal{M}_{\bullet\bullet}, z)\times$$

$$\times \frac{\mathrm{d}E}{\mathrm{d}f}(f(f_{\rm obs}, z)|\mathcal{M}_{\bullet\bullet}, q) \int \mathrm{d}\Delta t_{\rm obs}\, \frac{\mathrm{d}p}{\mathrm{d}\Delta t_{\rm obs}}\, \Theta[\bar{\rho}(\mathcal{M}_{\bullet\bullet}, q, \Delta t_{\rm obs}, z) \lesssim \rho_0] \tag{3.40}$$

where $\mathrm{d}E/\mathrm{d}f$ is the emitted GW energy spectrum (see Section 2.6), depending on the chirp mass $\mathcal{M}_{\bullet\bullet}$ and on the mass ratio q of the merging objects; the Heaviside function in the innermost integral ensures the summation

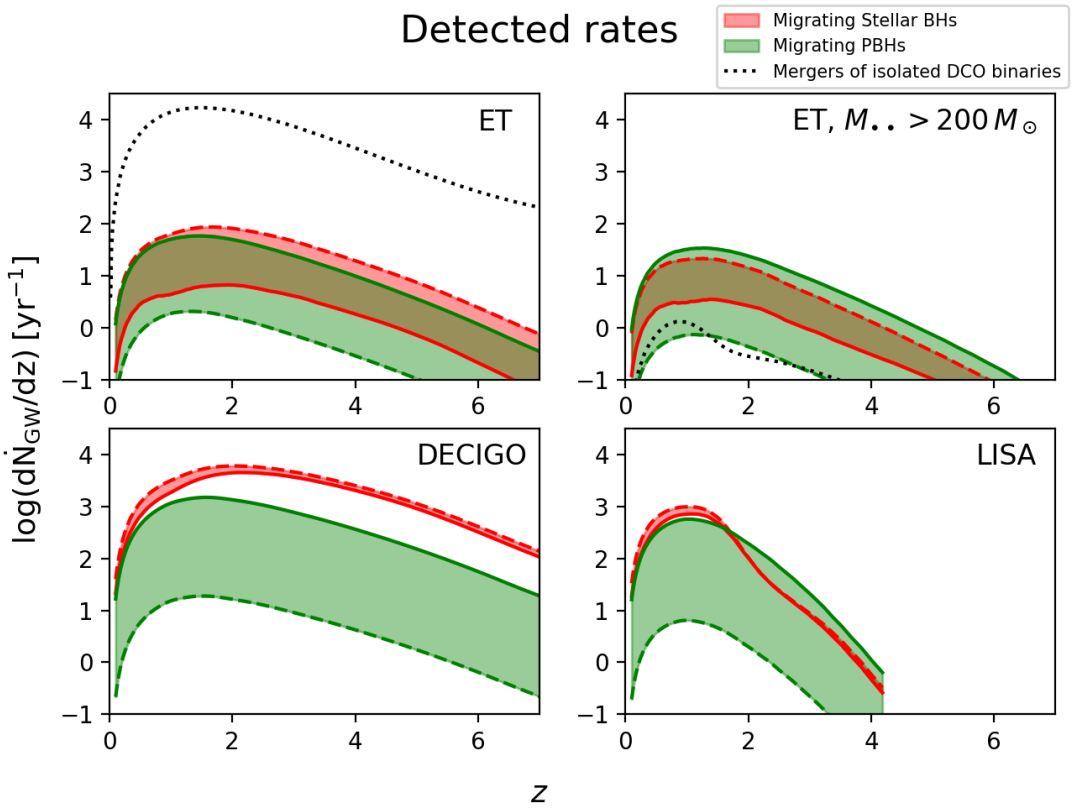

FIGURE 3.7: GW detected event rates for ET (top left panel), for ET and chirp masses $\mathcal{M}_{\bullet\bullet} > 200\,M_\odot$ (top right panel), DECIGO (bottom left panel) and LISA (bottom right panel). A signal-to-noise ratio $\rho > 8$ is adopted for ET and DECIGO, while $\rho > 30$ is adopted for LISA. Red shaded areas refer to migrating stellar compact remnants, green shaded areas to migrating pBHs, for different pBH-to-DM fraction $f_{\rm pBH}$ ranging from 0.01 (dashed edge lines) to 1 (solid edge lines). In the top panels, the dotted lines illustrates the detection rates for ET associated to mergers of isolated DCO binaries.

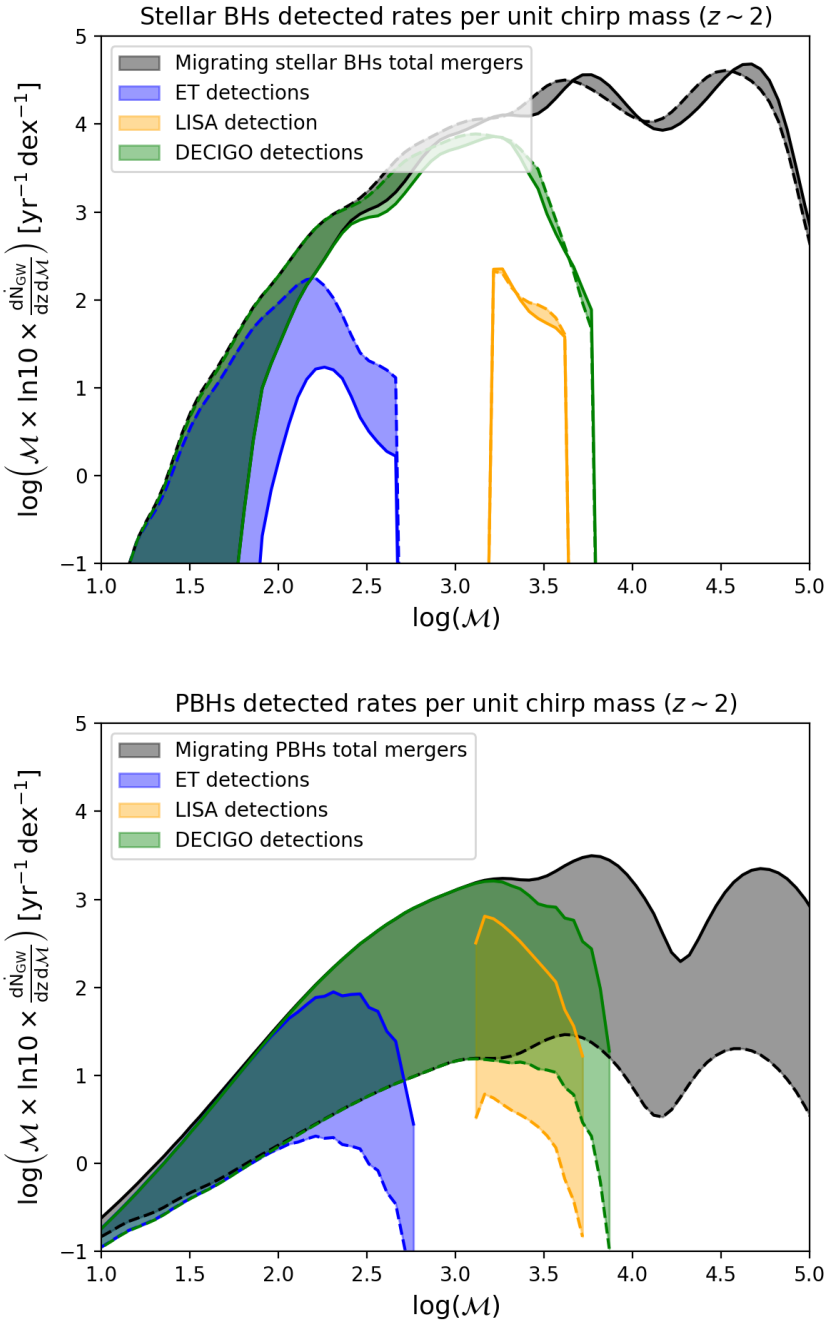

FIGURE 3.8: Chirp mass distribution of detected events at $z \sim 2$ for migrating stellar compact remnants (top panel) and for migrating pBHs (bottom panel). Grey shaded areas show the intrinsic distribution of all events independent of their detection, blue shaded areas refers to ET detections, yellow shaded areas to LISA detections and green shaded areas to DECIGO detections. The shaded areas show the effect of varying the pBH-to-DM fraction $f_{\rm pBH}$ from 0.01 (dashed edge lines) to 1 (solid edge lines).

over the unresolved signals with S/N $\bar{\rho} < \rho_0$. The SGWB generated by all events, resolved and unresolved, is obtained by setting the detection threshold $\rho_0 \to \infty$, so that the innermost integral goes to 1.

In Figure 3.9 I show the total SGWB originated from both resolved and unresolved events; the orange patch is for stellar compact remnants and the blue patch for pBHs. Solid lines are for $f_{\rm pBH} \approx 1$ while dashed ones for $f_{\rm pBH} \approx 0.01$. Plainly, the contribution to the SGWB from pBHs increases at higher $f_{\rm pBH}$ as the number of merging events is larger. On the other hand, the contribution from stellar compact remnants shifts towards lower frequencies as $f_{\rm pBH}$ increases. This reflects the shift at higher chirp masses of the stellar compact object merging rates, see discussion in Section 3.5. The red and blue patches, instead, represent the residual SGWB from stellar compact remnants and pBHs when the resolved events by ET are subtracted. This originates a sharp drop at $f \gtrsim 1$ Hz, where the ET starts detecting almost all the events, subtracting them from the unresolved background. For comparison, the SGWB originated by the merging of isolated BH-BH binaries is also plotted as a dotted grey line (e.g., Boco et al. 2019). Notice that the range of frequencies involved for the two processes is rather different, with $10^{-6} \lesssim f\,[\rm Hz] \lesssim 10$ for the dynamical friction induced mergers described in this Chapter and $10^{-2} \lesssim f\,[\rm Hz] \lesssim 10^4$ for the merging of isolated BH-BH binaries. As a matter of fact, since ET would be able to resolve almost all the events falling in its frequency sensitivity window, it would be very unlikely for it to detect the SGWB coming from the dynamical friction process.

In Figure 3.10, I show the corresponding results on the SGWB for DECIGO. The residual SGWB background of unresolved events is sharply truncated with respect to the total for frequencies $f \gtrsim 10^{-2}$ Hz, corresponding to the DECIGO sensitivity band. I also plot as black solid line the DECIGO sensitivity curve to the background (see Moore et al. 2015). The deep sensitivity to the background for DECIGO will allow to characterize the SGWB at frequencies $f \lesssim 10^{-2}$ Hz; this will be more easily achieved for the background originated by migrating stellar BHs, though also that from migrating pBHs can be detected, especially if $f_{\rm pBH} \lesssim 1$.

In Figure 3.11 I show the corresponding results on the SGWB for LISA. The residual SGWB background of unresolved events is reduced with respect to the total for frequencies $10^{-3} \lesssim f\,[\rm Hz] \lesssim 1$, corresponding to the LISA sensitivity band. However, the reduction is not as sharp as for ET or DECIGO since, as shown also in Figure 3.8, LISA will not detect all the events falling in its sensitivity band. I also plot as a black solid line the LISA sensitivity curve to the background (see Robson et al. 2019). The SGWB from the dynamical friction process is fully detectable with LISA (both for migrating stellar remnants and pBHs).

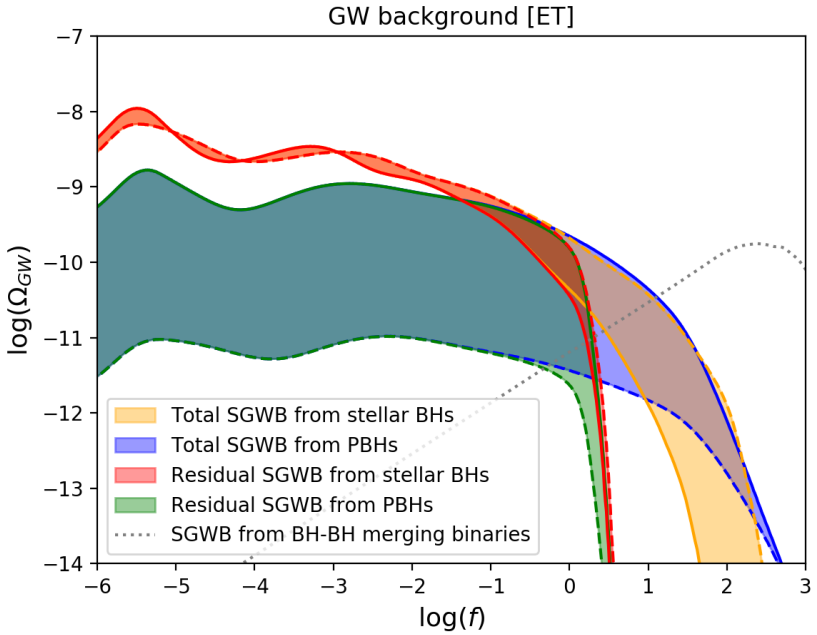

FIGURE 3.9: Stochastic GW background seen by ET. Yellow shaded area illustrates the background from all stellar compact remnants, blue shaded area from all pBHs, red shaded area from undetected stellar compact remnants, and green shaded area from undetected pBHs. All shaded areas show the effect of varying the pBH-to-DM fraction $f_{\rm pBH}$ from 0.01 (dashed edge lines) to 1 (solid edge lines). The dotted line illustrates the background from undetected mergers of isolated BH-BH binaries computed by Boco et al. 2019.

I caveat that the above predictions concerning the SGWB might be affected by many uncertainties. For example, as already discussed in Section 3.5, the duration of the dynamical friction process could be shorter, lowering the number of mergers and the amplitude of the SGWB (see Appendix D). On the other hand, the presence of compact objects binaries from stellar or primordial origin, could somewhat lower the dynamical friction timescales, increasing the number of compact objects merging with the central BH and making the SGWB stronger. This said, the prediction presented here is remarkable, because no other astrophysical mechanisms can originate such a strong background in this frequency range; a future detection of it could represent a smoking gun to test the occurrence of the dynamical friction and its role in the BH seed growth.

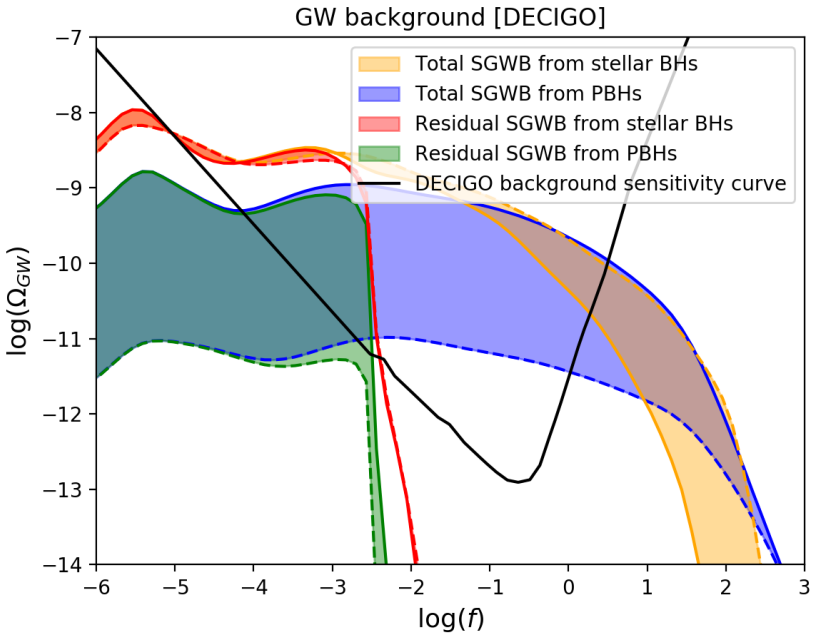

FIGURE 3.10: Same as previous Figure for DECIGO, whose sensitivity curve for the background is shown as a black solid line.

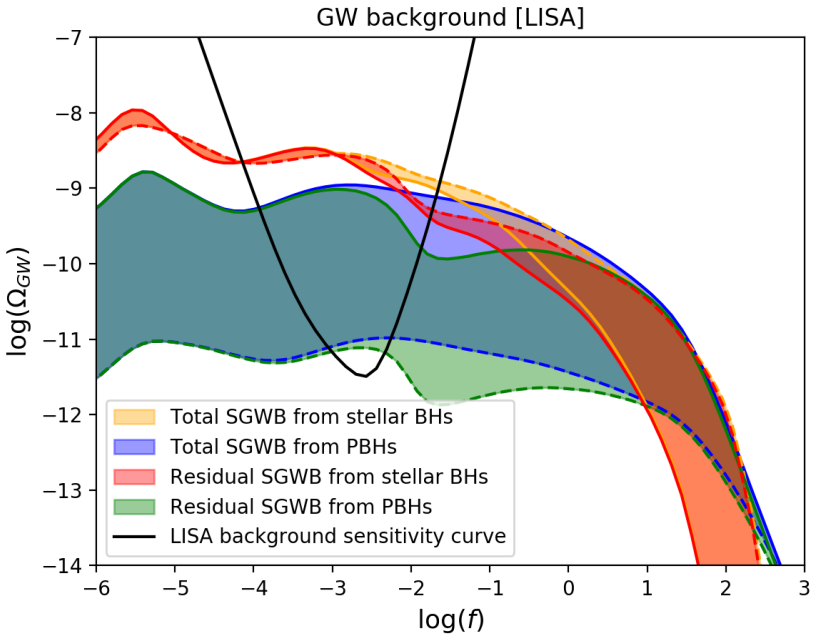

FIGURE 3.11: Same as previous Figure for LISA, whose sensitivity curve for the background is shown as a black solid line.

3.7 Discussion

In this Section I aim to critically discuss some of the main assumptions underlying my (semi)analytic treatment, that may affect the values of the dynamical friction timescale and its dependence on the physical parameters of the gaseous environment and of the migrating compact objects. Although a full assessment of these effects is beyond the scope of the present thesis, I provide here some order of magnitude estimates that could help the reader to understand the present limitations of this scenario.

- *Large-scale clumpiness.* I have assumed a smooth density distribution of the inner star-forming gas. Actually, the structure of high-z ETG star-forming progenitors is more complex. On kpc scales, both observations (e.g., Genzel et al. 2011; Tadaki et al. 2017a,b, 2018; Hodge et al. 2019; Lang et al. 2019; Rujopakarn et al. 2019) and simulations (e.g., Bournaud et al. 2014; Mandelker et al. 2014, 2017; Oklopcic et al. 2017) indicate the presence of clumps with masses $10^7 - 10^8\,M_\odot$ and sizes of 100 – 200 kpc; note that even more massive and extended clumps can be present but are rarer, and could be real outcomes from collisions of smaller ones (e.g., Tamburello et al. 2015) or apparent structures due to blending from observations with limited resolution (e.g., Tamburello et al. 2017; Behrendt et al 2016). The survival of the clumps is still a debated issue, with different simulations favoring short-lived clumps because of feedback and/or collisions (e.g., Hopkins et al. 2012; Oklopcic et al. 2017), or long-lived clumps that may eventually sink toward the center via gravitational torque and bar instabilities and contribute to the growth of a central bulge (e.g., Ceverino et al. 2012; Bournaud et al. 2014). Indubitably, the presence of such a clumpiness in the gaseous medium may in principle affect the dynamical evolution of compact remnants and pBHs. However, high-resolution observations with ALMA (see Hodge et al. 2019; Rujopakarn et al. 2019) have revealed that such clumps contribute less than 10% of the overall star formation; the latter mainly occurs in a rather smooth gaseous and dust-enshrouded medium within the central kpc scale. Provided that in my treatment most of the compact remnants effectively contributing to the growth of the central BH seed come from initial radii of $\lesssim 300$ pc, the assumption of a smooth distribution for the inner star-forming gas should hold to a good approximation.

- *Molecular clouds and stellar clusters.* On sub-kpc scales star formation is likely to occur preferentially in molecular gas clouds with masses $\sim 10^6\,M_\odot$ and radii of 10 – 20 pc. Observations show a rather smooth

distribution of the stellar mass in high-z star-forming systems (e.g., Swinbank et al. 2010; Hodge et al. 2016; Rujopakarn et al. 2016; Lang et al. 2019) and in their quiescent high-z (e.g., van der Wel & van der Marel 2008; Belli et al. 2017) and local descendants (e.g., Cappellari et al. 2013), indicating that molecular clouds are dissolved or a substantial amount of stars can escape quite rapidly from them. However, it could be that some compact remnants born within the cloud might remain bound to a stellar cluster originated there; this will reduce somewhat the number of remnants available for growing the central BH seed. On the other hand, during the formation of the bulge, the stellar clusters may themselves migrate toward the central region via dynamical friction against the background stars, and contribute to the growth of a nuclear star-cluster there (e.g., Antonini et al. 2015).

- *Local feedback from SN explosions and natal kicks.* Some progenitors of the compact remnants can have undergone a SN explosion, possibly removing a sizeable amount of gas from their surroundings; this in principle could hamper the effectiveness of the gaseous dynamical friction process. In addition, SN explosions could be asymmetric, expelling more material in a certain direction with respect to others, and consequently imprinting a momentum kick to the compact remnant, changing its velocity with respect to the progenitor star and breaking the hypothesis that compact remnants inherits the velocity distribution from their progenitor stars. However, both these effects are strongly mitigated in the present context by the fact that compact remnants which mainly contribute to the merging rates and to the growth of the central BH, especially in the initial phase, feature huge masses $m_\bullet \gtrsim 30\,\mathrm{M}_\odot$ (see Figure 3.3). These massive BHs are produced at low metallicities by stars with $m_\star > 30 - 35\,\mathrm{M}_\odot$ which are characterized by large fallback fractions f_fb; in other words, a large fraction of the envelope mass falls back onto the core and contributes to the BH formation, so reducing the power of SN feedback and the natal kick momentum (see Belczynski et al. 2008; Dominik et al. 2012). In particular, in Belczynski et al. 2010a it is estimated that stars with $m_\star \gtrsim 40\,\mathrm{M}_\odot$ have $f_\mathrm{fb} \sim 1$, undergoing a direct collapse characterized by no explosion and zero natal kick. Therefore the main contributors to the merging rates and to the central BH growth should be scarcely affected by these effects. Still, since these processes may affect the evolution of lower mass BHs and neutron stars at later times, an order-of-magnitude estimate of their impact is in order. As for the SN explosion, it can efficiently sweep up material during the energy-conserving expansion phase, out

to a radius $R_{\rm SN} \sim 5\, t_4^{2/(5-\alpha)}\, n_2^{-1/(5-\alpha)}\, E_{51}^{1/(5-\alpha)}$ pc where $E_{51} \equiv E_{\rm SN}/10^{51}$ erg is the energy of a SN explosion, $n_2 \equiv n/10^2$ cm^{-3} is the average gas density and $t_4 \equiv t/10^4$ yr the time since the explosion (e.g., Ostriker & McKee 1988; Mo et al. 2010); however, once formed the remnant will move in the gaseous medium at a typical velocity of $\sigma_{200} \equiv \sigma/200\,{\rm km\,s^{-1}}$ and thus will travel a distance $R_{\rm rem} \sim 2\,\sigma_{200}\,t_4$ pc, implying that most of the gas mass swept up by the remnant is replaced after $\lesssim 10^5$ yr. The natal kick, instead, can be estimated (following Mapelli et al. 2021a) as: $v_{\rm kick} \simeq v_H\,\langle m_{\rm NS}\rangle/m_\bullet$, where v_H is drawn from a Maxwelian distribution with $\sigma_H \sim 265\,{\rm km\,s^{-1}}$, observationally derived from the motion of pulsars in the Galaxy (Hobbs et al. 2005), and $\langle m_{\rm NS}\rangle = 1.33$ is the average NS mass. The resulting natal kick velocity is of the order of $\sim 30\,{\rm km\,s^{-1}}$ even for low mass BHs $m_\bullet \sim 10\,{\rm M}_\odot$, which is a factor $\sim 5-10$ below the typical velocities of the compact remnants considered $v \sim 150-300\,{\rm km\,s^{-1}}$. Still, for lower mass BHs and especially for NS the kick could have some impact on the dynamics, shortening or extending the dynamical friction timescale depending on the kick direction with respect to the initial velocity.

- *Feedback from the central BH seed.* Though at early times the BH seed growth is dominated by dynamical friction, some gas accretion onto it can occur; the ensuing feedback can partially remove gas from the central region, so offsetting further migration of compact objects by dynamical friction. The timescale for gas evacuation out to a radius $R_{100} \equiv R/100$ pc from the center due to a BH momentum-driven wind can be estimated as $t_{\rm evac} \sim 8{\times}10^7\, R_{100}\, \sigma_{200}\, M_{\bullet,4}^{-1/2}$ yr (see King 2003; King & Pounds 2015), where $\sigma_{200} \equiv \sigma/200$ km s^{-1} is the galaxy velocity dispersion and $M_{\bullet,4} \equiv M_\bullet/10^4\,M_\odot$ is the BH mass; however, the dynamical time for the gas to refill such a region amounts to $t_{\rm dyn} \sim 5{\times}10^5\, R_{100}\, \sigma_{200}^{-1}$ yr. Thus the feedback from the central BH will become truly effective as its mass attains $M_\bullet \sim 2.5\times10^8\,M_\odot\,\sigma_{200}^4$, when however the growth is already largely dominated by gas accretion. Incidentally, note that this condition has also been invoked to explain the $M_\bullet - \sigma$ relation observed between the relic supermassive BH mass and the velocity dispersion of the old population in ETGs (e.g., King & Pounds 2015; Kormendy & Ho 2013; McConnell & Ma 2013; Shankar et al. 2016). Moreover, as the central BH grows in mass, an accretion disk might form around it. This may influence the migration of compact objects lying in the disk plane, resulting in different sinking timescales with respect to the dynamical friction one considered in this thesis. The gravitational torques induced on perturbers moving in AGN disks has been

investigated via numerical simulations by Derdzinski et al. 2019, 2021, finding that the sinking timescale becomes strongly dependent on disk parameters such as viscosity and gas temperatures and on the mass ratio q. In the scenario presented in this thesis, while the presence of a gaseous disk might affect the motion of some compact objects, it should not strongly alter the global outcome of the process, since the remnant distribution considered is spherical and only a small fraction of them would lie in the disk plane. Still, at later times, when gas accretion is dominant and the BH is massive enough to inject a strong energy/momentum feedback into the environment, possibly cleaning the surrounding medium, the presence of a massive gaseous accretion disk may be the only possibility to drive compact objects towards the central BH.

- *Three-body encounters.* Interactions among the central BH seed and two migrating compact objects, that can eject from the central region the least massive one (e.g., Hills & Fullerton 1980), could in principle reduce the efficiency of the dynamical friction process in growing the seed. A detailed assessment of the issue clearly require a full dynamical simulation, but a simple argument can be provided along the following lines. The typical radius $r_\bullet$ within which the migrating compact objects start to feel the dynamical influence of the central BH seed with mass $M_{\bullet,4} \equiv M_\bullet/10^4\,M_\odot$ can be computed as $r_\bullet \sim G\,M_\bullet/\sigma^2(r_\bullet)$; on considering the approximate scaling with radius $r_{\rm pc} \equiv r/{\rm pc}$ of the velocity dispersion $\sigma(r) \approx 80\,r_{\rm pc}^{\alpha/2}$ km s^{-1}, this implies $r_\bullet \approx 0.05\,M_{\bullet,4}^{1/(1+\alpha)}$ pc. In addition, the timescale for three-body encounters (e.g., Heggie 1975; Binney & Tremaine 1987; Davies 2002) between the central seed and two remnants of total mass $m_{\bullet,40} \equiv m_\bullet/40\,M_\odot$ can be estimated as $\tau_{\rm 3b} \sim \sigma(r)/2\pi G\,M_\bullet\,\bar{n}_\bullet(r)\,r \approx 4\times10^7\,m_{\bullet,40}\,M_{\bullet,4}^{-(4-\alpha)/2\,(1+\alpha)}\,(r/r_\bullet)^{-(2-3\,\alpha)/2}$ yr; here I have evaluated $\bar{n}_\bullet(r) \approx 0.01\,m_{\bullet,40}^{-1}\,r_{\rm pc}^{-\alpha}$ pc^{-3} as the average density of remnants inside the radius r after a galactic age of $\sim 10^7$ yr by taking into account the radial dependence of the gas mass and the fraction of remnants per unit stellar mass according to a Chabrier IMF. The three-body timescale is to be compared with the typical gaseous dynamical friction timescale, that from equation (3.25) amounts to $\tau_{\rm DF} \approx 10^4\,m_{\bullet,40}^{-1}\,M_{\bullet,4}^{5/2\,(1+\alpha)}\,(j/j_c)^{3/2}\,(r_c/r_\bullet)^{5/2}$ yr; thus whenever r_c is close to $r_\bullet$, as required to have effective three-body interactions, $\tau_{\rm DF} \ll \tau_{\rm 3b}$ holds so that dynamical friction is expected to wash out the dynamical effects of possible three-body encounters.

- *Relativistic kicks.* Numerical relativity studies found that merging binary black holes could receive recoil velocities at the time of merger due to beamed momentum emission via GWs. A comprehensive study of these relativistic kicks has been carried out in Lousto et al. 2012, where the authors, fitting several numerical relativity simulations, propose a phenomenological formula to model these kicks as a function of the spin and masses of the binary. The formula envisages a component of the kick due to the merger of unequal mass BHs, reaching peak velocities of $\sim 150\,\mathrm{km\,s^{-1}}$ for $q \simeq 1/3$, and a component dependent on the spin magnitudes and orientations. The most common kicks are of the order of $100-200\,\mathrm{km\,s^{-1}}$, but some of them might reach $\gtrsim 1000\,\mathrm{km\,s^{-1}}$ (see Figure 9 of Lousto et al. 2012). Given that the typical escape velocities of the central regions ~ 300 pc of the considered galaxies are of the order of $\sim 400\,\mathrm{km\,s^{-1}}$, the majority of the relativistic kicks should not be able to expel BHs from the center; however, for some favourable spin configurations, kicks might effectively expel the newly formed BHs after the merger, so reducing the number of compact objects available for growing the seed. Moreover, even smaller kicks can temporarily displace the BH from the center making it not available for subsequent mergers. However, if the BH does not exit the central dense region, dynamical friction would make it sink again in an even shorter timescale for 2 reasons: (i) being a merger product, the BH would be massive and dynamical friction would be more efficient, (ii) the relativistic kick is mainly radial, therefore the tangential component of the BH velocity should be very small, maximizing the dynamical friction efficiency (see equation (3.25) and Table 3.2). Finally, as the central BH grows in mass, mass ratios become smaller and smaller and the kick velocities decrease with it (see model SMALL_M2 in Mapelli et al. 2021b). Still, even if relativistic kicks are not able to suppress the process, they may substantially modify the chirp mass distribution during the first stages. Indeed, removing massive BHs from the center, prompt subsequent mergers of the same BHs are hampered, favouring a first phase of first generation BHs mergers and a second phase of mergers of second generation BHs sinking again toward the center thanks to dynamical friction.

- *Long living stars.* In the treatment I have considered only massive stars $m_\star \geq 8\,\mathrm{M_\odot}$ which, after a short lifetime, produce NS or BHs. In principle gaseous dynamical friction could impact also less massive long living stars, not originating compact remnants, which could sink toward

the center as well. However the dynamical drag acting on these objects is less efficient for mainly 2 reasons. First of all the dynamical friction force scales as $F_{\rm DF} \propto m^2$ with the perturber mass, so being weaker on lighter perturbers, second stellar winds and energy feedback from stars not collapsed to compact objects could sweep up and and heat up the interstellar gas, making dynamical friction less effective. However, while in my treatment these stars are neglected, some of them, in fact, could reach the central regions of ETG progenitors and help in constituting a central stellar overdensity such as the nuclear star cluster. As for the central BH growth, stars in orbit around it are expected to be disrupted by the tidal effects due to the gravitational field of the BH; therefore mergers between long living stars and the central BH should not happen, but they could be accreted as gas. Indeed a star with mass $m_\star$ and radius $r_\star$ is tidally disrupted by a BH of mass $M_\bullet$ when it reaches the tidal radius $r_T = r_\star\,(M_\bullet/m_\star)^{1/3}$. In order to not be disrupted and contribute to the merging rates with the central BH the tidal radius should be smaller than the Schwarzschild radius $r_T < 2\,G\,M_\bullet/c^2$, implying, for a star as the sun, $M_\bullet \gtrsim 10^8\,{\rm M}_\odot$ which is not the case for the initial stages when the proposed mechanism is relevant.

- *Velocity structure.* I have adopted a velocity structure dominated by random motions with velocity dispersion $\sigma(r)$, that has been computed via the Jeans equation taking into account the overall mass distribution. Actually the situation in star-forming ETG progenitors is slightly more complex. On a scale of a few kpc, the velocity structure is dominated by rotational motions with $v/\sigma \gtrsim$ a few, in the way of a clumpy unstable disk (see Genzel et al. 2011; Tadaki et al. 2017a,b, 2018; Hodge et al. 2019). However, on sub-kpc scales both observations (e.g., Barro et al. 2016; Rujopakarn et al. 2019) and simulations (e.g., Danovich et al. 2015; Zolotov et al. 2015; Zavala et al. 2016) indicate that dynamical friction, gravitational torques, and violent relaxation will operate toward converting such rotation into random motions, setting up a bulge-like structure with $v/\sigma \lesssim 1$ (see also Lapi et al. 2018). Provided that the majority of the compact remnants contributing to the growth of the central seed BH come from a scale of $\lesssim$ 300 pc, the assumption of a dispersion-dominated velocity structure should hold to a good approximation. However, it is still possible that some of the remnants possess a residual rotational velocity component; in this case the angular momentum increases as $j \propto \sqrt{v^2+\sigma^2}$ and the timescale for dynamical friction is correspondingly enhanced as $\tau_{\rm DF} \propto j^{1.5}$. For example, in the rather extreme case $v/\sigma \sim 1$ this

amounts to roughly doubling $\tau_{\rm DF}$.

- *Dust component.* The central kpc regions of star-forming ETG progenitors are very dusty (e.g., Tadaki et al. 2017a,b, 2018; Hodge et al. 2019; Rujopakarn et al 2019). In principle, dust can cooperate with the gas component in making the dynamical friction of the compact remnants more efficient, and speed up the building up of the central BH seed. However, quantitatively the effect is expected to be small since the estimated dust-to-gas ratios amount to $M_{\rm dust}/M_{\rm gas} \sim 1-5\%$ (e.g., Berta et al. 2016; Scoville et al. 2016, 2017; Tacconi et al. 2018).

I also warn that the values of the dynamical friction timescale and its dependence on the physical parameters of the gaseous environment and of the migrating compact objects could be influenced by other concomitant and co-spatial astrophysical and dynamical processes, not included in this (semi)analytic, orbit-averaged treatment, like natal kicks imparted to the remnants, stellar hardening, development of a circum-binary disk around the central BH, tidal stripping effects. For these reasons a further investigation of the mechanism via a full hydrodynamical simulation at high spatial resolution is required.

Chapter 4

Conclusions and future perspective

In this Chapter I will summarize the main results presented throughout the thesis, I will give a brief overview on the related ongoing works I am carrying on and I will reveal some clues on the ideas for future research work.

4.1 Main results

The common thread of the whole thesis has been to well characterize different astrophysical processes leading to gravitational wave emission, heavily relying on observational data and theoretical arguments about galaxy formation and evolution. I believe that such a strong anchor on recent observational results and the detailed characterization of the galactic environment represents the main novelty point of the work. For this reason, Chapter 1 of the thesis is entirely dedicated to summarize the current knowledge about galaxy formation and evolution and to introduce some important concepts that are repeatedly used in the thesis. In Chapters 2 and 3, I have exploited this expertise to study different astrophysical sources of GWs.

In particular in Chapter 2, I focused on mergers of double compact objects, as the ones revealed by the LIGO/Virgo team, trying to compute their merging rates across the cosmic history and studying their dependence on the properties of the galactic environment in which they form and evolve. Such a study also lay the foundations for the possibility to link DCO properties, such as chirp mass, with their host galaxy.

In Chapter 3, instead, I proposed a novel scenario of dynamical mergers of stellar compact remnants and, possibly, primordial black holes in the central dense regions of high-z ETG progenitors to grow an heavy SMBH seed. This mechanism can help in alleviating the high redshift quasars tension and can be complementary to other processes to grow SMBHs in short timescales. GWs emitted by this process, as well as the associated SGWB,

could be detected by future ground- and space-based GW detectors and could constitute a smoking gun to test this proposal.

As for the isolated DCO mergers the main results of the thesis are the following:

- I have pointed out the importance of performing an analysis galaxy by galaxy, parametrizing them through an observable quantity such as their stellar mass or star formation rate and exploiting the empirically derived statistics, such as the star-forming galaxy stellar mass functions or the star formation rate functions, to account for the contribution of galaxies with different properties. This allow for an accurate reconstruction of the overall cosmic SFR density, without losing the link with the single galaxy history (Section 2.1). In principle, this would grant the possibility to select subsamples of galaxies and to study the DCO properties for the chosen subsample.

- I have shown the similarities and differences of using the 2 aforementioned statistics (GSMF and SFRF) to calculate the cosmic SFR density, finding a good agreement between the two at least up to $z \lesssim 2$ and quantifying the differences at higher redshifts. I have also discussed and emphasized the advantages and drawbacks of the two approaches: on the one hand the SFRF provide a more direct connection with the SFR of galaxies, on the other hand the GSMF can be more useful in the estimation of galaxies metallicities (Section 2.1).

- I have performed a separation between different galactic populations depending on the statistics adopted. In particular, when using the GSMF I have separated between main sequence galaxies and starbursts, finding, on average, slightly lower metallicities for the starburst population, leading to a relative overproduction of BH-BH mergers. When using the SFRF I divided the contributions of LTGs and ETG progenitors, finding that the bulk of the cosmic SFR at $z \gtrsim 1$ is originated by ETG progenitors, while LTGs contribute mostly in the local Universe, with slightly lower metallicities (Sections 2.1 and 2.2).

- I have extensively discussed many issues regarding star-forming galaxies gas-phase metallicity, which is a fundamental ingredient to correctly assess the merging efficiency and the compact object masses. First of all I have underlined why using a cosmic-averaged metallicity could strongly bias the results toward lower metallicities, remarking again the importance of considering metallicity scaling relations

for individual galaxies. Second, I have compared a sharply redshift-declining Mass Metallicity Relation and a redshift-independent Fundamental Metallicity Relation, finding that the results are significantly different at high-z ($z > 2$). In particular the FMR yields a slow metallicity decline with redshift, with rather high $Z_{\rm gas}$ values ($Z_{\rm gas} \sim 0.4$–$0.5\,Z_\odot$) even at $z > 2$, while the MZR usually implies very low metallicities ($Z_{\rm gas} < 0.1\,Z_\odot$) at $z > 2$. I have argued in favor of the FMR, since it appears to be more in line with the rapid metal enrichment in the early Universe suggested both by stellar archeological measurement and by recent dust mass determinations with ALMA, but also by state-of-the-art numerical simulations. Finally, I have exploited the results of an analytical chemical evolution model to assign metallicity to galaxies with different SFR, finding a pleasant agreement with the FMR results (Section 2.2).

- I have completed the work computing the DCO merging rates for the different statistics and metallicity relations adopted, highlighting the redshift-chirp mass and the time delay-chirp mass joint distributions. I have also calculated the detection rates for AdvLIGO/Virgo at its design sensitivity and for ET, also estimating the expected rate of GW lensed events. Finally I quantified the amount of SGWB emitted by undetected sources (Sections 2.4, 2.5, 2.6).

As for the process of heavy seed formation the highlights are the following:

- Employing the recent observations of high redshift star-forming galaxies properties, featuring an extremely high SFR $\psi \sim 100 - 1000\,{\rm M}_\odot\,{\rm yr}^{-1}$ in the central $\lesssim 1$ kpc region, with a large gas reservoir $M_{\rm gas} \sim 10^{10} - 10^{11}\,{\rm M}_\odot$, I have devised a new mechanism for heavy seeds formation via multiple mergers of stellar compact remnants and, eventually, pBHs, sinking toward the galactic center via gaseous dynamical friction at the beginning of the galaxy lifetime and merging with the central growing BH seed.

- I have quantitatively studied the effect of gaseous dynamical friction force in a galactic potential well finding a general formula for the dynamical friction timescale which is in remarkable agreement with previous studies looking at specific cases (Section 3.2).

- I have applied the formula to the case of the environment of high-z star-forming galaxies to find that a certain fraction of compact objects can effectively sink toward the center in a very short timescale. In particular I have found that from the merger of these compact objects a

BH seed of $M_\bullet \sim 10^4 - 10^5\,\mathrm{M}_\odot$ can be efficiently created in $\lesssim 3\times10^7$ yr. Standard Eddington-like accretion can then bring this already massive seed to $M_\bullet \sim 10^9\,\mathrm{M}_\odot$ in $\lesssim 300$ Myr, alleviating the high redshift quasar tension (Section 3.4).

- I argued that the mechanism proposed is important not only at high redshift, but also for $z \gtrsim 1$ ETG progenitors. Indeed these massive galaxies tend to have a short and intense star formation episode, accumulating some $10^{10} - 10^{11}\,\mathrm{M}_\odot$ in $\lesssim 1$ Gyr. Since relic SMBHs with mass of some $10^8 - 10^9\,\mathrm{M}_\odot$ are found in local ETGs and given the galaxy-SMBH co-evolution described in Section 1.3.5, it is believed that also the SMBH should have accumulated its mass in comparably short timescales. Even though standard Eddington accretion could be enough to originates such SMBHs, it would require an Eddingtoon ratio $\lambda \sim 1$ for the whole duration of the galaxy lifetime. I show that the eventual presence of an heavy seed, formed via dynamical friction, could allow for the SMBH formation even with $\lambda \sim 0.3$ which appears more in agreement with estimations by Vestergaard & Osmer 2009; Kelly & Shen 2013 and Vestergaard 2019 (Section 3.4).

- I have proposed a way to test the process via GW and SGWB detection. In fact, the dynamical mergers at the center of galaxies produce numerous GW signals that could be detected by future interferometers such as ET, DECIGO and LISA. I have shown that ET and LISA would be complementary, probing different phases of the process due to their frequency bands, while DECIGO would be able to accurately test the whole process. Also the prediction for the SGWB is remarkable; it would span a vast frequency range $10^{-6} \lesssim f\,[\mathrm{HZ}] \lesssim 10$ where no other astrophysical processes is believed to produce a GW background and it would be intense enough to be detected.

4.2 Ongoing works

Even though the results presented in this thesis are self-contained, I have a lot of ongoing projects, in collaboration with other Ph.D. students, where we are refining and exploiting the formalism to compute the galactic term developed in this thesis. In particular:

- I established a collaboration with Martyna Chruslinska for the realization of Boco et al. 2021. We are now working on an extension of that paper, Chruslinska et al. 2021, in which we try to accomplish 2 main goals: (i) following the observational results of Caputi et al. 2017

and Bisigello et al. 2018 we are modeling a mass- and redshift- dependent starburst fraction with the aim of understanding its impact on the metallicity dependent cosmic SFR, (ii) assuming that a redshift-independent FMR yields a good estimation for metallicity of galaxies at all redshifts, we are trying to relate the exact shape of such a FMR to observable properties of other scaling relations at $z \sim 0$. In particular we find that, under certain assumptions, the FMR shape can be derived directly from the $z \sim 0$ MZR and MS slopes. Examples of our determinations of the starburst fraction and FMR are given, respectively, in Figure 4.1 and 4.2.

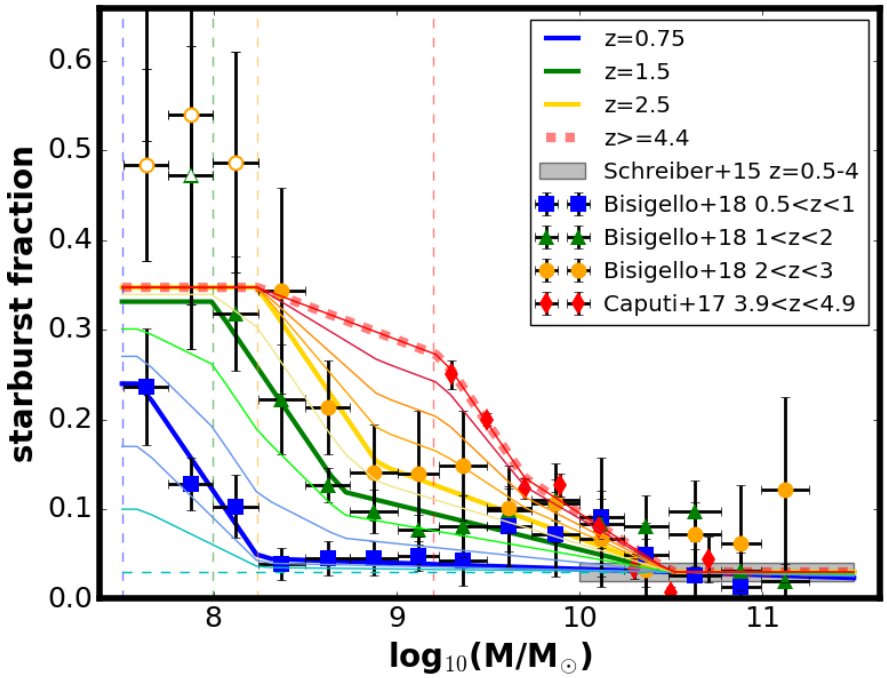

FIGURE 4.1: Starburst fraction as a function of stellar mass at different redshifts (color code).

- In collaboration with Alex Sicilia we are combining the galactic term computed as described in Chapter 2 with the output of the SEVN code (see Spera et al. 2019) to determine the stellar BH mass function over the whole history of the Universe (see Appendix C for more details). In particular we have considered various stellar evolution channels: (i) single stars evolving in isolation and collapsing to BH, (ii) isolated binary stars merging together to produce a remnant BH, (iii) isolated binary stars which, after binary evolution, end up in a BH-BH binary (eventually merging after a certain time) and (iv) stars evolving

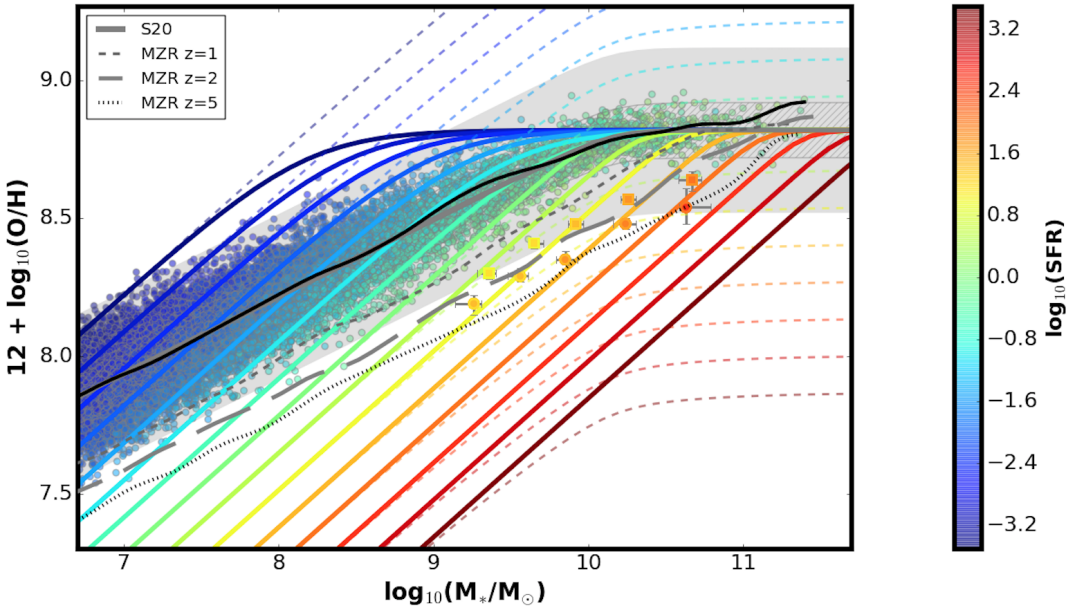

FIGURE 4.2: Example of FMR (colored lines corresponds to different SFR values) obtained from the $z \sim 0$ MZR and SFMR. Colored points are sampled from the GSMF and MS at z$\sim$ 0.

in dense environments such as young star clusters (see Di Carlo et al. 2019) originating single or binary BHs after dynamical interactions with other stars or compact objects in the cluster. The resulting mass function is shown in Figure 4.3 as a function of the parameter $f_{\rm field}$, i.e. the fraction of stars or binaries which evolve in isolation, not feeling the effect of dense environments.

- In collaboration with Giulia Capurri we are using the prescriptions for the SGWB estimation from DCO mergers presented in this thesis, in combination with the public code `CLASS`, to compute the angular power spectrum of SGWB anisotropies (Capurri et al. 2021). We identify the contributions coming from different type of sources (BH-BH, NS-NS and BH-NS) and from different redshifts and we interpret the spectral shape in terms of the redshift distribution of sources. We also simulate an high resolution full sky map of the SGWB starting from the power spectra obtained with `CLASS` and including Poisson statistics and clustering properties. The obtained angular power spectrum for all the merging events is shown in Figure 4.4.

- In collaboration with Giulio Scelfo we are cross-correlating the expected ET detected GW signals from DCO mergers with HI signals from

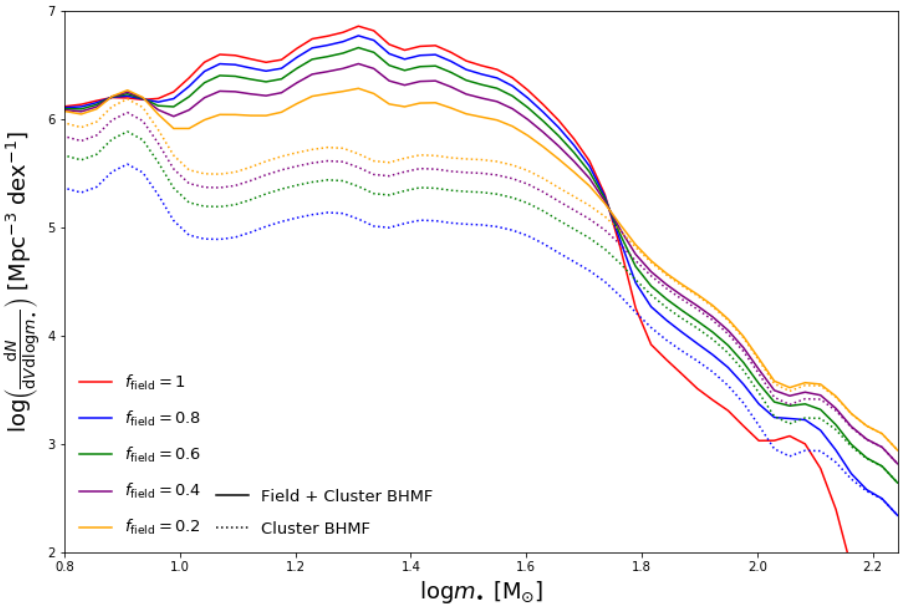

FIGURE 4.3: Stellar BH mass function at $z \sim 0$. The color code is for different $f_{\rm field}$.

intensity mapping (IM) experiments (Scelfo et al. 2021). We use this analysis (i) for a statistical inference of the GW redshift distribution in a cosmology-independent way, only relying on the GW×IM cross-correlation, (ii) to place constrains on the dynamical dark energy equation of state parameters and (iii) to disentangle an eventual contribution from pBHs to the detected GW events by ET. I show a result for this last application in Figure 4.5 illustrating the S/N of the cross-correlation signal after 10 yr of observations for different values of pBH fraction with respect to astrophysical BHs.

4.3 Future perspectives

Despite the efforts to correctly model galactic environments, uncertainties are still huge and much more work must be done to improve and test my results. My perspectives for research work in the next future go along the following lines:

- One of the most important and urgent questions still open after this

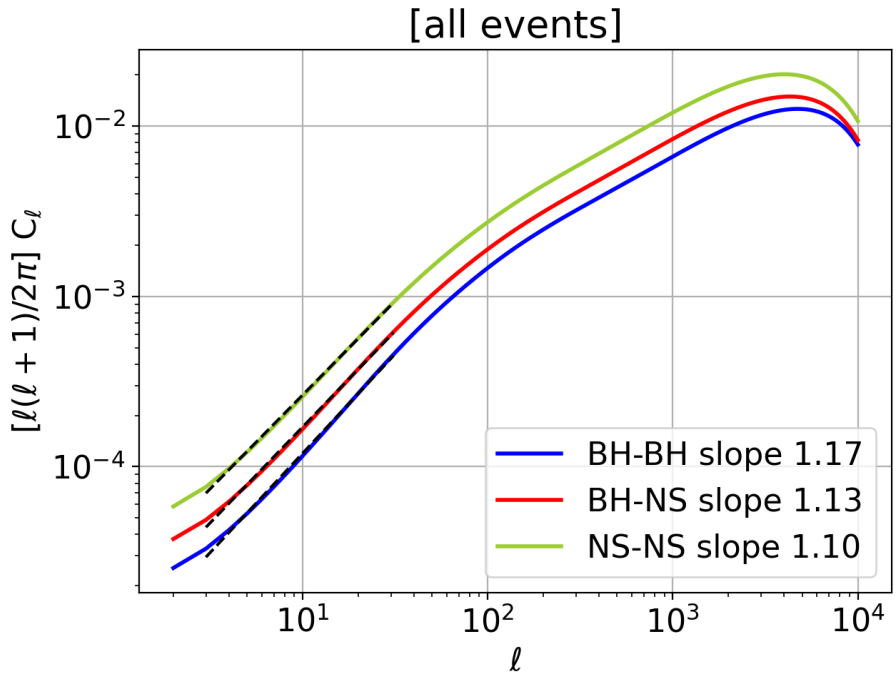

FIGURE 4.4: Angular power spectrum of SGWB anisotropies. Different colors are for different DCO types.

thesis is if the Fundamental Metallicity Relation is really able to represent the overall galactic population. Observational works (see Hunt et al. 2016) have been able to assess its validity up to $z \lesssim 3.5$ with very small dispersion, but there are no observational indications of its validity at higher-z. Moreover possible selection effects due to adopted surveys may impact on the results. Although in Chapter 2 I have brought many observational and theoretical hints in favor of the slow redshift decline of the FMR, showing also that it leads to results consistent with a chemical evolution model, I have never formally proven the robustness of such a relation. Moreover, even if a universal FMR existed, what would be its exact shape? Answering this question from the empirical point of view is extremely difficult, given the large uncertainties on metallicity calibration discussed in Section 1.3.4 and the possible bias in the computation of galaxies stellar mass and SFR. For these reasons I would like to face the problem with an ab initio computation. The idea is to theoretically derive a kind of FMR from the galaxy evolution model of Lapi et al. 2020. The most straightforward way to do this is to extract galaxies from a joint $SFR - M_\star$ distribution at fixed redshift. Since these 3 observables are related by the analytic equations of the model

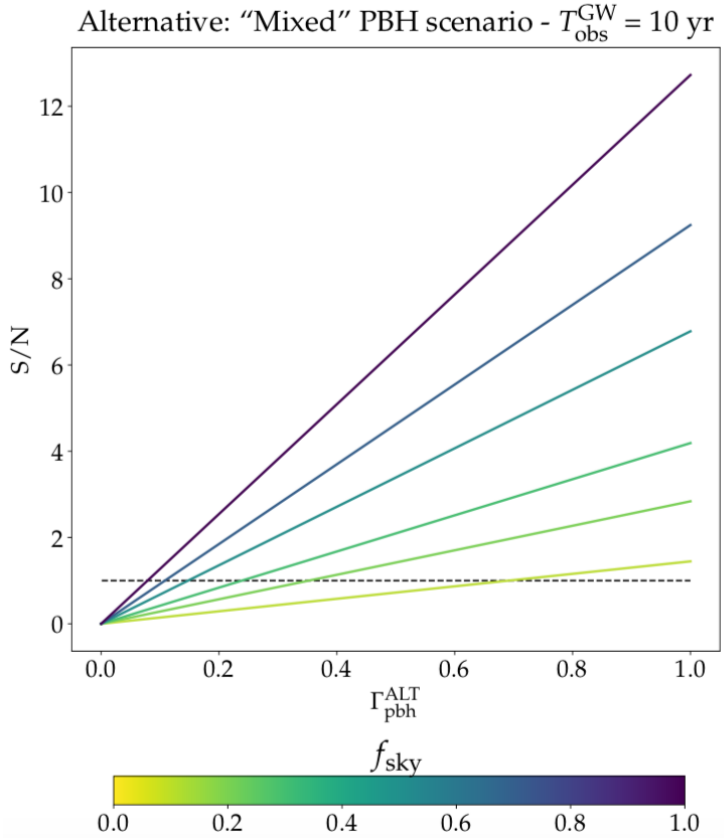

FIGURE 4.5: S/N of the cross-correlation signal after 10 yr of observations for different values pBH fraction with respect to astrophysical BHs.

to halo mass, formation redshift and galactic age (see Appendix A), it is possible to determine the latter reversing the system of equations and to finally self-consistently estimate the gas-phase metallicity. In Figure 4.6 (top row) I show the results for a $z \sim 0$ LTG population. The left panel represents the main sequence with metallicity as a color code, while in the right panel it is shown the metallicity as a function of SFR for different stellar masses. The agreement with the general behaviour of the FMR is astonishing: there is a clear correlation between metallicity and mass and an anti-correlation between metallicity and SFR whose strength decreases at higher masses and lower SFRs. The color code shows the role of the galactic age: less massive galaxies and highly star-forming ones tend to be younger and so less metallic. However the same computation for a $z \sim 2$ population of ETG progenitors gives significant differences, as displayed in Figure 4.6, bottom right panel. In fact, while the mass-metallicity correlation stays put, the metallicity-SFR anti-correlation seems preserved only at very high SFR, while a

flattish behaviour, or even a correlation, is visible at $\psi \lesssim 100\,M_\odot\,yr^{-1}$. From the color code, looking at the $M_\star \sim 10^{10}\,M_\odot$ case, it is possible to notice that only very young galaxies with $\tau \sim 100$ Myr are metal poor, while galaxies with $\tau \sim 300$ Myr and $\psi \sim 100\,M_\odot\,yr^{-1}$ seem to be richer in metals than galaxies with $\tau \sim 600$ Myr and $\psi \sim 10\,M_\odot\,yr^{-1}$. This effect is probably due to the larger halo mass for strongly star-forming systems, but a further investigation is needed to correctly interpret these results. What is sure is that the two different types of star formation histories of LTGs and ETG progenitors have a significant impact on the results.

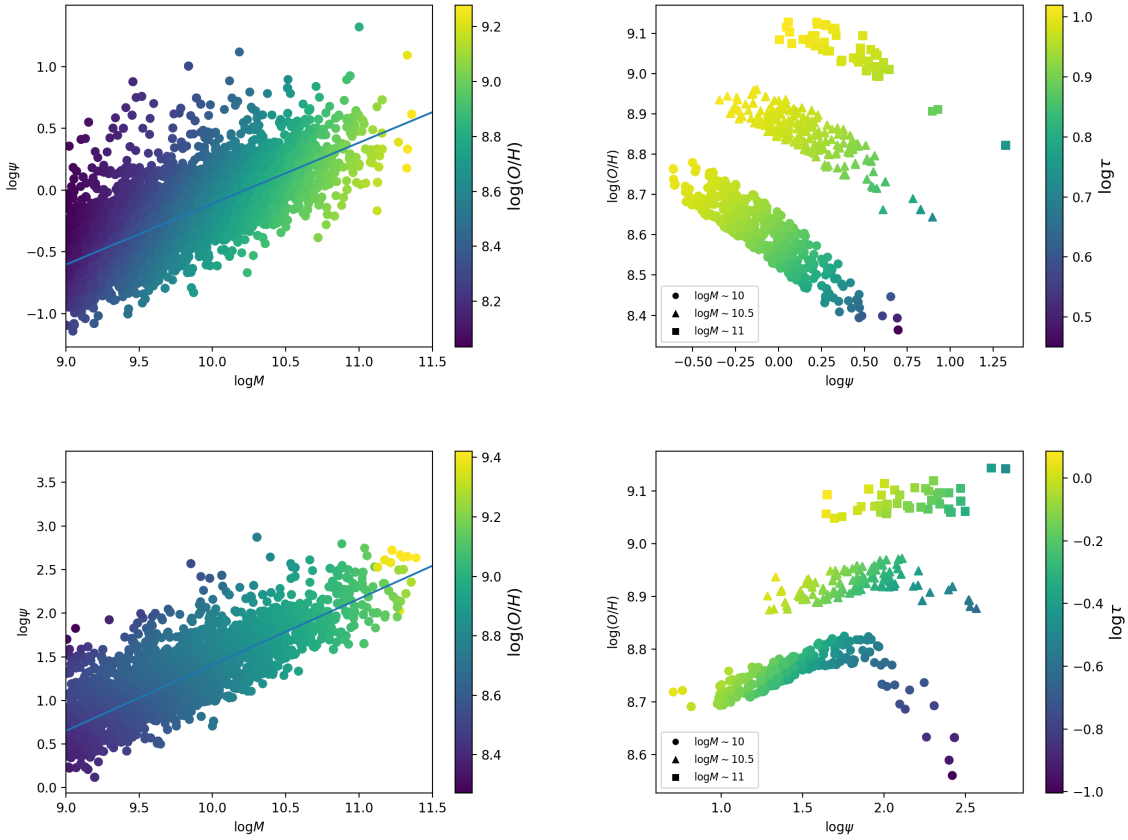

FIGURE 4.6: Top row: $z \sim 0$ LTG population. Top left: main sequence with metallicity as a color code, top right: metallicity as a function of SFR for different stellar masses: $10^{10}\,M_\odot$ circles, $10^{10.5}\,M_\odot$ triangles, $10^{11}\,M_\odot$ squares. Color code represents the galactic age. Bottom row: $z \sim 2$ ETG progenitor population. Top left: main sequence with metallicity as a color code, top right: metallicity as a function of SFR for different stellar masses: same code as top row. Color code represents the galactic age.

- Throughout the thesis I have effectively classified as LTGs all the galaxies with a dominating disk component and as ETGs the ones with a prominent spheroidal component. However, galaxies are usually mixed systems: LTGs often feature a spheroidal bulge with older stellar population, while ETG progenitors can feature rotating disks surrounding the central strongly star-forming region. Disentangling the 2 components and assigning to them a different star formation history would be a big step forward for an accurate computation of a metallicity dependent cosmic SFR density and in the next future I will work on developing a model able to reproduce this separation.

- A good theoretical test for the galaxy evolution model of Lapi et al. 2020, or for any further development, is to be able to provide an interlink between different galaxy statistics. In fact, the model propose a way to track the evolution of observable quantities, such as $M_\star$ and SFR, as a function of halo mass and formation redshift. Therefore a remarkable result would be to reconstruct the distribution of observable quantities such as the GSMF or the SFRF starting from an halo statistics like the halo mass functions. This computation, other then testing the model, would provide great theoretical insights on the link between halo mass, stellar mass and SFR.

- Once a correct astrophysical characterization of the galactic environments and of the population of merging binaries has been obtained, I would like to tackle 2 important questions: is it possible, with future GW observations, to place stringent constraint on the shape of the stellar IMF even in galaxies significantly different from the local ones (like high-z galaxies)? Can we extract some competitive cosmological information from GW observations, possibly using statistical information on the host galaxies?

- As for the heavy seed formation scenario, the treatment reported in this thesis is completely semi analytical. The various assumptions underlying the computation, together with some possible limitations have been explored in Section 3.7. The effect of such a wide range of possible astrophysical concomitant and co-spatial processes, together with the intrinsic stochastic nature of the processes in act (see Bortolas et al. 2020), can not be kept into account in a solely analytical treatment and a zoom-in numerical simulation is required to further test the mechanism. However the set up of the simulation would not be easy: the simulated BH and NS have relatively small masses ($1 \lesssim m_\bullet\,[\mathrm{M}_\odot] \lesssim 100$)

and the gas particles should be less massive than the perturber for dynamical friction to work. Therefore the resolution required for a full hydrodynamical simulation is extreme. Luckily, as shown in Section 3.2 and 3.4, the relevant timescales of the process are short $\lesssim 3\times10^7$ yr and the size of the interested region is not larger than $\sim$ 300 pc. These favorable features may allow to produce an high resolution simulation not extremely computational expensive. However the knowledge of an expert in the hydrodynamical simulation field is needed for the set up. If a full hydrodynamical simulation results unfeasible, a possible way-out is to approximate the gas as a mean field, not tracking the behaviour of single gas particles, but considering just the mean gas distribution and evolving only the perturbers in such an environment. With this kind of set up the simulation would be more handable and achievable in the next future.

- Carrying on the collaboration with Alex Sicilia, we would like to extend the work on the stellar BH mass function to self-consistently derive the overall BH mass function over the entire mass range [5 $M_\odot$ – 10^{10} $M_\odot$]. To do this we want to exploit the stellar BH mass function of Figure 4.3 and combine it with the mechanism of heavy seed formation described in this thesis. In this way we would be able to produce a mass function for transient intermediate mass BHs and, finally, after gas accretion takes over, for supermassive BHs, and compare it with literature estimations and observations.

Appendix A

A galaxy evolution model

In this Appendix I review the analytical galaxy evolution model I have employed to generate a metallicity distribution in Section 2.2.4. Although I presented an approximation to its results in equation (2.15), I believe it is important to show some more details because it can guide in understanding key points of the thesis and because, in the next future, I will fully exploit it to derive metallicity scaling relations for different galactic populations (see Section 4.3).

The model is based on the 2 works Pantoni et al. 2019, where only ETG progenitors are considered, and Lapi et al. 2020 where also LTGs are taken into account. I caveat that the model presented is completely analytical and therefore many of the astrophysical processes described are spatially or time-averaged; however the transparency and predictive power of an analytical approach allow to straightforwardly understand the main factors driving the evolution of physical quantities and to easily interpret its results.

A.1 Analytic solutions for gas and stars

Galaxies are considered as open, one-zone systems with three interlinked mass components: (1) infalling halo gas that is able to cool quickly, subject to condensation toward the central regions, and refurnished by outflows via wind recycling; (2) cold star-forming gas fed by infall and depleted by star formation and stellar feedback; and (3) stellar mass, partially restituted to

the cold phase by stellar evolution. The evolution of these quantities is described by the system of equations:

$$\begin{cases} \dot{M}_{\rm inf} = -\frac{M_{\rm inf}}{\tau_{\rm cond}} + \alpha_{\rm GF}\,\epsilon_{\rm out}\,\frac{M_{\rm cold}}{\tau_\star} \\ \dot{M}_{\rm cold} = \frac{M_{\rm inf}}{\tau_{\rm cond}} - (1-\mathcal{R})\,\frac{M_{\rm cold}}{\tau_\star} - \epsilon_{\rm out}\,\frac{M_{\rm cold}}{\tau_\star} \\ \dot{M}_\star = (1-\mathcal{R})\,\frac{M_{\rm cold}}{\tau_\star} \end{cases} \tag{A.1}$$

This system should be interpreted as: the infalling mass condensates in cold mass over typical timescales $\tau_{\rm cold}$, the cold gas form stars on timescales $\tau_\star$, while outflows driven by stellar winds and type II supernova explosions, parametrized by the mass loading factor $\epsilon_{\rm out}$, evacuate part of the cold gas over the same star formation timescales. However a fraction of the outflowing gas can be recycled and come back at later times in the way of an inward gas flow or of a "galactic fountain". This phenomenon has been recognized to have profound impact especially on the evolution of late-type disk galaxies (see Fraternali 2017 for a review) and is parametrized by $\alpha_{\rm GF}$. The instantaneous recycling approximation is adopted (see Section 1.3.4) and $M_\star$ represents the effective mass locked in long living stars; therefore the SFR can be obtained as $\dot{M}_\star/(1-\mathcal{R}) = M_{\rm cold}/\tau_\star$.

Under standard initial conditions the above system of equations can be solved defining two auxiliary quantities:

$$\begin{cases} \lambda_+ = \frac{s\,\gamma+1+\Lambda}{2} \\ \lambda_- = \frac{s\,\gamma+1-\Lambda}{2} \end{cases} \tag{A.2}$$

where $s \equiv \tau_{\rm cond}/\tau_\star$, $\gamma \equiv 1+\mathcal{R}+\epsilon_{\rm out}$ and $\Lambda \equiv \sqrt{(s\,\gamma-1)^2 + 4\,\alpha_{\rm GF}\,s\,\epsilon_{\rm out}}$. The solution of (A.1) as a function of the galactic age τ are:

$$\begin{cases} M_{\rm inf}(\tau) = \frac{f_{\rm inf}\,M_b}{\lambda_+-\lambda_-}\,[(1-\lambda_+)\,e^{-\lambda_-\,x} + (1-\lambda_-)\,e^{-\lambda_+\,x}] \\ M_{\rm cold}(\tau) = \frac{f_{\rm inf}\,M_b}{\lambda_+-\lambda_-}\,(e^{-\lambda_-\,x} - e^{-\lambda_+\,x}) \\ M_\star(\tau) = (1-\mathcal{R})\,\frac{s\,f_{\rm inf}\,M_b}{\lambda_+-\lambda_-}\,[\frac{1-e^{-\lambda_-}}{\lambda_-} - \frac{1-e^{-\lambda_+\,x}}{\lambda_+\,x}] \end{cases} \tag{A.3}$$

where $x \equiv \tau/\tau_{\rm cond}$ takes the role of the time variable, $M_b \equiv f_b\,M_H$ is the total baryon mass inside the DM halo and $f_{\rm inf} \equiv M_{\rm inf}(0)/M_b$ is the initial fraction

of baryons that can effectively cool quickly and inflow toward the inner regions of the halo over the timescale $\tau_{\rm cond}$.

It is instructive to examine the limits for $\tau \ll \tau_{\rm cond}$ and $\tau \gg \tau_{\rm cond}$ of equations (A.3). For $\tau \ll \tau_{\rm cond}$:

$$\begin{cases} M_{\rm inf} \simeq f_{\rm inf}\, M_b\, (1 - \frac{\tau}{\tau_{\rm cond}}) \\ \\ M_{\rm cold} \simeq f_{\rm inf}\, M_b\, (\frac{\tau}{\tau_{\rm cond}}) \\ \\ M_\star \simeq (1-\mathcal{R})\, \frac{s\, f_{\rm inf}\, M_b}{2} (\frac{\tau}{\tau_{\rm cond}})^2 \end{cases} \tag{A.4}$$

While the infall and cold gas mass are depleted and enhanced linearly, the stellar mass rises quadratically since it has to wait for the cold gas reservoir to set up. For $\tau \gg \tau_{\rm cond}$:

$$\begin{cases} M_{\rm inf} \simeq (\lambda_+ - 1)\, \frac{f_{\rm inf}\, M_b}{\lambda_+ - \lambda_-}\, e^{-\lambda_-\, \tau/\tau_{\rm cond}} \\ \\ M_{\rm cold} \simeq \frac{f_{\rm inf}\, M_b}{\lambda_+ - \lambda_-}\, e^{-\lambda_-\, \tau/\tau_{\rm cond}} \\ \\ M_\star \simeq (1-\mathcal{R})\, \frac{s\, f_{\rm inf}\, M_b}{\lambda_+\, \lambda_-} \left[1 - \frac{\lambda_+}{\lambda_+ - \lambda_-}\, e^{-\lambda_-\, \tau/\tau_{\rm cond}}\right] \end{cases} \tag{A.5}$$

The infall and cold gas masses decline exponentially, while the stellar mass converges to the relic value $\bar{M}_\star \simeq (1-\mathcal{R})\, f_{\rm inf}\, M_b / [1 - \mathcal{R} + \epsilon_{\rm out}\, (1 - \alpha_{\rm GF})]$.

The difference between the two galactic populations (LTGs and ETG progenitors) is determined by the values of the parameters entering in the equations above: $f_{\rm inf}$, $\tau_{\rm cond}$, s, γ, $\alpha_{\rm GF}$, which depend on halo mass and formation redshift. The computation of their values goes beyond the scope of the present thesis, but in Lapi et al. 2020 they are soundly estimated via analytical arguments; I refer the interested reader to that paper. In particular it is found that s and $\alpha_{\rm GF}$ make the biggest difference between the two galactic populations with $s \sim 1-3$ and $\alpha \sim 0.75 - 0$ for LTGs and ETG progenitors respectively. This yields $\lambda_- \sim 0.25 - 1$ for the two populations ensuing a different decay times for $M_{\rm cold}$ and a consequent different duration of the main star formation episode.

Some examples of the evolution described by equations (A.3) is shown in Figures A.1 and A.2 (top rows) for LTGs and ETG progenitors respectively and for different halo masses and formation redshifts. From the Figures it results evident that ETG progenitors attain large SFR values $\psi \lesssim 1000\, {\rm M}_\odot\, {\rm yr}^{-1}$ over short timescales $\tau \lesssim 1\, {\rm Gyr}$ (blue line in top left panel of Figure A.2),

especially for more massive halos (compare top left and top right panels), in agreement with the downsizing scenario. On the other hand, LTGs have smaller SFR values $\psi \lesssim 10\,\mathrm{M}_\odot\,\mathrm{yr}^{-1}$ extending over larger timescales $\lesssim 8\,\mathrm{Gyr}$ (blue line in top middle panel of Figure A.1). Also in this case the halo mass plays an important role, with galaxies in large halos featuring more bursty SFHs (compare top left, top middle and top right panels).

A.2 Metals

From the evolutionary tracks of gas and stellar components, it is possible to self-consistently derive the time evolution of metallicity in gas and stars, that can be described by the following system of coupled equations:

$$\begin{cases} \frac{\mathrm{d}(M_\mathrm{inf}\,Z_\mathrm{inf})}{\mathrm{d}\tau} = -\frac{M_\mathrm{inf}}{\tau_\mathrm{cond}}\,Z_\mathrm{inf} + \alpha_\mathrm{GF}\,\epsilon_\mathrm{out}\,\frac{M_\mathrm{cold}}{\tau_\star}\,Z_\mathrm{cold} \\ \frac{\mathrm{d}(M_\mathrm{cold}\,Z_\mathrm{cold})}{\mathrm{d}\tau} = +\frac{M_\mathrm{inf}}{\tau_\mathrm{cond}}\,Z_\mathrm{inf} - \gamma\,\frac{M_\mathrm{cold}}{\tau_\star}\,Z_\mathrm{cold} + y_Z\,(1-\mathcal{R})\,\frac{M_\mathrm{cold}}{\tau_\star} \\ \frac{\mathrm{d}(M_\star\,Z_\star)}{\mathrm{d}\tau} = (1-\mathcal{R})\,\frac{M_\mathrm{cold}}{\tau_\star}\,Z_\mathrm{cold} \end{cases} \tag{A.6}$$

The equations above prescribe that the mass of metals in cold gas, $M_\mathrm{cold}\,Z_\mathrm{cold}$, evolves because of dilution at a rate $M_\mathrm{inf}\,Z_\mathrm{inf}/\tau_\mathrm{cond}$, instantaneous metal production at a rate $y_Z\,(1-\mathcal{R})\,M_\mathrm{cold}/\tau_\star$, outflow depletion at a rate $\epsilon_\mathrm{out}\,M_\mathrm{cold}\,Z_\mathrm{cold}/\tau_\star$, and astration (metal mass locking into stellar remnants) at a rate $(1-\mathcal{R})\,M_\mathrm{cold}\,Z_\mathrm{cold}/\tau_\star$; on the other hand, the mass of the metals in the infalling gas varies because of condensation at a rate $M_\mathrm{inf}\,Z_\mathrm{inf}/\tau_\mathrm{cond}$ and of enrichment due to wind recycling at a rate $\alpha_\mathrm{GF}\,\epsilon_\mathrm{out}\,M_\mathrm{cold}\,Z_\mathrm{cold}/\tau_\star$.

Using equations (A.1) the system of the first two equations above can be recasted into the form

$$\begin{cases} \dot{Z}_\mathrm{inf} = \alpha_\mathrm{GF}\,s\,\epsilon_\mathrm{out}\,\frac{M_\mathrm{cold}}{M_\mathrm{inf}}\,\frac{Z_\mathrm{cold}-Z_\mathrm{inf}}{\tau_\mathrm{cond}} \\ \dot{Z}_\mathrm{cold} = -\frac{M_\mathrm{inf}}{M_\mathrm{cold}}\,\frac{Z_\mathrm{cold}-Z_\mathrm{inf}}{\tau_\mathrm{cond}} + \frac{s\,y_Z\,(1-\mathcal{R})}{\tau_\mathrm{cond}} \end{cases} \tag{A.7}$$

In many previous analytic models, to solve the chemical evolution equation an empirical shape of the SFH is adopted; remarkably, here I instead use the self-consistent solutions for the time evolution of the infalling and cold gas masses.

The system above can be analytically solved as:

$$\begin{cases} Z_{\rm inf}(\tau) = \bar{Z}_{\rm gas}\left\{(1-\lambda_-)\,x - 2\,\frac{1-\lambda_-}{\lambda_+-\lambda_-}\,\left[1 - \frac{(\lambda_+-\lambda_-)\,(1+\frac{\lambda_++\lambda_--2}{2}\,x)}{1-\lambda_-+(\lambda_+-1)\,e^{(\lambda_+-\lambda_-)\,x}}\right]\right\} \\ \\ Z_{\rm cold}(\tau) = \bar{Z}_{\rm gas}\left\{(1-\lambda_-)\,x + \frac{\lambda_++\lambda_--2}{\lambda_+-\lambda_-}\,\left[1 - \frac{(\lambda_+-\lambda_-)\,x}{e^{(\lambda_+-\lambda_-)\,x}-1}\right]\right\} \end{cases} \tag{A.8}$$

where

$$\bar{Z}_{\rm gas} = \frac{s\,y_Z\,(1-\mathcal{R})}{\lambda_+-\lambda_-} \tag{A.9}$$

represents the asymptotic value for $\tau \gg \tau_{\rm cond}$ of the difference $Z_{\rm cold} - Z_{\rm inf}$, which is finite since individually $Z_{\rm cold}$ and $Z_{\rm inf}$ diverge linearly in the same manner. Note that such a divergence is not an issue because the masses in metals $M\,Z$ for both the infall and the cold gas components are always finite and exponentially suppressed at late-times.

It is also worth looking at the initial behaviour of the gas metallicities for $\tau \ll \tau_{\rm cond}$, that reads

$$\begin{cases} Z_{\rm inf} \simeq \frac{s\,y_Z\,(1-\mathcal{R})}{6}\,s\,\epsilon_{\rm out}\,\alpha_{\rm GF}\,\left(\frac{\tau}{\tau_{\rm cond}}\right)^3 \\ \\ Z_{\rm cold} \simeq \frac{s\,y_Z\,(1-\mathcal{R})}{2}\,\frac{\tau}{\tau_{\rm cond}} \end{cases} \tag{A.10}$$

the cold gas metallicity increases almost linearly with galactic age, while the infalling gas metallicity evolution is cubic; this is because at early times the cold gas is rapidly enriched by direct production from stars, while the infalling gas has to wait the galactic fountain process to bring some metals from the cold gas into it.

The last of equations (A.6) implies that the metallicity $Z_\star$ in the stellar component is the average of the cold gas one over the star formation history:

$$Z_\star(\tau) = \frac{1}{M_\star(\tau)}\,\int_0^\tau {\rm d}\tau'\,Z_{\rm cold}(\tau')\,\dot{M}_\star(\tau') \tag{A.11}$$

Using the self-consistent solutions for $Z_{\rm cold}$ and $M_{\rm cold}$, one obtains:

$$\begin{aligned} Z_\star = \bar{Z}_\star\,&\left\{1 - \frac{\lambda_+\,\lambda_-}{(\lambda_+-\lambda_-)\,[\lambda_+\,(1-e^{-\lambda_-\,x}) - \lambda_-\,(1-\,e^{-\lambda_+\,x})]}\,\times\right. \\ &\left.\times\,\left[\frac{2\,\lambda_+\lambda_- - \lambda_+ - \lambda_-}{\lambda_+-\lambda_-}\left(e^{-\lambda_-\,x} - e^{-\lambda_+\,x}\right) + (1-\lambda_-)\,\lambda_+\,x\,e^{-\lambda_-\,x} - (\lambda_+-1)\,\lambda_-\,x\,e^{-\lambda_+\,x}\right]\right\} \end{aligned} \tag{A.12}$$

where the limiting value for $\tau \gg \tau_{\rm cond}$ writes:

$$\bar{Z}_\star = \frac{s\, y_Z\, (1-\mathcal{R})}{\lambda_+\, \lambda_-} = \frac{y_Z\, (1-\mathcal{R})}{1-\mathcal{R}+\epsilon_{\rm out}\, (1-\alpha_{\rm GF})} \tag{A.13}$$

it is seen that the analytic solutions predict that the asymptotic stellar metallicity $\bar{Z}_\star \simeq \bar{Z}_{\rm gas}\, (\lambda_+ - \lambda_-)/\lambda_+\lambda_-$ is not equal, but rather somewhat lower, than the gas one. The early-time behaviour of $Z_\star$ for $\tau \ll \tau_{\rm cond}$ reads

$$Z_\star \simeq \frac{s\, y_Z\, (1-\mathcal{R})}{3}\, \frac{\tau}{\tau_{\rm cond}}\,, \tag{A.14}$$

so that initially $Z_\star(\tau) \simeq 2\, Z_{\rm cold}(\tau)/3$, i.e., the stellar and cold gas metallicity evolve in parallel.

Some examples of stellar metallicity evolution are shown in in Figures A.1 and A.2 (bottom rows) for LTGs and ETG progenitors respectively and for different halo masses and formation redshifts.

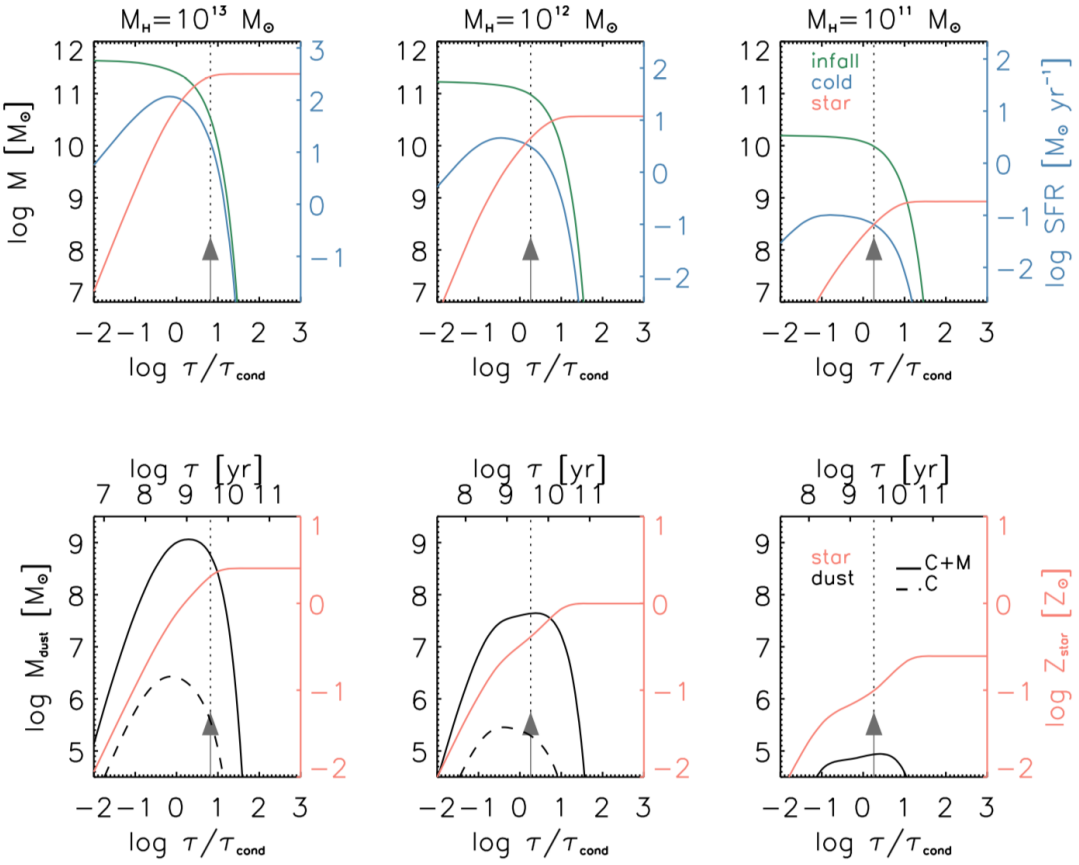

FIGURE A.1: Top panels: evolution of the infall (green), cold (blue), and stellar (orange) masses as a function of galactic age τ for LTGs hosted in halos with mass $M_H = 10^{13}\,\mathrm{M}_\odot$ (left panel), $M_H = 10^{12}\,\mathrm{M}_\odot$ (middle panel) and $M_H = 10^{11}\,\mathrm{M}_\odot$ (right panel) formed at $z_{\mathrm{form}} \sim 0.5$. Bottom panels: evolution of the dust mass and of the stellar metallicity.

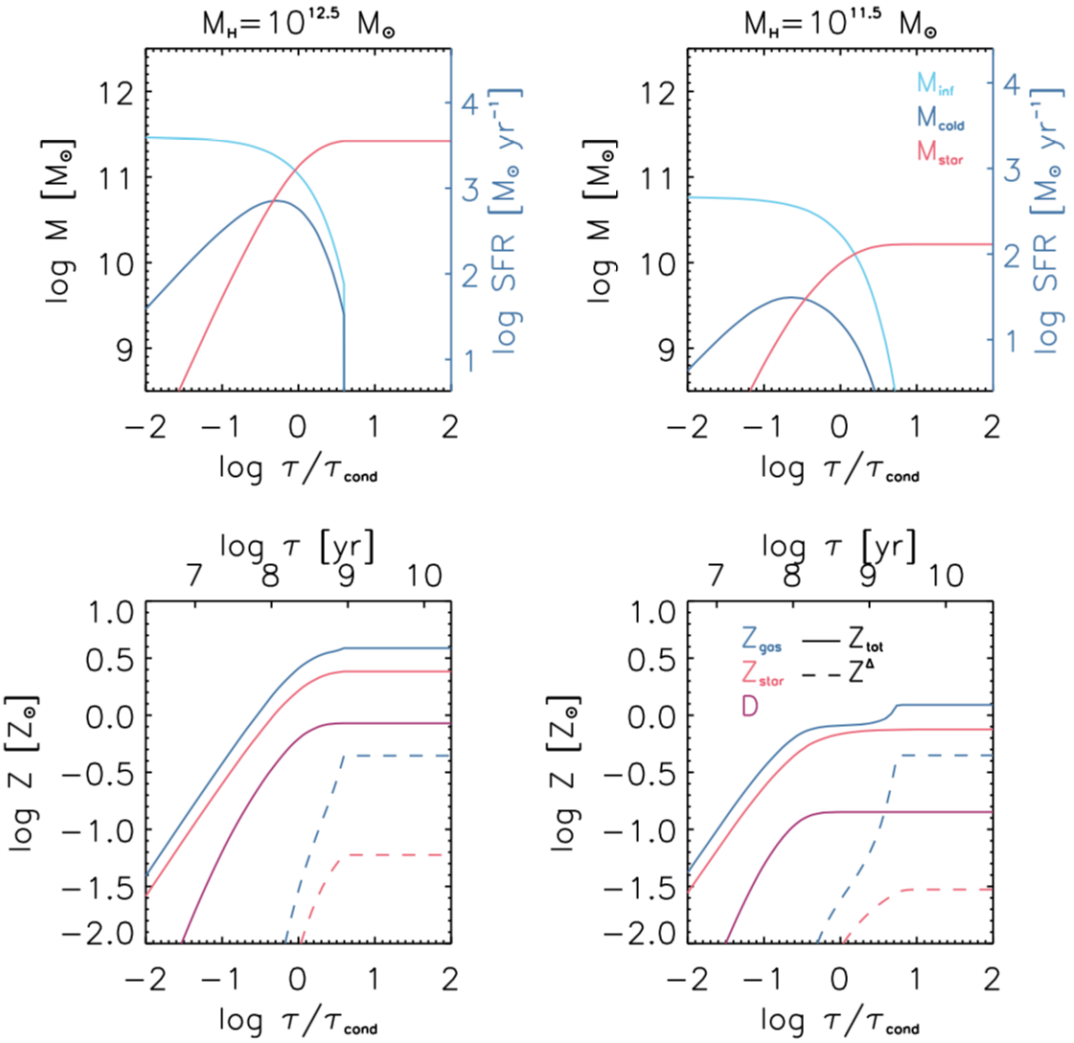

FIGURE A.2: Top panels: evolution of the infall (cyan), cold (blue), and stellar (red) masses as a function of galactic age τ for ETG progenitors hosted in halos with mass $M_H = 10^{12.5}\,\mathrm{M}_\odot$ (left panel), $M_H = 10^{11.5}\,\mathrm{M}_\odot$ (right panel) formed at $z_{\rm form} \sim 3$. Bottom panels: evolution of the dust mass and of the stellar metallicity. Credits: Pantoni et al. 2019.

Appendix B

Galaxies $\times$ GW cross-correlations

An intriguing possibility to extract both cosmological and astrophysical information from GW observations is to cross-correlate the detected signals with other tracers of the LSS such as the galaxy distribution. During my Ph.D. I worked on this idea in collaboration with Giulio Scelfo and a proof of concept computation has been carried out in Scelfo et al. 2020. Since this is an application of the formalism developed in Chapter 2, I summarize the main results in this Appendix, not including it in the main body of the thesis.

Adopting a galaxy statistics such as the SFRF it is possible to cross-correlate the resulting galactic distribution with GW events self-consistently computed from the aforementioned distribution. Thus, the two tracers considered are not coming from different and independent sources, but from the same objects (galaxies); however the two different messengers entering in the cross-correlation analysis, SFR and GWs, can trace the galaxy distribution in a different way. For example the GW event redshift distribution, as well as the chirp mass, is strongly influenced by metallicity and by stellar and binary evolution prescriptions adopted, as shown in Chapter 2. For these reasons cross-correlating the same sources via two different messengers can help not only in alleviating systematics but also in enhancing the amount of astrophysical information encoded in the signal.

A forecast on the cross-correlation signal can be obtained by realistically modeling these two types of tracers, especially awaiting the soon-to-come GWs detections from third generation observatories.

B.1 Galaxies

The galaxy redshift distribuiton can be reconstructed directly from the SFRF. Using SFR to parametrize galaxies also allow for the study of different kind of objects, subdividing them in SFR bins and separately investigating their cross-correlation signal. The redshift distribution for different SFR cuts can

be computed as:

$$\frac{\mathrm{d}N_{\bar{\psi}}}{\mathrm{d}z}(t,\psi\geq\bar{\psi})=\frac{\mathrm{d}V}{\mathrm{d}z}\int_{\bar{\psi}}\mathrm{d}\log\psi\frac{\mathrm{d}^2N}{\mathrm{d}\log\psi\,\mathrm{d}V}. \tag{B.1}$$

In particular I show results for galaxies with $\psi\geq 10\,\mathrm{M}_\odot\,\mathrm{yr}^{-1}$, $\psi\geq 100\,\mathrm{M}_\odot\,\mathrm{yr}^{-1}$ and $\psi\geq 300\,\mathrm{M}_\odot\,\mathrm{yr}^{-1}$.

A fundamental ingredient entering in the analysis is the bias parameter $b(z)$. Since the considered tracers are galaxies selected, counted and divided by their SFR, the bias parameter should be connected to this quantity. This has been done in Aversa et al. 2015, associating the luminosity/SFR of the galaxy to the mass of the hosting dark matter halo through an abundance matching technique and then assigning to a galaxy with given SFR the bias of the corresponding halo. Abundance matching is a standard method to derive a monotonic relationship between the galaxy and the halo properties by matching the corresponding number densities (in this case the SFRF and the halo mass functions). Once $M_H(\psi)$ is determined I assign to each galaxy the bias corresponding to the halo associated to its SFR: $b(z,\psi)=b(z,M_H(z,\psi))$, where $b(z,M_H)$ is computed as in Sheth et al. 2001 and approximated by Lapi & Danese 2014. It is now easy to compute an effective bias for all the galaxies above a certain SFR threshold $\bar{\psi}$ weighting $b(z,\psi)$ by the corresponding galaxy distribution:

$$b_{\bar{\psi}}(z,\psi\geq\bar{\psi})=\frac{\int_{\bar{\psi}}^{\infty}\mathrm{d}\psi\frac{\mathrm{d}^2N}{\mathrm{d}\psi\,\mathrm{d}V}\,b(z,\psi)}{\int_{\bar{\psi}}^{\infty}\mathrm{d}\psi\,\frac{\mathrm{d}^2N}{\mathrm{d}\psi\,\mathrm{d}V}} \tag{B.2}$$

The third important quantity to control for the cross-correlation analysis is the magnification bias: it quantifies the change in the observed surface density of sources of a given tracer induced by gravitational lensing. Two effects compete against each other: on one side the number of observed sources can increase due to a magnification of the received flux, which would make visible some sources right below the visibility threshold; on the other side an increase of the area reduces the observed number density of objects. The magnification bias for the 3 SFR cuts considered is proportional to the logarithmic slope of their dN_ψ/dz computed at $\psi=\bar{\psi}$:

$$s_{g,\bar{\psi}}(z)=-\frac{2}{5}\left.\frac{d\log\left(\frac{\mathrm{d}^2N_\psi(z,>\psi)}{\mathrm{d}z\,\mathrm{d}\Omega}\right)}{\mathrm{d}\log\psi}\right|_{\psi=\bar{\psi}} \tag{B.3}$$

In Figure B.1 I show the redshift distribution (left panel), bias (middle panel) and magnification bias (right panel) for galaxies in the different SFR bins considered.

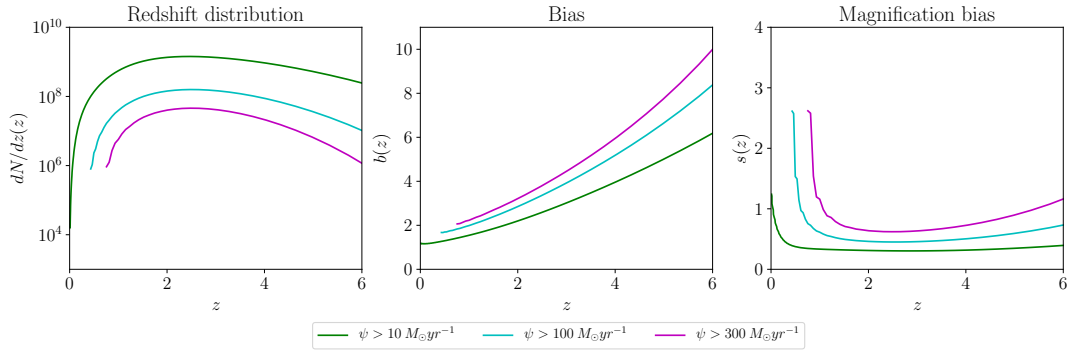

FIGURE B.1: Full-sky redshift distributions (*left*), bias (*center*) and magnification bias (*right*) for all galactic populations. Quantities referred to galaxies with SFR $\psi > 10\,\mathrm{M}_\odot\,\mathrm{yr}^{-1}$, $\psi > 100\,\mathrm{M}_\odot\,\mathrm{yr}^{-1}$, $\psi > 300\,\mathrm{M}_\odot\,\mathrm{yr}^{-1}$ are respectively in green, cyan and magenta lines.

B.2 Gravitational Waves

The redshift distribution of GW detected events can be computed with the formalism described in Section 2.5, using a galactic term derived from the SFRF (equations (2.13) or (2.21)). Such a distribution is shown in Figure B.2 (left panel). For reference, ET detection rates have been considered.

As for the GW bias, since GW signals come from stellar DCO mergers, they originate from galaxies and they trace the underlying total matter distribution in the same way their host galaxies do. For this reason, GWs events can be characterized by the same bias of their hosts. Since DCO mergers take place in all galaxy types with different rates, a correct estimate of their bias needs to take into account which galaxy types are contributing most/less to the detected mergers, giving proportioned weights to their bias values when estimating that of all GWs events.

In order to assign a redshift dependent bias to the GW events, I make use of the bias $b(z,\psi)$ associated to a galaxy at a given redshift with given SFR and I weight it through the quantity $d^3\dot{N}_{\mathrm{merge}}/dz/d\rho/d\psi$ which keeps into account the contribution of the different SFRs (i.e. of different galaxies) to the total merging rates at a given redshift and S/N. This differential merging rate can be computed from equation (2.13) or (2.21) not integrating over the

SFR. Therefore, to compute the bias for gravitational waves I use the following expression:

$$b_{GW}(z,\rho) = \frac{\int \mathrm{d}\log\psi \, \frac{\mathrm{d}^3\dot{N}}{\mathrm{d}z\,\mathrm{d}\rho\,\mathrm{d}\log\psi} b(z,\psi)}{\int \mathrm{d}\log\psi \, \frac{\mathrm{d}^3\dot{N}}{\mathrm{d}z\,\mathrm{d}\rho\,\mathrm{d}\log\psi}} \,. \tag{B.4}$$

The effective bias, i.e. the bias for GWs with a S/N above a certain threshold ρ_0, is now easy to compute:

$$b_{GW,\rho_0}(z,>\rho_0) = \frac{\int_{\rho_0} \mathrm{d}\rho \, \frac{\mathrm{d}^2\dot{N}}{\mathrm{d}z\,\mathrm{d}\rho} \, b_{GW}(z,\rho)}{\int_{\rho_0} \mathrm{d}\rho \, \frac{\mathrm{d}^2\dot{N}}{\mathrm{d}z\,\mathrm{d}\rho}} \tag{B.5}$$

The bias for the detected events ($\rho_0 = 8$) is shown in Figure B.2 (middle panel). The interpretation of the shape of the GW bias is not trivial and explained in the following. At low redshift its value is ~ 1 since the only galaxies that contribute to the GW signals have low SFR and consequently a smaller bias. The following rapid increase with redshift is due to two factors: the first is just the standard growth with redshift of the galaxy bias, the second is that, increasing redshift, there are more and more highly star-forming galaxies that contribute to the GW events. These galaxies, as shown in Figure B.1, are more biased. At redshift $z \gtrsim 5$ the GW bias flattens. Again, this is due to different astrophysical effects. In particular, the redshift increase of the galaxies bias is compensated by the fact that at high redshift the detected GW events receive a larger contribution by less star-forming and, thus, less biased galaxies. This is due to two facts: firstly, the number of highly star-forming galaxies tends to decrease at redshift $z \gtrsim 3-4$; secondly, in massive galaxies with high SFR the metallicity is also high and, consequently, the compact remnants produced are less massive. This means that galaxies with larger SFRs tend to produce GW events with lower chirp mass. However, at high redshift the detector starts not to see anymore these low chirp mass events and, due to this selection effect, the GW events detected at higher and higher redshifts come from galaxies with lower SFR and are, consequently, less biased.

Similarly to the galaxy case, the magnification bias for GW events with $\rho > \rho_0$ is the logarithmic slope of their $dN_\rho/dz\,(z,>\rho)$ computed at $\rho = \rho_0$:

$$s_{GW,\rho_0}(z) = -\left.\frac{\mathrm{d}\log_{10}\left(\frac{\mathrm{d}^2\dot{N}_\rho(z,>\rho)}{\mathrm{d}z\,\mathrm{d}\Omega}\right)}{\mathrm{d}\rho}\right|_{\rho=\rho_0} \tag{B.6}$$

In Figure B.2 (right panel) it is shown the magnification bias for detected mergers ($\rho_0 = 8$). It can be seen that the magnification bias for NS-NS events features a fast growth with redshift because the NS-NS distribution in S/N is peaked at lower values of ρ with respect to BH-BH or BH-NS events. So, as the redshift increases, the peak of such distribution shifts toward values $\rho \lesssim 8$: the choice of the faint end of S/N has then a huge effect on NS-NS events. Instead, for BH-BH and BH-NS events, the distribution in S/N is much broader, even at high redshifts: the choice of the faint end of S/N has not a large impact on the number of detections. For this reason the magnification bias for those events always remains at moderate values.

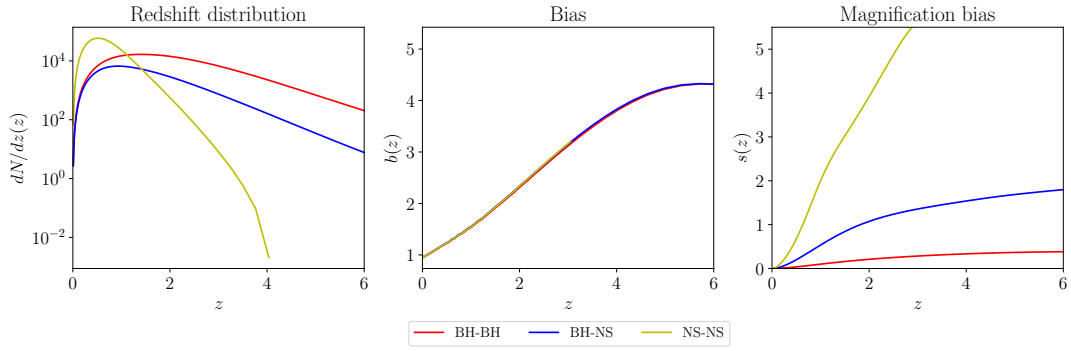

FIGURE B.2: Full-sky redshift distributions for an observation time $T_{\rm obs} = 1$yr (*left*), bias (*center*) and magnification bias (*right*) for all GWs tracers, as detected by ET. Quantities referred to BH-BH, BH-NS, NS-NS mergers are respectively in red, blue and yellow lines.

B.3 Application to astrophysics

Making use of this formalism, the cross-correlation angular power specta C_ℓ's can be computed using the code `CLASS`. In Scelfo et al. 2020 a tomographic analysis, considering the contribution of different redshift bins, has been performed and a S/N has been computed to characterize the magnitude of the signal that could be extracted by the cross-correlations and determine whether it could be discerned from the noise.

The results are shown in Figure B.3, as a function of the angular resolution, for the different SFR cuts considered, for different types of DCO mergers, with $f_{\rm sky} = 0.7$ and up to a maximum multipole of $\ell_{\rm max} = 100$, corresponding to the best angular resolution reachable by ET (see e.g. Klimenko et al. 2011). The cumulative S/N generally reaches values above unity for all the tracers combinations. Note that the cross-correlation signal overcomes

the noise already for relatively low multipoles, at around $\ell_{\rm max} \sim 10-40$. The S/N is particularly high especially for the $\psi > 10\,{\rm M}_\odot/{\rm yr}\times$NS-NS case, where it reaches a value of $\sim$ 10. The NS-NS case is also the most dependent on the chosen SFR cut, because the peak of the detected NS-NS distribution is at rather low redshift ($z \leq 1$), where the distribution of highly star-forming galaxies tends to fall down (see Figures B.1 and B.2, left panels). All in all, cross-correlations between the treated tracers, adopting a tomographic approach, can be informative given the rather high S/N ratio values.

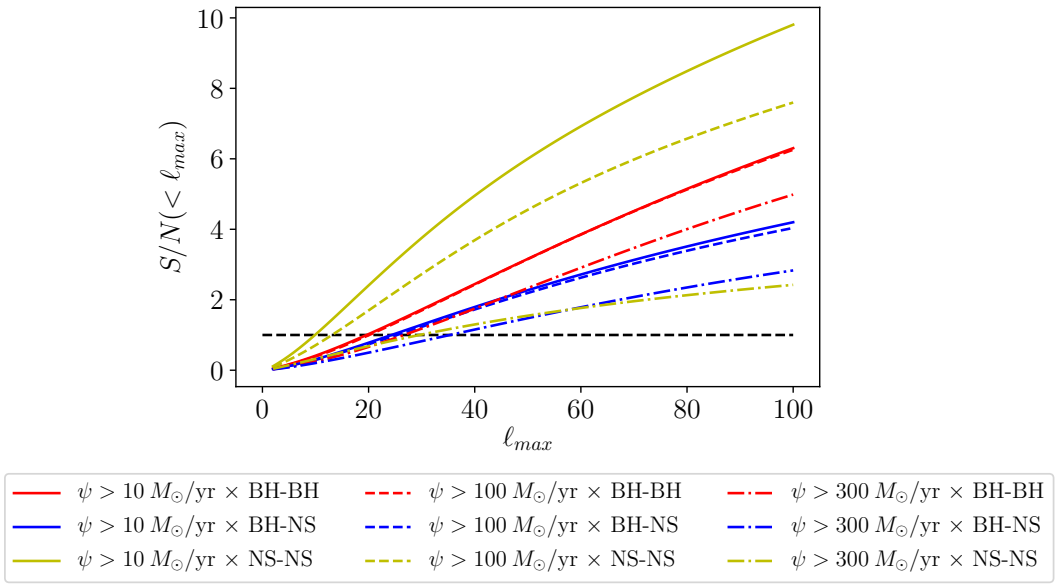

FIGURE B.3: Cumulative S/N($<\ \ell_{\rm max}$). The horizontal dashed line corresponds to S/N($<\ \ell_{\rm max}$) = 1. Line-styles refer to galaxies ($\psi > 10\,{\rm M}_\odot\,{\rm yr}^{-1}$ in full line, $\psi > 100\,{\rm M}_\odot\,{\rm yr}^{-1}$ in dashed line, $\psi > 300\,{\rm M}_\odot\,{\rm yr}^{-1}$ in dotted-dashed line) while colors refer to gravitational waves (BH-BH in red, BH-NS in blue, NS-NS in yellow). The plot refers to $T_{\rm obs}$ = 1yr and $f_{\rm sky}$ = 0.7.

This cross correlation analysis, in principle, can be exploited to extract astrophysical information. Given the uncertainties in the astrophysics and the enormous modeling possibilities, it is at the moment unlikely to be able to unequivocally determine the validity of one specific combination of prescriptions with respect to any possible other. For this reason, I report here just an extreme proof-of-concept case, following the lines of Scelfo et al. 2020, designed to apply this methodology, leaving the chance to use this formalism to whom is interested in applying it for specific tests. In fact, the application presented in this Section is not the only possible: any other astrophysical formulation and modeling that influences the estimate of redshift

distributions and/or biases of the considered tracers can in principle be addressed. This can cover a wide range of possibilities, from the stellar modeling (especially regarding the estimation of DCO masses and the constrain of all those processes influencing it) to galaxy evolution and SFRs calculation methods.

The case reported here concerns a different modelization of the merger efficiency as a function of metallicity (see Section 2.3). In particular I compare a rather unrealistic case in which the merger efficiency is constant with metallicity (called the benchmark case) with a case in which merger efficiency depend on metallicity as shown in Figure 2.10 (called Z-dependent case) in order to understand if it is possible to discriminate between these two scenarios from the cross-correlation analysis.

I make use of a $\Delta\chi^2$ statistics to evaluate a S/N, whose value (above/below unity) can provide information on how different the two models (one called as Fiducial and the other as Alternative) are. Following the same approach of Scelfo et al. 2018 the S/N is defined as:

$$\left(\frac{S}{N}\right)^2 \sim \Delta\chi^2 \equiv f_{\rm sky}\sum_{2}^{\ell_{\rm max}}(2\ell+1)(\mathbf{C}_\ell^{\rm Alternative}-\mathbf{C}_\ell^{\rm Fiducial})^T{\rm Cov}_\ell^{-1}(\mathbf{C}_\ell^{\rm Alternative}-\mathbf{C}_\ell^{\rm Fiducial}) \tag{B.7}$$

where ${\rm Cov}_\ell$ is the covariance matrix built from the C_ℓ's. Since the entries of the covariance matrix depend on which model is assumed as fiducial, the final forecasts also depend on this choice. For this reason, I compute S/N in both cases and compare them.

In Figure B.4 I provide the S/N obtained considering galaxies with $\psi > 10, 100, 300\,{\rm M}_\odot\,{\rm yr}^{-1}$. I show results for different observed sky-fractions $f_{\rm sky}$, observation times $T_{\rm obs}$ and for both models assumed as fiducial.

First of all, it can be seen that when the benchmark model is assumed as fiducial, the forecasts are significantly better compared to the opposite (for fixed $f_{\rm sky}$ and $T_{\rm obs}$): this is due to the fact that this model predicts a higher number of GWs mergers, providing a smaller shot noise contribution. For analogous reasons, when comparing the panels in Figure B.4, it can be seen that results are more optimistic when considering galaxies with $\psi > 10\,{\rm M}_\odot\,{\rm yr}^{-1}$: the higher the number of sources (galaxies in this case) the better the results. This is also reflected on the fact that the case with galaxies of $\psi > 300\,{\rm M}_\odot\,{\rm yr}^{-1}$ is the most pessimistic.

Looking in detail at each of the Figures, in the $\psi > 10\,{\rm M}_\odot\,{\rm yr}^{-1}$ case a S/N above unity can be reached in a relatively short time: even for small observed fractions of the sky (e.g., $f_{\rm sky} = 0.3$) not more than 3 years of observation would be required to marginally distinguish the two scenarios. Looking instead at the most pessimistic case, in which only galaxies with

$\psi > 300\,\mathrm{M}_\odot\,\mathrm{yr}^{-1}$ are considered, approximately 5 to 10 years of observation would be required to reach S/N $\sim$ 1 in the case of benchmark model assumed as fiducial. A much higher observation time (at least above 10 years) is required when assuming the Z-dependent scenario as fiducial. The case of $\psi > 100\,\mathrm{M}_\odot\,\mathrm{yr}^{-1}$ lies in between, with a still fairly optimistic prediction.

All in all the results are rather promising, especially when considering galaxies with $\psi > 10\,\mathrm{M}_\odot\,\mathrm{yr}^{-1}$ and $\psi > 100\,\mathrm{M}_\odot\,\mathrm{yr}^{-1}$: if the benchmark case is the fiducial one, deviations from it can be detected after just 2 yr of observational time. If the Z-dependent case is the fiducial, it is possible to detect variations from it in $\lesssim 5$ yr of observations. For highly star-forming galaxies with $\psi > 300\,\mathrm{M}_\odot/\mathrm{yr}$ instead, some more time is required to distinguish the two models. Still an observational time $\lesssim 10$ yr is enough if the benchmark case is considered as fiducial.

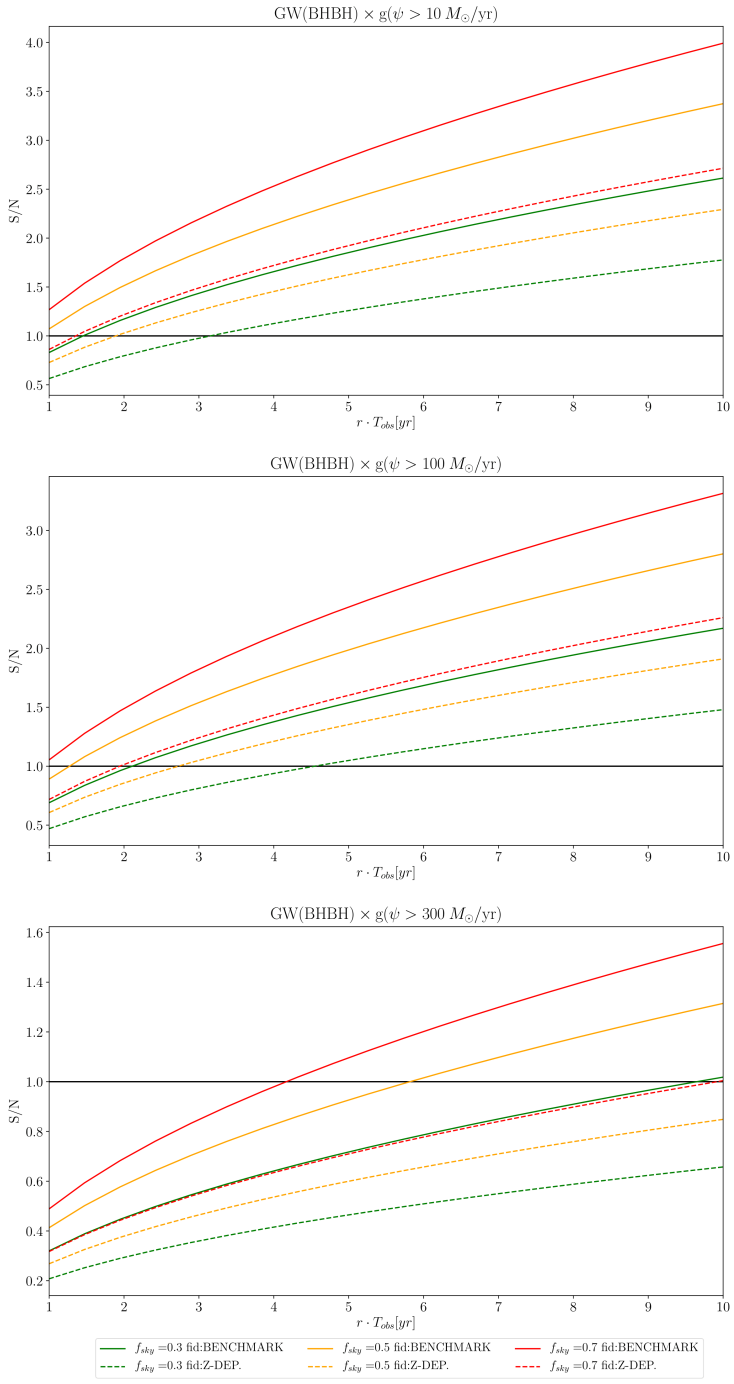

FIGURE B.4: S/N from $\Delta\chi^2$ analysis for discerning the two considered astrophysical scenarios. Galaxies with $\psi > 10, 100, 300\,\mathrm{M}_\odot\,\mathrm{yr}^{-1}$ are considered (top, central and bottom panel respectively). Continuous/dashed lines refer to the benchmark/Z-dependent model assumed as fiducial. Colors refer to different values of f_{sky} as shown in legend.

Appendix C

Stellar BH mass function

The study of the evolution of star formation across cosmic time and at different metallicities is useful not only to quantify the amount of mergers and GW signals, but more in general to understand many astrophysical phenomena related to stellar evolution. For example keeping track of the amount of stars and their metallicity at $z > 6$ is fundamental in order to correctly asses the number of ionizing photons available in the early Universe for theoretical reionization models, but also for computations regarding the supernova or gamma ray burst rates. Last but not least, the formalism developed in Chapter 2 of this thesis can be exploited for the computation of the stellar BH mass function over the whole history of the Universe.

Such an ab-initio approach has been undertaken in collaboration with Alex Sicilia (Sicilia et al. 2021, in preparation) and here I show the main results.

The relic BH mass function accumulated down to redshift z can be computed as:

$$\frac{\mathrm{d}^2 N_\bullet}{\mathrm{d}V\,\mathrm{d}\log m_\bullet}(m_\bullet|>z) = \int_z^\infty \mathrm{d}z' \frac{\mathrm{d}t_{z'}}{\mathrm{d}z'} \frac{\mathrm{d}^2 \dot{N}_\bullet}{\mathrm{d}V\,\mathrm{d}\log m_\bullet}(m_\bullet|z') \tag{C.1}$$

where the cosmic BH birthrate $\mathrm{d}\dot{N}_\bullet/\mathrm{d}V/\mathrm{d}\log m_\bullet$ is integrated over cosmic time. Such a birthrate is given by:

$$\frac{\mathrm{d}^2 \dot{N}_\bullet}{\mathrm{d}V\,\mathrm{d}\log m_\bullet}(m_\bullet|z) = \int \mathrm{d}\log Z \frac{\mathrm{d}^2 \dot{M}_{\mathrm{SFR}}}{\mathrm{d}V\,\mathrm{d}\log Z}(Z|z) \frac{\mathrm{d}^2 N_\bullet}{\mathrm{d}M_{\mathrm{SFR}}\,\mathrm{d}\log m_\bullet}(m_\bullet|Z) \tag{C.2}$$

where the first factor is the galactic term (as a reference I have used the SFRF+FMR case, equation (2.13)) and the second is the stellar term, this time including not only mergers, but all the possible channels to generate stellar BHs (see Section C.1). A cartoon representation of the computation of the BH cosmic birthrate and of the BH mass function is shown in Figure C.1.

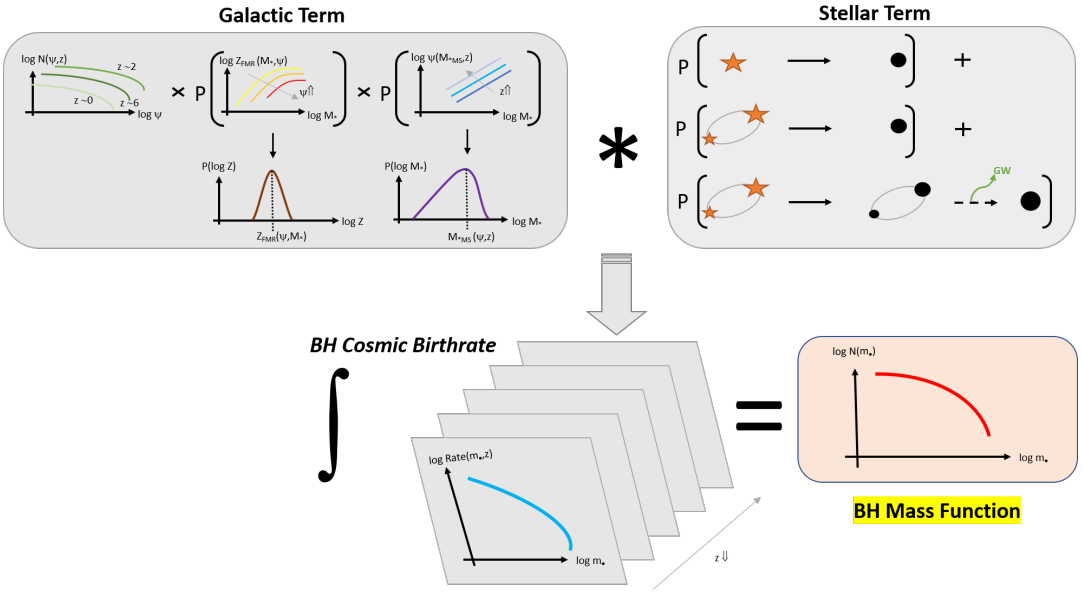

FIGURE C.1: Schematics showing the main steps to compute the stellar BH relic mass function (equation (C.1)). This is obtained by integration over redshift of the BH cosmic birthrate (equation (C.2)), which is in turn determined via the convolution of the galactic and the stellar terms. The galactic term is computed as in the SFRF+FMR case (equation (2.13)). The stellar term (equation (C.3)) is computed from the stellar and binary evolutionary code SEVN by summing up the numbers per unit star-formed mass that: (i) a single star evolves into a BH remnant (single stellar evolution); (ii) a binary stellar system evolves into a single BH remnant or two BHs no longer bounded (failed binaries); (iii) a binary stellar system evolves into a binary BH (binaries), that may eventually coealesce into a single BH via emission of gravitational waves.

C.1 Stellar term

The stellar term can be split in 3 different contributions:

$$\frac{\mathrm{d}^2 N_\bullet}{\mathrm{d}M_{\rm SFR}\,\mathrm{d}\log m_\bullet}(m_\bullet|Z) = \frac{\mathrm{d}^2 N_{\star\to\bullet}}{\mathrm{d}M_{\rm SFR}\,\mathrm{d}\log m_\bullet}(m_\bullet|Z) + \frac{\mathrm{d}^2 N_{\star\star\to\bullet}}{\mathrm{d}M_{\rm SFR}\,\mathrm{d}\log m_\bullet}(m_\bullet|Z) + \\ + \sum_{i=1,2} \frac{\mathrm{d}^2 N_{\star\star\to\bullet\bullet}}{\mathrm{d}M_{\rm SFR}\,\mathrm{d}\log m_{\bullet,i}}(m_\bullet|Z) \tag{C.3}$$

the first comes from the evolution of isolated, massive stars that evolve into BHs at the end of their life (hereafter referred to as 'single stellar evolution'); the second comes from stars that are originally in binary systems but end up

as isolated BHs because one of the companion has been ejected or destroyed or cannibalized (hereafter 'failed BH binaries'); the third comes from stars in binary systems that evolve into a binary BH with primary mass $m_{\bullet,1}$ and secondary mass $m_{\bullet,2}$ (hereafter 'binaries'). All these terms are strongly dependent on metallicity Z, since this quantity affects the efficiency of the various processes involved in stellar and binary evolution, like mass loss rates, mass transfers, core-collapse physics, etc. To compute the stellar term, I exploit the outcomes of the `SEVN` stellar and binary evolution code, that provides directly each of the above contributions (see Spera et al. 2019 for details).

In Figure C.2 I illustrate the stellar term $\mathrm{d}N_\bullet/\mathrm{d}M_{\rm SFR}/\mathrm{d}\log m_\bullet$, color coded, split in its various contributions. The top left panel refers to isolated stars evolving in BHs. It is seen that a roughly constant number of remnants with masses $m_\bullet \sim 5-30\,M_\odot$ is produced per logarithmic BH mass bin at any metallicity. Then there is a peak around $m_\bullet \sim 30-60\,M_\odot$, with the larger values applying to metal-poorer conditions, where stellar winds are not powerful enough to substantially erode the stellar envelope before the final collapse. Finally, the distribution rapidly falls off for larger $m_\bullet \gtrsim 50-60\,M_\odot$ even at low metallicity, due to the presence of pair-instability and pulsational pair-instability supernovae (see Woosley et al. 2002; Belczynski et al. 2016; Woosley 2017; Spera & Mapelli 2017). The top right panel refers to binary stellar systems failing to form a compact binary, and evolving instead into isolated BHs; this may happen because one of the progenitor star has been ejected far away or destroyed or cannibalized during binary stellar evolution. The distribution of failed BH binaries differs substantially from single stellar evolution, being skewed toward more massive BHs, and with an appreciable number of remnants of mass $m_\bullet \sim 50$–$160\,M_\odot$ produced especially at low metallicities. Such massive BH remnants are mainly formed when two (non-degenerate) companion stars merge during a common envelope phase, possibly leaving then a big BH remnant. Finally, notice that at high metallicity a non-negligible fraction of BHs in this channel has formed after the low-mass companion star had been ejected far away or destroyed by stellar winds and/or supernova explosions (see Spera et al. 2019 for details). The bottom left panel refers to binary stellar systems evolving into binary BHs; the distribution of primary and secondary BHs in the final configuration have been summed over. Although the overall number of binary BHs is substantially lower than the single BHs originated from the other two channels, most of them has a very similar mass spectrum; these remnants have formed from binary stars that underwent minor mass transfer episodes. However, at low metallicity stellar winds are reduced and hence the mass exchanged or lost during binary evolution may be significantly larger, implying a more

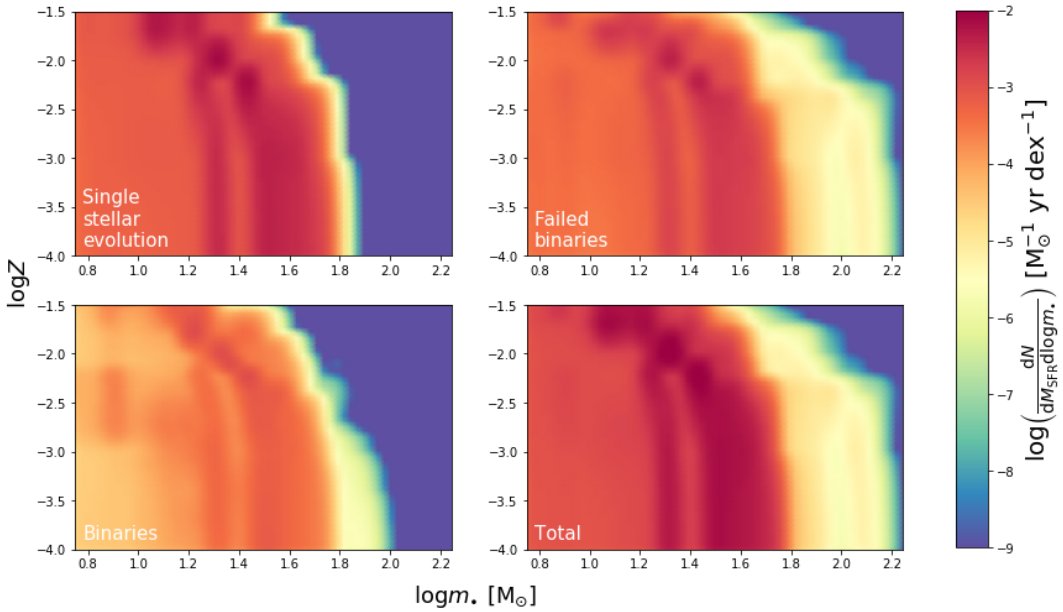

FIGURE C.2: The stellar term $\mathrm{d}N_\bullet/\mathrm{d}M_{\rm SFR}/\mathrm{d}\log m_\bullet$ of equation (C.3) expressing the number of BHs per unit star-formed mass (color-coded) as a function of BH mass $m_\bullet$ (on x-axis) and of metallicity Z (on y-axis). Different panels refer to: isolated stars evolving into single BH (top left); binary stars failing to form a compact binary and instead originating a single BH (top right); binary stars evolving in binary BHs (bottom left); summation of these contributions (bottom right).

extended tail toward masses $m_\bullet \lesssim 100\,M_\odot$ with respect to single stellar evolution. Finally, the bottom right panel illustrates the sum of all the previous formation channels.

C.2 Stellar BH mass function

The resulting stellar BH mass function (equation (C.1)) is shown in Figure C.3 (top panel) as a function of the remnant mass $m_\bullet$ for different redshifts $z \sim 0-10$. At given redshift, the mass function features a roughly constant behaviour for $m_\bullet \sim 5-50\,M_\odot$, followed by a quite steep decline for $m_\bullet \gtrsim 50\,M_\odot$. Noticeably, there are bumps at around $m_\bullet \sim 20\,M_\odot$, $m_\bullet \sim 30-50\,M_\odot$ and $m_\bullet \sim 120\,M_\odot$ reflecting features in the stellar terms; these are more pronounced at high redshift (where metallicity is smaller) and progressively washed out toward the local Universe. The mass function increases for decreasing redshift, quite rapidly down to $z \sim 2-3$ and then more mildly toward $z \sim 0$, following the behaviour of the cosmic SFR density. An analytic

rendition of the stellar BH mass function can be found in Sicilia et al. 2021 in preparation.

In Figure C.3 (bottom panel) it is highlighted the contribution of the different stellar evolution channels to the stellar BH relic mass function at $z \sim 0$ and at $z \sim 10$. In the range $m_\bullet \sim 5 - 50\,M_\odot$ the single stellar evolution and the failed BH binaries channels are very similar and dominates over BH binaries. For $m_\bullet \gtrsim 50\,M_\odot$ the single stellar evolution contribution sharply dies (due to the mass gap from pair-instability SNe) and the binary BH channel abruptly decreases (due to mass loss in common envelope phase), while the contribution from failed BH binaries dominates largely. Such a behaviour in the relative contributions is basically independent of redshift.

Since BHs in tight binaries may be able to progressively lose their energy via GW emission and to merge in a single, more massive BH, after a certain time delay t_d, part of BHs are subtracted from the lower mass end of the mass function and added to the high mass end. In Sicilia et al. 2021 authors have found an analytic formula to keep into account this effect, showing that its contribution to the overall mass function is negligible, since BH in bounded binaries give just a subdominant contribution to the BH mass function.

The contribution to the stellar BH mass function from merging binary BHs can be probed via gravitational wave observations. Recently, the LIGO/Virgo collaborations (Abbott et al. 2021b) has estimated the primary mass distribution for BH binaries that coalesce around $z \approx 0$. The result of the model illustrated in this Appendix and shown in Figure C.4 (top panel) is in remarkable agreement with LIGO/Virgo estimates up to $40\,M_\odot$. However, the observed primary mass distribution declines gently for $m_\bullet \gtrsim 40\,M_\odot$ out to $m_\bullet \sim 80 - 100\,M_\odot$ while the presented model dies off, since stellar evolution effects hinder the presence of very massive BHs in coalescing binaries. This occurs mainly for two reasons: the mass gap $m_\bullet \sim 50 - 120\,M_\odot$ for the production of BH due to pair-instability and pulsational pair-instability supernovae; (ii) the substantial mass loss during the common-envelope phase needed to produce a hardened compact binary that can merge within reasonable timescales. I also stress that such a sharp decline is not dependent on the specific galactic prescriptions nor scatter in the adopted relations, but it is instead common to any approach including the production and possible merging of only isolated BH binaries. A possible solution is explored in the next Section.

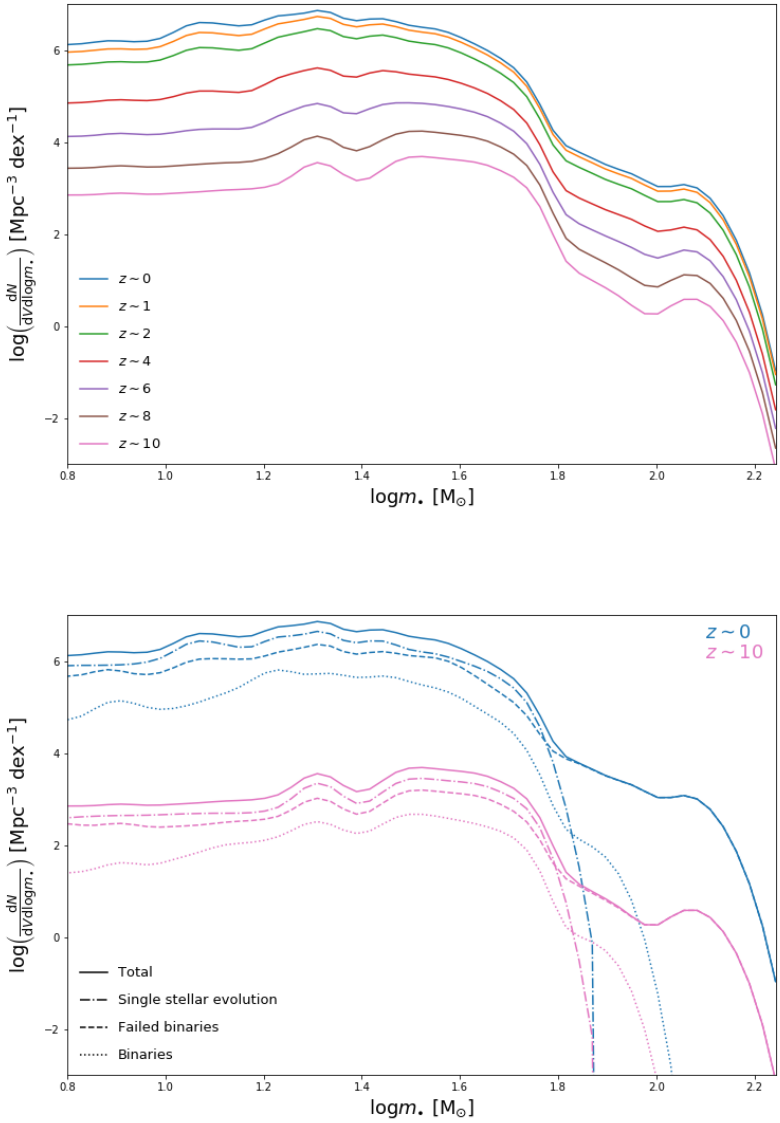

FIGURE C.3: Top panel: stellar BH relic mass function $\mathrm{d}N/\mathrm{d}V/\mathrm{d}\log m_\bullet$ as a function of the BH mass $m_\bullet$ at different redshifts $z \sim 0$ (cyan), $z \sim 1$ (orange), $z \sim 2$ (green), $z \sim 4$ (red), $z \sim 6$ (violet), $z \sim 8$ (brown) and $z \sim 10$ (pink). Bottom panel: stellar BH mass function at $z \sim 0$ (cyan) and $z \sim 10$ (pink) with different contributions from: single stellar evolution (dot-dashed lines), failed binaries (dashed lines) and binaries (dotted lines)

C.3 Dynamical channel

A viable solution to the issue highlighted in the previous Section could be that such large primary masses are produced in binary systems formed within the dense environment of young stellar clusters, open clusters, globular clusters, or nuclear star clusters (e.g., Di Carlo et al. 2019, 2020; Rodriguez et al. 2015, 2021; Antonini & Rasio 2016; Kumamoto et al. 2019; Arca-Sedda et al. 2020; Banerjee 2021; Mapelli et al. 2021). The central density of a star cluster can be so high that the orbits of binary stars are continuously perturbed by dynamical encounters with other members. Massive BHs $m_\bullet \gtrsim 40\,M_\odot$ in the pair instability mass gap can then be originated by hardening of BH binaries via dynamical exchanges in three-body encounters, and via the merging of massive progenitor stars; in addition, runaway collisions (i.e., a fast sequence of mergers; e.g., Portegies Zwart et al. 2004; Giersz et al. 2015; Mapelli 2016) in the densest cores of clusters with low metallicity can even produce intermediate mass BHs with $m_\bullet \gtrsim$ some $10^2\,M_\odot$.

To have a grasp on these effects, I proceed as follows. First, I construct the stellar term from the simulations by Di Carlo et al. 2020, that include dynamical effects in young star clusters. With respect to isolated conditions, these authors have found that an appreciable number of merging binaries with a primary mass $m_\bullet \gtrsim 40\,M_\odot$ is originated via dynamical exchanges, especially at low metallicities. Second, as mentioned in Section 4.2, I assume that a fraction $f_{\rm field}$ of the star formation occurs in the field and the complementary fraction $1 - f_{\rm field}$ occurs in star clusters (actually most of the stars are formed in young star clusters, but only a fraction of these may be subject to dynamical effects before exiting from the cluster or before the star cluster itself dissolves). Observations (see Goddard et al. 2010; Johnson et al. 2016; Chandar et al. 2017; Adamo et al. 2020) and cluster formation models (Kruijssen 2012; Pfeffer et al. 2018; Elmegreen 2018; El-Badry et al. 2019; Grudic et al. 2021) indicate that such a fraction is highly uncertain and possibly dependent on properties like the SFR spatial density and redshift; in this exploratory computation, I let the fraction $f_{\rm field}$ vary from 0.2 to 1 (which corresponds to isolated binaries only), and I split the galactic term accordingly. Finally, I combine the stellar and galactic term so derived and I compute the merging rates and the expected primary mass distribution.

The outcome is illustrated in Figure C.4 (bottom panel). As expected, increasing the fraction of SFR in star clusters (i.e., decreasing $f_{\rm field}$) produces a progressively more extended tail toward high primary masses, to the point that values $f_{\rm field} \lesssim 0.8$ actually can reconcile the theoretical prediction with the observational estimates.

The effect of the dynamical evolution channel on the overall relic BH mass function at $z \sim 0$ is illustrated in Figure 4.3 of Section 4.2. The marked difference with respect to the model with only isolated binaries is the absence of the drop at around $m_\bullet \sim 60\,M_\odot$ and of the abrupt cutoff for $m_\bullet \sim 150\,M_\odot$. Instead, the mass function declines smoothly for $m_\bullet \gtrsim 60\,M_\odot$.

Notice that in estimating the impact of the dynamical formation channel I have considered only young star clusters for the sake of simplicity (and because of the prompt availability of in-house dynamical simulations, that are extremely time-demanding to run from scratch). Globular clusters and nuclear star clusters could also be effective environments to build up massive binary BHs, since hierarchical mergers are more efficient in very rich and compact stellar systems (e.g., Miller & Hamilton 2002; Antonini et al. 2019; Mapelli et al. 2021). Hence, including models for globular and nuclear star clusters could allow to reproduce the observed primary BH mass function with an even larger value of $f_{\rm field}$.

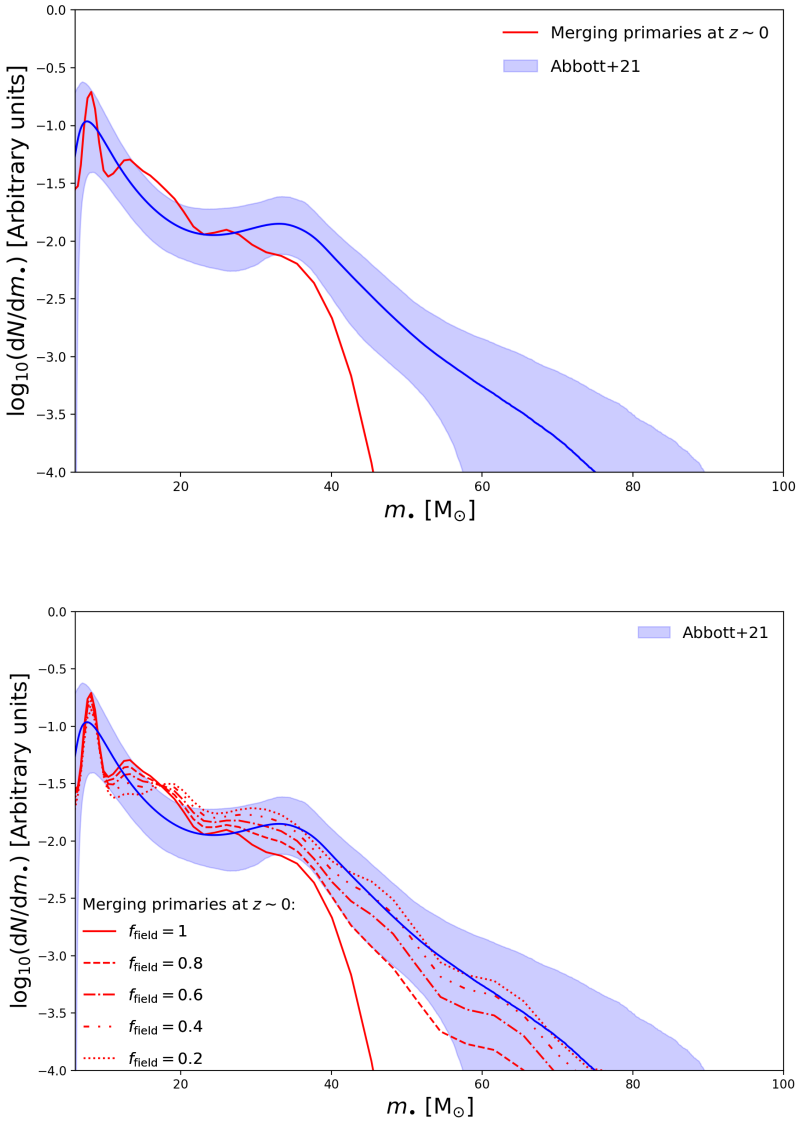

FIGURE C.4: Top panel: the primary BH mass function of merging BH binaries as a function of primary BH mass at $z \approx 0$. The model of this Appendix is illustrated by the red solid line. Estimate from the analysis of gravitational wave observations by Abbott et al. 2021b is reported as blue shaded area. Bottom panel: impact of the dynamical formation channel estimated from the simulations by Di Carlo et al. 2020. Lines refers to different fraction of star formation occurring in the field $f_{\rm field} \approx 1$ (solid; only isolated binaries), 0.8 (dashed), 0.6 (dot-dashed), 0.4 (dot-dot-dashed) and 0.2 (dotted).

Appendix D

Impact of the dynamical friction duration

In Section 3.5 I have discussed the role of the duration $t_{\rm max}$ over which the dynamical friction process is active. Throughout Chapter 3 I have shown results for my fiducial assumption $t_{\rm max} \sim \tau_\psi$, i.e. a dynamical friction process extending over the star formation duration in the host. However, energy/momentum feedback from the central BH could be effective in depleting the gas reservoir from the nuclear regions even before the galaxy-wide SFR is quenched, implying $t_{\rm max} \lesssim \tau_\psi$. As discussed in the text, a reasonable lower limit $t_{\rm max} \approx 5 \times 10^7$ yr applies; in this Appendix I discuss how the main results are affected by this choice.

In Figure D.1 (top panel) I show the merging rates density as a function of redshift. While pBHs mergers are reduced by a factor ~ 10, stellar compact remnants mergers are drastically cut by a factor $\sim 10^2$. The stronger impact on stellar compact remnants mergers can be understood since they tend to merge at later times, as seen from Figure 3.4. Merging rates from stellar compact remnants and pBHs now tend to be comparable for $f_{\rm pBH} \sim 1$, with a prevalence of pBH at $z \lesssim 2$ and of stellar compact remnants at $z \gtrsim 2$.

In Figure D.1 (bottom panel) I also present the chirp mass distribution of the merger events at $z \sim 2$. Since the process is stopped at a smaller $t_{\rm max} \approx 5 \times 10^7$ yr, when the central BH has still a mass $M_\bullet \lesssim 10^5\,{\rm M}_\odot$, the chirp mass distribution cannot extend above $\mathcal{M}_{\bullet\bullet} \sim 3000\,{\rm M}_\odot$.

In Figure D.2 I show the detection rates for ET, DECIGO and LISA as a function of redshift. The reduction of the detection rates for ET (top left panel) is not severe: a factor ~ 3 for stellar compact remnants and almost no reduction for pBHs. This is due to the fact that ET tends to detect low chirp mass events ($\mathcal{M}_{\bullet\bullet} \leq 500\,{\rm M}_\odot$) occurring during the early stages of the process; its detection rate is therefore only partially affected by a cut in the number of mergers at intermediate and late times. A slightly larger reduction can be seen in the ET detection rates for events with $\mathcal{M}_{\bullet\bullet} > 200\,{\rm M}_\odot$ (top

right panel); in particular, detected events from stellar compact remnants are reduced by a factor ~ 5 and from pBHs by a factor ~ 1.5.

For DECIGO (bottom left panel), probing both small and intermediate chirp mass regimes, the reduction is stronger with respect to ET: a factor ~ 30 for stellar compact remnants and ~ 3 for pBHs; however, a significant number of events per year is still detectable.

A dramatic effect can be seen for LISA (bottom right panel); the reduction of the detected events somewhat depends on redshift and on $f_{\rm pBH}$, being of the order of $\sim 10^2$ for stellar compact remnants and ~ 10 for pBHs. This is because LISA probes higher chirp masses $\mathcal{M}_{\bullet\bullet} \sim 1000-5000\,{\rm M}_\odot$ with respect to ET, where merging rates are suppressed (see bottom panel of Figure D.1).

Finally, in Figure D.3 I show the predictions for the SGWB generated by all the merging events (orange and blue patches for stellar compact remnants and pBHs, respectively) and by the residual unresolved events for ET (top panel), for DECIGO (middle panel) and for LISA (bottom panel). It can be noticed that there is an overall decrease of the intensity of the SGWB, especially at low frequencies $f \lesssim 0.1$ Hz, since late time mergers of a massive central BH contributing at those frequencies are cut away.

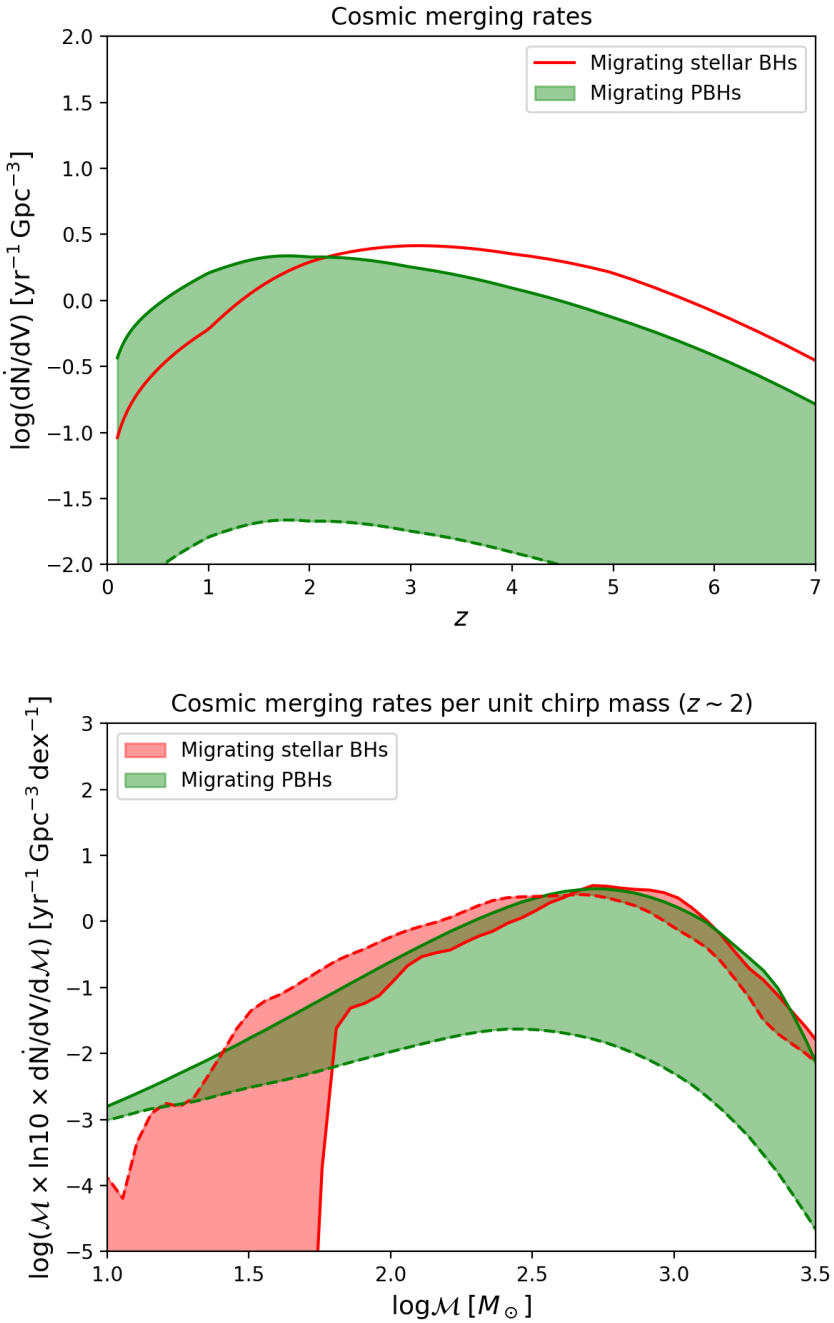

FIGURE D.1: Top panel: same as Figure 3.5 but for $t_{\rm max} \approx 5 \times 10^7$ yr. Bottom panel: same as Figure 3.6 but for $t_{\rm max} \approx 5 \times 10^7$ yr.

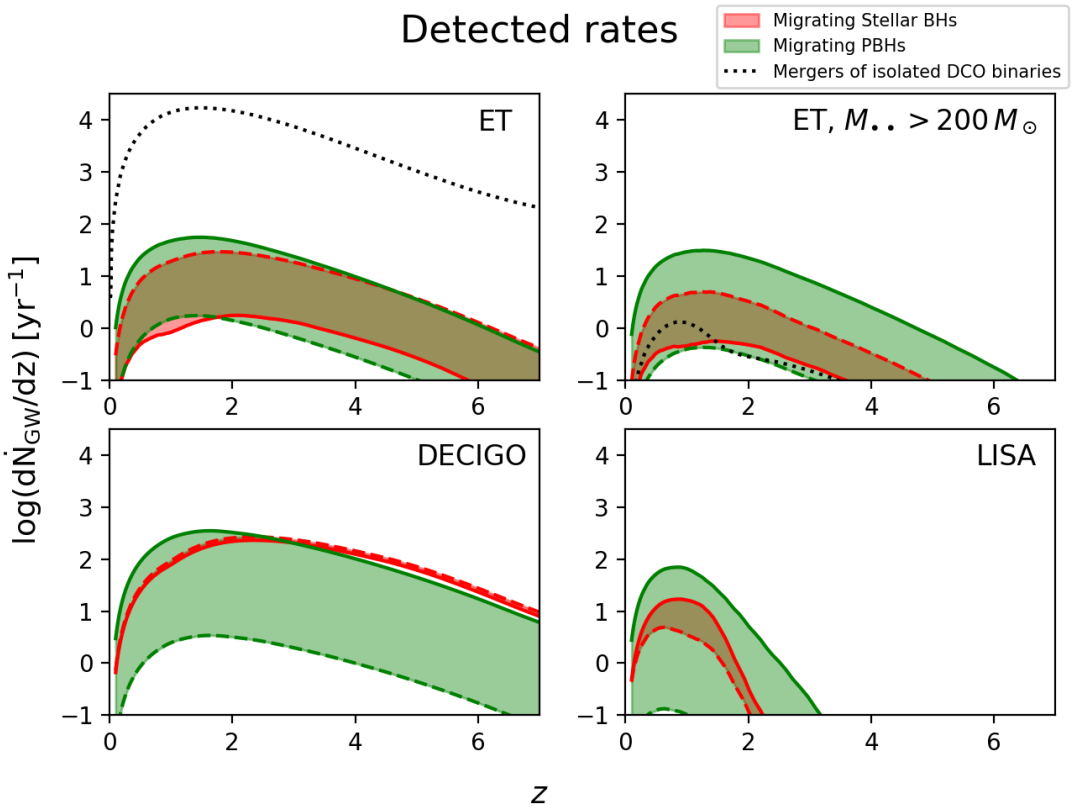

FIGURE D.2: Same as Figure 3.7 but for $t_{\rm max} \approx 5 \times 10^7$ yr.

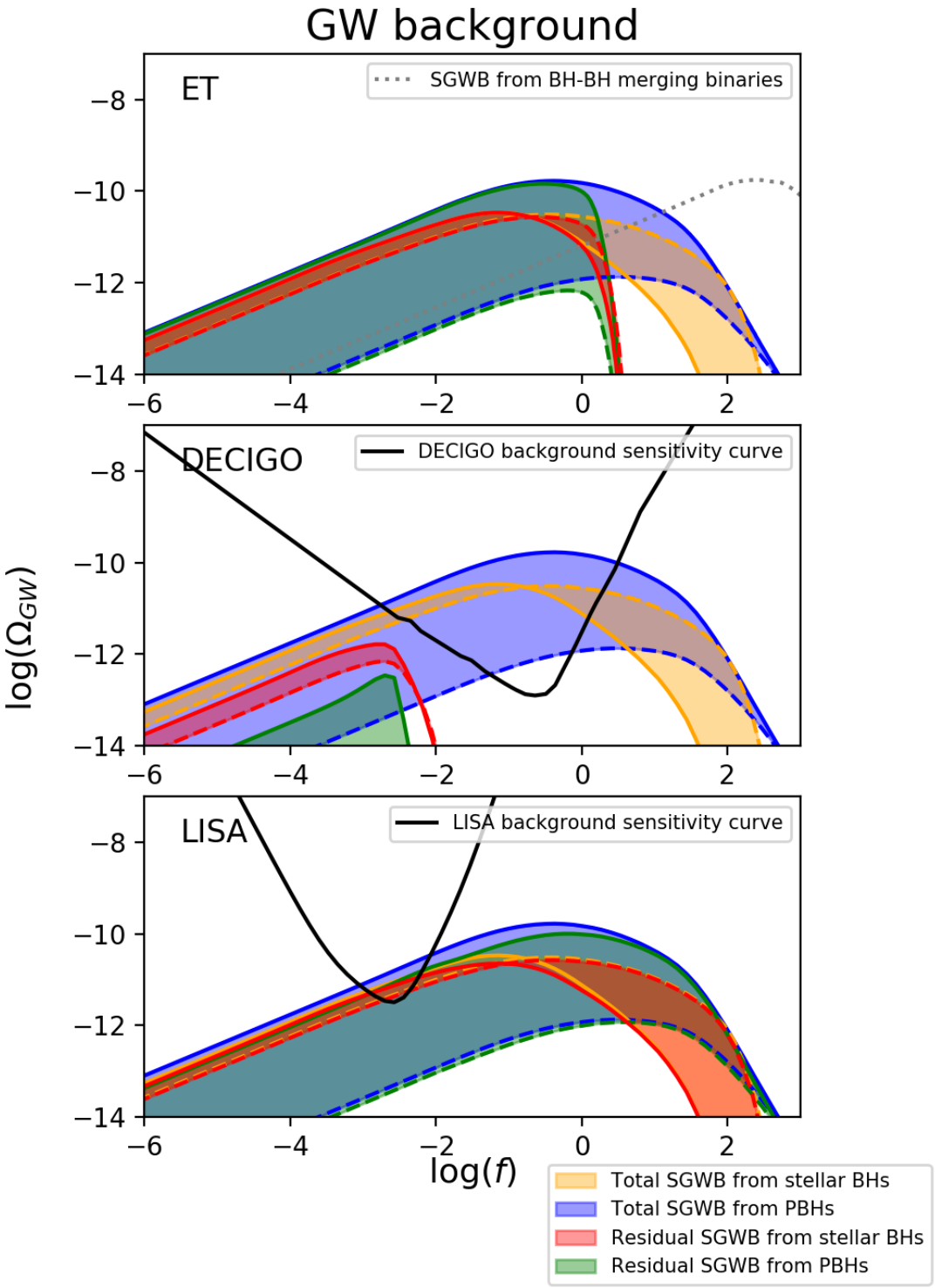

FIGURE D.3: Top panel: same as Figure 3.9 but for $t_{\rm max} \approx 5 \times 10^7$ yr. Middle panel: same as Figure 3.10 but for $t_{\rm max} \approx 5 \times 10^7$ yr. Bottom panel: same as Figure 3.11 but for $t_{\rm max} \approx 5 \times 10^7$ yr.

Bibliography

[1] Abbott, R., Abbott, T. D., Abraham, S., et al. 2021a, PhRvX, 11, 021053

[2] Abbott, R., Abbott, T. D., Abraham, S., et al. 2021b, ApJL, 913, L7

[3] Abbott, B. P., Abbott, R., Abbott, T. D., et al. 2018, PhRvL, 120, 091101

[4] Abbott, B. P., Abbott, R., Abbott, T. D., et al. 2017, PhRvL, 118, 221101

[5] Adamo, A., Zeidler, P., Kruijssen, J.M.D., et al. 2020, Sp. Sc. Rev., 470 216, 69

[6] Ajith, P., Babak, S., Chen, Y., et al. 2008, PhRvD, 77, 104017

[7] Aird, J., Coil, A. L., Georgakakis, A., et al. 2015, MNRAS, 451, 1892

[8] Alavi, A., Siana, B., Richard, J., et al. 2016, ApJ, 832, 56

[9] Andrews, B. H., & Martini, P. 2013, ApJ, 765, 140

[10] Antonini, F., Gieles, M., & Gualandris, A. 2019, MNRAS, 486, 5008

[11] Antonini, F., & Rasio, F. A. 2016, ApJ, 831, 187,

[12] Antonini, F., Barausse, E., & Silk, J. 2015, ApJL, 806, L8

[13] Arca Sedda, M., Mapelli, M., Spera, M., Benacquista, M., & Giacobbo, N. 2020, ApJ, 894, 133

[14] Arrigoni, M, Trager, S. C., Somerville, R. S., & Gibson, B. K. 2010, MNRAS, 402, 173

[15] Artale M.C., Mapelli, M., Giacobbo, N., et al. 2019, MNRAS 487, 1675

[16] Asano, R. S., Takeuchi, T. T., Hirashita, H., & Inoue, A. K. 2013, Earth Planets and Space, 65, 213

[17] Aversa, R., Lapi, A., de Zotti, G., Shankar, F., & Danese, L. 2015, ApJ, 810, 74

[18] Baldry, I. K., Driver, S. P., Loveday, J., et al. 2012, MNRAS, 421, 621

[19] Banados, E., Carilli, C., Walter, F., et al. 2018, ApJL, 861, L14

[20] Banerjee, S. 2021, MNRAS, 500, 3002

[21] Barack, L., Cardoso, V., Nissanke, S., et al. 2019, CQGra, 36, 14

[22] Barausse, E. 2012, MNRAS, 423, 2533

[23] Barrett, J.W., Gaebel, S.M., Neijssel, C.J., et al. 2018, MNRAS, 477, 4685

[24] Barro, G., Faber, S. M., Dekel, A., et al. 2016, ApJ, 820, 120

[25] Baxter, E.J., Croon, D., McDermott, S.D., & Sakstein, J. 2021, ApJL, 916, L16

[26] Begelman, M. C., Blandford, R. D., & Rees, M. J. 1980, Nat, 287, 307

[27] Behrendt, M, Burkert, A., & Schartmann, M. 2016, ApJL, 819, L2

[28] Behroozi, P., Wechsler, R. H., Hearin, A. P., & Conroy, C. 2019, MNRAS, 488, 3143

[29] Belczynski, K., Holz, D. E., Bulik, T., & O'Shaughnessy, R. 2016, Natur, 534, 512

[30] Belczynski, K., Dominik, M., Bulik, T., et al. 2010a, ApJL, 715, L138

[31] Belczynski, K., Bulik, T., Fryer, C.L., et al. 2010b, ApJ, 714, 1217

[32] Belczynski, K., Kalogera, V., Rasio, F. A., et al. 2008, ApJS, 174, 223

[33] Belli, S., Newman, A. B., & Ellis, R. S. 2017, ApJ, 834, 18

[34] Bernal, C. G., & Sanchez-Salcedo, F. J. 2013, ApJ, 775, 72

[35] Berta, S., Lutz, D., Genzel, R., Forster Schreiber, N. M., & Tacconi, L. J. 2016, A&A, 587, 73

[36] Béthermin, M., Daddi, E., Magdis, G., et al. 2015, A&A, 573, A113

[37] Béthermin, M., Daddi, E., Magdis, G., et al. 2012, ApJL, 757, L23

[38] Bhatawdekar, R., Conselice, C., Margalef-Bentabol, B., & Duncan, K. 2019, MNRAS, 486, 3805

[39] Bhattacharya, S. B., Heitmann, K., White, M., Lukic, Z., & Wagner, C. 2011, ApJ, 732, 122

[40] Binney, J., & Tremaine, S. 2008, Galactic Dynamics second edition

[41] Binney, J., & Tremaine, S. 1987, Galactic Dynamics (Princeton, NJ: Princeton Univ. Press)

[42] Bisigello, L., Caputi, K.I., Grogin, N., & Koekemoer, A. 2018, A&A, 609, 82

[43] Bisnovatyi-Kogan, G. S., Kazhdan, Ya. M., Klypin, A. A., Lutskii, A. E., & Shakura, N. I. 1979, SvA, 23, 201

[44] Blain, A. W. 1996, MNRAS, 283, 1340

[45] Boco, L., Lapi, A., Sicilia, A., et al. 2021, JCAP, 2021, 10, 035

[46] Boco, L., Lapi, A., Chruslinska, M., et al. 2021, ApJ, 907, 110

[47] Boco, L., Lapi, & Danese, L. 2020, ApJ, 891, 94

[48] Boco, L., Lapi, A., Goswami, S., et al. 2019, ApJ, 881, 157

[49] Boehringer, H., Chon, G., & Collins, C. A. 2014, A&A, 570, A31

[50] Bond, J. R., Cole, S., Efstathiou, G., & Kaiser, N. 1991, ApJ, 379, 440

[51] Bondi, H., & Hoyle, F. 1944, MNRAS, 104, 273

[52] Bonetti, M., Sesana, A., Haardt, F., Barausse, E., & Colpi, M. 2019, MNRAS, 486, 4044

[53] Boogaard, L. A., Decarli, R., González-López, J., et al. 2019, ApJ, 882, 140

[54] Boquien, M., Burgarella, D., Roehlly, Y., et al. 2019, A&A, 622, 103

[55] Bortolas, E., Capelo, P. R., Zana, T., et al. 2020, MNRAS, 498, 3601

[56] Bournaud, F., Perret, V., Renaud, F., et al. 2014, ApJ, 780, 57

[57] Bouwens, R. J., Oesch, P. A., Illingworth, G. D., Ellis, R. S., & Stefanon, M. 2017, ApJ, 843, 129

[58] Bouwens, R. J., Aravena, M., De Carli, R., et al. 2016, ApJ, 833, 72

[59] Bouwens, R. J., Illingworth, G. D., Oesch, P. A., et al. 2015, ApJ, 803, 34

[60] Boylan-Kolchin, M., Ma, C.-P., & Quataert, E. 2008, MNRAS, 383, 93

[61] Bromm, V., & Larson, R. B. , 2004, ARA&A, 42, 79

[62] Caffau, E., Ludwig, H. G., Steffen, M., Freytag, B., & Bonifacio, P. 2011, solphys, 268, 255

[63] Caldwell, R. R., Dave, R., Steinhardt, P. J. 1998, PhRvL, 80, 1582

[64] Calzetti, D., Armus, L., Bohlin, R. C., et al. 2000, ApJ, 533, 682

[65] Cantó, J., Esquivel, A., Sanchez-Salcedo, F. J., & Raga, A. C. 2013, ApJ, 762, 21

[66] Cao, L., Lu, Y., & Zhao, Y. 2018, MNRAS, 474, 4997

[67] Cappellari, M., McDermid, R. M., Alatalo, K., et al. 2013, MNRAS, 432, 1862

[68] Capurri, G., Lapi, A., Baccigalupi, C., et al. 2021, arXiv:2103.12037

[69] Caputi, K. I., Deshmukh, S., Ashby, M. L. N., et al. 2017, ApJ, 849, 45

[70] Carr, B., Kohri, K., Sendouda, Y., & Yokoyama, J. 2020, arXiv:2002.12778

[71] Carr, B.; Raidal, M.; Tenkanen, T.; Vaskonen, V.; & Veermäe, H. 2017, PhRvD, 96, 023514

[72] Carretta, E., Gratton, R. G., Clementini, G., & Fusi Pecci, F. 2000, ApJ, 533, 215

[73] Casey, M.C., Zavala, J.A., Spilker, J., et al. 2018, ApJ, 862, 67

[74] Casey, C. M., Narayanan, D., & Cooray, A. 2014, PhR, 541, 45

[75] Cassará, L. P., Maccagni, D., Garilli, B., et al. 2016, A&A, 593, A9

[76] Castro, T., Marra, V., & Quartin, M. 2016, MNRAS, 463, 1666

[77] Ceverino, D., Dekel, A., Mandelker, N., et al. 2012, MNRAS, 420, 3490

[78] Chabrier, G. 2003, ApJL, 586, L133

[79] Chandar, R., Fall, S.M., Whitmore, B.C., & Mulia, A.J. 2017, 510 ApJ, 849, 128

[80] Chandrasekhar, S. 1943, ApJ, 97, 255

[81] Chapon, D., Mayer, L., & Teyssier, R. 2013, MNRAS, 429, 3114

[82] Chiappini, C., Matteucci, F., & Gratton, R. 1997, ApJ, 477, 765

[83] Choi, J. H., Shlosman, I., & Begelman, M. C. 2013, ApJ, 774, 149

[84] Choi, J.H., Shlosman, I., & Begelman, M. C. 2015, ApJ, 450, 4411

[85] Chruslinska, M., Nelemans, G., Boco, L., & Lapi, A. 2021, arXiv:2109.06187

[86] Chruslinska, M., Nelemans, G., & Belczynski, K., 2019a, MNRAS, 482, 5012

[87] Chruslinska, M., & Nelemans, G. 2019b, MNRAS, 488, 5300

[88] Chruslinska, M., Belczynski, K., Klencki, J., & Benacquista, M. 2018, MNRAS, 474, 2937

[89] Cimatti A., Fraternali F., & Nipoti, C. 2020, Introduction to Galaxy Formation and Evolution

[90] Citro, A., Pozzetti, L., Moresco, M., & Cimatti, A. 2016, A&A, 592, A19

[91] Clemens, M. S., Negrello, M., de Zotti, G., et al. 2013, MNRAS, 433, 695

[92] Cooray, A., Calanog, J., Wardlow, J. L., et al. 2014, ApJ, 790, 40

[93] Coppin, K. E. K., Geach, J. E., Almaini, O., et al. 2015, MNRAS, 446, 1293

[94] Courteau, S., Cappellari, M., de Jong, R. S., et al. 2014, RvMP, 86, 47

[95] Crocce, M., Fosalba, P., Castander, F. J., & Gaztanaga, E. 2010, MNRAS, 403, 1353

[96] Crocker, K., Prestegard, T., Mandic, V., et al. 2017, PhRvD, 95, 063015

[97] Cucciati, O., Tresse, L., Ilbert, O., et al. 2012, A&A, 539, A31

[98] Cueli, M. M., Bonavera, L., González-Nuevo, J., & Lapi, A. 2021, A&A, 645, A126

[99] Cuesta, A. J., Prada, F., Klypin, A., & Moles, M. 2008, MNRAS, 389, 385

[100] Curti, M., Mannucci, F., Cresci, G., Maiolino, R. 2020, MNRAS, 491, 944

[101] da Cunha, E., Walter, F., Smail, I. R., et al. 2015, ApJ, 806, 110

[102] da Cunha, E., Charlot, S., & Elbaz, D. 2008, MNRAS, 388, 1595

[103] Daddi, E., Alexander, D. M., Dickinson, M., et al. 2007, ApJ, 670, 173ù

[104] Danovich, M., Dekel, A., Hahn, O., Ceverino, D., & Primack, J. 2015, MNRAS, 449, 2087

[105] Davé, R., Anglés-Alcázar, D., Narayanan, D., et al. 2019, MNRAS, 486, 2827

[106] Davé, R., Rafieferantsoa, M. H., Thompson, R. J., & Hopkins, P. F. 2017, MNRAS, 467, 115

[107] Davidzon, I., Ilbert, O., Laigle, C., et al. 2017, A&A, 605, A70

[108] Davies, F. B., Hennawi, J. F., & Eilers, A.-C. 2019, ApJL, 884, L19

[109] Davies, M. B. 2002, in ASP Conf. Proc. 263, Stellar Collisions, Mergers and their Consequences, ed. M. M. Shara (San Francisco, CA: ASP), 17

[110] Davis, S. W., & Laor, A. 2011, ApJ, 728, 98

[111] de la Rosa, I. G., La Barbera, F., Ferreras, I., et al. 2016, MNRAS, 457, 1916

[112] de Mink, S. E., & Belczynski, K. 2015, ApJ, 814, 58

[113] de Mink, S. E., Langer, N., Izzard, R. G., Sana, H., & de Koter, A. 2013, ApJ, 764, 166

[114] Delvecchio, I., Lutz, D., Berta, S., et al. 2015, MNRAS, 449, 373

[115] Delvecchio, I., Gruppioni, C., Pozzi, F., et al. 2014, MNRAS, 439, 2736

[116] Derdzinski, A. M., D'Orazio, D., Duffell, P., Haiman, Z., & MacFadyen, A. 2021, MNRAS, 501, 3540

[117] Derdzinski, A. M., D'Orazio, D., Duffell, P., Haiman, Z., MacFadyen, A. 2019, MNRAS, 486, 2754

[118] Devecchi, B., Volonteri, M., Rossi, E. M., Colpi, M., & Portegies Zwart, S. 2012, MNRAS, 421, 1465

[119] Di Carlo, Ugo N., Mapelli, Michela, Giacobbo, N., et al. 2020, MNRAS, 498, 495

[120] Di Carlo, U.N., Giacobbo, N, Mapelli, M., et al. 2019, MNRAS, 487, 2947

[121] Diemand, J., Moore, B., & Stadel, J. 2005, Natur, 433, 389

[122] Diemer, B., Mansfield, P., Kravtsov, A. V., & More, S. 2017, ApJ, 843, 140

[123] Diemer, B., More, S., & Kravtsov, A. V. 2013, ApJ, 766, 25

[124] Dokuchaev, V. P. 1964, SvA, 8, 23

[125] Dominik, M., Belczynski, K., Fryer, C., et al. 2012, ApJ, 759, 52

[126] Dominik, M., Berti, E., O'Shaughnessy, R., et al. 2015, ApJ, 806, 263

[127] Donevski, D., Lapi, A., Malek, K., et al. 2020, A&A, 644, A144

[128] Dong, F., Zhang, J., Yang, X., Zhang, J., & Luo, W. 2019, ApJ, 883, 155

[129] Dunlop, J. S., McLure, R. J., Biggs, A. D., et al. 2017, MNRAS, 466, 861

[130] Dvorkin, I., Vangioni, E., Silk, J., Uzan, J.-P., & Olive, K. A. 2016, MNRAS, 461, 3877

[131] Eales, S. A. 2015, MNRAS, 446, 3224

[132] Edgar, R. 2004, NewAR, 48, 843

[133] Efstathiou, A., Rowan-Robinson, M., & Siebenmorgen, R. 2000, MNRAS, 313, 734

[134] Eke, V. R., Cole, S., & Frenk, C. S. 1996, MNRAS, 282, 263

[135] El-Badry, K., Quataert, E., Weisz, D.R., Choksi, N., & Boylan-Kolchin, M. 2019, MNRAS, 482, 4528

[136] Elbaz, D., Daddi, E., Le Borgne, D., et al. 2007, A&A, 468, 33

[137] Elbert, O. D., Bullock, J. S., & Kaplinghat, M. 2018, MNRAS, 473, 1186

[138] Eldridge, J.J., Stanway, E.R., Xiao, L., et al. 2017, PASA, 34, e058

[139] Eldridge, J.J. , & Stanway, E.R. 2016, MNRAS, 462, 3302

[140] Elmegreen, B.G. 2018, ApJ, 869, 119

[141] Escala, A., Larson, R. B., Coppi, P. S., & Mardones, D. 2004, ApJ, 607, 765

[142] Fabian, A. C. 1999, MNRAS, 308, L39

[143] Fakhouri, O., & Ma, C.-P. 2008, MNRAS, 386, 577

[144] Fan, X., Strauss, M. A., Richards, G. T., et al. 2006, AJ, 131, 1203

[145] Finkelstein, S. L., Ryan, R. E., Jr., Papovich, C., et al. 2015, ApJ, 810, 71

[146] Franciolini, G., Baibhav, V., De Luca, V., et al. 2021, arXiv:2105.03349

[147] Fraternali, F. 2017, Gas Accretion onto Galaxies, Vol. 430 (Berlin: Springer), 323

[148] Fudamoto, Y., Oesch, P. A., Schinnerer, E., et al. 2017, MNRAS, 472, 483

[149] Fujii, M., Funato, Y., & Makino, J. 2006, PASJ, 58, 743

[150] Fukugita, M., & Peebles, P. J. E. 2004, ApJ, 616, 643

[151] Gallazzi, A., Charlot, S., Brinchmann, J., & White, S. D. M. 2006, MNRAS, 370, 1106

[152] Gallazzi, A., Bell, E. F., Zibetti, S., Brinchmann, J., & Kelson, D. D. 2014, ApJ, 788, 72

[153] Genel, S., Bouché, N., Naab, T., Sternberg, A., & Genzel, R. 2010, ApJ, 719, 229

[154] Genzel, R., Forster Schreiber, N. M., Ubler, H., et al. 2017, Natur, 543, 397

[155] Genzel, R., Tacconi, L. J., Lutz, D., et al. 2015, ApJ, 800, 20

[156] Genzel, R., Newman, S., Jones, T., et al. 2011, ApJ, 733, 101

[157] Giersz, M., Leigh, N., Hypki, A., Lutzgendorf, N., & Askar, A. 2015, MNRAS, 454, 3150

[158] Greif, T. H., Glover, S. C. O., Bromm, V., & Klessen, R. S. 2010, ApJ, 716, 510

[159] Grudic, M.Y., Kruijssen, J.M.D., Faucher-Giguere, C.A., et al. 2021, MNRAS 506, 3239

[160] Giacobbo, N., & Mapelli, M. 2018, MNRAS, 480, 2011

[161] Giacobbo, N., Mapelli, M., & Spera, M. 2018, MNRAS, 474, 2959

[162] Ginolfi, M., Jones, G. C., Béthermin, M., et al. 2020, A&A, 633, A90

[163] Goddard, Q.E., Bastian, N., & Kennicutt, R.C. 2010, MNRAS, 405, 857

[164] Grisoni, V., Spitoni, E., Matteucci, F., et al. 2017, MNRAS, 472, 3637

[165] Gruppioni C., Béthermin, M., Loiacono, F., et al. 2020, A&A, 643, A8

[166] Gruppioni, C., & Pozzi, F. 2019, MNRAS, 483, 1993

[167] Gruppioni, C., Calura, F., Pozzi, F., et al. 2015, MNRAS, 451, 3419

[168] Gruppioni, C., Pozzi, F., Rodighiero, G., et al. 2013, MNRAS, 432, 23

[169] Hansen, B. M. S., Brewer, J., Fahlman, G. G., et al. 2002, ApJL, 574, L155

[170] Hao, C.-N., Kennicutt, R. C. m., Johnson, B. D., et al. 2011, ApJ, 741, 124

[171] Hashimoto, Y., Funato, Y., & Makino, J. 2003, ApJ, 582, 196

[172] Heggie, D. C. 1975, MNRAS, 173, 729

[173] Hernquist, L. 1990, ApJ, 356, 359

[174] Hills, J. G., & Fullerton, L. W. 1980, AJ, 85, 1281

[175] Hirano, S., Hosokawa, T., Yoshida, N., et al. 2014, ApJ, 781, 60

[176] Hobbs, G., Lorimer, D. R., Lyne, A. G., & Kramer, M. 2005, MNRAS, 360, 974

[177] Hodge, J. A., Smail, I., Walter, F., et al. 2019, ApJ, 876, 130

[178] Hodge, J. A., Swinbank, A. M., Simpson, J. M., et al. 2016, ApJ, 833, 103

[179] Hopkins, P. F., Quataert, E., & Murray, N. 2012, MNRAS, 421, 3522

[180] Hopkins, A. M., & Beacom, J. F. 2006, ApJ, 651, 142

[181] Hosokawa, T., Omukai, K., & Yorke, H. W. 2012, ApJ, 756, 93

[182] Hosokawa, T., Yorke, H.W., Inayoshi. K., Omukai, K., & Yoshida, 2013, ApJ, 778, 178

[183] Howell, J. H., Armus, L., Mazzarella, J. M., et al. 2010, ApJ, 715, 572

[184] Hunt, L., Dayal, P., Magrini, L., & Ferrara, A. 2016, MNRAS, 463, 2002

[185] Hurley, J.R., Pols, O.R., & Tout, C.A. 2000, MNRAS, 315, 543

[186] Ikarashi, S., Ivison, R. J., Caputi, K. I., et al. 2015, ApJ, 810, 133

[187] Ilbert, O., Arnouts, S., Le Floc'h, E., et al. 2015, A&A, 579, 2

[188] Ilbert, O., McCracken, H. J., Le Févre, O., et al. 2013, A&A, 556, 55

[189] Jenkins, A., Frenk, C. S., White, S. D. M., et al. 2001, MNRAS, 321, 372

[190] Jiang, C. Y., Jing, Y. P., Faltenbacher, A., Lin, W. P., & Li, C. 2008, ApJ, 675, 1095

[191] Jimenez, R., Thejll, P., Jorgensen, U. G., MacDonald, J., & Pagel, B. 1996, MNRAS 282, 926

[192] Johansson, J., Thomas, D., & Maraston, C. 2012, MNRAS, 421, 1908

[193] Johnson, L.C., Seth, A.C., Dalcanton, J.J., et al. 2016, 827, 33

[194] Jones, T., Sanders, R., Roberts-Borsani, G., et al 2020, ApJ, 903, 150

[195] Juarez, Y., Maiolino, R., Mujica, R., et al. 2009, A&A, 494, L25

[196] Katz, M. L., Kelley, L. Z., Dosopoulou, F., et al. 2020, MNRAS, 491, 2301

[197] Kauffmann, G., White, S. D. M., & Guiderdoni, B. 1993, MNRAS, 264, 201

[198] Kelly, B. C., & Shen, Y. 2013, ApJ, 764, 45

[199] Kelvin, L. S., Driver, S. P., Robotham, A. S. G., et al. 2014a, MNRAS, 444, 1647

[200] Kelvin, L. S., Driver, S. P., Robotham, A. S. G., 2014b, MNRAS, 439, 1245

[201] Kennicutt, R. C., & Evans, N. J. 2012, ARA&A, 50, 531

[202] Kennicutt, R. C. 1998, ApJ, 498, 541

[203] Kewley, L. J., & Ellison, S. L. 2008, ApJ, 681, 1183

[204] Khusanova, Y., Le Févre, O., Cassata, P., et al. 2020, A&A, 634, A97

[205] Kim, H., & Kim, W.-T. 2009, ApJ, 703, 1278

[206] Kim, H., & Kim, W.-T. 2007, ApJ, 665, 432

[207] King, A., & Pounds, K. 2015, ARA&A, 53, 115

[208] King, A. 2005, ApJL, 635, L121

[209] King, A. 2003, ApJL, 596, L27

[210] Kistler, M. D., Yuksel, H., Beacom, J. F., et al. 2009, ApJL, 705, L104

[211] Kistler, M. D., Yuksel, H., & Hopkins, A. M. 2013, arXiv:1305.1630

[212] Klencki, J., Moe, M., Gladysz, W., et al. 2018, A&A, 619, A77

[213] Klimenko, S., Vedovato, G., Drago, M., et al. 2011, PhRvD, 83, 102001

[214] Klypin, A., Kravtsov, A. V., Valenzuela, O., & Prada, F. 1999, ApJ, 522, 81

[215] Koprowski, M. P., Dunlop, J. S., Michalowski, M. J., et al. 2016, MNRAS, 458, 4321

[216] Koprowski, M. P., Dunlop, J. S., Michalowski, M. J., Cirasuolo, M., & Bowler, R. A. A. 2014, MNRAS, 444, 117

[217] Kormendy, J., & Ho, L. C. 2013, ARA&A, 51, 511

[218] Kroupa, P. 2001, MNRAS, 322, 231

[219] Kruijssen, J.M.D. 2012, MNRAS, 426, 3008

[220] Kulkarni, G., & Loeb, A. 2012, MNRAS, 422, 1306

[221] Kulkarni, G., Worseck, G., & Hennawi, J. F. 2019, MNRAS, 488, 1035

[222] Kumamoto, J., Fujii, M. S., & Tanikawa, A. 2019, MNRAS, 486, 3942

[223] Lacey, C. G., & Cole, S. 1993, MNRAS, 262, 627

[224] Lahav, O., Lilje, P. B., Primack, J. R., & Rees, M. J. 1991, MNRAS, 251, 128

[225] Lamberts, A., Garrison-Kimmel, S., Clausen, D. R., & Hopkins, P. F. 2016, MNRAS, 463, L31

[226] Lamberts, A., Garrison-Kimmel, S., Hopkins, P. F., et al. 2018, MNRAS, 480, 2704

[227] Lang, P., Schinnerer, E., Smail, I., et al. 2019, ApJ, 879, 54

[228] Lapi, A., Pantoni, L., Boco, L., & Danese, L. 2020, ApJ, 897, 81

[229] Lapi, A., Pantoni, L., Zanisi, L., et al. 2018, ApJ, 857, 22

[230] Lapi, A., Mancuso, C., Bressan, A., & Danese, L. 2017a, ApJ, 847, 13

[231] Lapi, A., Mancuso, C., Celotti, A., & Danese, L. 2017b, ApJ, 835, 37

[232] Lapi, A., & Danese, L. 2014, JCAP, 2014, 044

[233] Lapi, A., Raimundo, S., Aversa, R., et al. 2014, ApJ, 782, 69

[234] Lapi, A., Negrello, M., Gonzalez-Nuevo, J., et al. 2012, ApJ, 755, 46

[235] Lapi, A., Gonzalez-Nuevo, J., Fan, L., et al. 2011, ApJ, 742, 24

[236] Lapi, A., Shankar, F., Mao, J., et al. 2006, ApJ, 650, 42

[237] Latif, M. A., & Ferrara, A. 2016, PASA, 33, 51

[238] Latif, M.A., & Schleicher, D. R. G. 2015, A&A, 578, 118

[239] Latif, M. A., Schleicher, D. R. G., Schmidt, W., & Niemeyer, J. 2013, MNRAS, 433, 1607

[240] Lee, A. T., & Stahler, S. W. 2011, MNRAS, 416, 3177

[241] Lee, A. T., & Stahler, S. W. 2014, A&A, 561, A84

[242] Li, L.-X. 2012, MNRAS, 424, 1461

[243] Li, J., Wang, R., Cox, P., et al. 2020, ApJ, 900, 131

[244] Li, P., Lelli, F., McGaugh, S., et al. 2019, ApJL, 886, L11

[245] Li, S. S., Mao, S., Zhao, Y., & Lu, Y. 2018, MNRAS, 476, 2220

[246] Liu, D., Schinnerer, E., Groves, B., et al. 2019, ApJ, 887, 235

[247] Liu, D., Daddi, E., Dickinson, M., et al. 2018, ApJ, 853, 172

[248] Lousto, C. O., Zlochower, Y., Dotti, M., & Volonteri, M. 2012, PhRvD, 85, 084015

[249] Lupi, A., Haardt, F., Dotti, M., et al. 2016, MNRAS, 456, 2993

[250] Lynden-Bell, D. 1967, MNRAS, 136, 101

[251] Madau, P., & Dickinson, M. 2014, ARA&A, 52, 415

[252] Madau, P., Haardt, F., & Dotti, M. 2014, ApJL, 784, L38

[253] Maeder, A. 1992, A&A, 264, 105

[254] Magnelli, B., Popesso, P., Berta, S., et al. 2013, A&A, 553, A132

[255] Magnelli, B., Lutz, D., Berta, S., et al. 2012, A&A, 548, A22

[256] Maiolino, R., Mannucci, F. 2019, A&AR, 27, 3

[257] Maiolino, R., Nagao, T., Grazian, A., et al. 2008, A&A, 488, 463

[258] Mancuso, C., Lapi, A., Prandoni, I., et al. 2017, ApJ, 842, 95

[259] Mancuso, C., Lapi, A., Shi, J., et al. 2016a, ApJ, 823, 128

[260] Mancuso, C., Lapi, A., Shi, J., et al. 2016b, ApJ, 833, 152

[261] Mandelker, N., Dekel, A., Ceverino, D., et al. 2014, MNRAS, 443, 3675

[262] Mandelker, N., Dekel, A., Ceverino, D., et al. 2017, MNRAS, 464, 635

[263] Mannucci, F., Salvaterra, R., Campisi, M. A. 2011, MNRAS, 414, 1263

[264] Mannucci, F., Cresci, G., Maiolino, R., Marconi, A., & Gnerucci, A. 2010, MNRAS, 408, 2115

[265] Mannucci, F., Cresci, G., Maiolino, R., et al. 2009, MNRAS, 398, 1915

[266] Maoz, D., Mannucci, F., & Nelemans, G. 2014, ARA&A, 52, 107

[267] Mapelli, M., Dall'Amico, M., Bouffanais, Y., et al. 2021a, MNRAS, 505, 339

[268] Mapelli, M., Santoliquido, F., Bouffanais, Y., et al. 2021b, Symmetry, 13, 1678

[269] Mapelli, M., Giacobbo, N., Santoliquido, F., & Artale, M. C. 2019, MNRAS, 487, 2

[270] Mapelli, M., Giacobbo, N., Toffano, M., et al. 2018, MNRAS, 481, 5324

[271] Mapelli, M., & Giacobbo, N. 2018, MNRAS, 479, 4391

[272] Mapelli, M., Giacobbo, N., Ripamonti, E., & Spera, M. 2017, MNRAS, 472, 2422

[273] Mapelli, M. 2016, MNRAS, 459, 3432

[274] Marrone, D. P., Spilker, J. S., Hayward, C. C., et al. 2018, Natur, 553, 51

[275] Martinez, H. J., Zandivarez, A., Merchan, M. E., & Dominguez, M. J. L. 2002, MNRAS, 337, 1441

[276] Massardi, M., Enia, A. F. M., Negrello, M., et al. 2018, A&A, 610, A53

[277] Mayer, L., & Bonoli, S. 2019, RPPh, 82, a6901

[278] Mayer, L., Fiacconi, D., Bonoli, S., et al. 2015, ApJ, 810, 51

[279] Mayer, L., Kazantzidis, S., Escala, A., & Callegari, S. 2010, Natur, 466, 1082

[280] Mayer, L., Kazantzidis, S., Madau, P., et al. 2007, Sci, 316, 1874

[281] McConnell, N. J., & Ma, C.-P. 2013, ApJ, 764, 184

[282] Mehrgan, K., Thomas, J., Saglia, R., et al. 2019, ApJ, 887, 195

[283] Merritt, D., & Milosavljevic, M. 2005, LRR, 8, 8

[284] Meurer, G. R., Heckman, T. M., & Calzetti, D. 1999, ApJ, 521, 64

[285] Miller, M.C., & Hamilton, D.P. 2002, ApJ, 576, 894

[286] Mo, H., van den Bosch, F., & White, S. D. M. 2010, Galaxy Formation and Evolution (Cambridge: Cambridge Univ. Press)

[287] Moffett, A. J., Ingarfield, S. A., Driver, S. P., et al. 2016, MNRAS, 457, 1308

[288] Moore, C. J.; Cole, R. H.; & Berry, C. P. L. 2015, CQGra, 32, 1

[289] More, S., Diemer, B., & Kravtsov, A. V. 2015, ApJ, 810, 36

[290] Morishita, T., Abramson, L. E., Treu, T., et al. 2019, ApJ, 877, 141

[291] Mortlock, D. J., Warren, S. J., Venemans, B. P., et al. 2011, Natur, 474, 616

[292] Moster, B. P., Naab, T., & White, S. D. M. 2013, MNRAS, 428, 3121

[293] Moustakas, J., Coil, A. L., Aird, J., et al. 2013, ApJ, 767, 50

[294] Mullaney, J. R., Daddi, E., Bethermin, M., et al. 2012, ApJL, 753, L30

[295] Muzzin, A., van der Burg, R. F. J., McGee, S. L., et al. 2014, ApJ, 796, 65

[296] Muzzin, A., Marchesini, D., Stefanon, M. 2013, ApJ, 777, 18

[297] Navarro, J. F., Frenk, C. S., & White, S. D. M. 1996, ApJ, 462, 563

[298] Negrello, M., Hopwood, R., De Zotti, G., et al. 2010, Sci, 330, 800

[299] Negrello, M., Perrotta, F., Gonzalez-Nuevo, J., et al. 2007, MNRAS, 377, 1557

[300] Neijssel, C.J., Vigna-Gomez, A., Stevenson S., et al. 2019, MNRAS, 490, 3740

[301] Novak, M., Banados, E., Decarli, R., et al. 2019, ApJ, 881, 63

[302] Novak, M., Smolcic, V., Delhaize, J., et al. 2017, A&A, 602, 5

[303] O'Shaughnessy, R., Bellovary, J. M., Brooks, A., et al. 2017, MNRAS, 464, 2831

[304] Oguri, M. 2018, MNRAS, 480, 3842

[305] Oesch, P. A., Bouwens, R. J., Carollo, C. M., et al. 2010, ApJL, 725, L150

[306] Oklopcic, A., Hopkins, P. F., Feldmann, R., et al. 2017, MNRAS, 465, 952

[307] Onodera, M., Carollo, C. M., Lilly, S., et al. 2016, ApJ, 822, 42

[308] Onoue, M., Banados, E., Mazzucchelli, C., et al. 2020, ApJ, 898, 105

[309] Ostriker, E. C. 1999, ApJ, 513, 252

[310] Ostriker, J. P., & McKee, C. 1988, RvMP, 60, 1

[311] Page, M. J., Symeonidis, M., Vieira, J., et al. 2012, Natur, 485, 213

[312] Pantoni, L., Lapi, A., Massardi, M., Goswami, S., & Danese, L. 2019, ApJ, 880, 129

[313] Papovich, C., Finkelstein, S. L., Ferguson, H. C., Lotz, J. M., & Giavalisco, M. 2011, MNRAS, 412, 1123

[314] Pearson, E. A., Eales, S., Dunne, L., et al. 2013, MNRAS, 435, 2753

[315] Peng, Y., Maiolino, R., & Cochrane, R. 2015, Natur, 521, 192

[316] Perlmutter, S., Aldering, G., Goldhaber, G., et al. 1999, ApJ, 517, 565

[317] Perrotta, F., Baccigalupi, C., Bartelmann, M., De Zotti, G., & Granato, G. L. 2002, MNRAS, 329, 445

[318] Peters, P. C. 1964, PhRv, 136, 1224

[319] Pezzulli, G., & Fraternali, F. 2016, MNRAS, 455, 2308

[320] Pfeffer, J., Kruijssen, J.M.D., Crain, R.A., & Bastian, N. 2018, MNRAS, 475, 4309

[321] Popesso, P., Concas, A., Morselli, L., et al. 2019, MNRAS, 483, 3213

[322] Popping, G., Somerville, R. S., & Galametz, M. 2017, MNRAS, 471, 3152

[323] Portegies Zwart, S. F., Baumgardt, H., Hut, P., Makino, J., & McMillan, S. L. W. 2004, Natur, 428, 724

[324] Portegies Zwart, S.F. , & Yungelson, L.R. 1998, A&A, 332, 173

[325] Press, W. H., & Schechter, P. 1974, ApJ, 187, 425

[326] Prugniel, P., & Simien, F. 1997, A&A, 321, 111

[327] Raimundo, S. I., Fabian, A. C., Vasudevan, R. V., Gandhi, P., & Wu, J. 2012, MNRAS, 419, 2529

[328] Reddy, N. A., Kriek, M., Shapley, A. E., et al. 2015, ApJ, 806, 259

[329] Regan, J. A., Downes, T. P., Volonteri, M., et al. 2019, MNRAS, 486, 3892

[330] Rephaeli, Y., & Salpeter, E. E. 1980, ApJ, 240, 20

[331] Riechers, D. A., Leung, T. K. D., Ivison, R. J., et al. 2017, ApJ, 850, 1

[332] Riess, A. G., Filippenko, A. V., & Challis, P. 1998, AJ, 116, 1009

[333] Robson, T., Cornish, N. J., & Liu, C. 2019, CQGra, 36, j5011

[334] Rodighiero, G., Enia, A., Delvecchio, I., et al. 2019, ApJL, 877, L38

[335] Rodighiero, G., Brusa, M, Daddi, E., et al. 2015, ApJL, 800, L10

[336] Rodighiero, G., Daddi, E., Baronchelli, I., et al. 2011, ApJL, 739, L40

[337] Rodriguez, C.L., Kremer, K., Chatterjee, S., et al. 2021, RNAAS, 5, 19

[338] Rodriguez, C.L., Morscher, M., Pattabiraman, B., et al. 2015, PhRvL, 115e1101

[339] Romano, D., Silva, L., Matteucci, F., & Danese, L. 2002, MNRAS, 334, 444

[340] Rowan-Robinson, M., Oliver, S., Wang, L., et al. 2016, MNRAS, 461, 1100

[341] Rowlands, K., Dunne, L., Dye, S., et al. 2014, MNRAS, 441, 1017

[342] Rubin, V. C., Ford, W. K., & Thonnard, N. 1980, ApJ, 238, 471

[343] Ruderman, M. A., & Spiegel, E. A. 1971, ApJ, 165, 1

[344] Rujopakarn, W., Daddi, E., Rieke, G. H., et al. 2019, ApJ, 882, 107

[345] Rujopakarn, W., Dunlop, J. S., Rieke, G. H., et al. 2016, ApJ, 833, 12

[346] Ryden B. S. 2003, Introduction to Cosmology

[347] Sanchez-Salcedo, F., & Brandenburg, A. 2001, MNRAS, 322, 67

[348] Sanchez-Salcedo, F. J., & Chametla, R. O. 2018, MNRAS, 481, 4863

[349] Sanders, R. L., Shapley, A. E., Jones, T., et al. 2021, ApJ, 914, 19

[350] Sanders, R. L., Shapley, A. E., Reddy, N. A., et al. 2020, MNRAS, 491, 1427

[351] Santoliquido, F., Mapelli, M., Giacobbo, N., Bouffanais, Y., & Artale, M. C. 2021, MNRAS, 502, 4877

[352] Saracco, P., Marchesini, D., La Barbera, F., et al. 2020, ApJ, 905, 40

[353] Sargent, M. T., Béthermin, M., Daddi, E., & Elbaz, D. 2012, ApJL, 747, L31

[354] Sasaki, M.; Suyama, T.; Tanaka, T.; & Yokoyama, S. 2018, CQGra, 35, 6

[355] Scelfo, G., Spinelli, M., Raccanelli, A., et al 2021, arXiv:2106.09786

[356] Scelfo, G., Boco, L., Lapi, A., Viel, M. 2020, JCAP, 2020, 10, 045

[357] Scelfo, G., Bellomo, N., Raccanelli, A., Matarrese, S., & Verde, L. 2018, JCAP, 2018, 9, 039

[358] Schechter, P. 1976, ApJ, 203, 297

[359] Schiminovich, D., Ilbert, O., Arnouts, S., et al. 2005, ApJL, 619, L47

[360] Schmidt, M. 1959, ApJ, 129, 243

[361] Schreiber, C., Labbé, I., Glazebrook, K., et al. 2018, A&A, 611, A22

[362] Schreiber, C., Pannella, M., Elbaz, D., et al. 2015, A&A, 575, 74

[363] Scoville, N., Aussel, H., Sheth, K., et al. 2014, ApJ, 783, 84

[364] Scoville, N., Lee, N., Vanden Bout, P., et al. 2017, ApJ, 837, 150

[365] Scoville, N., Sheth, K., Aussel, H., et al. 2016, ApJ, 820, 83

[366] Sersic, J. L. 1968

[367] Shakura, N. I, & Sunyaev, R. A. 1973, A&A, 24, 337

[368] Shankar, F., Bernardi, M., Sheth, R. K., et al. 2016, MNRAS, 460, 3119

[369] Shapley, A. E., Cullen, F., Dunlop, J. S., et al. 2020, ApJL, 903, L16

[370] Sheth, R.K., & Tormen, G. 2002, MNRAS, 329, 61

[371] Sheth, R. K., Mo, H. J., & Tormen, G. 2001, MNRAS, 323, 1

[372] Sheth, R.K., & Tormen, G. 1999, MNRAS, 308, 119

[373] Shi, J., Lapi, A., Mancuso, C., Wang, H., & Danese, L. 2017, ApJ, 843, 105

[374] Sicilia, A., Lapi, A., Boco, L., et al. 2021, in preparation

[375] Silk, J., & Rees, M. J. 1998, A&A, 331, L1

[376] Silva, J. M., Lima, J. A. S., & de Souza, R. E. 2016, JCAP, 05, 021

[377] Silva, L., Granato, G. L., Bressan, A., & Danese, L. 1998, ApJ, 509, 103

[378] Simpson, J. M., Smail, I., Swinbank, A. M., et al. 2015, ApJ, 807, 128

[379] Smail, I., Duszeviciute, U., Stach, S. M., et al. 2021, MNRAS, 502, 3426

[380] Smit, R., Bouwens, R. J., Franx, M., et al. 2012, ApJ, 756, 14

[381] Song, M., Finkelstein, S. L., Ashby, M. L. N., et al. 2016, ApJ, 825, 5

[382] Sonnenfeld, A., Wang, W., & Bahcall, N. 2019, A&A, 622, A30

[383] Speagle, J. S., Steinhardt, C. L., Capak, P. L., & Silverman, J. 2014, ApJS, 214, 15

[384] Spera, M., Mapelli, M., Giacobbo, N., et al. 2019, MNRAS, 485, 889

[385] Spera, M., & Mapelli, M. 2017, MNRAS, 470, 4739

[386] Spera, M., Mapelli, M., & Bressan, A. 2015, MNRAS, 451, 4086

[387] Spilker, J. S., Marrone, D. P., Aravena, M., et al. 2016, ApJ, 826, 112

[388] Spolaor, M, Kobayashi, C., Forbes, D. A., Couch, W. J., & Hau, G. K. T. 2010, MNRAS, 408, 272

[389] Springel, V., Frenk, C. S., & White, S. D. M. 2006, Natur, 440, 1137

[390] Stacey, H. R., McKean, J. P., Robertson, N. C., et al. 2018, MNRAS, 476, 5075

[391] Stanley, F., Alexander, D. M., Harrison, C. M., et al. 2017, MNRAS, 472, 2221

[392] Stanley, F., Harrison, C. M., Alexander, D. M., et al. 2015, MNRAS, 453, 591

[393] Steinhardt, C. L., Speagle, J. S., & Capak, P. 2014, ApJL, 791, L25

[394] Stevenson, S., Vigna-Gómez, A., Mandel, I., et al. 2017, NatCo, 8, 14906

[395] Strait, V., Bradac, M., Coe, D., et al. 2020, ApJ, 888, 124

[396] Strandet, M. L., Weiss, A., Vieira, J. D., et al. 2016, ApJ, 822, 80

[397] Swinbank, A. M., Smail, I., Longmore, S., et al. 2010, Natur, 464, 733

[398] Tacconi, L. J., Genzel, R., & Sternberg, A. 2020, ARA&A, 58, 157

[399] Tacconi, L. J., Genzel, R., Saintonge, A., et al. 2018, ApJ, 853, 179

[400] Tadaki, K., Iono, D., Yun, M. S., et al. 2018, Natur, 560, 613

[401] Tadaki, K.-I., Genzel, R., Kodama, T., et al. 2017a, ApJ, 834, 135

[402] Tadaki, K.-I., Kodama, T., Nelson, E. J., et al. 2017b, ApJL, 841, L25

[403] Tagawa, H., Umemura, M., & Gouda, N. 2016, MNRAS, 462, 3812

[404] Takahashi, R., & Nakamura, T. 2003, ApJ, 595, 1039

[405] Tan, Q., Daddi, E., Magdis, G., et al. 2014, A&A, 569, A98

[406] Talia, M., Pozzi, F., Vallini, L., et al. 2018, MNRAS, 476, 3956

[407] Tamburello, V., Capelo, P. R., Mayer, L., Bellovary, J. M., & Wadsley, J. W. 2017, MNRAS, 464, 2952

[408] Tamburello, V., Mayer, L., Shen, S., & Wadsley, J. 2015, MNRAS, 453, 2490

[409] Tanaka, T., & Haiman, Z. , 2009, A&A, 696, 1798

[410] Taylor, S. R., & Gair, J. R. 2012, PhRvD, 86, 023502

[411] Teklu, A. F., Remus, R.-S., Dolag, K., et al. 2018, ApJL, 854, L28

[412] Thomas, D., Maraston, C., Schawinski, K., Sarzi, M., & Silk, J. 2010, MNRAS, 404, 1775

[413] Thomas, D., Maraston, C., Bender, R., & Mendes de Oliveira, C. 2005, ApJ, 621, 673

[414] Thrane, E., & Romano, D. 2013, PhRvD, 88, 124032

[415] Thun, D., Kuiper, R., Schmidt, F., & Kley, W. 2016, A&A, 589, A10

[416] Tinker, J. L., Leauthaud, A., Bundy, K., et al. 2013, ApJ, 778, 93

[417] Tinker, J. L., Kravtsov, A. V., Klypin, A., et al. 2008, ApJ, 688, 709

[418] Tomczak, A. R., Quadri, R. F., Tran, K. H., et al. 2014, ApJ, 783, 85

[419] Tonini, C., Lapi, A., & Salucci, P. 2006, ApJ, 649, 591

[420] Torrey, P., Vogelsberger, M., Hernquist, L., et al. 2018, MNRAS, 477, L16

[421] Tumlinson, J., Peeples, M. S., & Werk, J. K. 2017, ARA&A, 55, 389

[422] van den Bosch, F. C., Lewis, G. F., Lake, G., & Stadel, J. 1999, ApJ, 515, 50

[423] van der Burg, R. F. J., Hildebrandt, H., & Erben, T. 2010, A&A, 523, A74

[424] van der Wel, A., & van der Marel, R. P. 2008, ApJ, 684, 260

[425] van Dokkum, P. G., Nelson, E. J., Franx, M., et al. 2015, ApJ, 813, 23

[426] Venemans, B. P., Decarli, R., Walter, F., et al. 2018, ApJ, 866, 159

[427] Venemans, B. P., Walter, F., Decarli, R., et al. 2017a, ApJL, 851, L8

[428] Venemans, B. P., Walter, F., Decarli, R., et al. 2017b, ApJ, 845, 154

[429] Vestergaard, M. 2019, NatAs, 3, 11

[430] Vestergaard, M., & Osmer, P. S. 2009, ApJ, 699, 800

[431] Vijayan, A. P., Clay, S. J., Thomas, P. A., et al. 2019, MNRAS, 489, 4072

[432] Vink, J.S., de Koter, A., & Lamers H.J.G.L.M. 2001, A&A, 369, 574

[433] Volonteri, M., Silk, J., & Dubus, G. 2015, ApJ, 804, 148

[434] Volonteri, M. 2012, Science, 337, 544

[435] Wang, T., Schreiber, C., Elbaz, D., et al. 2019, Natur, 572, 211

[436] Warren, M. S., Abazajian, K., Holz, D. E., & Teodoro, L. 2006, ApJ, 646, 881

[437] Watson, W. A., Iliev, I. T., D'Aloisio, A., et al. 2013, MNRAS, 433, 1230

[438] Weiss, A., De Breuck, C., Marrone, D. P., et al. 2013, ApJ, 767, 88

[439] Weinberg, S. 2008, Cosmology (Oxford: Oxford Univ. Press)

[440] Weinberg, S. 1972, Gravitation and Cosmology

[441] Whitaker, K. E., Franx, M., Leja, J., et al. 2014, ApJ, 795, 104

[442] Woosley, S. E. 2017, ApJ, 836, 244

[443] Woosley, S. E., Heger, A., & Weaver, T. A. 2002, RvMP, 74, 1015

[444] Wyder, T. K., Treyer, M. A., Milliard, B., et al. 2005, ApJL, 619, L15

[445] Wu, S., Lu, Y., Zhang, F., & Lu, Y. 2013, MNRAS, 436, 3271

[446] Yu, Q. 2002, MNRAS, 331, 935

[447] Zahid, H. J., Kashino, D., Silverman, J. D., et al. 2014, ApJ, 792, 75

[448] Zavala, J. A., Montana, A., Hughes, D. H., et al. 2018, NatAs, 2, 56

[449] Zavala, J., Frenk, C. S., Bower, R., et al. 2016, MNRAS, 460, 4466

[450] Zehavi, I., Zheng, Z., Weinberg, D. H., et al. 2011, ApJ, 736, 59

[451] Zehavi, I., Zheng, Z., Weinberg, D. H., et al. 2005, ApJ, 630, 1

[452] Zemp, M. 2014, ApJ, 792, 124

[453] Zheng, Z., Zehavi, I., Eisenstein, D. J., Weinberg, D. H., & Jing, Y. P. 2009, ApJ, 707, 554

[454] Zheng, Z., Coil, A. L., & Zehavi, I. 2007, ApJ, 667, 760

[455] Zhu, X.-J., Howell, E., Regimbau, T., Blair, D., & Zhu, Z.-H. 2011, ApJ, 739, 86

[456] Zolotov, A., Dekel, A., Mandelker, N., & Tweed, D. 2015, MNRAS, 450, 2327

[457] Zwicky, F. 1933, Helvetica Physica Acta, 6, 110